DEPARTMENT OF CIVIL & ENVIRONMENTAL ENGINEERING

University of Strathclyde

Department of Civil and Environmental Engineering

Prediction of cracking in steel joint subjected to high cyclic strains

by

Wajdi Aboalriha B.Eng, MSc

A thesis presented in fulfilment of the requirements for the Degree of Doctor of Philosophy

Glasgow, United Kingdom

2015

Copyright statement

Signed: *Date:*

In the name of God the Merciful the Most Gracious

I would like to dedicate this thesis to my parents, my wife and my children:

ASAL and MOHAMMED,

the best gifts that God ever gave me.
And also to my brothers and sisters.

ABSTRACT

During earthquakes, structures can be subject to many cycles of high strain. This can lead to cracking and a serious reduction in strength in comparison with the usual assumption of maintained strength during ductile cycling.

This study reviews various methods for the prediction of cracking and compares them with results available in the literature.

Crack prediction can be performed using one of the three basic methodologies: stress-life theory, strain-life theory, and the crack growth approach. These techniques are developed to determine the number of cycles to failure. Stress life theory is suitable when elastic stresses and strains are considered. However, for the components having nominal cyclic elastic stresses but local plastic deformation, local strain-life theory is used for predicting the fatigue life. In this work, the behaviour of a fully welded steel connection subjected to cyclic displacement loading, is analysed using the strain-life theories.

Based on the results, it can be concluded that:
FE modelling, in conjunction with strain life equations can approximately estimate the cycles to failure at the observed crack location on a beam framing into the connection.

However the more highly stressed area in the connections “panel zone” did not crack in the experiments, perhaps because of the more complex stress field and defect orientation to the tensile stresses in this location.
The connection was improved by adding triangular bracing gussets, in the plane of the beam and column webs. The FE model showed that stress and strain were decreased and the high strains moved from the panel zone to the gussets.

ACKNOWLEDGEMENTS

The author would like to express his deepest and most sincere gratitude to his supervisor Prof. Nigel Barltrop, Department of Naval and Architectural Engineering, for his continuous guidance, encouragement and sharing valuable time throughout the work. It is also much pleasure to acknowledge his untiring help, without supplying supporting valuable references and information this work could not have been completed.

The author would like to thank Prof. Luis Calado of the Dept. of Civil Engineering and Architecture, Instituto Superior Tecnico, Lisbon, for his experimental related work information and support without his invaluable help this research could not have been completed.

Special thanks extended to Dr. Karim Jaballi of the Department of Mechanical Engineering, Caledonian college of Engineering in Oman for his SolidWorks software support. The author also wishes to thank his friend Layth Abbas (Information Technology engineer) for his computer hardware and software support and his encouragement to finish this work successfully.

The author would like to thank Dr.Abas Hadawey of the Department of Mechanical Engineering, University of Ulster, Northern Ireland, UK for his advice and support.

The author also wishes to thank his colleagues and staffs of the Department of Civil & Environmental Engineering and Department of Naval and Architectural Engineering of their sincere co-operation during this research work especially Mr. Gurpreet Grewal for his support and help in ANSYS programme.

The author is deeply indebted to his parents for their encouragements and support. The author also wishes that very special thanks go to his wife, who has sacrificed time and companionship to complete this work.

The author is expressing his feeling towards his children *ASAL and MOHAMMED* during his research work when he was living far from them.

TABLE OF CONTENTS

Page

LIST OF FIGURES

Page

LIST OF TABLES

Page

NOTATIONS

All symbols used in this thesis are defined where they first appear. For the reader's convenience, the principal meanings of the commonly used notations are contained in the list below. The reader is cautioned that some symbols denote more than one quantity; in such cases the meaning should be clear when read in context.

Abbreviations

ACI	American Concrete Institute
AISC	American Institute of Steel Construction
ASCE	American Society of Civil Engineers
ASTM	American Society of Testing and Materials
AISI	American Iron and Steel Institute
BS	British Standard
ECCS	European Convention for Constructional Steelwork
ISMC	Indian standard medium channel

Roman Symbols

$a_{\circ}$	initial crack depth
b	fatigue strength exponent
c	fatigue ductility exponent
CVN	Charpy V-Notch
CTOD, δ	Crack Tip Opening Displacement
CJP	Complete Joint Penetration
CFSHS	cold-formed structural hollow section

dc	column depth
db	beam depth
da/dN	Crack growth rate
d/*H*	applied interstory drift angle
DNV	DET NORSKE VERITAS
DIF	fatigue crack initiation damage
DF	fatigue crack propagation damage
DMA	damage mechanics approach
D_f	fatigue damage
E	Modulus of elasticity
EPFM	elastic-plastic fracture mechanics
Ei	energy absorbed in single plastic cycle
*E*el,pl	energy absorbed in elastic-perfectly plastic cycle
ELCF	extremely low cycle fatigue
*f*y	yield stress
*f*u	ultimate tensile strength
f	frequency
FE	Finite Element
FEA	Finite Element Analysis
FAD	Failure Assessment Diagram
FCAW	Flux Core Arc Welding
FEM	Finite Element Method

FF	free flange connections
FDI	Fatigue damage index
FMA	fracture mechanics approach
FDI	fatigue damage index
G	strain energy release rate
HAZ	Heated Affected Zone
HCF	High cycle Fatigue
HFSHS	hot-formed structural hollow section
Ib	strong axis section moment of inertia for beam
Ic	strong axis section moment of inertia for column
J	J integral
K	stress intensity factor
K_{mat}	fracture toughness
K_{th}	Threshold for the crack
Kc	critical stress intensity factor (fracture toughness)
Kr	toughness ratio
K_I	stress intensity factor (mode I)
LVDT	Linear variable displacement transducer
LCF	Low Cycle Fatigue
L/D	length to the depth ratio
LCF	Low cycle Fatigue
LEFM	linear-elastic fracture mechanics

Lr	stress ratio
Lc	column length
Lb	beam length
m	a dimensionless constant that depends on the material properties and the stress states
MP	Moment resistance
n'	strain hardening exponent
N*f*	number of cycles to failure
PL	point load
PZ	Panel Zone
R	stress ratio
RBS	reduced beam sections
SINTAP	Structural Integrity Assessment Procedure
SMRF	steel moment resisting frames
SINTAP	Structural Integrity Assessment Procedure
SMRFs	steel moment resisting frames
SIF	stress intensity factor
twc	web thickness for column
UTS	Ultimate tensile strength
UDL	uniformly distributed load
UW	unreinforced connection
ν	Poisson's ratio

VLCF	very low cycle fatigue
WUF-W	welded unreinforced flange-welded web
WCPF	welded cover plated flange
WUF-B	welded un-reinforced flange/welded beam
YR	Yield rotation

Greek Symbols

$\Delta\varepsilon_e$	elastic strain range
$\Delta\varepsilon_p$	plastic strain range
$\Delta\varepsilon$	total elastic strain range
$\Delta\varepsilon/2$	total strain amplitude
$\Delta\sigma$	stress range
εe	elastic component of the cyclic amplitude
ε_{ap}	plastic strain amplitude
$\varepsilon`f$	fatigue ductility coefficient
εr	ratcheting strain
μ	Coefficient of Friction
σ_a	cyclic stress amplitude
σ_d	Minimum stress
$\sigma' f$	fatigue strength coefficient
σ_g	Maximum stress
σ_y	yielding stress
σ_{ys}	the small scale yielding stress

CHAPTER 1
INTRODUCTION

The 1994 Northridge and 1995 Hyogoken-Nanbu (Kobe) earthquakes highlighted the need for understanding and explaining some ‘‘unexpected’’ aspects of the seismic response exhibited by steel buildings during these events. In particular the extensive damage and brittle failure modes which occurred at beam-to-column connections of frame structures were of major concern. During the earthquakes in Japan and California in the 1990s, some weld connections had some cracks in heavy rigid steel frame buildings. Therefore it is required to assess the performance of the welded connection in term of rotation capacity and crack propagation strength. Some experimental tests were performed prior to this work. The weld connections were submitted to cyclic loading with increasing amplitude until a macro crack event occurred. However the crack phenomenon depends on many parameters such as geometry, material and the welding process.

Several experimental programs on steel connections have been carried out in the United States Mahin *et al*. [1996]; Malley [1998]; Kunnath and Malley [2002] and in Japan JCSS [1997]; Tanaka *et al*. [1997]; Nakashima *et al*. [1998]; Suita *et al.* [1998] in order to understand the causes of the observed damage, to assess the major parameters affecting the cyclic behaviour of steel connections, and to suggest modifications in the connection layout for improving the seismic performance [Mele *et al.* 2003].

This research describes numerical models of steel welded connections using ANSYS V14.5. The results are compared with four specimens test (BCC5A,BCC5B,BCC5C and BCC5D), the experimental program was carried out, prior to this work, at the Material

and Structures Test Laboratory of the [Instituto Superior Técnicoof Lisbon] [Mele *et al.* 2003].

The experimental tests were performed on specimens representative of moment resisting frame (MRF) beam-to-column joints. The beam section is typically welded to the column in the shop: complete joint penetration welds are applied at the beam flanges and fillet welds are applied at both sides of the beam web. Continuity plates - are commonly utilized for stiffening the column panel zone (PZ) (the column web bounded by the stiffeners aligned with the beam flanges) [Mele *et al.*2003].

1.1 Objectives of the research

The primary objective of this research is to evaluate the performance of steel connections, designed and constructed according to practices commonly used prior to the 1994 Northridge Earthquake to achieve the following:

- Further the understanding of the force and deformation environment at steel welded connections.
- Further understand why ductile materials fail in brittle manner.
- To investigate the possibility of predicting the extremely large cyclic strain fatigue and fracture performance of steel welded connections based on finite element simulations, fracture mechanics and strain life equations.
- To investigate alternative design configurations for steel connections considering the determined structural performance characteristics.
- To work towards recommended design guidelines, to the extent possible, for avoiding fracture in steel connection during seismic events.

1.2 Methodology

Four numerical analyses of three-dimensional (3D) beam-to-column joints subjected to cyclic displacement loading were modelled using the FE technique. The models are made in the Solid works V13 software programme and then exported to ANSYS V14.5 workbench where the structural analysis was made.

The steel fully welded connection for the four specimens considered are a beam with a profile of - IPE300, and a column with a HE160B profile. The displacement time history data for four BCC5 specimens are considered and applied to the four BCC5 numerical models. The constructed numerical models were validated with experimental data that was obtained from [Calado, 2010-2014, per. comm.].

For each case, the original steel connection (base model), was modelled as a fully welded beam to column connection with four column web bracing plates (10mm thickness) as shown in Figure 4.1 chapter 4. A modified model was made with fully welded beam to column connection but with two welded column flange to beam flange bracing gussets size 125 x125 x10 mm at the area of connection (improved model) as shown in Figure 5.1 chapter 5.

The FE results for each numerical model and the experimental results are compared to examine the validity and the predictability. The FE force-displacement hysteresis loops results have satisfactory agreement with the experimental work at different stages of cyclic displacement loading. The FE shows that the failure location occurred in the same location as experimental work. A structural plan for the project is summarised in the flowchart as shown in Figure 1.1.

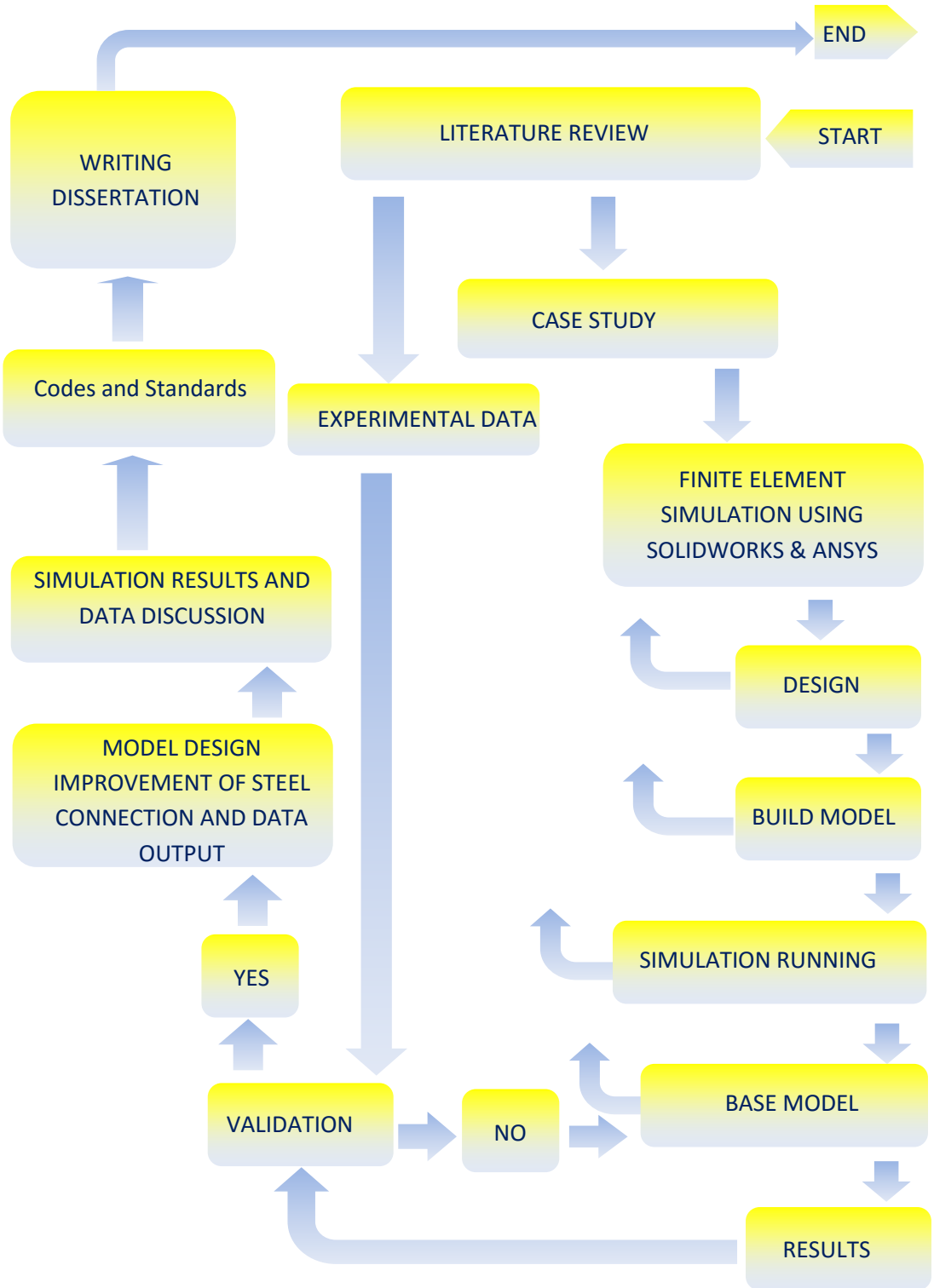

Figure 1.1: Flowchart of the thesis

1.3 Failure criteria

A cyclic displacement load was applied to a vertical cantilever beam, that was connected to a horizontal beam, at a point 862.5mm distance from the top of the connection. A linear variable displacement transducer (LVDT),which is a type of electrical transformer used for measuring linear displacement, was placed in the same place where the load was applied. The arrangement is as shown in Figure1.2. In practice this arrangement would be rotated through 90 degrees with the IPE300 member representing a beam (the head in the profile IPE300 is to avoid beam rotation) and the HE160B member representing a column.

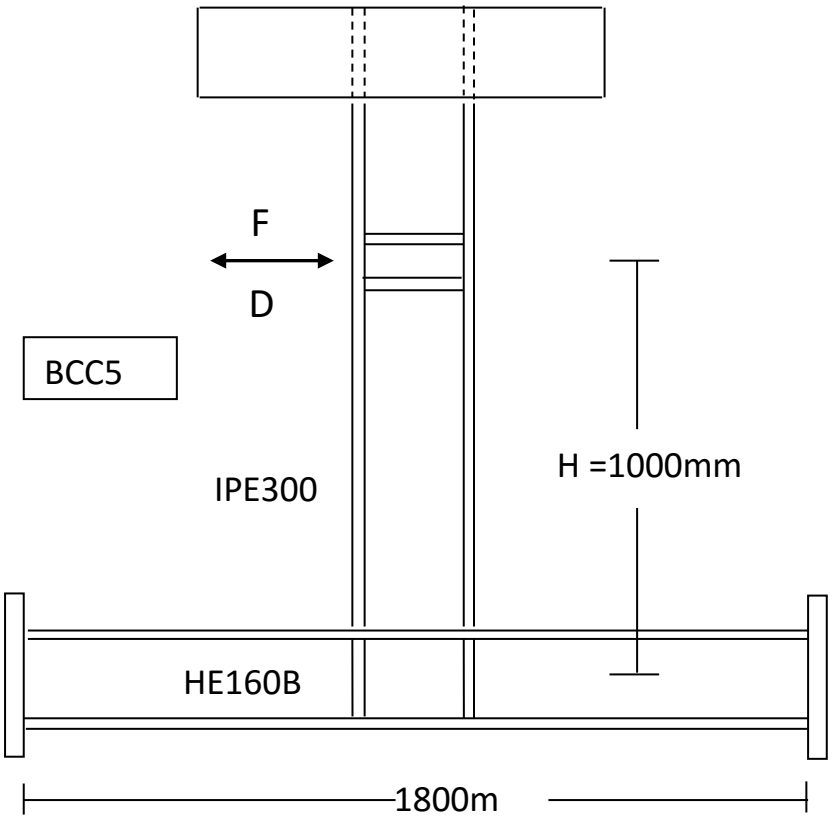

Figure 1.2: Specimen instrumentation

The applied cyclic displacement was continued until failure, as determined by cracking and a change in the force-displacement relationship.

The hysteresis (Force-displacement) loops are also obtained from FE analysis. With some adjustment to allow for the boundary conditions, the applied cyclic displacement load was, before failure, similar to the shape of the hysteresis loop for each force-displacement cycle from the experimental work.

When the structure starts to fail, the shape of the hysteresis loops differs between the experiments and the FE analysis be. This sudden change in the shape of the experimental hysteresis loops may be considered as a failure criteria.

It has been chosen to perform the crack calculations during post processing rather than to perform the crack growth calculations within the FE analysis.
The post processing options considered included application of the Coffin-Manson method, cumulative strain methods and fracture mechanics methods.

The dominant area of failure for the considered steel joint structure is the Heated Affected Zone (HAZ) area where higher stress and strain occur and therefore fracture will be presented [Omer *et al*., 1999]. This also appears to be the location for the start of the cracks in these experiments.

1.4 Contribution to knowledge

1. It was demonstrated that the standard low cycle fatigue equations, and the related constants, considerably overestimated the cycles to failure, modification is needed to the fatigue ductility coefficient. Modification factors were proposed.

(These were determined by using low cycle fatigue equations with aid of finite element stress and strain results and comparing the results with experimental work.)

2. Fracture mechanics was applied to try and better understand the cracking behavior:
    - Paris Law methods were found to considerably overestimate the cycles to failure.
    - As Paris Law is based on stress I used the actual stress, an artificial stress of strain*E, the geometric mean of stress and strain*E and mean of stress and strain*E ranges to calculate crack growth. All methods under estimated the crack extension. (The methods used were otherwise as recommended, "for high cycle fatigue", by BS7910 [2013] and DNV-RP-F108 [2006]).

3. Cumulative increasing true strain compared with the true strain corresponding to UTS is an indicator of failure.
    - The application of the Failure Assessment Diagram tentatively appears to be valid if based on the extreme stress at failure. There is no evidence of a significant reduction in the fracture resistance as a result of the cyclic strain time history. This is based on an estimate of the likely CTOD of the steel and is why this contribution is only tentative.
    - Estimation of improvement of fatigue life of a connection detail as a result of the addition of gusset plates.

1.5 Outline of the dissertation

In order to address the objectives mentioned above, a comprehensive literature review was conducted, followed by a combined experimental and numerical study.
Firstly, Chapter 2 of this dissertation discusses the background and scope of the research program. A comprehensive literature review of low cycle fatigue and numerical models of steel welded connections due to cyclic loading is provided. Emphasis is placed on recent research in the same area and the extensive efforts in the US and Japan on the development of improved moment connections following the Northridge and Kobe Earthquakes. The review is synthesized and analysed to provide a detailed scope of the research program.

Chapter 3 discusses the background and scope of the research program. A comprehensive literature review of fatigue of steel welded connections due to cyclic loading is provided. Emphasis is placed on recent research in the same area and the extensive efforts in the US and Japan on the development of improved moment connections following the Northridge and Kobe Earthquakes. Cracking and ratcheting are included in this chapter. The review is synthesized and analysed to provide a detailed scope of the research program.

Chapter 3: describes the analytical portion of the research program. A detailed 3-D nonlinear finite element simulation of the tested specimen was performed to supplement
the findings from the tests. Correlation between the experimental performance and numerical modelling analysis was studied to investigate the possibility of predicting the connection performance controlled by fracture in the heat affected zone near weldments, based on finite element simulations. Additional analyses were conducted to study the effect of four different types of cyclic displacement loading on the performance of beam-to-column connections. FE simulation results, comparison/validation with experiments, and discussion are included.

Chapter 4: in this chapter, prediction of cracking ,weld defects and fracture failure have been discussed, and also the behaviour of a fully welded steel connection subjected to cyclic displacement loading, is analysed using the strain-life theories, where the FE output of chapter 3 is used to establish a general model to evaluate the number of cycles to failure based on total stain amplitude. The effect of strain hardening on the number of cycles to failure is also considered. Further investigations are also carried out to construct the failure assessment diagram (FAD) to reflect the safety of welded steel connection considered in this investigations in comparison with a methodology used in pipeline engineering. Fatigue damage index and crack growth rate are included.

Chapter 5: describes the design modelling improvement of the modified case, including modelling data output, discussion and conclusion.

Chapter 6: conclusion and design recommendations, is developed and suggestions for further research are provided.

Appendix A: experimental data related to this investigation was obtained from literature and includes the test plan, test setup, test procedure, and material test results. Followed by the design and fabrication details of the beam-column test specimens. The effect of the three primary test parameters, namely the welded connection type, beam and column length, and loading protocol are discussed.

Appendix B: finite element results input and output.

Appendix C: calculating - strain amplitude and fatigue damage index

Appendix D: stress and strain failure location for specimens and numerical analysis, joint and section contours for all BCC5 FE models are included.

1.6 Summary

Explanations of objectives of dissertation, methodology, failure criteria, and outline of dissertation for six chapters, are included in this introduction. The following chapter report a detailed: literature review, analytical and experimental work and a case study.

CHAPTER 2
LOW CYCLE FATIGUE AND NUMERICAL MODELS

2.1 Overview

This chapter reviews past research on cyclic loading including the effect of low cycle fatigue in the steel connection and other issues related to the extreme strength of beam-to-column connections which were designed, detailed, and constructed in a manner very similar to that of beam-to-column connections in steel special moment frames (which are used as a part of the seismic force-resisting systems in buildings designed to resist earthquakes with substantial inelastic energy dissipation, with the exception that a welded web connection is now more commonly used) [Ronald *et al*., 2009].

Before the Northridge Earthquake 1994, steel moment resisting frames were believed to have ductile behaviour that would achieve high-cycle fatigue. As a result, fatigue was not considered to be a failure mode for these connections during a seismic event. Observations after the Northridge Earthquake indicated that these connections essentially failed at relatively low stress levels with only a few high-strain cycles.

As result of these failures, many researchers tried to gain a better understanding of the causes of damage observed in the connections of steel moment frames. Therefore, the extensive research programs conducted following the Northridge Earthquake to improve moment connections were central to the goals of this research program on beam-to-column connections. Based on the synthesis of available research, many types of beam-to-column connections were detailed investigation.

Section 2.2 summarizes significant research that forms the introduction about fatigue, fracture and crack growth due to cyclic loading. Factors that affect fatigue life and fatigue crack growth of welded joint:

Applied strains, strain and stress concentrations, mechanical factors (geometry, loading condition, weld imperfections and loading rate), environmental influence (such as low and high temperatures and corrosive media), residual stresses, material properties, and weld quality were described.

Section 2.3 summarizes a number of technical papers that dealt with both the experimental and analysis techniques which were used to investigate the behaviour of welded connection of steel frame under seismic loading.
Section 2.4 summarizes a number of finite element method models (model analysis).
Section 2.5 conclusion

2.2 Introduction

Fracture mechanics is the study of the influence of loading, and structural geometry on the crack growth and fracture resistance of materials containing natural flaws and cracks. The objective of the fracture mechanics analysis is to predict the operating stress level so that the crack would not grow to a critical size during the service life of the structure. Steel structures may have face flaws and cracks and hence, should be designed for fatigue under cyclic loading.

Fatigue is the study of the effects of repeated loading on a structural element, and how those loads with other combination factors (which are explained below) may make the life of the structure shorter than it was originally designed for [Alan, 2005].

If the fatigue life is relatively short, say (less than ten thousand cycles) then the failure is considered a low cycle fatigue (LCF) . In steel structures, low cycle fatigue failures are typically observed when the applied load cycles produce large plastic strains within the specimen, this was presented by Chemin [2009].

Sometimes extremely low cycle fatigue (ELCF) is also defined by Xue [2008], in term of very low cycle regime in the range of about less than 100 cycles.

Generally, fatigue in steel welded joints subjected to repeated cyclic loading is considered to be due to crack initiation (stage 1),crack growth and propagation (stage 2), and final failure. Fatigue life is usually divided into a crack initiation period and a crack growth period as illustrated in Figure 2.1 by Schijve [2003].

In the first period of the fatigue life the crack nucleation can be initiated on a microscopically small scale, followed by crack grows (second period) to a macroscopic size, and finally to the failure in the last cycle of the fatigue life as reported by Schijve [2003]. For welded construction cracks are assumed initiated by welding and the crack initiation period is often neglected.

Estimation of fatigue crack propagation life in butt welds analytical model assesses the influence of joint geometry, weld reinforcement and other factors relative to the propagation of fatigue cracks are reported by Lawrence [1973].

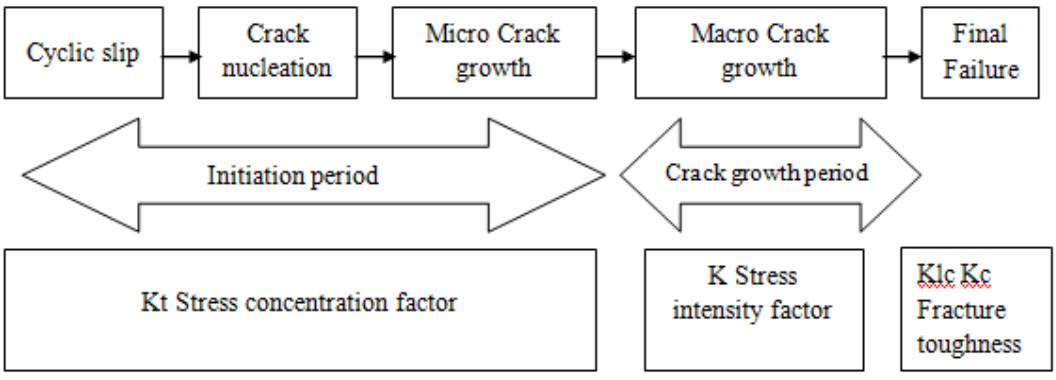

Figure 2.1: Fatigue life and fatigue crack growth [Schijve, 2003]

The following section considers the factors that affect fatigue life and fatigue crack growth of welded joint which are mechanical factors, environmental influence, residual stresses, material properties, and weld quality.

2.2.1 Mechanical factors

Mechanical factors include: geometry, loading condition, weld imperfections and loading rate. Structural geometry and loading condition are required elements in stress analysis, and also contribute to how a structural part will fail. Loading condition (including loading rate) plays an important role in the mode of structural failure, interacting with structural geometry and ambient environment to govern whether the failure mode is brittle or ductile. Table 2.1 is showing the mechanical factors for ductile and brittle fracture.
Environmental effects, such as low and high temperatures and corrosive media, can have a significant impact on the mechanical behaviour and fracture appearances of solid bodies. For example, ductile steel may become brittle at low temperatures was reported by Nestor [2004].

It is normally found that residual stresses are present in the weldment area, and these can be high and can approach the yield strength of the material. These residual stresses occur due to the thermal expansion and contraction during welding, as a result of constraint provided by the fabrication: or by the fixtures: and, as a result of distortion in the structure during fabrication; these residual stresses act at the weld zone and are self-balancing (both tensile and compressive stresses).

The residual stress is typically tensile and can approach the yield point. When a load cycle is applied to the structure, it is superimposed onto the residual stresses field, and the effective stresses acting at the weld joint can fluctuate down from yield level [ASM, Vol 19].

2.2.2 Material properties

Toughness is the main factor of material properties that must be taken into account in the case of fracture in welded steel frame joints. In tough material having fine structure and good ductility, the work of fracture can be very high, so that the material is able to absorb energy and resist fracture. This is quite different from brittle behaviour where the material is unable to absorb energy and fracture will occur without warning and with very small yielding or sometimes without any yielding, as presented by Arun[2005].

The parameters that affect the material toughness are: material grade & chemistry, strength & hardness, microstructure & level of impurities, grain orientation, size of structure or specimen (constraint), notch/crack acuity, loading rate and temperature [AISC, 2009].

Fatigue cracks generally grow from welds in steel welded structures. The reason is that the welding process invariably leaves metallurgical discontinuities of minute sizes in the welds and cracks develop from these discontinuities. Welds are usually rough in toes of butt welds and toes and roots of fillet welds, there are sharp changes incurvature and “slag inclusions” that run along the weld toes and hence they have local stress concentration. Cracks may develop from these areas.

All welded structures contain defects at some level of examination, and the joint itself is a discontinuity in the structure. Welding defects fall into three board categories: planar, volumetric, and geometrical defects [ASM, Vol19].

Table 2.1: Mechanical factors for ductile and brittle fractures

Parameters	Ductile	Brittle
Temperature	Higher	Lower
Rate of loading	Lower	Higher
Geometry	No-stress concentration	Stress concentration
Size	Smaller or thinner	Larger or thicker
Type of loading	Torsion	Tension
Pressure (hydrostatic)	Higher	Lower
Strength of metal	Lower	Higher
Toughness	Higher	Lower
Steel grade	Higher	Lower

[Özkumur, 2004]

Strength and ductility are the two main characteristics that govern the behaviour of steel welded connection in a seismic area. Therefore the structural engineering earthquake design community thought that the frame connections should be designed to be strong enough to resist the resulting stresses, and ductile enough to accommodate the distortions generated by a severe earthquake. Thus, the design should be consider materials selection due to a strong earthquake, type of connections and welded fabrication as reported by Özkumur [2004]. Note that Özkumur [2004] refers to torsion as encouraging ductile behaviour. (This would also apply to shear forces and it is notable in the comparison of experiments and FE analysis reported below that failures appeared to occur preferentially in areas of high uniaxial strain in preference to areas of high shear strain.)

In Table 2.1 for both metallurgical and geometrical reasons, smaller or thinner sections usually are more likely to have ductile behaviour. Conversely, larger, thicker sections are more likely to have brittle behaviour, partly because there is a higher probability that serious discontinuities -stress concentrations - will be present in the larger, thicker sections. Also, triaxial tensile stresses - which promote brittle fracture - are more likely in large sections.

2.3 Background

This section discusses a number of technical papers that dealt with both the experimental and analysis techniques which were used to investigate the behaviour of welded connection of steel frame under seismic loading.

Recommendations for future research made by the authors are reviewed and a path into the aims and objectives of this research work was drawn accordingly by the author.

2.3.1 Experimental tests

Numerous tests have been conducted to investigate the behaviour of steel welded connection under seismic loading. These tests investigated the effects of various parameters such as: thickness, depth and length of the connection members, type of welding, type and size of strengthener, and material properties of the welded connection.

Dubina and Stratan [2002] tested 54 ‘T’ specimens, in order to investigate the seismic performance of beam-column joints in steel moment-resisting frames with different types of weld (fillet weld, double bevel butt weld, and single bevel butt weld). Each specimen was composed of an end plate (t =20mm) and two flanges (t=12mm), Steel grade S275, S355. Cyclic loading was considered in order to study the low-cycle fatigue phenomenon as illustrated in Figures 2.2 & 2.3.

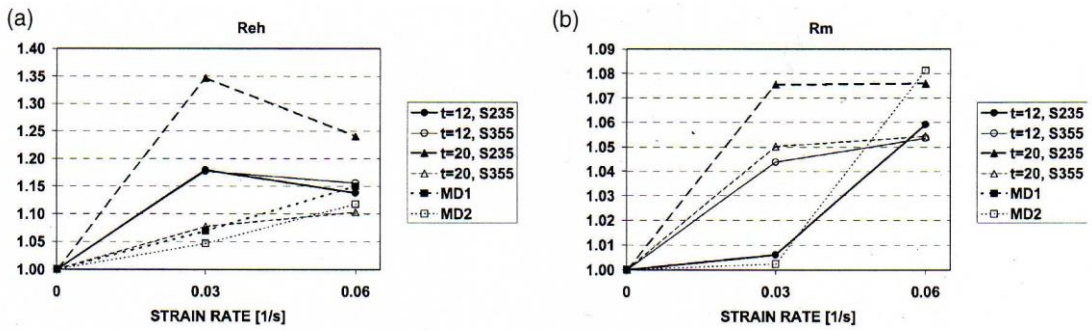

Figure 2.2: (a) Variation of upper yield strength (Reh),(b) ultimate tensile (Rm) for component materials [Dubina and Stratan , 2002]

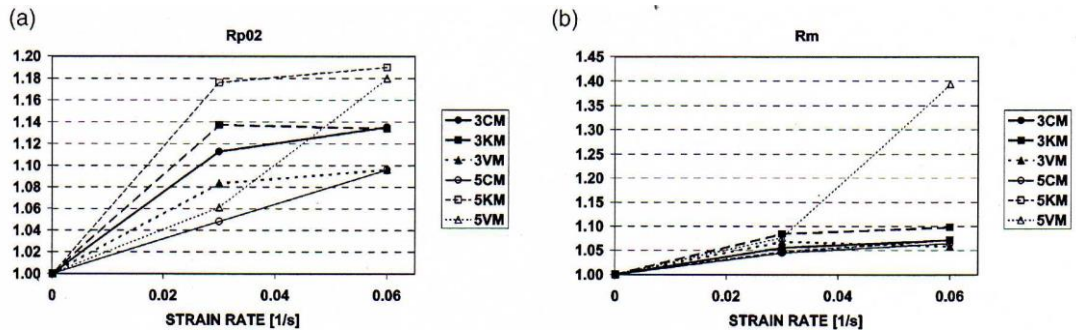

Figure 2.3: (a) Variation of conventional strength(Rp02),(b) ultimate strength (Rm-b) for the monotonically loaded specimens [Dubina Stratan , 2002].

The Authors noted that:

- From the three types of welds studied (double bevel, fillet, and single bevel). Rupture in the base metal was observed for the double bevel welds. Fillet weld specimens were characterized by an intermediary behaviour, the main cause of failures in welds being the undersized welds.
- Tests on fillet weld specimens showed: growth of the gap among the end plate and flanges, crack initiation from the corners of the gap, initiation of detachments of the deposited weld metal from the base metal, and crack initiation at the weld corners. Weld defects (detachments of weld metal and cracks) had a limited growth under applied loading, due to inhibition of crack growth by the deposited weld metal.

- The rupture in the weld zone was caused by the undersized fillet welds, and the reduced deformation capacity under cyclic loading.
- A double bevel weld specimens was characterized by higher values of ultimate strength and ductility, in comparison with fillet and single bevel welds.
- A strain rate in the range of 0.03–0.06 s-1 (typical for steel members yielding under seismic action) has the effect of increasing in the yield strength and, to a lesser extent, the ultimate strength of welded connections.
- The ultimate tensile strength increases at higher strain rates (0–8% for 3%/sec) and (5–8% for 6%/sec).
- The maximum influence of the ultimate tensile strength was observed for the mild steel (S275) as illustrated in Figures 2.4 & 2.5.
- A reduction of ductility (up to 27%) was presented in the case of high strain rates for monotonic loading.

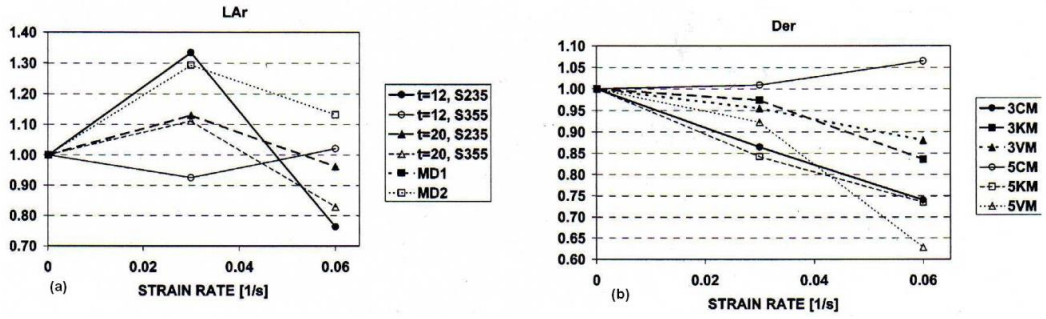

Figure 2.4: (a) Variation of ductility (elongation at rupture) with strain rate for the component material, (b) monotonically loaded welded specimens [Dubina and Stratan , 2002].

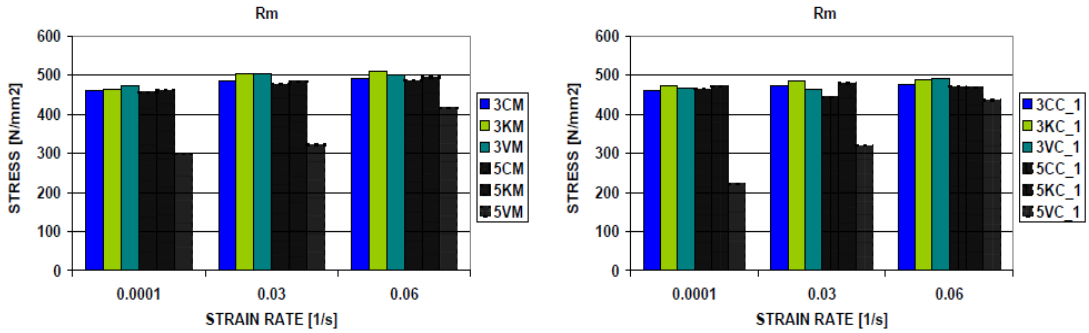

Figure 2.5: Influence of the weld type on the ultimate strength of the welded specimens [Dubina and Stratan , 2002].

It is not possible to make a direct comparison of the three types of welds from the point of view of *type of welding*, due to certain defects of the welds (the fillet weld size was smaller than the specified one-5.5 mm instead of 8.0 mm, while the single bevel weld was characterised by incomplete penetration at the root of the weld). It could be observed that generally, double bevel weld specimens were characterised by higher values of ultimate strength (see Figure 2.1) and ductility, in comparison with fillet and single bevel welds.

Mele *et al*. [2003] tested a total of 18 beam-to-column fully welded joints (3 series X 6 specimens) with different values of the relative column-beam-panel zone strengths up to failure under different loading histories, in order to study the effect of column-to-beam strength ratio and of panel zone (PZ) design on the cyclic behaviour and failure modes of the connections as illustrated in Figure 2.6 by Mele *et al.* [2003].

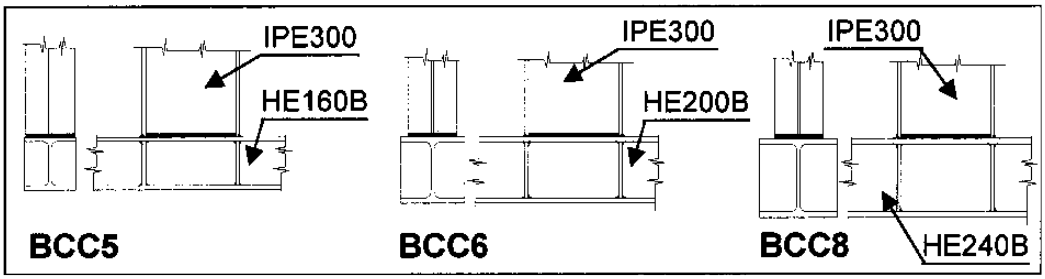

Figure 2.6: Outlines of the fully welded connections [Mele *et al*., 2003]

The (vertical) beam was a 1000 mm long and the (horizontal) column was 1800 mm long. The continuity of the beam flange connection through the column has been ensured by 10 mm thick plate stiffeners, fillet welded to the column web and flanges. The beam flanges have been connected to the column flange by means of complete joint penetration (CJP) groove welds, while fillet welds have been applied between both sides of the beam web and the column flange.

This test type has been carried out according to the basic loading history recommended by ECCS [1986].

The Authors concluded that:

- Concerning the effect of the column size and of the panel zone (PZ) properties:
    - Specimens with the smallest column section by the lowest PZ strength value (BCC5), a ‘‘brittle’’ failure mode was observed in all the tests, due to the governing role of the PZ in the inelastic deformation mode.
    - Specimens with the strongest PZ (BCC8): as a result of inelastic deformations, mainly in the beam, a typical ductile behaviour was always observed throughout the experimental program, with formation of a well defined plastic hinge in the beam starting from the first plastic cycles.
    - Specimens with the intermediate size (BCC6), characterized by close values of beam and PZ plastic capacity (by occurrence of inelastic deformations both in the beam and in the PZ noted), the experimental evidence suggested an intermediate behaviour, with a strong dependence of the cyclic behaviour, of the performance parameters values and dependence of the failure mode on the applied loading history, therefore for a specimen with close values of beam and PZ plastic capacity, the loading history has significantly affected the failure mode.

- The quite high values of the maximum plastic rotations experienced by these European type welded connections were related to the significant contribution of PZ deformation.
- There is a possibility of utilizing the PZ for providing energy dissipation and stable behaviour of the welded connections even at a large number of cycles. A weak PZ, however, will give rise to an inelastic deformation mode of the beam-column sub-assemblage which produces high stress concentrations and large plastic strains at the beam-to-column welded zones, and finally drives the specimen to a brittle collapse mode.
- The behaviour of the various specimens in the ‘‘brittle’’ failure mode, showed large scatter in the number of cycles to collapse and in the values of the cycle energy at collapse but, in the ‘‘ductile’’ failure mode, the various specimens showed a similar behaviour in all tests, with absorbed energy steadily decreasing up to failure.
- Computer analysis is needed to properly compare the test results.

Byfield *et al.*[2005] tested a numerical model for steel sections (S275, 203×102×23UB) in order to estimate values of the strain hardening factor during elastic-plastic design.

A comparison was made between the predicted moment vs. end rotation behaviour of restrained steel beams and the behaviour observed through six identical bending tests obtained from Byfield and Nethercot [1998].

The Authors found that:

- The moment resistance Mp was increasing due to strain hardening.
- The higher grade steel was found to require greater end rotation than low grade steel in order to strain harden.
- The strain hardening occurred at a strain of approximately 6 times the yield strain, and the strain hardening modulus was approximately 2700 N/mm^2.

- According to the test, steel grade S355 required 20% greater end rotation to develop 1.0*Mp* if subjected to a single point load, 25% greater if subjected to a UDL and 56% greater rotation if subjected to 2-point loads. Approximately 28% extra end rotation was required for S355, in comparison with S275 steel as illustrated in Figures 2.7 & 2.8.

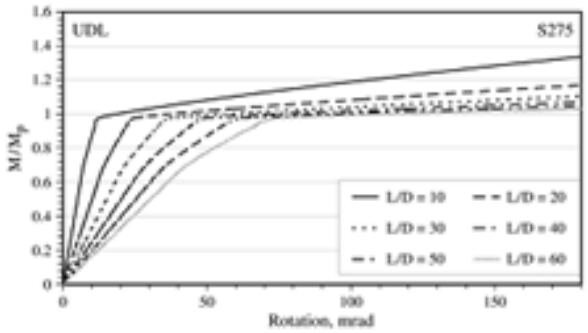

2.7 (a) Uniform load case

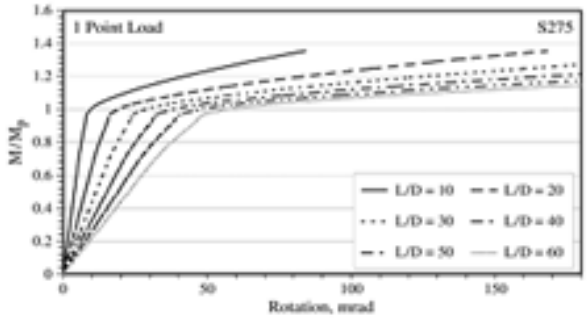

2.7 (b) Single point load case

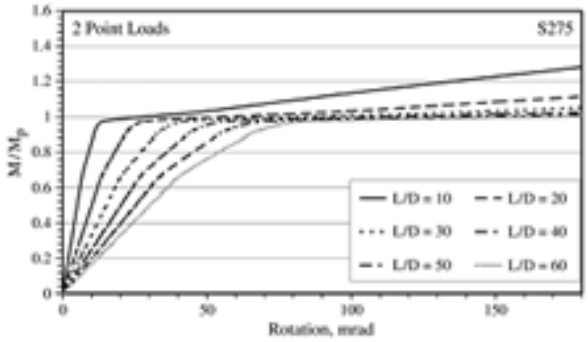

2.7 (c) Two points load case

Figure 2.7: (a, b and c): Normalised M- θ curves for different L/D ratios-275 grade [Byfield *et al.*, 2005]

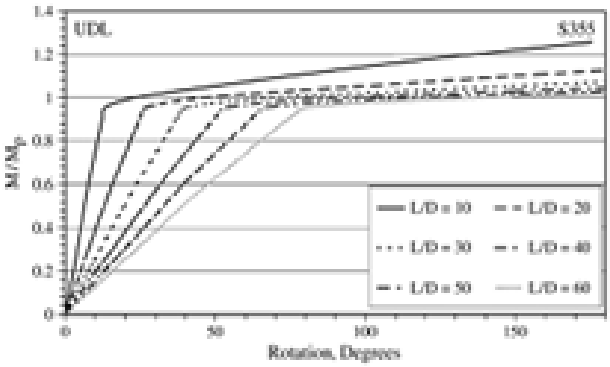

2.8 (a) Uniform load case

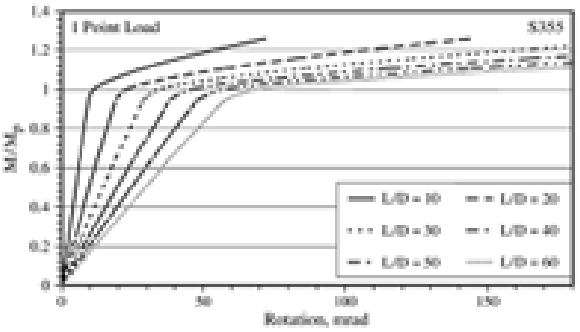

2.8 (b) Single point load case

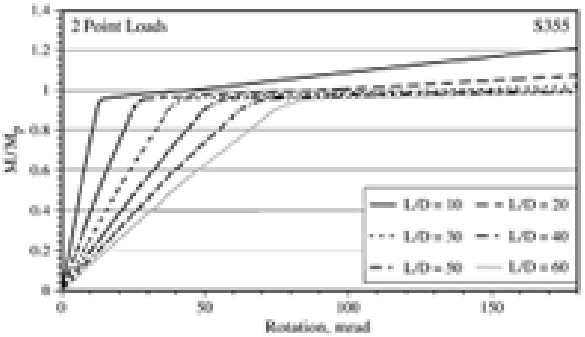

2.8 (c) Two points load case

Figure 2.8: (a, b and c): Normalised M- θ curves for different L/D ratios-S355 grade [Byfield *et al.*, 2005]

- For the two point load (2PL) case, the integral of curvature (using section S275, 203×102×23UB) between the support and the point of maximum deflection (i.e. the end rotation) was greater than for the one point load (1PL) case or the UDL case. The rotation requirement (the end rotation to achieve 1.0*Mp*, 1.1*Mp*, and 1.15*Mp*) of beams resisting 2PL's (at third span points) was greater than beams loaded by UDL's and single point loads as shown in Table 2.2.

Table 2.2: Required rotation to achieve 1.0Mp,1.1Mp and 1.15Mp

		$L/D = 10$			$L/D = 20$			$L/D = 30$			$L/D = 40$			$L/D = 50$			$L/D = 60$		
Grade	Load	1PL	UDL	2PL	1PL	UDL	2PL	1PL	UDL	2PL	1PL	UDL	2PL	1PL	UDL	2PL	1PL	UDL	2PL
S275	$1.0M_p$	9.6	18.8	28.3	19	37.5	56.5	28.6	56.5	84.6	38.2	75.4	112.9	47.8	94.1	141.2	57.4	113.1	169.5
S275	$1.1M_p$	21.6	58.3	82.9	43.3	116.6	165.6	65.1	175.1	248.7	86.7	233.4	331.4	108.4	291.6	414.5	130	349.9	497.2
S275	$1.15M_p$	30.9	81.3	108.4	61.8	162.5	216.6	92.7	243.8	325	123.7	325.2	433.4	154.5	406.3	541.6	185.5	487.6	650
S355	$1.0M_p$	11.3	23.6	44	22.9	47.1	88	34.2	70.7	131.8	45.7	94.4	175.8	57.1	118	219.7	68.6	141.5	263.7
S355	$1.1M_p$	27.4	74.7	106.6	54.8	149.4	213.3	82.2	224.1	319.9	109.8	298.8	426.6	137.2	373.3	533.2	164.6	448	639.8
S355	$1.15M_p$	39.4	104.4	139.5	78.7	208.7	278.9	118.2	313.1	418.5	157.6	417.5	558	196.9	521.9	697.4	236.3	626.2	836.9

[Byfield *et al.*, 2005]

- The difference in length to the depth (L/D) beam ratios was showing that the higher beam's ratio require greater end rotation. Therefore the rotation requirement increases linearly with L/D ratio, regardless of load case and steel grade.
- The mill tests had shown that the onset of strain hardening and the strain hardening modulus were independent of section size, steel grade and L/D beam ratio.

Wilkinson *et al*. [2006] tested two identical samples of Universal Beam Sections under cyclic loading to values of tip displacement that were estimated to produce plastic rotation with an increasing increment of 0.01 rad.

The Authors found that:

- There was little local deformation of the beam connection under seismic loading (of 0.03 rad). The beam web showed signs of initiation of buckling, but of minimal magnitude. By increasing the cycle of rotation to 0.04 rad in the first cycle, local buckling of the beam web was observed.
- In the second cycle of plastic rotation at 0.04 rad the buckling was more severe. Local buckling of the bottom flange of the beam at the peak of the wedge detail (pinching) occurred, which increased the web buckling.
- The first cycle was the only cycle of plastic rotation past 0.04 rad, the buckling of top and bottom flanges and the web became more prominent. A full plastic region had formed and the beam began to behave in a manner that would be unrealistic in a building. The rotation of the beam was of such great magnitude that to approach anywhere near that degree of rotation in a real structure the columns would have had to undergo plastic deformation.

The Authors concluded that:

- There were three criteria that could be established for a connection in a steel moment resisting frames (SMRF) in a seismic area:
- The connection must possess sufficient strength.
- The connection must possess sufficient stiffness to satisfy the assumption of a fully rigid connection.
- The connection must have a large post-yield deformation capacity without significant loss of strength.
- Reducing the plastic modulus of the beam near the beam–column connection, was effective in transferring the plastic hinge from the connection to the beam.

Kiral and Erim [2005] tested four different beam-to-column welded connections subjected to earthquake loads, in order to determine accurate and quick defect assessment of connections and to examine the effect of the different connection types. The dimensions were W30×99 for beams and W14×176 for columns, beams and columns both were A 572 steel Gr. 50. The flange welds used the Flux Core Arc Welding (FCAW) process.

The Authors concluded that:

- Structural Integrity Assessment Procedure (SINTAP) provided an accurate evaluation of the fracture behaviour of the connections by considering the interaction of local fracture demands, crack size, connection geometry details and material properties.
- Using cover plates, diaphragms and additional haunch in beam-to-column connections increased the load limit and maximum loads of the welded structures.
- Limit and maximum loads were dependent on the yield and ultimate strength, and independent of fracture toughness of the materials.
- In order to see the effect of the fracture toughness value of the weld material on the structural safety. Four different beam to column connections are chosen as shown in Figure 2.9. Four different types of weld electrodes are taken into consideration.

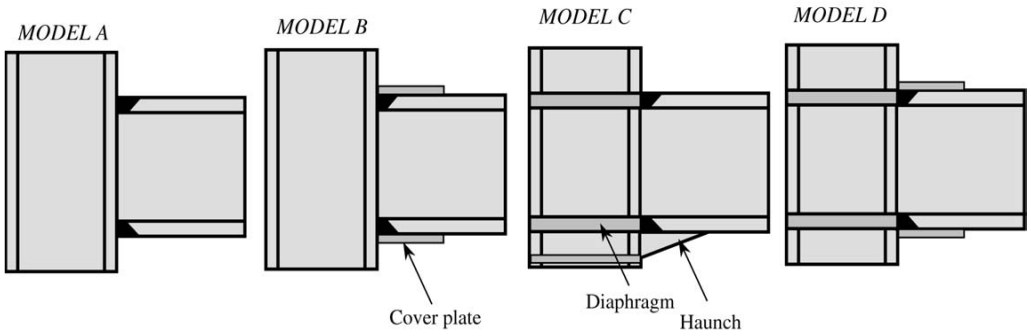

Figure 2.9: Beam-to-column connection details [Kiral and Erim , 2005]

- Figure 2.10 and Table 2.3 show the stress-strain curves and fracture toughness values of weld and base metals, respectively.
- Table 2.3 the material properties are shown and compared with those of Electrode E70T-4 a low toughness flux core electrode and commonly used in steel structures before the 1994 Northridge earthquake.

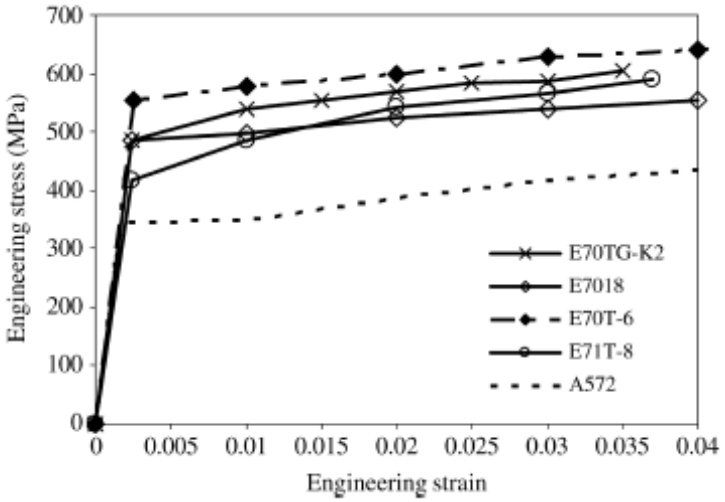

Figure 2.10: Stress-strain curves for base and weld metals

[Kiral and Erim , 2005]

Table 2.3: Material properties for base and weld material at 21ºC

Material	CVN_{static} (J)	$CVN_{dynamic}$ (J)	K_{mat} (MPa $\sqrt{m}$)
A572	266	266	252
E70T-4	54	14	85
E70T-6	68	50	100
E70TG-K2	120	98	120
E71T-8	250	109	140
E7018	197	185	204

[Kiral and Erim , 2005]

- K_{mat} is calculated using the fracture toughness value obtained by CVN (Charpy V-Notch). Because of expense and size limitations associated with fracture toughness tests, it is useful to make estimations of fracture toughness

  from CVN toughness requirements. The empirical correlation between CVN and K_{mat}, fracture toughness, is as shown in Equation 2.1.

$$K_{mat} = \sqrt{\frac{E(0.53\text{CVN}^{1.28}) \times 0.2^{(0.133\text{CVN}^{0.256})}}{1000(1-v^2)}} \qquad 2.1$$

  where:

  K_{mat} is in MPa√m and CVN is in Joule, ν is Poisson's ratio and E is the modulus of elasticity of the material
- The critical crack length decreases as the applied load approaches the limit load. But, when the strengthened connection types such as models C and D, as shown in Figure 2.9, are used in the structures, the critical crack length may be larger than in the elastic region when a ligament collapse occurs. That is, after the yielding, relatively larger crack lengths can be permitted in the structure.
- The fracture toughness of the weld material did not significantly affect the limit or maximum load values. The critical crack length was relatively larger when tougher weld electrode was used in the welded steel structure as illustrated in Figure 2.11.

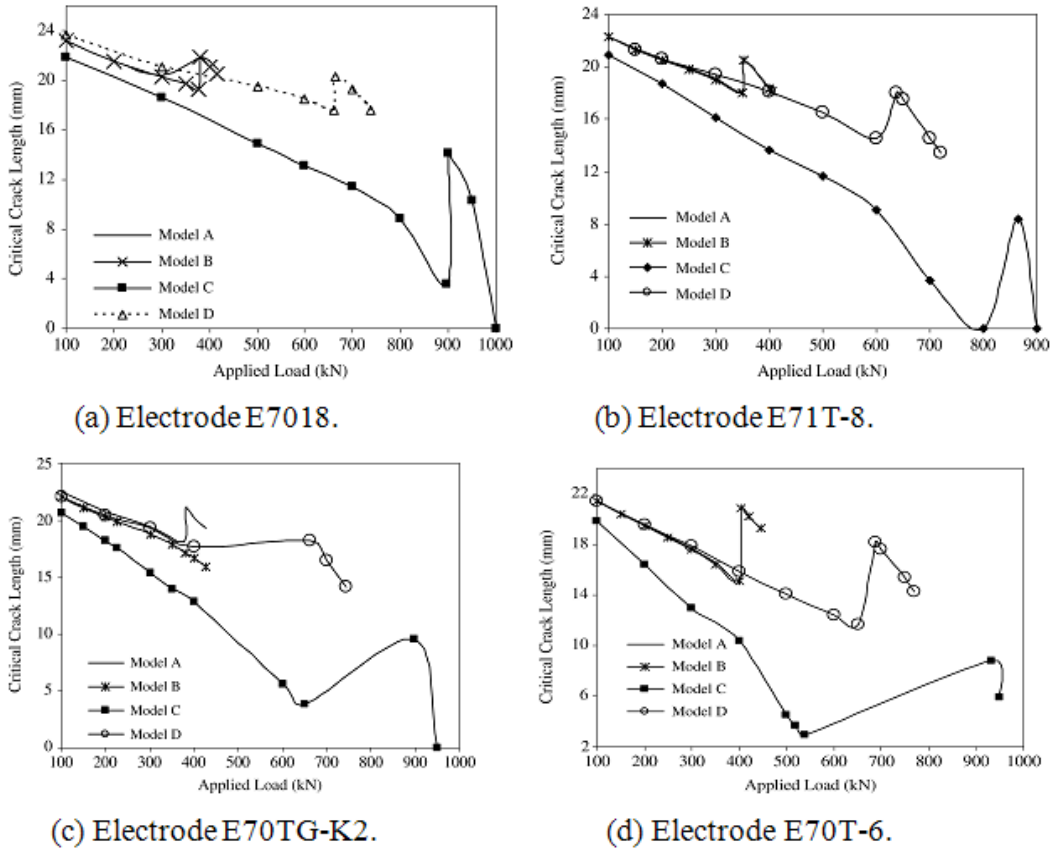

Figure 2.11: (a, b, c, and d): Critical size versus applied load for various electrodes [Kiral and Erim , 2005]

Chen *et al*. [2006] tested three full-scale specimens of steel column tree moment-resisting frames with four different types of the connections were modeled under the seismic loading condition. The "column-tree" system involves column-trees that are fabricated in the shop by welding stub beams to the column. Link beams are connected to the stubs in the field. This can reduce the cost. This system has been widely used in Japan, frequently in the shop welded, field-bolted form as illustrated in Figures 2.12&2.13. However, a number of column-tree connections were damaged during the 1995 Kobe earthquake.

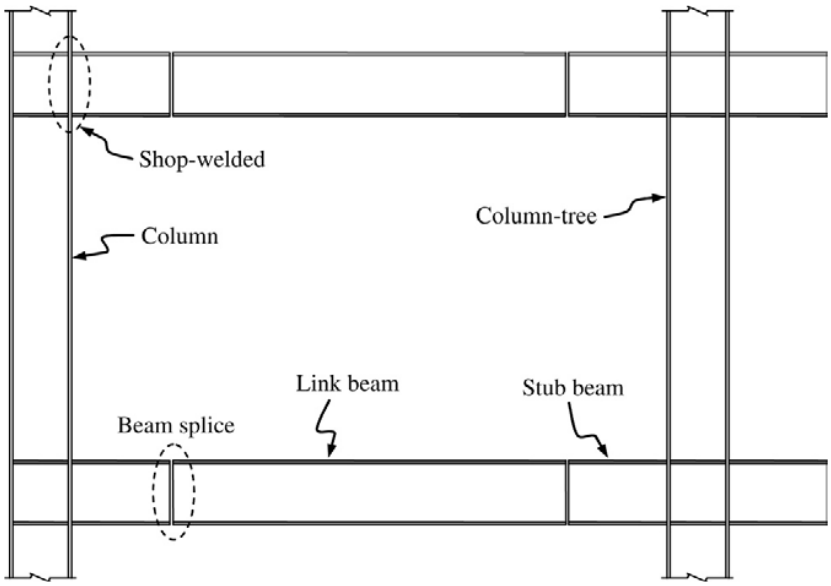

Figure 2.12: Column-tree construction system [Chen *et al*., 2006]

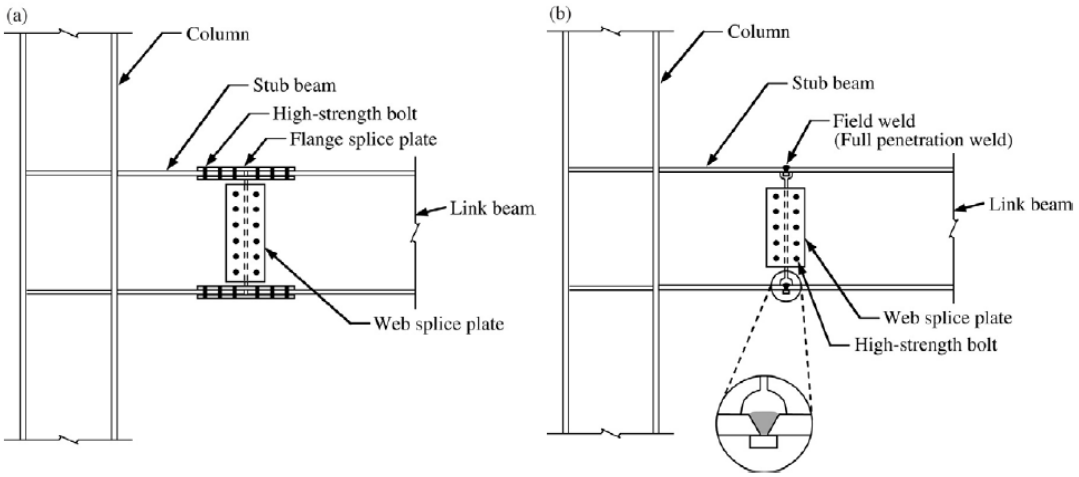

Figure 2.13: Beam splice options joining the link beam to the column-tree [Chen *et al*., 2006]

FEM analysis and experiments were carried out in order to understand the seismic performance of the widened flange connection used in tree moment-resisting frames. The connection with unreinforced connection (UW) had the same size and geometry as the sub-assemblages used in the finite element analysis (FEM), and both the beam and column were all ASTM A572 Grade 50 steel.

The shape of the widened flange was fabricated by a flame cutting process and was ground with a hand grinder. The sub-assemblage consists of an H-shaped H588 ×300 × 12 × 20 mm, 3030 mm long and a box column of 550×550×27×27 with 3000 mm span length as set up in the test diagram Figure 2.14.

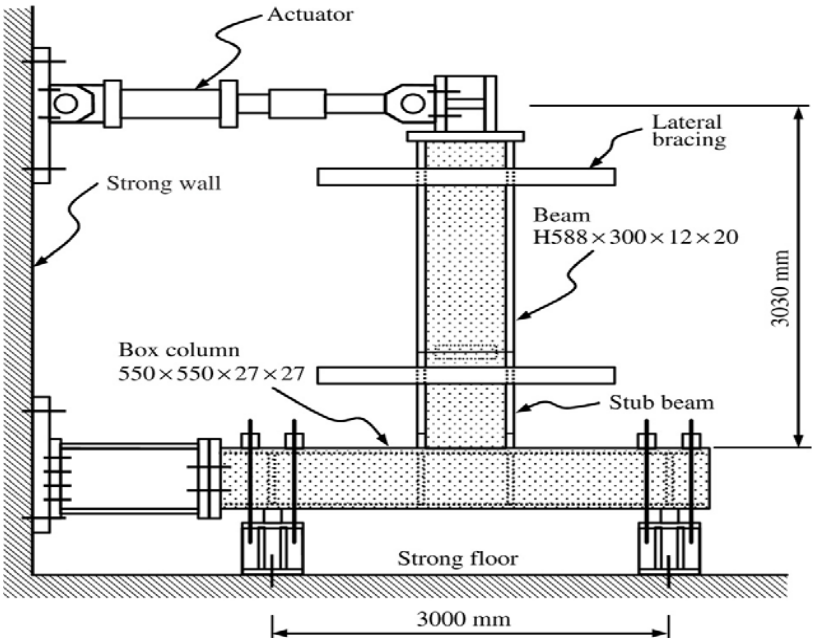

Figure 2.14: Schematic diagram of the test set-up [Chen *et al*., 2006]

Two major design parameters were studied: the maximum width and the length of the enlarged beam flange.

The Authors found that:

- Brittle fractures occurred at the beam to column joint, due to stress concentration in weld access hole regions, an initiating crack due to back-up bars at the beam bottom flanges, weld defects, and material deficiencies.
- The widened beam flange was intended to reinforce the beam-to-column joint and form the plastic hinge away from the column face (rather than stiffening the structure).

The Authors concluded that:

- Both test and FEM results proved that the widened flange connection associated with no weld access hole detail can reduce the potential for brittle fracture which was caused by the peak plastic strain demand in the weld access hole region.
- The cyclic performance of the widened flange connection was confirmed by the tests conducted for all three specimens. All specimens showed ductile behaviour by forming a plastic hinge in the beam section away from the column face owing to the intended effect of the widened flange.

Kim and Kim [2009] designed 3 and 6 story steel frames structures with three-types of seismic joints: the welded unreinforced flange-welded web (WUF-W) in accordance with inelastic cyclic testing of welded unreinforced moment connections tests by Ricles *et al*. [2002]. Reduced beam section (RBS) according to experimental evaluation of cyclically loaded reduced beam section moment connections tests by Jones *et al*. [2002] and the welded cover plated flange (WCPF).

The steel moment frames were designed for both moderate and high seismic load, in order to investigate progressive collapse.

The Authors concluded that:

- The vertical deflection, ductility demand, and plastic rotation of the structures with RBS connections turned out to be larger than those of the structures with the WUF-W and the WCPF connections.
- The ductility capacity of a RBS connection may be larger than those of the other connections, the ductility demands for the 6-story structures were less than those for the 3-story structures. However in the 3-story structure designed for moderate seismic load the ductility demand of the RBS connection exceeds 10, which was much higher than those of the other

connection types as shown in Table 2.4.

- Table 2.4 shows that the ductility demand of the structure reduces when the structure is taller, therefore displacement is decreasing in tall building because ductility demand reduced. Vulnerability index is more for structures with higher floor height and higher number of floors. Hence tall structures are most vulnerable to seismic excitation compared to low height structures.
- The performances of the structures with WUF-W connections were similar to those of the structures with WCPF connections.
- The structures designed for high seismicity turned out to be safer for progressive collapse caused by sudden loss of column, whereas the structures designed with moderate seismic load were showing high potential for progressive collapse.

Table 2.4: Ductility demands of model structures designed for medium seismicity obtained from progressive collapse analysis

Connection Types	Yield displacements (cm)	Maximum displacement (cm)	Ductility demands
(a) 3-story structure			
WUF-W	11.6	19.6	1.7
WCPF	10.7	14.2	1.3
RBS	8.09	94.21	11.8
(b) 6-story structure			
WUF-W	11.7	12.7	1.1
WCPF	10.6	9.8	1.1
RBS	8.0	30.0	3.8

[Kim and Kim, 2009]

2.3.2 Low Cycle Fatigue

Fatigue can be defined as a process caused by time-varying loads which causes a failure and damages the material. The damages, usually cracks, initiate and propagate in regions where the strain is largest. When the local damages grow out of control, a sudden fracture/rupture ends the service life of the structure. There are two methods describing the failure: low cycle fatigue (including extremely low cycle fatigue) and high cycle fatigue.

A comparison between these two methods is illustrated in Table 2.5. The low cycle fatigue method is considered in this investigation, therefore the literature will concentrate on this method only.

Table 2.5: Comparison between low and high cycle Fatigue

Low cycle Fatigue (LCF)	High cycle Fatigue (HCF)
• The (low cycle) *S-N* curve estimate the service life of materials below 10^4 (often < 10^5) cycles. The corresponding stress level is usually below 2/3 of yield stress. The stress level usually steps into plastic range. • Small stress increment -> large strain increment. • Only finite fatigue life is possible and should be analyzed using LCF-criteria • Best "resolution" if strains are employed in fatigue model. • For high load amplitudes (and/or high maximum magnitudes of loading) global plasticity will be the dominating cause. • low cycle fatigue shows straight line relationships in log log scale between strain increments in percent Vs number of cycles to failure for common materials such as steel and is often referred as the Coffin-Manson relation.	• When the fatigue occurs above 10^4 cycles (usually 10^5 or more), it is usually called high-cycle fatigue. The material is subject to lower loads, usually less than 2/3 of the yield stress. The deformation is in elastic range. • Small strain increment -> large stress increment. • Both infinite or finite fatigue life is possible and can be analyzed. • Best "resolution" if stress are employed in fatigue model. • For low load magnitudes, the model should tend to similar results as for HCF criteria (*i.e.* the Wöhler curve) • The *S-N* curve, Stress Life Method, is the basic method presenting fatigue failure in high cycles ($N > 10^4$) which implies the stress level is relatively low and the deformation is in elastic range.

[eFunda, 2014]

Stojadinovic [2003] modeled post-peak behaviour of pre-qualified fully restrained steel moment connections using the ABAQAS finite element analysis program, in order to investigate the failure modes of post-Northridge connections and to develop ductile design recommendations regarding beam slenderness, lateral bracing and connection configuration.

A low-cycle fatigue analysis approach was applied to a welded un-reinforced flange/welded-web (WUF-W), welded un-reinforced flange/welded beam (WUF-B) and free flange connections (FF).
SAC [1997] Steel Project test data collected during WUF-B and free flange tests conducted at the University of Michigan were used as well.

Rain-flow analysis procedure and Miner's rule were used to convert these test data into an equivalent constant-amplitude form, assuming that a damage index of 1.0 was attained when the test was terminated.

The connection rotation capacity data can be interpreted using a low cycle fatigue approach.

The objectives of the work were to:

- Investigate failure modes of pre-qualified US steel moment connections between wide-flange beams and wide-flange columns.
- Find connection rotation limits imposed by these failures modes and
- Propose design criteria to promote design of ductile moment connections.

The Author found that:

- The analytical model which was developed to examine the low-cycle fatigue limit state of post-Northridge moment connections was based on the plastic collapse yield-line mechanism model. When the beam buckles under monotonic loading, it deformed and developed a set of yield lines.

Rotation capacity of this yield-line plastic hinge model was computed using two limit state assumptions based on monotonic deformation capacity.

- An adequately braced connection, whose beam and column were not slender, should be able to sustain a number of displacement reversal cycles without substantial deterioration of its strength and stiffness.

Madi *et al*. [2004] applied the simplified suggested method in order to evaluate the fatigue life of the welded tube tested within the framework of this study. The total loading was applied to the welded structure so as to obtain, in the useful part of the homogeneous tube, an axial strain level equal to 0.6% ($\Delta \epsilon_{global} = 0.6\%$).

The adopted model consists of analyzing separately the behaviour and the damage evolutions which allows the determination of the damage ratio corresponding to initiation and propagation of a significant crack in order to determine the life duration. This model suggests the existence of a threshold level of loading, above which micro-cracks initiate. The initiation fatigue life can then be neglected below the threshold level.

In order to experimentally and numerically analyze the behaviour specimens were taken from a butt-welded annular joint to determine reduction factor.

Non-linear calculations integrating the consolidation of two materials were done in order to deduce the fatigue life to crack initiation.

The damage analysis was done at two critical points in the structure. The more damaged point in the parent metal presents the two phases related to fatigue crack initiation damage (DIF) and to fatigue crack propagation damage (DF).

The damage at the more damaged point in the weld metal was expressed only in terms of damage fraction per cycle of propagation.

The Authors concluded that:

- The welded joint tests reveal two types of crack initiation according to the loading level. The first type of failure (type I) was characterized by the low levels loading. The second type of failure (type II) was characterized by a crack initiation in the interior of the specimen close to the interface of weld and parent metal.
- The application method of testing tube must taking into account the threshold loading level to predict the failure in weld metal in accordance with the experimental observations.
- The values of the fatigue life reduction factor (Jf) calculated for the welded joint test when compared with the experimental data were equal to 1.25. These were valid only for the low loading levels when the level of applied loading was lower than the threshold. For the joint with an X-shaped weld, the threshold value $\Delta\varepsilon$th was established as equal to 0.6%. In general, if all the loading were lower than the threshold there would be no cracking.

Burzic *et al*. [2007] tested four sets of smooth welded specimens as shown in Figure 2.15, OM, from the parent metal and from welded samples; XN, in the as-welded condition; XB, with the overfill removed by grinding and XO, with both sides machined to 15 mm and so the rough layer of rolling was removed together with the overfill tested on a hydraulic machine, with the lower grip fixed and the upper grip oscillating with the frequency (f) = 9 Hz to 15 Hz, depending on the maximum load in the cycle. At the stress ratio $R = \sigma_g/\sigma_d = 0.1$ (σ_g is the maximum stress in the cycle and σ_d is the lower stress in the cycle).

The Authors found that:

- Low-cycle fatigue initiation could be expected in the region of welded joints, because the yield stress could be achieved locally by stress concentration. Local plastic deformation ahead of the crack tip was typical for crack initiation and growth in the early stage of low-cycle fatigue was followed by shear lips.
- The XN, in the as-welded specimens fractured with low cycle fatigue after 6700 cycles. The fatigue crack initiated in the region of stress concentration, in the transition from overall to the heat affected zone (HAZ), and developed through the HAZs coarse-grain region.

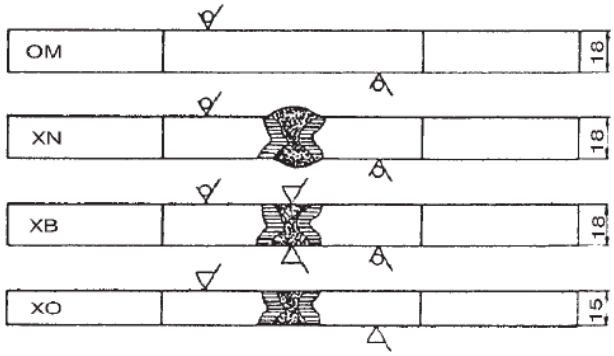

Figure 2.15: Smooth specimens for testing by variable loading [Burzic *et al*., 2007]

The Authors concluded that:

- The importance of reducing the stress concentration for fatigue life as shown in Figure 2.16. The critical load for N = 10^5 cycles for the smooth parent metal specimen is 625 MPa, reduced in the machined specimen of the welded joint to 530 MPa. With the overfill ground away the reduction was to 415 MPa and down to 370 MPa in the as-welded condition.
- In a welded specimens; specimens in the as-welded condition XN, the crack-growth rate was low since the threshold for the crack K_{th} was approached.
- In specimens with the overfill XB, the Paris law was obeyed, while in machined specimen XO, the crack growth rate increased above that predicted by the Paris relation [$da/dN=C\ (\Delta K)^m$].

- The fatigue resistance of the weld metal and the HAZ was reduced, compared to the parent metal.
- The fatigue behaviour of a welded joint could be improved by removing the overfill.

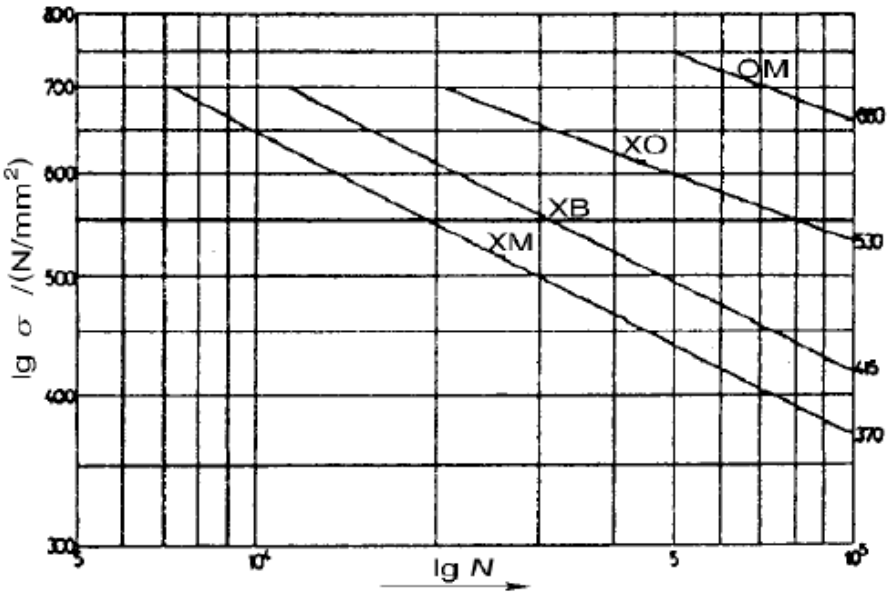

Figure 2.16: Upper part of the relationship applied σ Vs number of cycles *N* [Burzic *et al*., 2007]

Campbell *et al*. [2008] modeled a moment resisting frame structure with W27x94 girders, W14x159 columns, and double plates added to the panel zone to ensure their response remains elastic.

The structure was subjected to gravity loads plus a 1200 Pa live load followed by an earthquake with a peak ground acceleration of 0.632g. The nonlinear behaviour and design limit states of the elements were modeled using FEMA-356 in accordance with the guidelines in ASCE-41 [1969] and the calculations were carried out in perform-3D (CSI, Inc.).

The response parameters of plastic hinge rotation and story drift were compared to FEMA-356 acceptance criteria and used to calculate damage using low cycle fatigue.

Usage ratios for the ASCE-41 limits states were obtained directly from perform-3D for the immediate occupancy (IO), life safety (LS), and collapse prevention (CP) levels.

The Authors found that:

- The results illustrated the relationship between the damage measures according to the ASCE-41 criteria, the connection has failed the immediate occupancy (IO) level but passed the life safety (LS) level.
- The beam sizes were changed to W27x117 in order to exam the differences between the two calculations.
- The ASCE-41 usage ratios decreased by 18-21%, corresponding to the lessening of the peak end rotation.
- The fatigue damage index (FDI) or total damage to the element due to the cyclic load was decreased significantly more: up to 62%.

The Authors concluded that:

- An estimation of the remaining method life of a member allowed the engineer to predict the cumulative effect of multiple earthquakes over the life of a structure.
- FDI gave the engineer an additional tool that can be used to better understand the performance of their design under seismic loads.
- An adequate bracing and non-slender members, which prevented the local beam buckling and lateral-torsional buckling, led to low cycle fatigue failures.

  However, properly designed connections were found to have adequate ductility to sustain typical earthquake loads before the onset of the eventual fatigue failure.

Rosien and Ostertag [2009] tested twelve circumferentially notched AISI 1018 cold rolled steel specimens with different notch depth. The notches were strain hardened like many structural steel shapes (K-line, I-shape) which were subjected to different heat treatments to produce microstructure similar to the fusion line in welded steel moment resisting frames (SMRFs) with various yield strengths and toughness values.

The Authors found that:

- Microstructure changed due to heat treatment in 30 minutes with 1,095˚C temperature and proved sufficient to increase the grain size of the original steel by a factor of about three.
- The material properties, such as yield strength and ductility, were also remarkably changed.

The Authors concluded that:

- The Microstructure of the AISI 1018 had been modified by heat treatment to simulate microstructures, commonly found at crack initiation sites in (SMRFs) due to welding.
- The heat treatments produced soft steel with a coarse-grained microstructure and low yield strength and hard steel with high yield strength but low fracture toughness.
- Increased yield strength led to increase in the constraint; both effects reduced the corresponding local strains at the notch tip.
- Toughness had almost no influence on cyclic performance because the cyclic influences were only on the crack propagation phase.
- All specimens were showing a ductile crack initiation.
- At low stress level, the number of cycles, the specimens was able to withstand prior to failure, was influenced by the material properties, specially the yield strength. The samples with higher yield strength reveal a longer cyclic life by extending the crack initiation phase considerably compared to specimens with lower yield strength.

Nastar *et al*. [2010] created a two dimensional model using SAP 2000 of a ten-story steel building during the Northridge Earthquake, in order to understand the behaviour of the frame beams and columns connections through during the event. A series of modal analyses for mode shapes and frequencies, linear modal time-history, and nonlinear direct integration time-history were also analyzed.

The Authors found that:

- The connections failed in a brittle manner in low cycle fatigue and the damage was more significant for the buildings that have experienced two or more earthquakes in their life.
- The behaviour of the building during an earthquake depends on the fatigue accumulated in the connections from all the past major seismic events.

The Authors concluded that:

- Yield and slightly above yield stress levels occurred only in a few cycles, and as a result didn't justify the observed connection failures.
- Low-cycle fatigue was significant at all the investigated members, and the result of the current research emphasizes that low-cycle fatigue may be the cause of connection damage in the investigated building, similar to that observed during the Northridge Earthquake.
- Cumulative fatigue distribution at the investigated beams and columns reasonably matches the observed damage during the Northridge Earthquake.
- Low damping and vertical irregularity (set-back) were the characteristics of the investigated ten-story building which contributed to the results.
- Response data didn't support the existence of plastic hinges at failure locations. Recorded data and calculations indicated a predominantly elastic response.

The tests were used to develop S-N curves in the low-cycle region. These were mostly comprised of specimens that were built at the fabrication shops with higher

quality control measures. Considering the defects due to variations in construction quality specifically in regards to field welding can significantly reduce the fatigue life cycle of the pre-Northridge connection which will result in higher cumulative fatigue values.

2.3.2.1 Extreme Low Cycle Fatigue

Xue [2008] defined the very low cycle regime is termed ‘‘extremely low cycle fatigue” (ELCF) i.e. about less than 100 cycles.

The Coffin-Manson relationship does not give satisfactory results in the ELCF regime for many metals when the fatigue tests are conducted at elevated temperatures [Xue, 2008].

Several models are proposed to reduce the over-predicted life cycles by the Coffin-Manson law in the ELCF regime, it is found an exponential damage potential function which fits the $\Delta\varepsilon$-N curve in the ELCF regime. The exponential damage potential is defined as:

$$\Psi\left(\frac{\varepsilon_d}{\varepsilon_f}\right) = \frac{e^{\lambda\frac{\varepsilon_d}{\varepsilon_f}} - 1}{e^{\lambda} - 1} \qquad 2.2$$

where λ is a damage parameter, ε_d is equivalent plastic distortion. The damage rule can be derived from Equation 2.2 to get Equation 2.3 as:

$$dD = \frac{\lambda e^{\lambda\frac{\varepsilon_d}{\varepsilon_f}}}{(e^{\lambda} - 1)} \frac{1}{\varepsilon_f} d\varepsilon_p \qquad 2.3$$

where :

e is exponential function (Napiers constant) approx. value is [2.718*(εd/εf)]

ε_f is a fracture strain under monotonic loading path

The damage rule and the damage potential are plotted in Figure 2.17, for three different values of λ. When λ = 0, the damage potential function degenerates to the linear form.

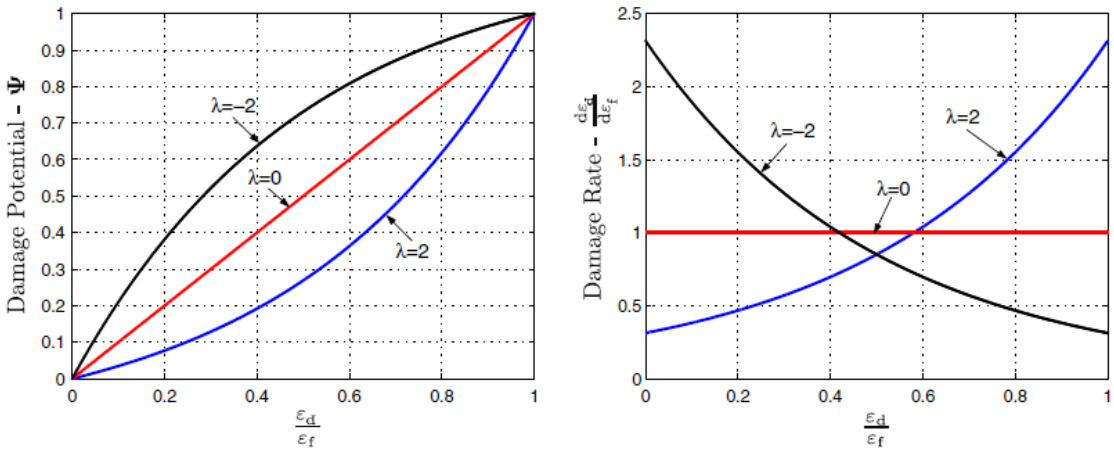

Figure 2.17: The damage potential function and the damage rate for three different values of λ. [Xue, 2008]

The $\Delta\varepsilon$- N relationship is readily to be derived from Equation 2.4, for materials obeying the exponential damage potential function for R = 0 loading.

The type of cyclic plastic loading can be characterized by the ratio of the minimum and the maximum plastic strain, i.e. R = εmin/εmax. The damage related to the Palmgren–Miner's rule is associated with the relative reduction of deformability to quantify the damage, i.e., for fully reversed loading).

$$D = \frac{4n\Delta\varepsilon_p}{4N\Delta\varepsilon_p} = \frac{n}{N} \qquad 2.4$$

where:

$\Delta\varepsilon_p$ is the plastic strain amplitude, n is the current number of cycles and N is the number of life cycles. In Equation 2.4, the numerator $4n\Delta\varepsilon$ denotes the current plastic strain and the denominator $4N\Delta\varepsilon$ denotes the total plastic deformability, which varies depending on the given plastic strain amplitude [Xue, 2008].

The Author concluded that:

- Experiments find that the empirical Coffin-Manson relationship for low cycle fatigue fits well in the strict sense of low cycle fatigue regime. However, it does not predict satisfactory life cycles for extremely low cycle fatigue due to the nonlinear nature of the life cycle curve.
- A new life prediction model is proposed for the entire range of the broad sense of the low cycle fatigue which covers the extremely low cycle fatigue regime.
- An exponential function is found to fit the extremely low cycle regime satisfactorily. This exponential function requires an additional material constant λ and can be calibrated from experimental $\Delta\varepsilon$-N data.
- A new expression by combining the exponential damage function and the power law Manson-Coffin relationship is proposed to describe the nonlinearity and provide a smooth transition between the LCF and ELCF regimes. The exponential function for ELCF and the power function for LCF become two limiting cases of this new expression.

Nip *et al*. [2010] carried out cyclic material tests in the low and extremely low cycle fatigue regime to study the properties of structural carbon steel and stainless steel. A total of 62 experiments were performed in cyclic axial and bending configurations, with strain amplitudes up to ±15%. Materials from hot-rolled carbon steel (S355J2H), cold-formed carbon steel (S235JRH) and cold-formed austenitic stainless steel (EN 1.4301 and EN 1.4307) structural sections were tested and the results were compared.

The strain life data from the axial tests were used to derive suitable Coffin-Manson parameters for the three materials: two further extremely low cycle fatigue life prediction models were also considered.

The Authors found that:

- The results revealed that the three materials exhibit similar strain life relationships despite significantly different elongations at fracture measured in monotonic tensile tests.

  The hysteretic responses of the materials at different strain amplitudes were used to calibrate a combined isotropic/kinematic cyclic material hardening model which can be incorporated into numerical models of structural members.
- The stainless steel specimens displayed significantly greater levels of cyclic hardening than the corresponding carbon steel samples.
- A relationship between the results obtained from axial and bending test arrangements was established through consideration of energy dissipation, enabling strain life models to be derived from either means of testing.

The Authors concluded that:

- The test results revealed that the three materials exhibit similar strain life relationships despite significantly different elongations at fracture measured in monotonic tensile tests.
- The hot-rolled (annealed) material generally displayed marginally better fatigue performance than the cold-formed material, attributed to the increased level of damage and reduced ductility caused by cold work.
- Stainless steel, which displays substantial strain hardening in monotonic tensile tests, also demonstrated a much larger degree of cyclic hardening than the two carbon steel materials.
- Material parameters for strain life relationships and cyclic stress-strain curves for the three materials were obtained from the test results.
- In order to model stress-strain hysteresis behaviour prior to the attainment of a stabilized state, the nonlinear combined isotropic/kinematic hardening model in ABAQUS was calibrated on the basis of total least squares fits to

the generated test data. Although there is some variability in the individual model parameters between different tests, the FE simulated hysteresis loops generated by the combined isotropic/kinematic hardening model (on the basis of average parameters for each material) are able to capture the key observed behavioural features.

- Bending tests were carried out without the concerns of slippage and buckling that are possible in axially loaded tests; the scatter of the generated test data was lower in the bending configuration.

2.3.3 Analytical modelling reported work

Carlo and Castiglioni [2005] tested twelve beam specimens fabricated by welding plates with different width-to-thickness ratios. Three for each type (group of four specimens) were subject to constant amplitude loading histories. Different cycle amplitudes were applied to each group of four specimens, in order to investigate the influence of the flange and web slenderness ratios on local buckling behaviour and failure mode of welded beam-to-column joints in moment resistance (MR) steel frames under seismic loading.

The Authors concluded that:

- A thin web could not restrain a thin flange and local buckling occurred at the first cycle in the plastic range, with consequent loss of strength capacity.
- High ductility was developed by cross sections with thin flanges and a thick web.
- For thick flanges, local buckling effects were limited and larger plastic deformations were occurred in the web which was significantly contributed to dissipate energy.
- The presence of a thick web was beneficial effects. It restrained the out-of-plane buckling of the thin flange. Strain hardening could be developed, resulting in higher ductility and a progressive loss of resistance and stiffness.
- Strain values indicated an earlier collapse due to either weld failure or cracking

of the base material in the weld area.

- The joint behaviour depended on the loading history, and geometric section properties.

Satish and Prasada [2006] tested four beam-to-column welded connections. The same hot-rolled rectangular hollow section (RHS) shape was used for both members, in order to develop and extend the use of RHS to multi-storied frames a connection.

The RHS were fabricated by two methods. In the first method, two Indian standard medium channel (ISMC) 200 sections were welded toe-to-toe and a box beam was fabricated by welding four plates using full-penetration groove welds.

The RHS obtained by welding two ISMC 200 channel sections was used for all the columns. The channel connectors were fabricated by welding two Indian standard angle (ISA) 75 × 75 × 10mm equal angle sections toe-to-toe or by welding 8 mm thick plates. Two channel connectors were welded to the column by full-penetration butt welds.

Comparison was made between the four specimen test and analytical results obtained from finite element analysis software [MSC/NASTRAN, 2000].

Comparison of test and analytical results indicated that the finite element analysis can be used to predict the behaviour of the connection with sufficient accuracy as shown in Figure 2.18.

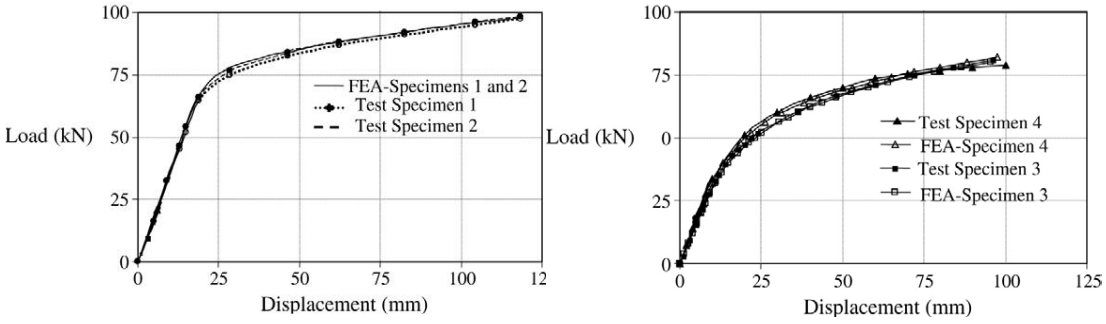

(a) Specimens 1 and 2. (b) Specimens 3 and 4.

Figure 2.18: Comparison between test and finite element analysis results [Satish and Prasada , 2006]

The Authors concluded that:

- When the depth and thickness of the channel connector were 75 mm and 10 mm respectively, the connection was able to carry increasing load with increase in the tip displacement.
- The failure was away from the column face and similar to beams with reduced beam sections (RBS).
- The connections were able to dissipate large amounts of hysteretic energy.
- The stiffness of the connection has been reduced due to the reduction in channel connector depth.
- It was found that the strain-hardening slope of E/80 was more appropriate to account for cyclic strain-hardening effects.
- The load-displacement hysteretic loops of the four tested specimens indicated that the connection possesses considerable hysteretic energy dissipation capacity and sufficient ductility.
- Modelling of the connection can be incorporated in semi-rigid frame analysis programs to get the performance of the frame under various design loads as shown in Figure 2.19.

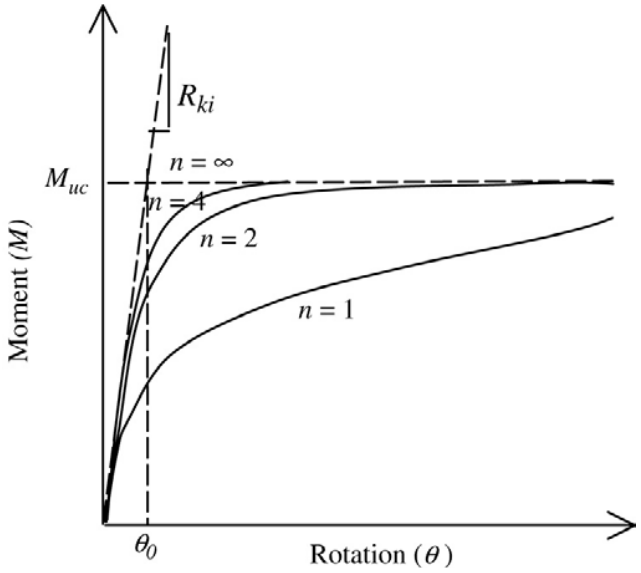

Figure 2.19: Three parameter power model [Satish and Prasada, 2006]

Björk *et al*. [2006] tested four welded joints as part of an extensive series of laboratory experiments performed at temperatures +20°C…- 60°C.
Two of the X-joints were fabricated from hot-formed structural hollow section (HFSHS) and two nominally identical joints were fabricated from cold-formed structural hollow section (CFSHS), in order to study the effect of the geometry and material properties on the ultimate strength of welded joints. The major difference between the above X-joints was the SHS corner geometries.

Finite element (FE) analyses were used to define the theoretical ultimate load-carrying capacity and expected failure mechanism. Experimental results have also been compared with analytical joint strength capacities calculated using current design guidance documents Eurocode3[1993].

The Authors found that:

- Strain hardening increased the material strength but decreased the plastic deformation capacity.
- A member with large filled radius between flange and web has greater flange stiffness and strength and increased the ultimate load-carrying capacity of an X-joint.
- The large corner radius resulted in a slightly smaller load-carrying capacity for cold hollow section (CFSHS) than hot-hollow section (HFSHS) with sharper corners.
- The main differences between CFSHS and HFSHS profiles are the corner geometry and the increased material strength and lower ductility properties in the corners of the CFSHS due to cold forming.
- For HFSHS, the primary failure mode was ductile fracture in the region of the welds followed by a brittle fracture, but for CFSHS joints, the primary failure mechanism was ductile yielding of the bracing members remote from the weld region.

- The heat input due to welding can change the material properties, these effects may increase the probability of brittle fracture as the failure mode for an X-joint fabricated with cold-formed structural hollow section (CFRHS).

Khandelwal and El-Tawil [2007] analyzed a steel frame with 8 story two interior bays using a computational simulation FEM analysis in order to investigate catenary action in a moment resisting frame connection, including: hardening, softening and ductile fracture behaviour, under seismic loading .
The analyses included the first, fifth, and seventh-story beam-column sub-assemblages of the eight-story prototype building.

Comparisons were made between FEM analysis and experimental results, which were obtained in a Gurson model (Gurson proposed a yield criterion and flow rules for a porous ductile, isotropic material by assuming that the material behaves as a smeared continuum. Yielding is governed by a yield surface that exhibits weak hydrostatic stress dependency, while the classical plasticity rules assume that yielding is independent of the hydrostatic stress) from Dos Santos and Ruggieri [2003], where the Gurson model was modified by Tvergaard [1981], and Tvergaard and Needleman [1984] for modeling ductile fracture in structural steel.

The Authors concluded that:

- Improving the web connection could likely improve the response of the sub-assemblage.
- The stronger web connection shifted fracture initiation to the RBS region and was the stronger and the more ductile connection.
- The simulation results demonstrated that with the ductility of a seismic design the frame had the ability to deform in catenary mode. That ductility and strength was adversely influenced by an increase in beam depth and an increase in the yield to ultimate strength ratio.

- Smaller beam sections were stronger and more ductile than assemblies without reduced beam sections (RBS).
- To improve the beam web connection, either improve the response of the sub assemblage or the beam web should be directly welded to the column through full penetration groove welds.

Bleck *et al*. [2009] tested small scale specimens experimentally and numerically in order to calibrate damage parameters for monotonic and cyclic loading and to determine damage curves.

The work studied both plate and beam materials. For the plate material three different steels according to EN [10025] were investigated in different thicknesses: S355J2 + N, S460N and S690QL. For the beam material two different steel grades (S355J2 and S460M) with two different sections (IPE500 and HEA300) were examined.

The influence of increasing steel grade is to increase the connection flexural strength and stiffness and a decrease in rotation capacity. The ductility and fracture toughness are less in high grade steel compared to low steel grade.

In general, the choice of the steel grade is ruled in Eurocode EN 1993-1-1.
Several requirements are specified: choice according to the material properties, ductility requirements, toughness properties and through-thickness properties. With reference to these requirements on the mechanical characteristics

The Authors concluded that:

- For high constraint level (h > 1) which is typical for flawed structures, either the fracture mechanics approach (FMA) or the damage mechanics approach (DMA) can be used.

- The transferability of the models for cyclic loading will be demonstrated on the rotation tests under cyclic loading.

Chen *et al*. [2006] tested steel H- shape elastic-plastic numerical model with the partial fracture beam-column connection (which is limited to beam flange fracture). The analysis included several non-linear springs at the end of the members. The plastic element assumed to be 1/10 of the total length of the beam, and the beam was welded to the column flange when the column was continuous with a rigid connection. The research focused on several key issues: (1) Fracture mechanism of beam-column connections; (2) Repair details for existing buildings and revisions to moment-frame connection details; (3) Assessment of the structural response after connection failure.

The Authors concluded that:

- There was a sudden drop of the strength when the fracture occurred as shown in point A Figure 2.20, and the joint can be loaded in a stable manner as shown in point B Figure 2.20.
- When the compression loading reached a specific value, the stiffness increased suddenly due to crack closure and regeneration of stiffness.
- When the compression loading reaches a specific value, the stiffness increases suddenly. The hysterical loop exhibits "pinch" behaviour as shown in point C in Figure 2.20. It is due to crack closure and regeneration of stiffness.
- The unloading stiffness from compression side was similar to the un-fractured elastic stiffness as shown in point D Figure 2.20. The stiffness deteriorated as the deformation decreased.
- The model presented the global structural analysis, which was useful for the assessment of the influence of the partial connection fracture to the whole structural system.
- The fracture was limited to beam flange fracture. For the other types of the fracture failure, the applicability of the current model needs further research.

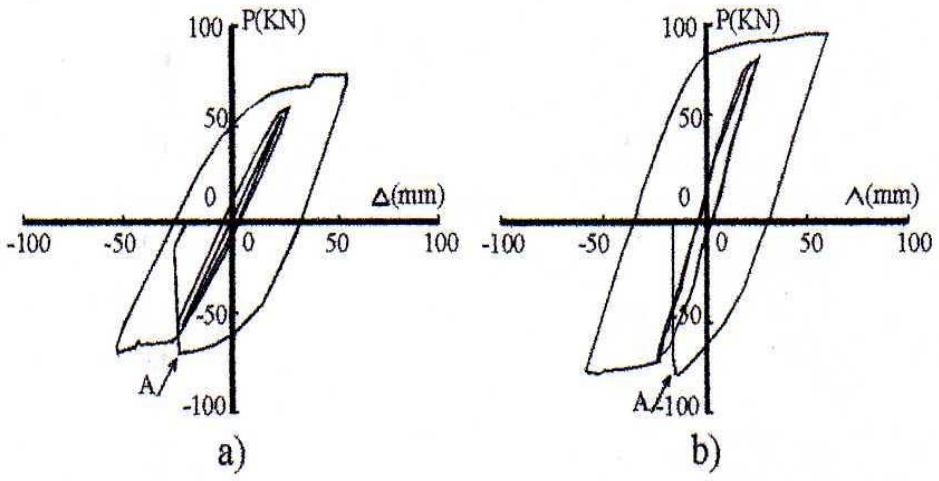

Experimental results

Simulation results

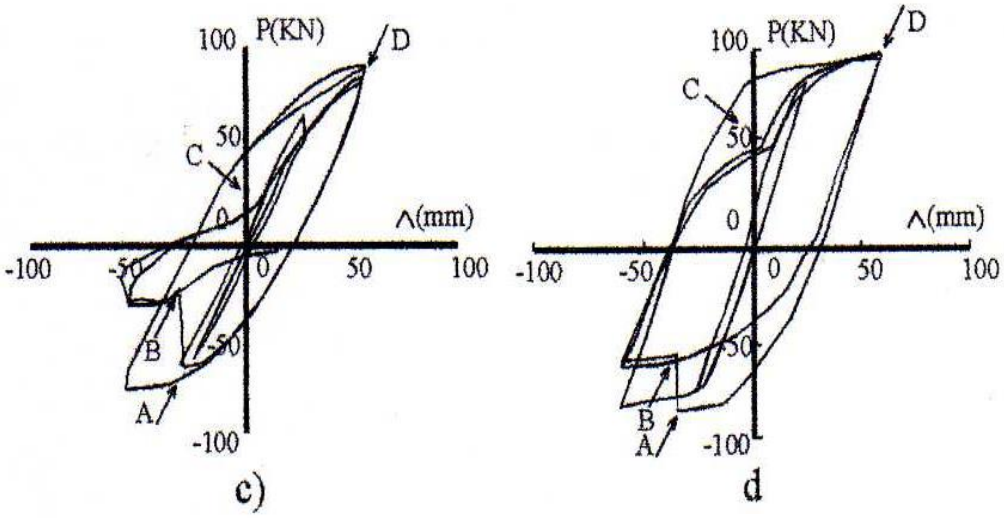

Experimental results

Simulation results

Figure 2.20: Comparison between analytic model and test data [Chen *et al*., 2006]

2.4 Finite element method (model analysis)

Righiniotis *et al*. [2002] used a simplified two-dimensional crack model for assessing the fracture of bottom flange welds in steel beam-to-column connections. The formulation of the model includes the determination of approximate expressions for stress intensity factors related to the cracked geometry, accounting for typical stress conditions and taking due consideration of the presence of the backing bar.

Comparisons were made between the results obtained from the proposed model and those available from a number of experimental investigations as well as two-dimensional finite element analyses. The proposed model was shown to provide good, but generally conservative, predictions in terms of both the fracture moments and reduction in stiffness.

The Authors concluded that:

- Stress intensity factor results were compared with finite-element fracture analyses of welded beam-column connections, experimental data by Chi *et al*. [2000] was used, and good agreement was observed.

  Comparisons were made between the experimentally observed beam stiffness of six test specimens in SAC experimental investigations of beam-column sub-assemblages, and the stiffness obtained from the proposed crack model. Also comparison was made in terms of both the fracture moment and the increased beam flexibility caused by the presence of the crack. These comparisons demonstrated the ability of the proposed crack model to capture important features of the Northridge connections.
- With a backing bar, on the lower side of the flange where the crack tip occurred, the stress concentration effect increased, but there is no effect of the stress concentration on the upper side of the flange boundary. Typical pre-Northridge moment connection with a backing bar is shown in Figure 2.21.

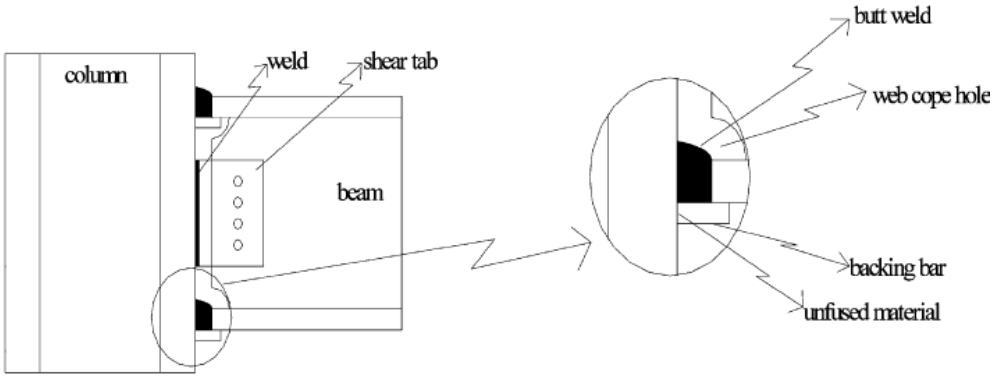

Figure 2.21: Typical pre-Northridge moment connection [Righiniotis *et al*., 2002]

Righiniotis and Imam [2004] used a simplified two-dimensional model to evaluate the reliability of a typical pre-Northridge connection. Comparisons were made with available experimental data reported by Matos *et al*. [2001] and analytical evidence model proposed by Righiniotis *et al*. [2002].

The reliability of the connection was examined using the fracture mechanics-based deterministic model proposed by considering the statistical scatter in material parameters (yield strength, fracture toughness) as well as manufacturing and inspection parameters (crack depth), the improved model was then used to perform a reliability analysis.

The Authors concluded that:

- Significant improvement was achieved by using higher toughness electrodes or by removing the backing bar.
- The reliability of a typical connection was still rather low.
- The model presented by Righiniotis *et al*. [2002] was used as a basis, with an improved estimate for the residual stress intensity factor being calculated using the weight function method.

- A statistical treatment of the important parameters observed in Northridge was presented and the inspection as well as repair events were quantified. Results compared with the results of Matos *et al*. [2001] were found to be conservative for a typical connection when leaving the backing bar in place and less conservative, when the backing bar was removed.
- Fracture toughness was found to have a significant.

Chi *et al*. [2000] using a finite element analysis (FEM) tested 2D and 3D finite-element models of the beam-column connection subassembly, in order to calculate fracture toughness demands at the welded-root in welded beam-column connections.

The Authors concluded that:

- The backing bar did not increase the fracture toughness demands, and the stress intensity factor was roughly linearly proportional to the root defect size and was unaffected by the backing bar thickness.
- Welding-induced residual stresses increased the fracture demands at low stress levels equivalent to that imposed by a nominal bending stress.
- Large panel zone deformations in connections with weak joint panels showed a roughly double fracture toughness demand compared with connections with strong panels zones.
- The connections with backing bars which was fabricated with low-toughness E70T-4 weld metal were likely to fracture from the weld root at or below the plastic moment.
- With higher toughness materials and significant detailing improvements, such as: backing bar removal, slight overmatching of weld strengths, and limited panel shear deformations, connections can achieve the target inelastic rotation of ɵ inelastic = 0.03 rad prior to weld root fractures.

Kuntiyawichai and Burdekin [2002] analyzed a number of series of cracked connections in steel framed structures using the finite element method (FEM), in

order to study the effects of dynamic loading on fracture toughness specimens under seismic loading.

The sub model (FEM) results were compared with the results obtained from a simplified method (the simplified method can determine approximate values of toughness and defect size requirements for given peak stress and strain level).

The Authors found that:

- The bottom haunch connection and cover plate connections can dramatically reduce the level of applied crack-tip-opening displacement (CTOD) at the beam to column weld. The reduced beam section (RBS or ‘‘dog bone’’) connections appeared to be partially effective in reducing the maximum applied CTOD but not as much as the bottom haunch connection and the cover plates connection.
- From finite element results of sub-model connections, the results showed that the strengthening of connections can significantly improve the connection performance.

Nakano *et al*. [2003] tested eleven T-shaped wide flange WF beam-to-SHS column connections specimens under cyclic loading in order to investigate the influence of reinforcement and width-to-thickness ratio of SHS column and the influence of yield ratio (yield stress to ultimate stress) of beam flange material and type of web connection.
One of the connections was all welded type (W series) with steel grade of SS400, and the other was web bolted flange welded type (B series) with steel grade of SN400B.

For wide flange (WF) beams size was used H-section, the overall depth of the section is 500mm and the overall width of the section is 200mm, web thickness is 10mm and

flange thickness is 16mm (500 x 200x10x16) for all specimens. Cold-formed SHS columns with width of 350mm and the steel grade of BCR295 were used for all specimens. The thickness of column skin plate was 9mm, 12mm, 16mm at W series and 12mm, 16mm at B series.

The methods of reinforcement were inserting horizontal diaphragms (HD) or vertical stiffeners (VS) inside panel zone.
The usual beam-to-column connection without any reinforcement (N type) was prepared for comparison with the reinforced specimens.

The Authors concluded that:

- The out-of-plane stiffness of the column skin plate influenced the maximum strength and the plastic deformation ability of beam-to-column connection.
- By the reinforcement of panel zone at web connected parts of the beam, the final mode of the specimen changed from ductile fracture of the flange of the beam to local buckling of the beam.
- The yield ratio of the beam flange material had a large influence on the maximum strength and the plastic deformation ability of the beam-to-column connection.

Kiral [2004] tested a welded steel beam-to-column connection by using the European flaw assessment procedure (SINTAP) Level II, in order to examine the effects of the toughness of weld metal, and to study the assessment of the safety of the welded beam-to-column connections under earthquake loads to avoid the brittle fracture.

The connection consists of a W30× 99 beams connected to a W14×176 column with welding operation and they both were A 572 steel Gr. 50. Two different electrodes were used, namely E70TG-K2 and relatively tougher E-7018. The limit load of the

connection was determined by the Net-Section-Collapse Method (NSC). The model was the common connection used before the Northridge earthquake.

The Author concluded that:

- The structure was safe if the work condition for the structure was below the failure assessment line.
- The limit load values of welded steel connection for both electrodes, E70TG-K2 and E-7018 were equal, because the yield strength values of both electrodes were equal.
- The maximum load value of the connection increased when E70TG-K2 electrode was used because the ultimate strength of E70TG-K2 electrode was higher than that E-7018.
- The structure collapsed when the applied load reached the maximum load.
- The critical crack length size permitted in the structure was larger when the electrode E-7018 was used.
- The critical crack length decreased until the applied load reached to limit load. There was some increasing in the critical crack size after the yielding occurred.
- SINTAP provides an accurate evaluation of the fracture behaviour of the connections by considering the interaction of local fracture demands, crack size, connection geometry details and material properties.

Ricles *et al*. [2004] tested six full-scale interior RBS connections specimens in order to investigate the seismic behaviour of reduced a beam section (RBS) moment connections to a deep wide flange column, where the column for the ranged in depth from a W24 to a W36 wide flange section.
The results of the experimental study, along with a nonlinear finite element study were used to develop seismic design recommendations for RBS connections to deep columns.

The Authors concluded that:

- The performance of each test specimens was found to meet the seismic connection qualification criteria of the AISC Seismic Provisions, and thereby have sufficient ductility for seismic resistant design.
- All the specimens were able to satisfy the criteria in the AISC Seismic provisions for qualifying the connection for seismic use.
- A weaker panel zone in a deep column RBS connection would not develop as much column twist and strength degradation as a connection with a stronger panel zone.
- A weaker panel zone can significantly increase the potential for ductile fracture of the connection.
- A supplemental brace at the end of the RBS significantly reduced the transverse movement of the beam flanges in the RBS and column twist that leads to cyclic degradation in specimen capacity.
- A new procedure for estimating the torsional load which was applied to the column due to the local and lateral buckling in the RBS, showed an improved method for correcting for the normal stress in column flange.

Höhler and Sedlacek [2005] tested large scale solid bars or I-profiles with slotted gusset plate welded connections. The test specimens contained initial cracks at locations of high stress concentrations. For the theoretical studies, the K-concept was applied. Formulae for K-requirements were developed for such details with numerical simulations using boundary element (BE) methods. The steel grades were S235J2G3 and S355J2G3 with thicknesses of 20 mm or 40 mm. Beams representing diagonal components were welded into the slotted gusset plates leaving a gap at the weld ends.

The fracture mechanical calculations were carried out using stress intensity factors (K-concept). The numerical BE- method (only requires modeling of the outer surface boundaries of the detail, the complex geometry with initial cracks could be modeled

with surface boundary elements) was applied for three-dimensional simulation of the crack behaviour. The above investigations were carried out for typical details as used in buildings, both experimentally and theoretically in order to select steels to avoid brittle fracture according to Eurocode 3[2005].

The Authors found that:

- The worst case combination was a short weld length L and a great height of component H.
- The test provided the highest toughness requirements for the connection.
- A method had been developed for the choice of material for members with particular details to avoid brittle fracture.
- The numerical method was compared with the experimental results obtained from large scale tests. The comparison proved that the BE-method was a suitable method for calculating stress intensity factors and crack growth.

Jiaru *et al*. [2005] tested ten full-scale steel beam-to-column moment connection specimens under cyclic loading in order to investigate and compare the seismic behaviour of steel beam-to-column connections with various details of four groups specimen. Comparison was made between nonlinear finite element analysis and experiment results.

The Authors concluded that:

- Cracks occurred at the weld toe of the beam flange and web juncture adjacent to the weld access hole and also occurred in the fillet weld which was connecting the shear plate (or the beam web) to the column. Slippage of the shear plate was observed.
- Three types of fractures were observed at the end of the beam. They were: fracture at the interface between the beam flange and groove welds; fracture at the interface between the groove welds and column flange; or accompanied

by tearing of the column or column corner welds, and tearing of the base metal of the beam flange and/or tearing of diaphragm.

- For all specimens, beams reached their plastic moment capacity. The measured yield strength and the ultimate strength of the dog-bone specimens were less than the strengths of the reference specimen.
- The beam plastic rotation of the connection with cover plates and the dog-bone connections was larger than 0.03reds. These connections satisfy the beam inelastic rotation demand for ductile moment resisting frames (MRFs).
- At the end of the beam, the web was taking shear force and bending moment, but the flange was taking moment and shear force. The tri-axial stresses and the residual welding stresses at the end of beam flange were the essential course of fractures of the beam end.

The Authors recommended that:

- Reducing the residual welded stresses at the end of the beam flanges is important to prevent fracture of the beam end.
- Connections with beam flange cover plates and with bottom beam haunch are recommended for steel ductile moment-resisting frames. Connections with trimmed beam flanges are also recommended.
- Continuous fillet welding along the back-up bar should be provided:

a) A fully welded connection is recommended for steel beam-to-column moment connections.

b) When the welded flange-bolted web connection is adopted, the shear plate should have a certain thickness, two rows of bolts should be used, and fillet welds are recommended to connect the shear plate to the beam web.

Chen *et al*. [2008] tested a steel frame connection model and the beam-column connection was designed to be an anticipated failure connection, in order to test the

impact effect of the partial fracture at beam-column connections. The beam and column members remained elastic when the connection was likely to fracture.

The measuring points were set on three sections per member to obtain the moment distribution of the member and the correctness of every measured value could be checked.

The Authors found that the measured moments of the beam and column still kept a linear distribution after connection fracture occurred.

The Authors concluded that:

- The connection fractured in a short time which was characterized by progressive collapse and partial fracture.
- The impact effect of fracture in connection was relatively small, and the dynamic magnification factor of steel frame with natural period in the range of 0.3-2.0 s was relatively small.

Hedayat and Celikag [2009] modeled one of the pre-tested post-Northridge connections, using the finite-element method (FEM), in order to examine the reliability of pre- and post-Northridge connections; the results of the analysis were used as typical examples of the behaviour of these connections.

The fracture mechanics-based deterministic model proposed by Righiniotis *et al.* [2002] was used. Also, experimental fracture moment and ductility data from previously conducted full-scale tests on T-connections by Lee *et al.* [2000] and Chen *et al.* [2005], were used to obtain suitable cumulative distribution functions for normalized fracture moment (fracture moment divided by plastic moment of the beam) and plastic rotation of these types of connections.

The Authors concluded that:

- A decrease in the yield stress of the beam material delayed the initiation of fracture and led to an increase in the ratio of the beam fracture moment to the beam plastic moment capacity and in the connection ductility.
- A decrease in the post-yielding stiffness of the beam materials caused a reduction in the connection moment capacity and an increase in the connection ductility.
- A decrease in the crack depth (removal of the bottom backing bar) and an increase in the fracture toughness of the weld metal (E70TGK2) caused a significant reduction in the hazard and a remarkable increasing in the probability of ductile behaviour of welded connections.
- The detrimental (bad) effects of residual stresses on the structural performance were increasing in SIF and stress triaxiality, (a) increasing promotion of connection brittle fracture and (b) finally reducing connection ductility. These effects depend on weld joint geometry, welding process, restraint conditions, basic and weld material properties.
- Although temperature plays an important role in fracture, it played a very small part in the fracture behaviour of the connections at Northridge Earthquake.
- Results showed that by increasing the level of desired normalized fracture moment, Mf /Mp (Mf is moment at failure and Mp is beam plastic moment), the results became non-conservative & non-reliable, especially by improving the connection behaviour (using E70TGK2 weld metal and removing the backing bar). Therefore, in order to predict the probability of ductile behaviour of post-Northridge connections, a multi-random variable function should be defined by considering all parameters which contribute to the fracture of welded connections.

2.5 Conclusion

A detailed literature review has been carried out; analytical and experimental work has been considered, and the main conclusions are summarized as follows:

- The literature review was looked at the effect of low-cycle fatigue in steel welded connection after the Northridge Earthquake which indicated that these connections essentially failed after only a few high-stress cycles. Brittle behaviour and low-cycle fatigue were important and need to be considered in evaluating and predicting various types of connection damage similar to that observed in the steel moment frames during the Northridge Earthquake.
- The low cycle fatigue concept has been developed through the extensive research and this concept has been used to predict the life of structures subjected to the cyclic load.
- Many researchers are interested in cyclic strain rather than cyclic stress, because low cycle fatigue failures are typically observed when the applied cyclic loading produce large plastic strains, therefore strains (displacement) must be controlled rather than stress (load). Very low cycle fatigue from very large strains results in fatigue failure in less than 100 cycles. Low cycle fatigue, which is also calculated based on strains, results in failure in up to 10^5 cycles. Otherwise high cycle fatigue, based on stress needs more than 10^5 load cycle before fatigue failure.
- It should be noted that plastic strain amplitude is the key factor to cause the LCF damage. It can be assumed that the LCF damage under the large plastic strain amplitude will affect the ratcheting behaviour under the subsequent asymmetrically cyclic stressing.
- The low cycle fatigue (LCF) model can be use to predict the life to failure.
- The displacement load can successfully be used within the LCF model to predict cracking of a steel connection.

- Low-cycle fatigue initiation could be expected in the region of welded joints, because the yield stress could be achieved locally by stress concentration. Local plastic deformation ahead of the crack tip was typical for crack initiation and growth in the early stage of low-cycle fatigue, followed by shear lips [Burzic *et al*., 2007].
- In low cycle fatigue the crack is formed when the applied stress exceeds the critical strength of the steel welded joint due to the repeated cyclic load.
- It is not clear whether the very low cycle fatigue (VLCF) is better considered as a fatigue process or a fracture process. Approaches include ordinary LCF (Coffin-Manson type methods) and cumulative cyclic stress (brittle fracture type method). The approaches will be compared in this work.
- The very low cycle regime is termed ‘‘extremely low cycle fatigue” (ELCF) i.e. less than about 100 cycles. It is observed that the Coffin-Manson law does not fit well in the range of very low life cycles at elevated temperatures [Xue, 2008].
- Strain (displacement) rather than stress (load) must be controlled. The strain life methods, often called the local strain approach, can be used for fatigue life predictions considering material properties, geometry, stress-strain analysis at the critical location, including damage assessment and summation techniques.
- Welds are usually rough in toes of butt welds and toes and roots of fillet welds, there are sharp changes in curvature and sharp inclusions and hence they have local stress concentration, therefore fracture toughness is reviewed in this literature.
- The weld imperfections significantly reduce the fatigue crack propagation life and fatigue strength of welded joints. Solidification cracks and undercut are more serious than embedded porosity. Improvement of weld geometry decreases the stress concentration and increases the fatigue strength. The

residual stress, bending stress and dissimilar mechanical properties of base, weld and HAZ metals also decrease the fatigue strength of welded structure.

Bi-axial loading and the combined effect of a solidification crack and spherical porosity reduce the fatigue crack propagation life. But when they interact with each other, the fatigue life can increase compared to when they occur separately.

- Steel welded connection behaviour depends on the loading history and geometric section properties. To design a steel welded connection under cyclic loading, three parameters should be taken in consideration; The connection must possess sufficient strength, must possess sufficient stiffness to satisfy the assumption of a fully rigid connection and finally the connection must have a large post-yield deformation capacity without significant loss of strength.
- Data from literature related to steel welded connection showed that two types of investigations were carried out experimentally and numerically.
- Welded steel joints can be mathematically modelled and the numerical method can be used for design optimization.
- The contribution of welding continuation flange plates to the column flange and web, to surround the "panel zone" is to increase of the connection overall stiffness and to control the stress and strain distribution.
- In a welded specimens; specimens in the as-welded condition, the crack-growth rate was low since the threshold for the crack K_{th} was approached. [Burzic *et al*.,2007].
- The heat input due to welding can change the material properties, these effects may increase the probability of brittle fracture [Björk *et al*., 2006].
- Fatigue cracks almost always grow from welds in steel welded structures. The reason is that the welding process invariably leaves metallurgical discontinuities of minute sizes in the welds and cracks develop from these discontinuities.

- Damage leads to failure and failure leads to fracture. When a material is damaged it has not necessarily failed in service and can be repaired somewhat, but when it fails it cannot be used in service, i.e. it has lost its integrity. However, when a material fractures it is broken into two or more parts. Fracture occurs once the 'damage' reaches a critical limit.
- Cracks occurred at the weld toe of the beam flange and web juncture adjacent to the weld access hole and also occurred in the fillet weld which was connecting the shear plate (or the beam web) to the column [Jiaru *et al*., 2005].
- The FE model can provide a variety of results at any location within the model. A viewing of the full fields of stresses and strains are possible in the FE model. This provides a great advantage in monitoring the components of the connection under continues cyclic loading.
- Validation of numerical analysis and experimental work can result in good comparison of force-displacement hysteresis loops from experimental work and FE analysis. However, there may be differences due to the environment of experimental work, and exact modelling of the considered T-steel connection.
- The numerical modelling can predict crack locations by using maximum strains and stresses as the location criterion.
- The FE modelling showed that, the most critical zone to failure are the welding connection including heat effected zone (HAZ) and panel zone.
- Numerically, using strain life theory to predict cracking in steel connection seems to be workable and reasonable without modelling the crack and can give acceptable results.

CHAPTER 3
FATIGUE LIFE METHODS, CRACKING AND RATCHETING

Outline of this chapter; Fatigue life methods, define fracture mechanics, evaluate cracking and define ratcheting strain

Fracture mechanics have been investigated in this chapter of looking at the results. Sections are included in this chapter as follows:

Section 3.1 summarizes fatigue life estimation methods integrated with literature.

Section 3.2 summarizes evaluation of cracking

Section 3.3 defines fracture mechanics approaches

Section 3.4 defines ratcheting strain effect by many researches.

Section 3.5 conclusion.

3.1 Fatigue life estimation methods

A fatigue life can be measured by the number of load cycles it takes to produce a failure (usually a fracture) within the specimen or member. If the fatigue life is relatively short, less than a hundred thousand cycles, then the failure is considered a low cycle fatigue (LCF) failure, but if fatigue life exceeds a hundred thousand cycles, the failure is considered a high cycle fatigue (HCF) [ASTM, 1969].

All structures and mechanical components that are cyclically loaded can fail by fatigue. Two methods are widely used to estimate fatigue life; Stress life method (HCF) and Strain life method (LCF).

3.1.1 The stress life method

In this method, analysis assumes that the stresses always remain elastic even at the stress concentration. For plain steel, most of the fatigue lives is consumed during the nucleating small micro cracks stage. This is typical for long life situations (millions of cycles) where the fatigue resistance is controlled by nominal stresses and material strengths. For welded structures the welding process leaves small defects in the structure and the crack initiation stage is probably much shorter.

The stress-life method was the first approach used to understand and quantify metal fatigue. The stress-life approach is generally categorized as a high-cycle fatigue methodology, and is still widely used in design applications where the applied stress is primarily within the elastic range of the material and the resulting fatigue lives (cycles to failure) are long.
The stress life method is the classical method for fatigue analysis of metals and has its origins in the work of Wöhler [1850] as reported by Pook [2007].

3.1.1.1 Cyclic Loading

A typical stress history during cyclic loading is shown in Figure 3.1.

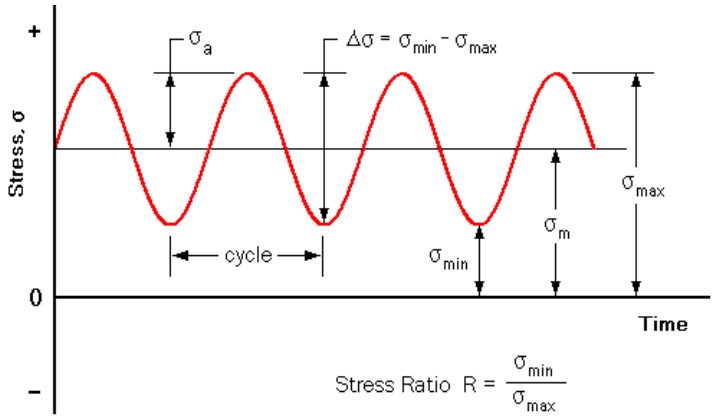

Figure 3.1: Stress-time relationship [Tamin, 2012]

where:

Stress Range: $\Delta\sigma = \sigma_{max} - \sigma_{min}$

Stress amplitude: $\sigma_a = ½ (\sigma_{max} - \sigma_{min})$

Mean stress: $\sigma_m = ½ (\sigma_{max} + \sigma_{min})$

Load ratio: $R = \sigma_{min} / \sigma_{max}$

The basis of the method is the materials S-N curve which is obtained by testing small laboratory specimens until failure is presented by Pook [2007] in Figure 3.2.

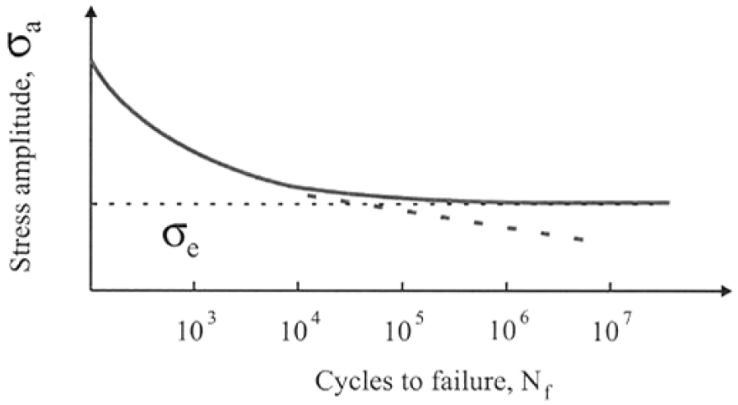

Figure 3.2: S-N curve [Pook, 2007]

Figure 3.2, shows that, if the stress is below σ_e (fatigue limit), the component has effectively infinite life. $\sigma_e \approx 0.35\sigma_{TS}$ - $0.50\ \sigma_{TS}$ for most steels and copper alloys, (where σ_{TS} is tensile strength). If the material does not have a well defined σ_e, often σ_e is arbitrarily defined as the stress that gives $N_f = 10^7$. If a plot is prepared of log (σ_a) versus log ($2N_f$) (where $2N_f$ represents the number of reversals to failure, one cycle equals two reversals) a linear relationship is commonly observed. The following relationship between stress amplitude and life time has been proposed [Basquin,1910]:

$$\frac{\Delta\sigma}{2} = \sigma_a = \sigma`f(2Nf)^b \qquad 3.1$$

where σ'_f is the fatigue strength coefficient, *b* is the fatigue strength exponent or Basquin's exponent (≈ -0.05 to -0.12), and N_f is the number of cycles to failure. The total fatigue life of a component can be considered to have two parts, the initiation life and the propagation life is reported by Basquin [1910] as shown in Figure 3.3 .

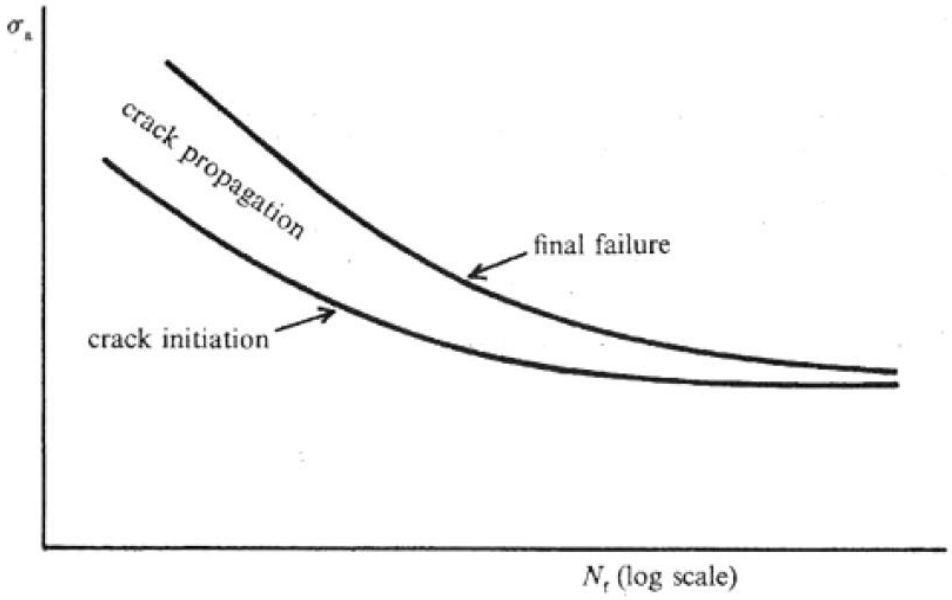

Figure 3.3: The initiation and the propagation life curves [Basquin, 1910]

Note that under variable stress amplitude loading the larger stress amplitudes may propagate cracks that the smaller stresses can then continue to propagate.

3.1.2 The strain-life

This method is known as low cycle fatigue (LCF) and it is used for situations where plastic deformation occurs around the stress concentrations. The strain life method had its major development during the 1960's. It is based on the idea that the local stresses and strains around a stress concentration control the fatigue life. Although most structures components have nominal stresses that remain elastic, occasional high loads and stress concentrations cause plastic deformation around notches. The

strain-life methodology is based on the observation that in many critical locations such as notches the material response to cyclic loading is strain rather than load controlled [ASTM, 1969]. The material surrounding the plastically deformed zone remains fully elastic but the deformation at the notch root is considered to be strain controlled as reported by Darrell [2008, 2013].

In steel structures, low cycle fatigue failures are typically observed when the applied load cycles produce large plastic strains within the specimen, therefore strains (displacement) must be controlled rather than stress (load).

From 1950s, many researchers were interested in cyclic strain rather than cyclic stress because there was a need for information on metals subjected to relatively few cycles of controlled cyclic strain.

Coffin and Manson [1950] first developed methods for low cycle fatigue problems associated with gas turbines and nuclear reactors. Coffin [1954] was interested in thermal loading causing large plastic strain and very short fatigue lives. And they determined a power relationship existed between plastic strain amplitude and fatigue life [Chemin, 2009].
The method, refined in 1960s to deal with wider variety of fatigue situations, is reported by Morrow [1965] and Neuber, [1961].

3.1.2.1 Cyclic stress-strain behaviour

Tucker [1972] mentioned that the extent and rate of cyclic hardening or softening under strain-controlled testing conditions can be evaluated by recording stress variation as a function of cycles, as shown in Figure 3.4. Cyclic hardening, shown in Figure 3.4b, indicates increased resistance to deformation, whereas cyclic softening, shown in Figure 3.4c, indicates the opposite effect. Changes in cyclic deformation behaviour are more pronounced at the beginning of cyclic loading.

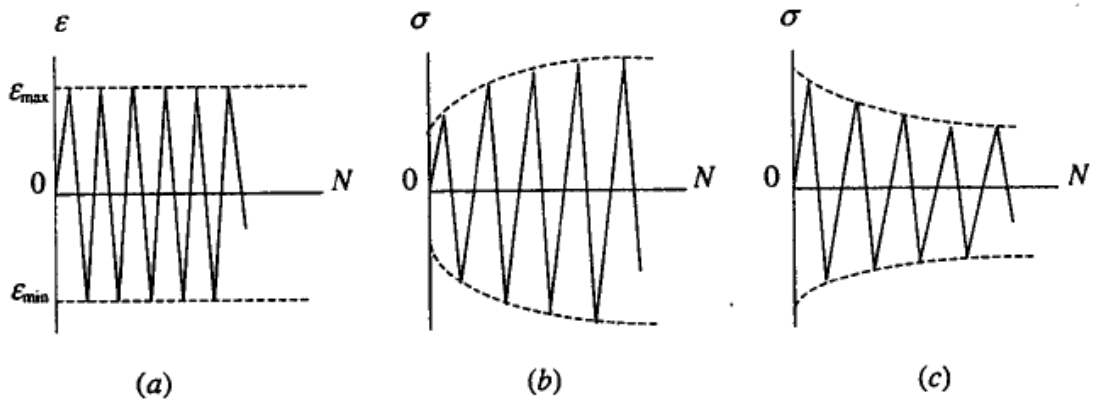

Figure 3.4: Stress responses under constant strain amplitude cycling. (a) constant strain amplitude, (b) cyclic hardening and (c) cyclic softening [Tucker,1972]

Bauschinger [1886] did the same work of Tucker [1972] and went further in that, he did not stop the unloading process at the zero stress level but he continued on down into full compression to point C in Figure 3.5.

Figure 3.5 shows a specimen of a material loaded in tension to beyond the yield stress to a maximum stress of σ_{max}, point A. At this point the loading direction is reversed and the specimen is unloaded from point A through the zero stress level and on into compression to a stress equal to $-\sigma_{max}$, point B. The interesting point to note is that the material appears to yield at a stress level before $-\sigma_y$ is reached. This observation has nothing to do with the fact that the yield strength in compression might be different from that in tension.

The whole experiment could be repeated, but this time loading in compression first by going to $-\sigma_{max}$. Yield would take place at $-\sigma_y$ but would again occur before σ_y was reached when the loading direction was reversed, this behaviour is known as the Bauschinger effect and, as reported by Amandeep *et al* .[2008] and Tamin [2012], its importance cannot be overstated.

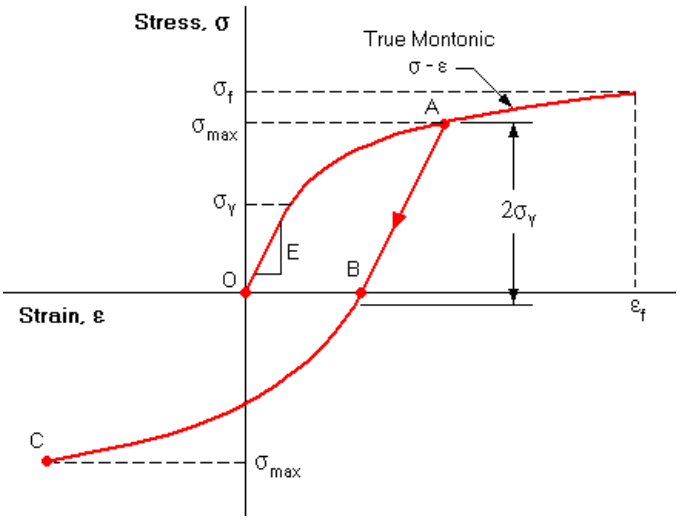

Figure 3.5: Stress-strain behaviour after a reversal [Amandeep *et al.*, 2008]

If the loading process shown in Figure 3.5 is continued from $-\sigma_{max}$ to $+\sigma_{max}$, then a hysteresis loop will result as shown in Figure 3.6.

Tucker [1972] mentioned that a hysteresis loop from about half of the fatigue life is often used to represent the stable or steady-state cyclic stress-strain behaviour of the material. A stable stress-strain loop is shown in Figure 3.6. The total true strain range is denoted by $\Delta\varepsilon$, and $\Delta\sigma$ is the true stress range. The true elastic strain range, $\Delta\varepsilon_e$, can be calculated from $\Delta\sigma/E$. By definition:

$$\Delta\varepsilon = \Delta\varepsilon_e + \Delta\varepsilon_p = \frac{\Delta\sigma}{E} + \Delta\varepsilon_p \qquad 3.2$$

where:

$\Delta\sigma$ is the stress range, $\Delta\varepsilon_e$ is the elastic strain range, $\Delta\varepsilon_p$ is the plastic strain range and $\Delta\varepsilon$ is the total elastic strain range.

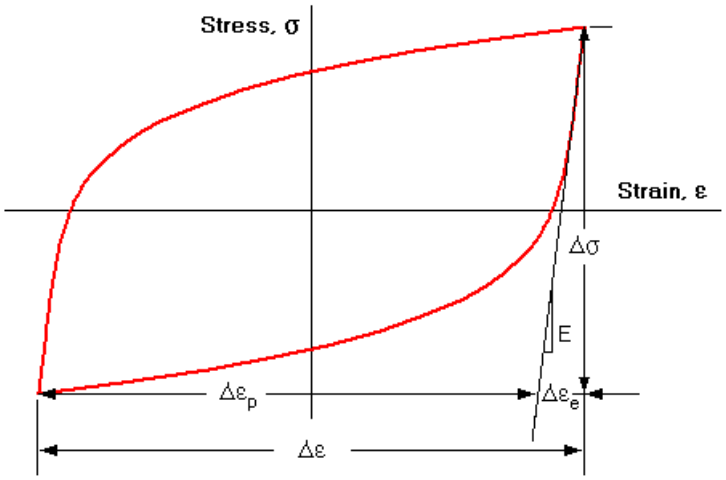

Figure 3.6: Typical cyclic stress-strain curve [Tamin, 2012]

Tucker [1972] mentioned that the repeated stabilized hysteresis loops (family) at different strain amplitudes can be used to obtain the cyclic stress-strain curve for a given material. The tips from the family of multiple loops are connected to form the cyclic stress-strain curve as shown in Figure 3.7.

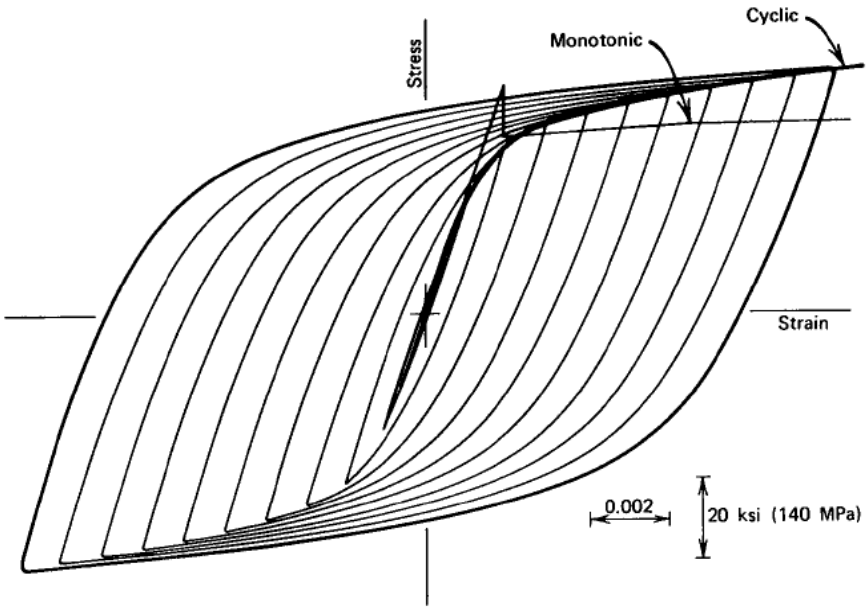

Figure 3.7: Stable hysteresis loops for determining the cyclic stress-strain [Tucker, 1972]

Bauschinger [1886] obtained a stress-strain behaviour from a monotonic tension or compression test under cyclic loading. This was first observed during the late nineteenth century by his work that indicated the yield strength in tension or compression was reduced after applying a load of the opposite sign that caused inelastic deformation. This can be clearly seen in Figure 3.8, where the yield strength in compression is significantly reduced by prior yielding in tension. Thus, one single reversal of inelastic strain can change the stress-strain behaviour of metals.

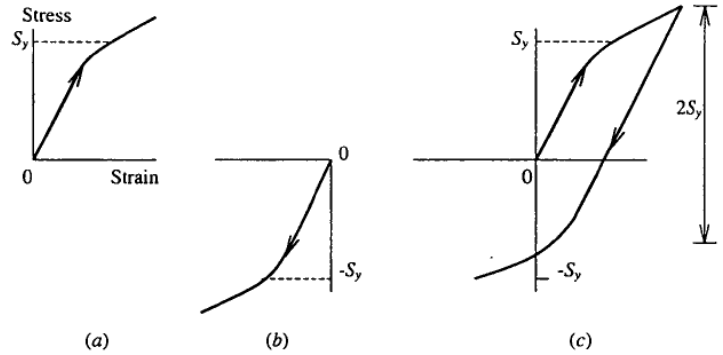

Figure 3.8: Bauschinger effect. (a) tension loading,(b) compression loading and (c) tension loading followed by compression loading [Bauschinger, 1886]

Morrow [1965] reported a work of copper subjected to a controlled cyclic strain in three initial conditions as shown in Figure 3.9. These tests were performed on axially loaded specimens in the (a) fully annealed condition, (b) partially annealed condition and (c) cold worked condition. The number of applied reversals at different positions of the hysteresis loops are indicated. The area within a hysteresis loop is the energy per unit volume dissipated during a cycle.

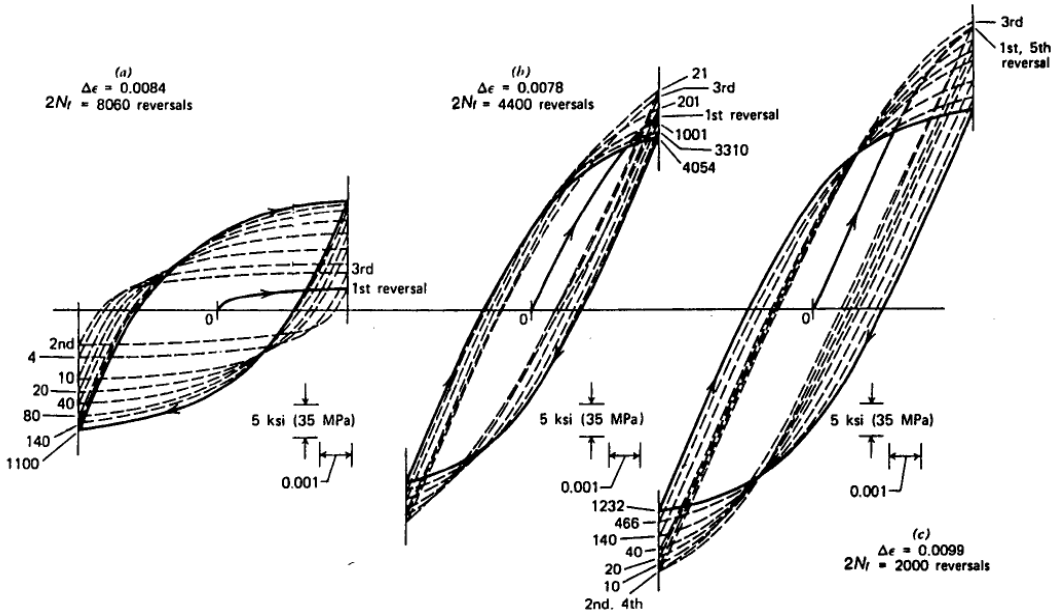

Figure 3.9: Stress-strain behaviour of copper subjected to cyclic strain-controlled axial loads.(a) fully annealed is showing cyclic hardening,(b) partially annealed is showing small cyclic hardening and softening and (c) cold worked is showing cyclic softening [Morrow, 1965]

3.1.2.2 Strain-life formulas

When plastic strain occurs, the service life of material decreases, often to no more than 10^5 cycles in low-cycle fatigue range.

Most of the reported research work of low-cycle fatigue was traditionally done for pressure vessels, power machinery that are exposed to a heat source/sink which induces thermal expansion (thermal stress) to the structure. The low-cycle fatigue is usually presented as the plastic strain $\Delta\varepsilon_p$ in log scale against reversals cycles to failure $2Nf$, also in log scale as shown in Figure 3.10.

Basquin [1910] has observed that stress-life data could be modelled using a power relationship, which results in a straight line on a log-log plot. This observation corresponds to elastic material behaviour in the strain-life approach.

The Basquin formula can be expressed in terms of true elastic strain amplitude as:

$$\varepsilon_e = \frac{\sigma_a}{E} = \frac{\sigma'_f}{E}(2N_f)^b \qquad 3.3$$

where:

- ε_e is the elastic component of the cyclic strain amplitude
- σ_a is the cyclic stress amplitude
- σ'_f is the regression intercept called the fatigue strength coefficient
- N_f is the number of cycles to failure
- b is the regression slope called the fatigue strength exponent

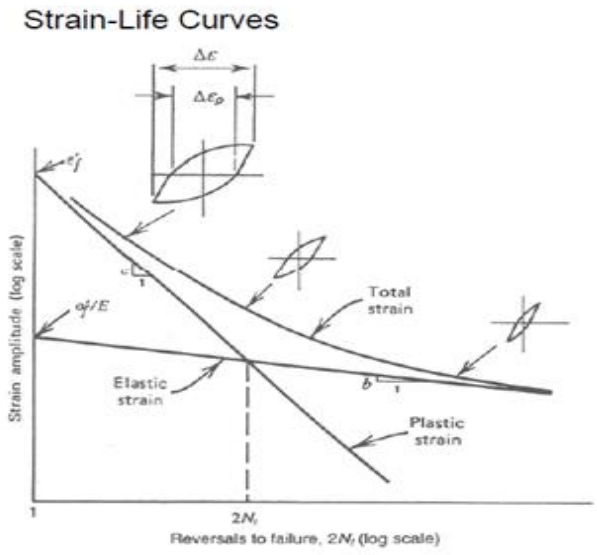

Figure 3.10: Total elastic and plastic strain components strain-life curves [Basquin, 1910]

In the Figure 3.10, it can be observed that for a given life N, the total strain is the sum of the elastic and plastic strains. Both the elastic and plastic curves can be approximated as straight lines. At short fatigue lives, low cycle fatigue, plastic stains dominate and at long fatigue lives, high cycle fatigue, elastic strains dominate the

fatigue life. This method allows for the characterization of fatigue properties for a material throughout the entire life range.

Coffin and Manson [1950] proposed that the fatigue life could be explicitly related to the plastic strain amplitude. Where the stress is high enough for plastic deformation to occur, the account in terms of stress is less useful and the strain in the material offers simpler description. Low-cycle fatigue is usually characterized by the Coffin-Manson relation popularized by Coffin [1979] based on Manson's [1960] work. Mathematically, the expression may be written as:

$$\varepsilon_{ap} = \varepsilon'_f (2N_f)^C \qquad 3.4$$

where:

$\varepsilon_{ap} = \Delta\varepsilon/2p$, the plastic strain amplitude is half width of the hysteresis loop.

$\varepsilon`f$ is an empirical constant known as the *fatigue ductility coefficient*, the failure strain for a single reversal. C is an empirical constant known as the *fatigue ductility exponent*, commonly ranging from -0.5 to -0.7 for metals. It can be calculated from experimental data using the least square fit procedure if the experimental data are plotted in a log ($\Delta\varepsilon_p/2$) and log ($2N\,f$). $2N$ is the number of reversals to failure (Nf cycles).

Coffin [1954] and Manson [1953] have established a mathematical relationship between the total strain amplitude $\Delta\varepsilon/2$ and the reversals to failure cycles $2Nf$ as:

$$\frac{\Delta\varepsilon}{2} = \frac{\sigma'_f}{E}(2N_f)^b + \varepsilon'_f(2N_f)^c \qquad 3.5$$

where:

$\Delta\varepsilon/2$ is the total strain amplitude, $\sigma'f$ is the fatigue strength coefficient, $\varepsilon'f$ is the fatigue ductility coefficient, E is the Young's modulus of elasticity, $2Nf$ is the fatigue life, b is the fatigue strength exponent, and c is the fatigue ductile exponent.

Because of the welded and weld-repaired joints have lower fatigue life than un-welded joint [Alam, 2005], therefore Almar [1985] recommended that fatigue ductility coefficient should be divided by 2 ($\varepsilon' f/2$) to allow for difference between welded and un-welded structure.

Morrow [1968] and Smith *et al*. [1970] have studied the effect of mean stresses on fatigue behaviour of a component. Morrow has established a relationship between the mean stress σ_{mean} and fatigue life $2Nf$ as:

$$\varepsilon_a = \frac{\sigma_f^{'} - \sigma_{mean}}{E}\left(2N_f\right)^b + \varepsilon_f^{'}\left(2N_f\right)^c \qquad 3.6$$

Smith *et al*. [1970] have established another relationship, Smith-Watson-Topper (SWT) mean stress correction model, expressed as:

$$\sigma_{max}\,\varepsilon_a E = \left(\sigma_f^{'}\right)^2\left(2N_f\right)^{2b} + \sigma_f^{'}\varepsilon_f^{'}E\left(2N_f\right)^{b+c} \qquad 3.7$$

where: σ_{max} represents the maximum stress.

Ramberg-Osgood [1943] has characterized the cyclic stress-strain behaviour of a component as:

$$\varepsilon = \frac{\sigma}{E} + \left(\frac{\sigma}{K'}\right)^{\frac{1}{n'}} \qquad 3.8$$

where:

ε is the total strain, σ is the stress, K' is the cyclic strength coefficient, and n' is the cyclic strain hardening exponent as presented by Bishop and Sherratt [2000] .

Strain-life formulas were used by Morrow [1968] and Smith-Watson-Topper (SWT) [1970] for predicting the fatigue life of a forged steel crankshaft. It is observed that the Coffin-Manson strain-life formula is found to be conservative for estimating the fatigue life as compared to Morrow and SWT strain-life formulas; moreover, the optimized model (five design variable for the shape for the optimization of

model are: crankpin fillet radius R_f = 3.00 mm, crankpin oil hole diameter D_0 = 20.20 mm, crank web thickness W_t = 18.10mm depth of drilled hole L_h = 74.30 mm and diameter drilled hole D_h = 10.64mm at the back of crankshaft) of crankshaft possesses higher fatigue life.

Figure 3.11 shows S-N curves based on Coffin-Manson, Morrow and Smith-Watson-Topper (SWT) strain life formulas corresponding to the optimized values of design parameters.

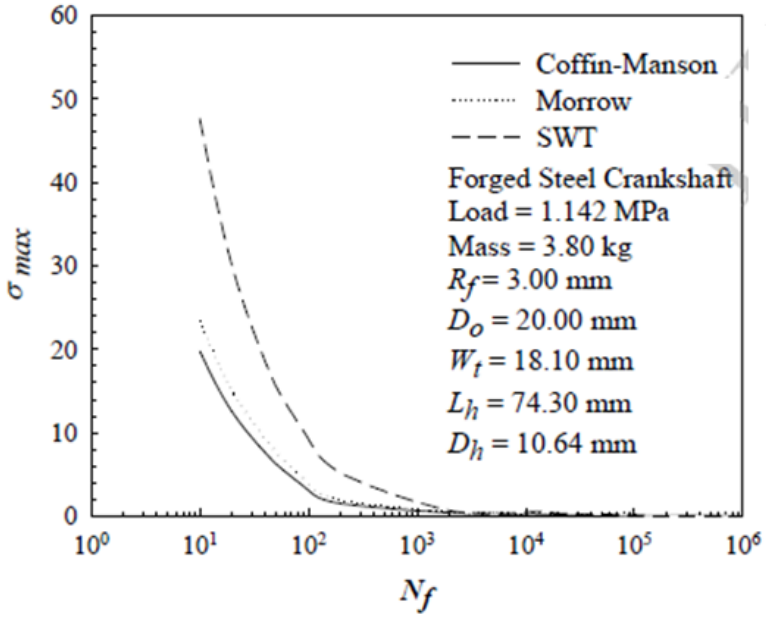

Figure 3.11: S-N curves for optimized crankshaft model based on three different strain life formulas [Anant and Srivastava, 2012]

Similar work was done by Agrawal and Srivastava [2012], where they carried out a mathematical modelling using finite element fatigue analysis (FEFA) of forged steel crankshaft. They implemented the three strain-life formulas (Coffin-Manson, Morrow and SWT) for the prediction of fatigue life under 20 load cycles.

Table 3.1 presents the maximum stresses at critical/failure location and fatigue life based on the three strain-life formulas for original and optimized forged steel crankshaft models. The critical location is elected as the point for fatigue failure.

As far as fatigue life is concerned, the optimized model possesses higher fatigue life (in seconds) irrespective of the strain-life formulas.

Moreover, for a given model, Coffin-Manson formula gives conservative results; consequently, estimates the lowest fatigue life, hence safe. Finally, it is concluded that the forged steel optimized shape crankshaft model, is the best when both elastic and plastic strains are considered, i.e., Coffin-Manson theory is used for estimating the fatigue life.

Table 3.1: Maximum stresses and fatigue life for original optimized crankshaft

Crankshaft	**Maximum stresses at critical location σ_{max} (MPa)***	**Fatigue life X10^6 (Sec)***		
		Coffin-Manson	**Morrow**	**SWT**
Original model	32.453	15.34	16.21	17.70
Optimized model	28.071	21.73	22.56	24.05
*** Mass = 3.80 Kg (approximately constant) Load = 1.142 MPa (fully reversible cyclic)**				

[Anant and Srivastava, 2012]

Tevatia *et al.* [2011] performed FEFA of plus section connecting rod for three different materials and predicted fatigue life based on Coffin-Manson, Morrow and Smith-Watson-Topper (SWT) strain life formulas. They concluded that Coffin-

Manson strain-life formula gives better design values for the fatigue life, because Coffin-Manson strain-life formula consider both the elastic and plastic strains.

Rahman *et al.* [2009] conducted FEFA of Aluminum suspension arm subjected to variable amplitude loading conditions. They have identified the critical location and predicted the fatigue life using strain-life theory. The stress-life theory was found to have a better correlation at high cycle fatigue; however, the strain-life theory must be used if plastic overloads are observed.

3.1.2.2.1 The effect of strain hardening exponents (n') using Coffin-Manson and Morrow & Smith et al. formulas

Tomkins has given relation between fatigue exponents (c and b) and strain hardening exponents as follows:

$c = -1/(1+2n`)$ and

$b = -n`/(1+2n`)$

In the above relations, both exponents are independently related to $n`$, therefore any change in $n`$ will affect the values of both c and b [Raman and Radhakrishnan, 2002].

Figures 3.12 & 3.13 show total strain amplitude variation as a function of number of life cycles representing Coffin-Manson and Morrow & Smith *et al.* relationship respectively.

The relationship plotted in (log-log scale graph) with red colour (considering strain hardening exponent n`) and blue (not considering strain hardening exponent n`).

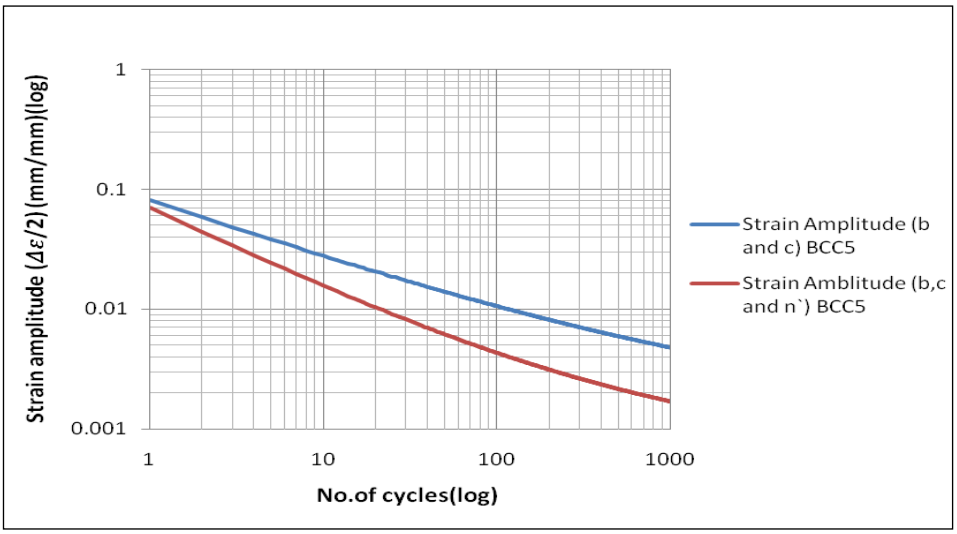

Figure 3.12: Strain amplitude applied for each cycle (log -log scale) shows the effect of strain hardening exponent using Coffin-Manson formula

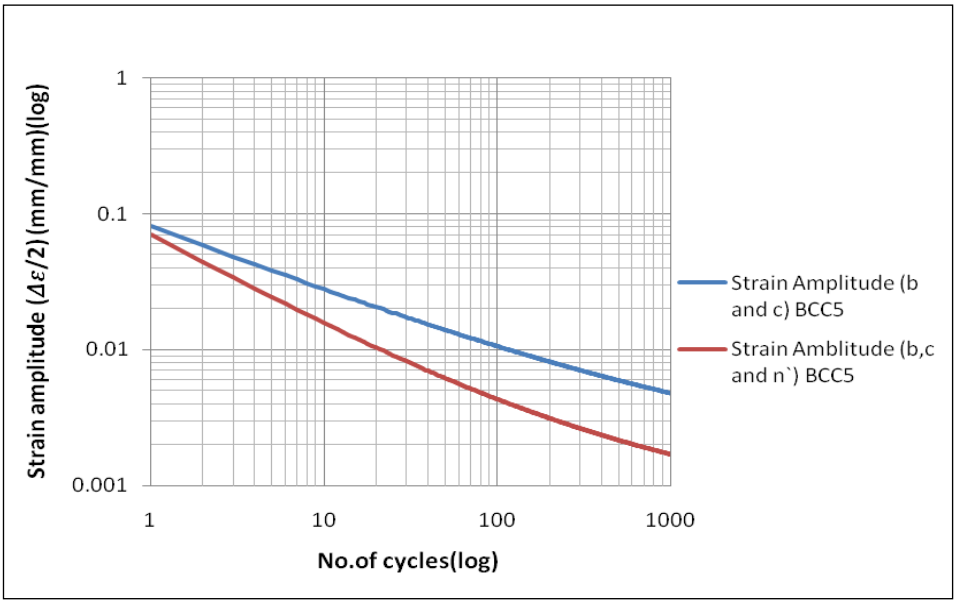

Figure 3.13: Strain amplitude applied for each cycle (log -log scale) shows the effect of strain hardening exponent using Morrow &Smith *et al.* formula

Figures 3.12 & 3.13 show that the slop of coffin- Manson and Morrow and Smith *et al.* relationship considering strain hardening exponent (n`) is greater than the slop of coffin-Manson and Morrow and Smith *et al.* relationship without considering strain hardening exponent (n`), and they showing that strain amplitude for red colour is less than the strain amplitude for blue colour which indicate that using (n`) in coffin-Manson and Morrow and Smith *et al.* made structure more stiff which lead to brittle failure and then less cycles life than without using (n`).

3.2 Evaluation of cracking

All structures and mechanical components that are cyclically loaded can fail by fatigue. Fatigue analysis, based on constant amplitude experimental data, is used to make a simple and quick estimate of the likely fatigue performance or durability.

In most structural failures, a crack growth process occur until the crack reaches a critical size for final fracture. Over the service life various crack growth mechanisms such as fatigue, creep, and hydrogen-induced cracking can occur. Each of these cracking mechanisms has certain characteristic features that are used in failure analysis to determine the cause of cracking or crack growth. The majority of structural failures are by brittle fracture and these almost invariably initiate at defects, notches, or discontinuities as reported by Hoeppner [1981].

Brittle fracture gives a final fast growth of a crack or cracks in the body. Metals which are usually ductile can behave in a brittle manner, leading to fast crack propagation after cyclic loading has been applied and small cracks have extended. It is possible in some cases to have limited plasticity near the crack tip, and such failures are referred to as quasi-brittle failures. In practice most materials are brittle and show very limited plasticity at the crack tip.

In low cycle fatigue the crack is formed when the applied stress exceeds the critical strength of the steel welded joint due to the repeated cyclic load. The strength in joint

decreases with cyclic load and progressively the joint becomes weak. Finally the atomic bonds lose their strength and break and the cracks form and extend, usually slowly. The total stiffness of the material decreases with the decreases of strength.

3.2.1 Crack initiation and heat affected zone (HAZ)

Understanding the mechanism of the crack initiation due to welding process needed to improve quality of welding area in steel frame structure. And it's a key to produce soundness steel structure. There are two types of the crack: internal cracks and external cracks this classification depend on the position of crack in the metal.
Welding process in the steel structure can be simply defined as follows: join the two parts of metal when metal in liquid state. The operator during welding process melts and moves the liquid metal using the torch or the welding machine to fill the groove between these two parts [Campbell, 2003].

A number of different mechanisms can cause defects in the weld:
The movement of the liquid metal will generate a gravity wave, if the velocity of the surface of the liquid metal exceeds a critical velocity, then the gravity wave will capture some air under a folding action, the air which is captured by the wave will sink into the bulk of the liquid metal and is a cause of porosity [Danielb, 1997].

Campbell [2003] is the first researcher which has commented on and emphasized the role of entrained oxide films as the main cause of defects in most welding. The new concept proposed by Campbell is a defect structure constituted by fragments of the entrained oxidized liquid surface. Since the liquid surface is commonly covered with an oxide film, it is entrained into the melt by a simple folding action. This doubled-over film can remain unbonded (essentially folded dry side) containing a film of air between surfaces which do not touch each other Figure 3.14. This defect has been called a "bifilm" and behaves like a crack in the liquid.

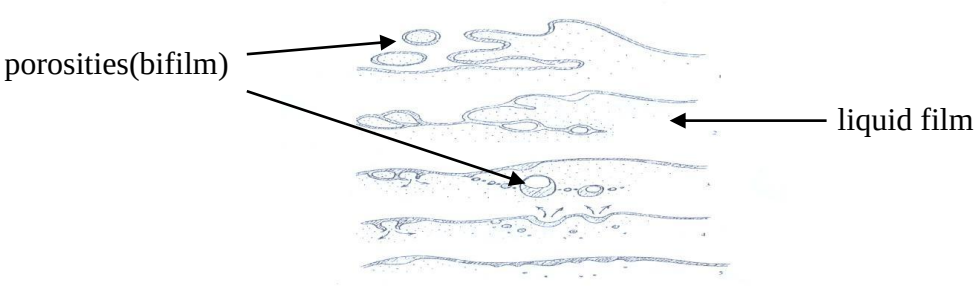

Figure 3.14: Entrainment of a liquid film, showing the subsequent detrainment of metal, gases and most of the entrained liquid (should be occur in any welding)
[Campbell, 2003]

Danielb [1997] has stated that external crack-like defects form during the later stage of solidification. A crack occurs when the partially solidified metal is placed in tension by the constrained cooling and contraction of the surrounding welding.
Hot tears are characterized by a heavily oxidized surface, as compared with the relatively clean surface of a crack made at room temperature.

Danielb [1997] has confirmed that the porosity is caused by precipitation of gases dissolved in the molten metal or by volumetric contraction occurring during solidification. Hydrogen can enter into a weld pool from a variety of sources. Moisture and organic compounds are the primary sources of hydrogen. It may be present on the steel, the electrode, in the shielding materials, and is present in atmosphere. To limit hydrogen content in deposit welds, welding consumables must be properly maintained, and welding must be performed on the surface that are clean and dry. The soluble gases such as hydrogen and oxygen get into the steel and will occur as a bubble or porosity. The gas bubbles may float to the surface and then explode, however some of them satellite inside the metal during solidification process and become a source of cracking a little later: heat affective zone (HAZ) cracking is characterized by separation that occurs immediately adjacent to the weld bed as illustrated in Figure 3.15. Although it is related to the welding process, the

crack occurs in the base material, not in the weld material. This type of cracking is also known as under bead cracking, toe cracking or delayed cracking. Because this cracking occurs after the steel cooled below approximately 400F (approx 200C), it can be called cold cracking, and it is also commonly called hydrogen assisted cracking or simply hydrogen cracking.

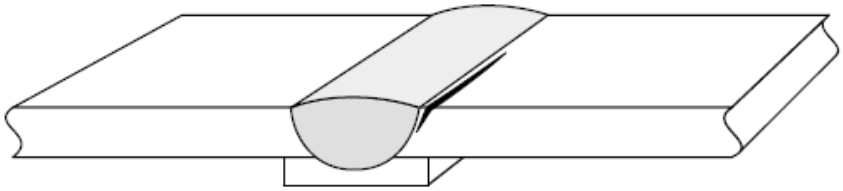

Figure 3.15: Cracking in heat affected zone [Omer *et al*., 1999]

There are three conditions must be present for heat affected zone (HAZ) cracking to occur: sufficient level of hydrogen, sufficient high level of residual stress and sufficient sensitive material.
The area of interest is the heat affected zone that results from the thermal cycle experienced by the region immediately surrounding the weld nugget.

During the welding process this area will be heated by the welding arc, it is transformed from its room temperature structure to elevated temperature structure of welding. The subsequent cooling rate will determine the resultant HAZ properties. Conditions that encourage the development of cracking sensitive microstructure include high cooling rate and higher harden ability level in the steel. For steel alloys, the most effective way to reduce the cooling rate is by raising the temperature of the surrounding steel through preheat. This reduces the temperature gradient, slowing cooling rate and limiting the formation of a sensitive microstructure. Effective preheat (with other measures such as low hydrogen electrodes) is the primary means by which acceptable heat affected zone properties are created, although heat input also has a significant effect on cooling rates in the zone [Omer *et al*., 1999].

The major weld imperfections include porosity, lack of penetration, lack of fusion, slag inclusion, undercut, misalignment etc. [Maddox, 1994]. The size and frequency of imperfection depends on the welding process, weld procedure, geometry of weldment including ease of access for welding, and the care exercised in making the weld. These imperfections have different characteristics and, in most cases, are difficult and costly to detect and define non destructively. The majority of fatigue cracks in welded structures originate at a weld toe or a weld termination rather than from internal imperfections [Alam, 2005].

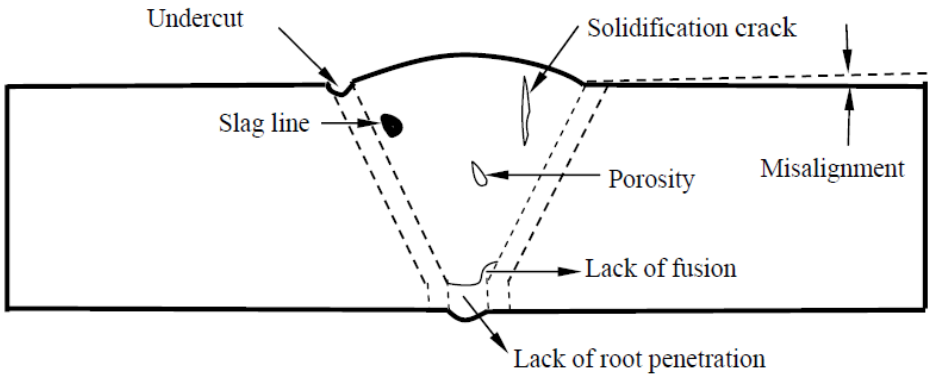

Figure 3.16: Different weld imperfections in a butt-joint [Alam, 2005]

This behaviour is attributed to the fact that for a given fatigue life, a much larger embedded imperfection can be tolerated than a surface imperfections [Barsom, 1994]. Different weld imperfections as described by Maddox [1994] are shown in Figure 3.16. The welded joints also contain residual stresses that arise due to incompatible thermal strains caused by heating and cooling cycles of welding process and affect the fatigue crack propagation life.

3.2.2 Numerical methods of model cracking

In the events of severe seismic demands, earthquake induced stresses may exceed the elastic strength capacity of the material. This may cause the structural elements to respond in-elastically and may result in progressive failure of the structure and

requires accurate and efficient methods to numerically model and simulate the structural behaviour and damage pattern. All this requirements result in the need to carry out a FE analysis to determine the ultimate capacity of the materials and structures.

Modelling has always remained a challenge in the field of computational mechanics. Cracks when modelled with the standard finite element method (FEM) requires the FEM mesh to match the geometry of the crack. Additionally in order to capture the true stress and strain field around the crack tip substantial mesh refinement is required [Ahmed, 2009].

Numerical methods have been classified into three main approaches:
The finite element (FE) method (which is been used in this work), the boundary element (BE) method and the finite difference (FD) method are the three major numerical methods in continuum mechanics and were explained in Figure 3.17 by Da Silva and Campilho [2012].

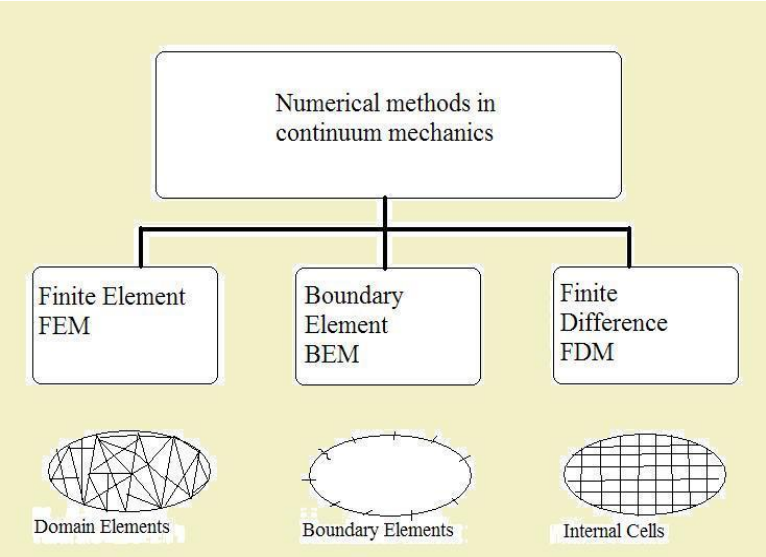

Figure 3.17: Numerical methods in continuum mechanics
[Da Silva and Campilho , 2012]

3.2.2.1 The finite element method (FEM)

Finite element method has become well established as the main tool for engineering analysis since 1980s, engineering analysis have extensively used FE software in analysing many engineering problems, from elastic analysis to nonlinear deformations. The real challenge in using FE software is knowing how to translate a real-life problem into a computational model and how to assess the accuracy of the FE solution is reported by Becker [2004].
The FE method is very suitable for practical engineering problems of complex geometries.

The entire solution domain is divided into small finite segments (finite element), over each element, the behaviour is described by the displacement of the elements and the material properties. To obtain good accuracy in regions a large number of small elements must be used (refine meshing), therefore all elements are assembled together and the requirements of continuity and equilibrium are satisfied between neighbouring elements is explained by Becker [2004] .

There are number of instance where the usual FEM method poses restrictions in efficient application of the method, such problems involving interior boundaries, discontinuities or singularities, because of the need of re-meshing and high mesh densities. The term FE was introduced by Clough [1960].

In this work, beam-column steel joint have been modelled using ANSYS finite element method re-meshing the joints which is explained in chapter 4.

Swenson and Ingraffea [1988] have reported that a re-meshing technique is traditionally used for modelling cracks within the frame work of finite element method. Where a re-meshing is done near the crack to line up the element edges with the crack faces. This becomes quite burdensome in case of static or quasi-static

evolving cracks or dynamic crack propagation problems, where each time a new mesh is generated as the crack grows. This results in construction of totally new shape functions and all the calculations have to be repeated. Furthermore, the dynamic solution represents an evolving history because of inertia, and whenever the mesh is changed. This is accomplished by transferring the data from the old mesh to the new mesh. The process of mapping variables from the old mesh to the new mesh may also result in loss of accuracy.

The stress distribution can be obtained by a FE analysis or a closed-shape model. For complex geometries and complex material models, the FE method is preferable. One of the simplest failure models is that based on a stress or strain limit state, i.e. based on a continuum mechanics approach.
Fracture mechanics principles can also be used within a FE analysis.

Melenk and Babuska [1996] have reported that the extended finite element method (X-FEM) is a numerical method for modelling strong (displacement) as well as weak (strain) discontinuities within a standard finite element framework. In the X-FEM, special functions are added to the finite element approximation using the frame work of partition of unity. For crack modelling in isotropic linear elasticity a discontinuous function and the two-dimensional asymptotic crack-tip displacement fields are used to account for the crack. This enables the domain to be modelled by finite elements without explicitly meshing the crack surfaces, and hence quasi-static crack propagation simulations can be carried out without re-meshing.

Belytschko and Black [1999] were modelled the crack with a near-tip enrichment functions throughout its length and required a sequence of mapping that rotates each segment of the crack onto the crack model, to align the discontinuity in the enriching functions with the crack.

3.2.2.2 Failure criteria of FEM

In the field mechanics approach, the maximum values of stress, strain or strain energy, predicted by the FE analyses, are usually used in the failure criterion and are compared with the experimental data recorded by Adams *et al.*[1997].

Adams *et al.* [1997] have extensively used this criterion to predict joint strength with success. However, because of the singularity of stresses at re-entrant corners of joints, the stresses depend on the mesh size used and how close to the singular points the stresses are taken. Values of stresses calculated at Gauss points near the singularity or extrapolation of Gauss point values to the singularity were, in fact, used.
Adams and Harris [1984] have used the maximum principal strain as failure criterion for predicting the joint strength. This criterion can also predict the failure mode. However, it is equally sensitive to the mesh size.

Hart-Smith [1973] proposed that the maximum shear strain might be used as a failure criterion when plastic deformation was apparent.
Adams and Harris [1987] have stated that the strain energy is the area under the stress-strain curve. Therefore, both stress and strain criteria can be related to strain energy. However, it should be noted that criteria based on strain energy take account of all the stress and strain components. As a result, they are more suitable as a failure criterion than either stresses or strains alone. Plastic energy density has also been used as a failure criterion.

3.3 Fracture mechanics

3.3.1 Stress intensity factor and fracture toughness

Based on the linear theory the stresses at the crack tip are infinite but in reality there is always a plastic zone at the crack tip that limits the stresses to finite values. It is

very difficult to model and calculate the actual stresses in the plastic zone and compare them to a maximum allowable stresses of the material to determine whether a crack is going to be stable or not.

An engineering approach is to perform a series of experiments to determine a critical stress intensity factor *Kc* for each material, called the fracture toughness of the material. One can then determine the crack stability by comparing *K* and *Kc* directly [Shih and German, 1981].

3.3.1.1 Relationship between G and K

Some literature may uses strain energy release rate *G* instead of stress intensity factor *K*. These two factors are however directly related by the following formulas:

$G = K^2/E$ (Plane stress)

$G = K^2/E\ (1-\upsilon^2)$ (Plane strain)

$K_I = \sigma \sqrt{\pi}\ a$

where:

G is a linear version of J, which was described above. Figure 3.18 shows a through crack in an infinite plate under uniform tension (Mode I).

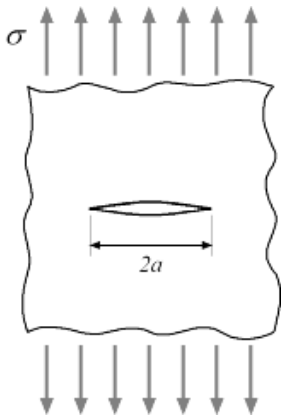

Figure 3.18: A through crack in an infinite plate under uniform tension (Mode I) [eFunda, 2014]

3.3.2 Linear and non-linear fracture mechanics

The fracture mechanics field of interest is the analysis of the mechanisms of the crack propagation in materials. Usually, two categories are identified: the linear-elastic fracture mechanics (LEFM) and the elastic-plastic fracture mechanics (EPFM). The LEFM theory, which is governed by brittle fracture, is reasonably well established, and the stress intensity factor (SIF or *K*) approach is the most widely employed. Thus, some situations require the use of the EPFM using approaches such as J or the crack-tip opening displacement (CTOD).

Modern pipeline design is normally based on the principles of Limit State Design. This implies that each failure mode shall be considered and designed for independently. Many design codes, e.g. DNV-OS-F101[2012], Submarine Pipeline Systems, 2000, give general requirements for such Limit State Design and for many of the failure modes specific requirements are given.

For pipelines installed by the reeling method, and also other methods introducing large plastic cyclic strains, fracture of the girth welds during installation is one of the potential failure modes and it needs to be demonstrated that the pipeline system has adequate resistance against both crack extension by tearing and unstable fracture during installation as well as during operation.

‘‘Pipeline like structures in earthquake subject to large amplitude cyclic load and seems sensible to review pipeline guideline relevant to earthquakes’’.

The Recommended Practice [DNV-OS-F101, 2012] assumes overmatching weld strength, it is recommended to assume the same strength properties as for the parent pipe (even matching) when assessing flaws in the weld metal. The reason for this is that the strength of the weld metal varies from the HAZ and into the un-affected weld metal and it is not always obvious how to determine the exact location of a weld

flaw. Furthermore, the amount of over-matching varies due to variability in both parent pipe and weld metal strength.

Assessments are commonly made of the initiation of fracture. However it is possible that the combination of the crack and the maximum applied loads will result in some stable crack growth that is coupled with increasing material toughness. This may prevent overall failure but also the stable crack growth coupled with the fatigue loading will result in cracks growing faster than predicted by Paris' Law (see section 3.3.4) and the two effects need to be added together. Methods of predicting the stable crack growth behaviour require J-R curves that are not usually available at the design stage, although previous experience might be used. Stable crack growth is not considered further in this work.

3.3.2.1 Failure assessment diagram (FAD)

The FAD method is described in BS 7910 [2005], the engineering best practice code API 579l ASME FFS-1(API 2007), and in the fracture mechanics text book by Anderson [Anderson, 2005].

The FAD can be thought of as providing an interaction between a failure caused by fracture and a failure caused by general yielding.
The fracture toughness of the material (Kc) that is used in conjunction with the method is based on tests where the average stress levels are well below yield so that they are not reducing the fracture toughness through the interaction with yielding. When the fracture toughness is high, this requires large test specimens, with large cracks, to obtain a failure at low general level of applied stress. (Note this does not imply that there is no yielding at the crack tip.)

When using the FAD, the applied stress intensity factor (Ka) also does not take into account the detrimental effects of a generally high applied stress. (If a non-linear

fracture mechanics calculation was performed to determine the applied J or CTOD value then the interaction would be included as shown diagrammatically in Figure 3.19.

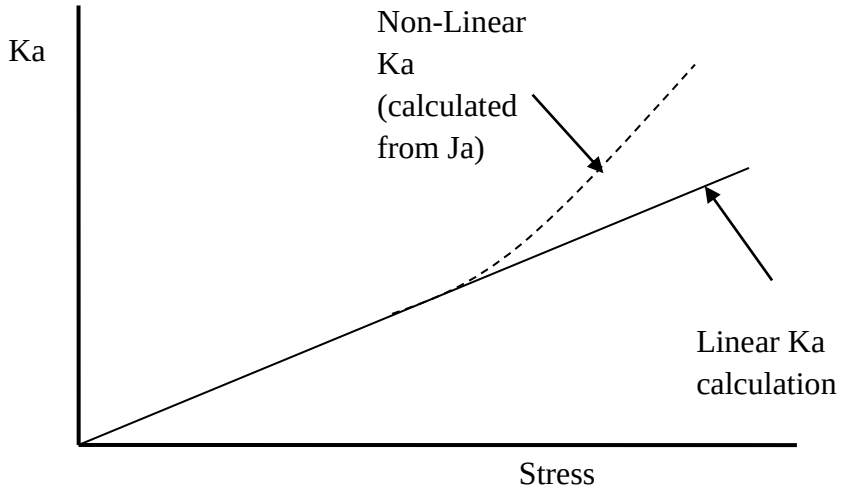

Figure 3.19: Comparison of the applied K (Ka), estimated by linear analysis and determined from the Ja value calculated in a non-linear analysis [Barltrop, 2009-2014, per. comm.]

The brittle fracture ratio Kr = Ka/Kc is computed from the crack front stress intensity, obtained by an elastic finite element analysis [Tipple C. and Thorwald G., 2012].

The effect of the interaction between fracture and general yielding (or the effect of the difference between the elastic Ka and the Ka derived from Ja) is taken into account by the shape of the FAD itself. This considerably simplifies both the required testing (as results are not required for different levels of general applied stress) and the analysis as the linear Ka value is much easier to calculate or estimate than the non-linear Ja value.

The effect of the general stresses is taken into account by the plastic collapse ratio: Lr (reference stress / yield stress), which is computed using results from an elastic-plastic finite element analysis.

The plastic collapse ratio is not influenced by "secondary" self equilibrating stresses e.g. from welding or from differential temperature effects. However these can still have an effect on the occurrence of fracture and this is taken into account by correcting Kr (e.g. as discussed in BS 7910 [2013] using V or ρ).

Figure 3.20 shows an example of the API 579 default failure assessment curve (FAC) and crack evaluation points. The axes of the FAD chart use the non-dimensional ratios *Lr* (plastic collapse ratio) on the X-axis, and *Kr* (brittle fracture ratio) on the Y-axis. The example evaluation points inside the FAD curve indicate acceptable cracks (providing suitable safety factors been applied), and the evaluation points above the FAD curve are unacceptable cracks that indicate a predicted structural failure, which can be useful to determine predicted critical crack sizes. When an analysis for a specific structural component and a stress-strain curve is available, a material specific FAD can be computed [Tipple and Thorwald, 2012].

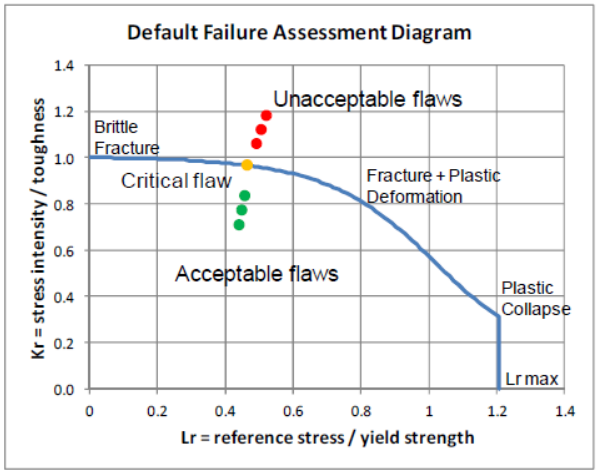

Figure 3.20: Example of default FAD and crack evaluation points

[Tipple and Thorwald , 2012]

The FAD methodology is used in the British standard [BS7910, 2005 and BS7910, 2013]. The British Standard proposes three levels of fracture assessment:
option1: is a conservative procedure that is relatively simple to employ and does not require detailed stress/strain data for the materials being analyzed.
option 2: is based on the use of a material-specific stress-strain curve.
option 3: uses numerical analysis to generate a FAD and is not confined to use with materials showing ductile tearing [Yann *et al*., 2013].

BS 7910 (2005) also had several levels of fracture assessment. Level 2a in the 2005 document is broadly similar to option1 in the 2012 document but it is less pessimistic when general stresses exceed yield. This work, has been based on the Level 2a curve in the 2005 document.

Equation 3.10, provides the FAD for BS7910, 2005, option 2a.

The curves contain a plastic collapse cut-off Lr_{max}. This is to avoid plastic collapse of the structure. However in displacement controlled experiments plastic collapse is probably prevented by the test rig so the Lr_{max} may not be appropriate. It should however be applied when assessing structures which are not loaded under displacement control.

3.3.2.2 The failure assessment diagram (FAD) (DNV-RP-F108, 2006)

The following is a summary of the DET NORSKE VERITAS (DNV) method, which has been applied later in this research in conjunction with document DNV-RP-F108[2006]. The DNV document is relevant to this thesis because it also considers failure at a very small number of cycles of applied strain.

DNV suggests using the FAD in conjunction with the cumulative stable crack growth from a J-R curve to handle the very low cycle fatigue associated with reeling pipe

onto barges, offshore unreeling and laying to the seabed may be appropriate. “FEM analyses have shown that the range of the Crack Driving Force, Δ J or ΔCTOD, both for the first strain cycle and subsequent strain cycles, is essentially determined by the positive strain increment for the respective loading steps”.

When the exact defect location is known, it may be justified to derive the FAD from weld metal tensile properties. The weld metal properties should then be determined in the cross weld direction, either by notched tensile specimens, or specimens instrumented with strain gauges or a small extensometer in the weld metal. Since the “applied load” on the weld is determined from the bending moment set up by the parent pipe, the weld metal stress-strain curve shall be representative for the lower end of the weld metal strengths, e.g. mean minus two standard deviations or “lowest expected value” of the strength for the weld metal to be employed. The Bauschinger effect (a reduction in yield stress) due to cyclic plastic straining should then also be considered. Expert advice is recommended for such cases.

It is normally conservative to base the assessment (both the FAD and the applied stress) on the as-received parent pipe stress-strain curve. This is because a high yield strength and a low strain hardening will result in a high crack driving force when the “applied load” is determined from a given applied strain.

For assessing flaws at the fusion line or within the HAZ, the FAD shall be derived from the parent pipe tensile tests. Since the “applied load” is determined from the applied strain the stress-strain curve used to derive the FAD shall be representative for the higher end of the pipe strengths, i.e. representing a pipe with high yield strength and low strain hardening. e.g. mean plus two standard deviations or “highest expected value” of the strength for the material to be employed.

The FAD cannot be extended to arbitrarily large plastic deformations and a cut-off limit for Lr ($Lr = \sigma_{ref} / \sigma_Y$) must be defined.
For displacement controlled or displacement restricted situations, such as reeling, it is acceptable to increase the cut-off level in the FAD, Lr_{max}, from $Lr_{max} = \sigma_{flow} / \sigma_Y$ as suggested in BS 7910 [2013] provided there is experimental support for such an extension.

Such support can be provided by testing specimens with a constraint similar to the constraint in the pipe, e.g. the SENT (Single Edge Nothched Tensile) specimen or the segment specimen with crack depth similar to the flaw size considered in the pipe. If results from testing are available the following procedure for establishing FAD is acceptable:

- The maximum load shall be determined from at least three tests. The location of the cracks in the specimens must correspond to the location considered in the pipe
- $Lr_{max} = \sigma_{ref} / \sigma_Y$, corresponding to the recorded maximum loads shall be calculated and used to define Lr_{max}
- The actual value of Lr_{max} to be used in the analyses shall be chosen taking scatter in the results into consideration.

3.3.2.3 BS 7910 [2005] Option 2a

Definition of Lr and Kr for option 2a curve are defined by R6 and BS 7910 [2005] standards approach, they consist of evaluating parameters Kr and Lr, dependent on the applied loads, material properties, and geometry including crack size and shape.
The parameters Lr and Kr are defined as follows [Buddena *et al*., 2002]:

$$Kr = K /Kc + \rho \qquad 3.9$$

where:

K is the stress intensity factor

Kc is the fracture toughness

ρ is a plasticity correction (zero for very high levels of primary stress)

$Lr = \sigma_m / \sigma_Y$

where: σ_m is the maximum stress

σ_y is the yield stress

The assessment point (Lr,Kr) is plotted on the failure assessment diagram (FAD), and compared with a bounding curve defined by Kr in Equation 3.9. [Davies *et al*., 2003].

The option 2a failure assessment curve [BS7910, 2005] is defined by Equation 3.10.

$$Kr = (1-0.14Lr^2).[(0.3 + 0.7 \exp(-0.65\, Lr^6)] \qquad 3.10$$

where:

Lr is defined above.

Lr_{max} = is a cut-off, maximum permitted value of Lr to avoid plastic collapse.

Figure 3.21 shows flowchart for option 2a fracture assessment constructed by BS7910 [2013].

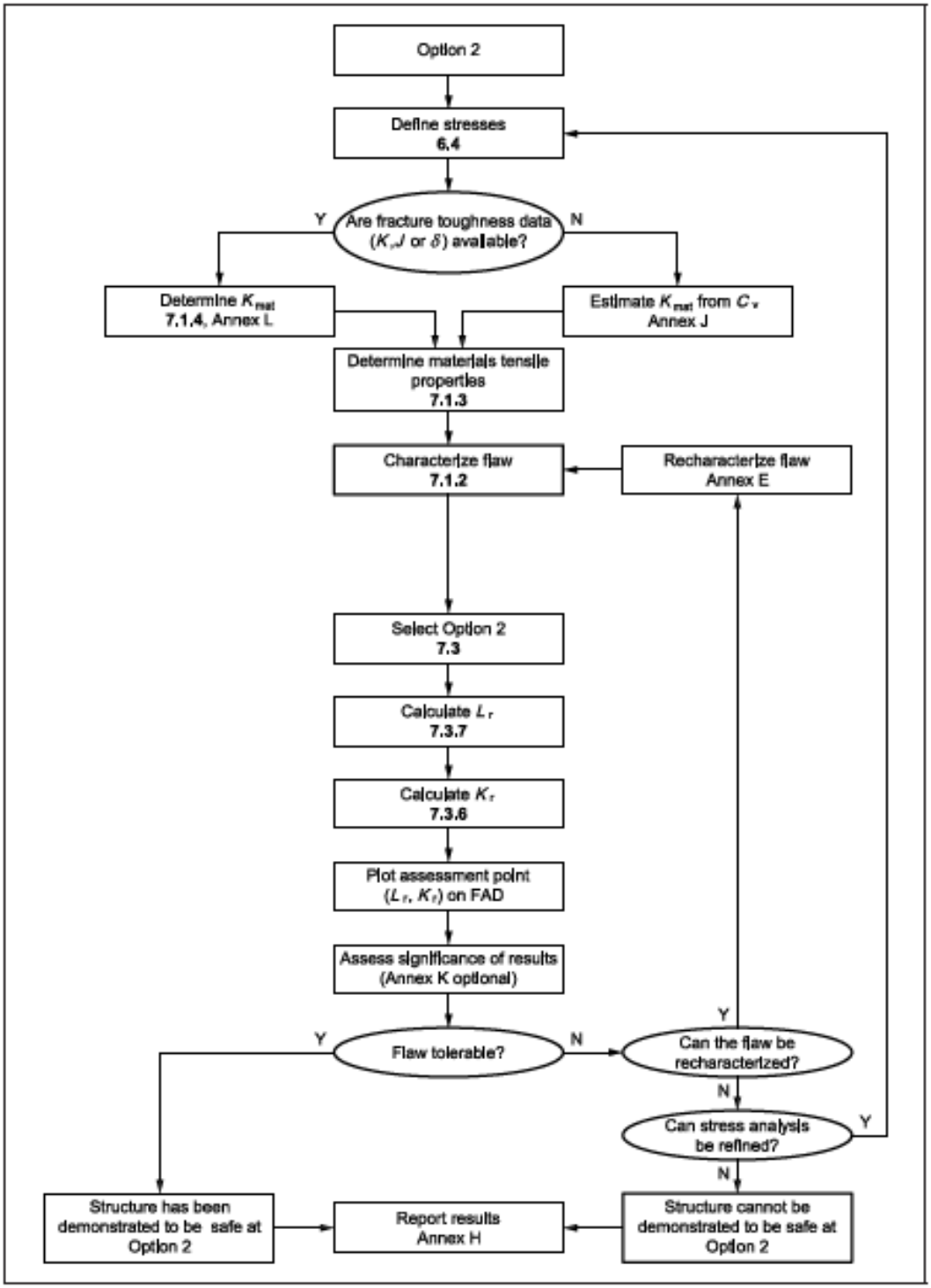

Figure 3.21: Flowchart for option 2a fracture assessment [BS7910, 2005]

3.3.2.4 Crack tip opening displacement (CTOD)

Crack tip opening displacement test or CTOD is one of a family of fracture mechanics tests that measures the resistance of a material to growing a crack.

Historically, the first parameter for the determination of fracture toughness in the elasto-plastic regime was the crack tip opening displacement (CTOD) or "opening at the apex of the crack". This parameter was determined by Wells [1961] during the studies of structural steels which, due to the high toughness could not be characterized with the linear elastic fracture mechanics. He noted that, before fracture, the walls of the crack were separating and that the crack tip, after fracture, rounded off due to plastic deformation. In addition, the rounding of the apex was more pronounced in steels with superior toughness.
There are two common definitions of the crack tip opening displacement (CTOD):

1. The opening displacement of the original crack tip as shown in Figure 3.22.

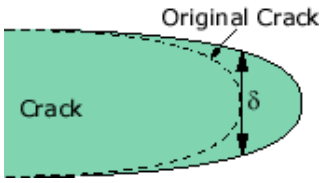

Figure 3.22: Opening displacement of the original crack tip [eFunda, 2014]

2. The displacement at the intersection of a 90° vertex with the crack flanks as shown in Figure 3.23.

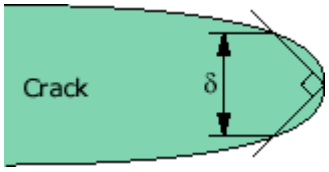

Figure 3.23: Displacement at the intersection of a 90° vertex with the crack flank [eFunda, 2014]

These two definitions are equivalent if the crack blunts in a semicircle.

The crack tip opening displacement (CTOD) of a crack at the edge of a three-point bending specimen is shown in Figure 3.24.

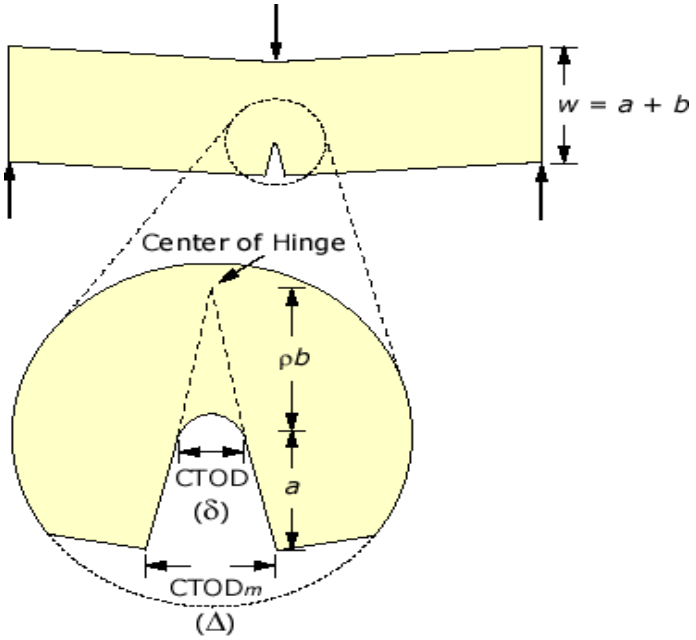

Figure 3.24: Crack tip opening displacement (CTOD) at the edge of a three-point bending specimen [eFunda, 2014]

Where: $CTOD_m$ is the measured crack tip opening displacement, usually near the edge of the specimen for ease of access, CTOD is the real crack tip opening displacement, *a* is the length of the crack, and *b* is the width of the rest of the specimen.

From simple geometry of two similar triangles [eFunda, 2014] CTOD may be determined from $CTOD_m$.

Considering a linear elastic body containing a crack, the J-integral and the crack tip opening displacement (CTOD) have the following relationship:

$$J = \frac{K^2}{E} = m\sigma_{ys}\delta \qquad 3.11$$

where σ_{ys} is the small scale yielding stress and *m*. is a dimensionless constant that depends on the material properties and the stress states. For plane stress and non

hardening materials, m = 1. Hence, for a through crack in an infinite plate subjected to a remote tensile stress σ (Mode I), the crack tip opening displacement δ is

$$\delta = \frac{K_I^2}{E\sigma_y} = \frac{\pi a \sigma^2}{E\sigma_y} = \frac{G}{\sigma_y} = \frac{J}{\sigma_y} \qquad 3.12$$

Shih and German [1981] took a step further and showed that a unique relationship exists between J and CTOD beyond the validity limits of LEFM. He introduced the 90° intercept definition of CTOD, as illustrated in Figures 3.22 and 3.25.

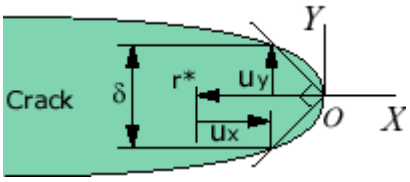

Figure 3.25: The 90° intercept definition of CTOD [eFunda, 2014]

3.3.2.5 Crack loading modes

The theory of stress field at the crack tip indicates that there are three types of loading that a crack can experience as shown in Figure 3.26. Mode I loading, where the principal load is applied normal to the crack plane, tend to open the crack.
Mode II corresponds to in-plane shear loading and tends to slide one crack face with respect to the other. Mode III refers to out-of-plane shear. A cracked body can be loaded in any one of these modes, or a combination of two or three [Alam, 2005].

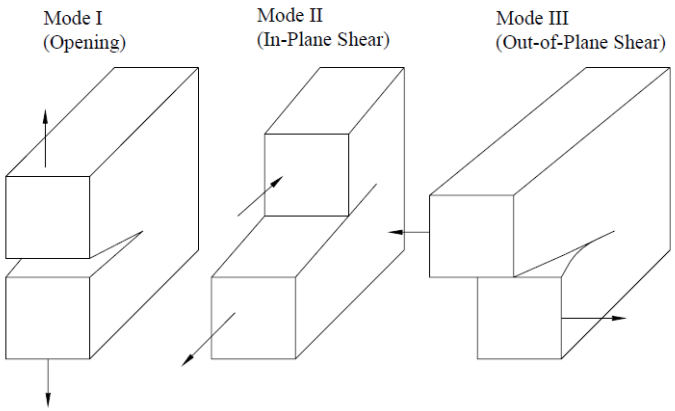

Figure 3.26: Three modes of loading that can be applied to a crack [BS7608, 2014]

A material's fracture resistance is usually described by a single parameter, either K (Stress Intensity Factor), CTOD (crack tip opening displacement) or the J-integral. It is however known that the stress and strain state at a crack tip is not fully characterised by such a single parameter alone but that the crack tip constraint, i.e. the degree of crack tip stress tri-axiality, will also influence the fracture resistance.

3.3.2.6 Relationship between different toughness parameters

To determine a material CTOD from K or J, Det Norske Veritas DNV-RP-F108 [2006] recommended to use the highest expected value" of the strength for the material to be employed.

To calculate the applied CTOD BS 7910 [2013] recommended to use total strain range.

$K_f = \sigma_T \sqrt{\pi}\, a_\circ$

$G = K_f^2/E$ (Plane stress)

$CTOD = G/\sigma y$

where:

Kf is the stress intensity factor = $\sigma T \sqrt{\pi}\, a_\circ$

$a_\circ$ is crack depth take it 0.2mm

$K_f = \sigma_T \sqrt{\pi a_\circ}$

$G = K_f^2/E$ (Plane stress)

$CTOD = G/\sigma y$

3.3.3 Fatigue damage index (FDI)

Variable amplitude loading, which occurs during earthquakes, produces strain cycles of variable amplitude. A cycle counting method, such as the rain-flow method may be used to count the number of cycles in each strain range.

The number of cycles to failure may, then be determined using the Coffin-Manson relation that gives the numbers of cycles to failure under constant strain range [Kyungkoo and Bozidar, 2004]. The Palmgren-Miner rule is used to predict the damage per cycle as reported in Miner [1945]. Adopting Miner's rule that accumulates damage induced by cycles of constant strain range linearly, a damage index *D*, can be expressed as follows:

$$FDI = \sum_{i}^{n} ni/Ni \qquad 3.13$$

Where *FDI* is the fatigue damage index, or total damage to the element due to the cyclic load, ni is the number of different cycle amplitudes in the loading history, *Ni* is the number of cycles at amplitude i and n is the total number of cycles. Values of *FDI* greater than or equal to 1.0 indicate a low-cycle fatigue fracture of the member as reported by Campbell *et al.* [2008]. In the following description there are two methods to calculate cyclic strain amplitude:

1. *Rainflow cycle counting method* has initially been proposed by Matsuiski and Endo [1968] to count the cycles or the half cycles of strain-time signals. Rainflow counting algorithm-adapted by Wikipedia [2014] as shown in Figure 3.27.

- Reduce the time history to a sequence of (tensile) peaks and (compressive) valleys.
- Imagine that the time history is a template for a rigid sheet.
- Turn the sheet clockwise 90° (earliest time to the top).
- Each ***tensile peak*** is imagined as a source of water that "drips" down the pagoda.
- Count the number of half-cycles by looking for terminations in the flow occurring when either:
    - ❖ It reaches the end of the time history;
    - ❖ It merges with a flow that started at an earlier ***tensile peak***; or
    - ❖ It flows when an opposite ***tensile peak*** has greater magnitude.
- Repeat step 5 for ***compressive valleys***.
- Assign a magnitude to each half-cycle equal to the stress difference between its start and termination.
- Pair up half-cycles of identical magnitude (but opposite sense) to count the number of complete cycles. Typically, there are some residual half-cycles.

Example

i. The stress history in Figure 3.27 (A) is reduced to peaks and valleys in 1 Figure 3.27 (B).
ii. Half-cycle (A) starts at tensile peak (1) and terminates opposite a greater tensile stress, peak (2). Its magnitude is 16 MPa.
iii. Half-cycle (B) starts at tensile peak (4) and terminates where it is interrupted by a flow from an earlier peak, (3), Its magnitude is 17 MPa.
iv. Half-cycle (C) starts at tensile peak (5) and terminates at the end of the time history.
v. Similar half-cycles are calculated for compressive stresses in Figure 3.27 (C) and the half-cycles are then matched.

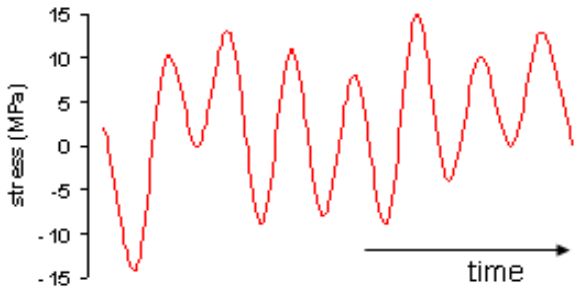

(A): Spectrum loading

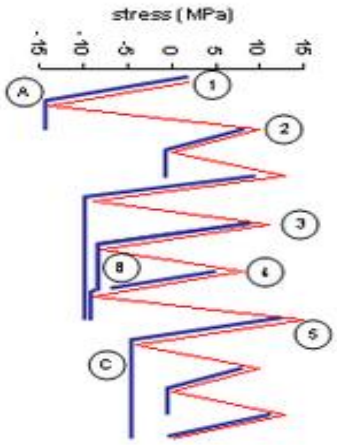

(B): Rainflow tensile peaks

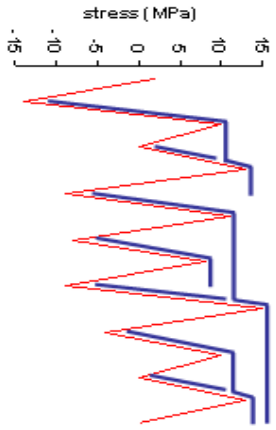

(C): Rainflow compressive valleys

Stress (MPa)	Whole cycles	Half cycles
10	2	0
13	0	1
16	0	2
17	0	2
19	1	0
20	0	1
22	0	1
24	0	1
27	0	1

(D) calculation Table

Figure 3.27: Rainflow calculating procedure [Wikipedia, 2014]

[Matsuiski and Endo, 1968]

2. *Cycle counting by the reservoir method*

The purpose of cycle counting is to reduce an irregular series of stress fluctuations to a simple list of stress ranges. The method is shown in Figure 3.28, it is easy to apply by hand and suitable when dealing with short stress histories, such as those produced by individual loading events, therefore this method is considered in this investigation. It consists of imagining a plot of the graph of each individual stress history as a cross section of a reservoir, which is successively drained from each low point, counting one cycle for each draining operation. The result, after many repetitions of the loading event, will be the same as that obtainable by the rain flow method [BS 7608,1993]. The following procedure explain this method:

- Derive the peak and trough values of the stress history, due to one loading event. Sketch the history due to two successive occurrences of this loading event. The calculated values of peak and trough stresses may be joined with straight lines if desired. Mark the highest peak of stress in each occurrence. If there are two or more equal highest peaks in one history, mark only the first such peak in each occurrence.
- Join the two marked points and consider only that part of the plot which falls below this line, like the section of a full reservoir.
- Drain the reservoir from the lowest point leaving the water that cannot escape. If there are two or more equal lowest points the drainage may be from any one of them. List one cycle having a stress range Sr1 equal to the vertical height of water drained.
- Repeat previous point **(**drain the reservoir from the lowest point) successively with each remaining body of water until the whole reservoir is emptied, listing one cycle at each draining operation.
- Compile the final list which contains all the individual stress ranges in descending order of magnitude Sr1, Sr2, etc. Where two or more cycles of equal stress range are recorded, list them separately [BS7608, 2014].

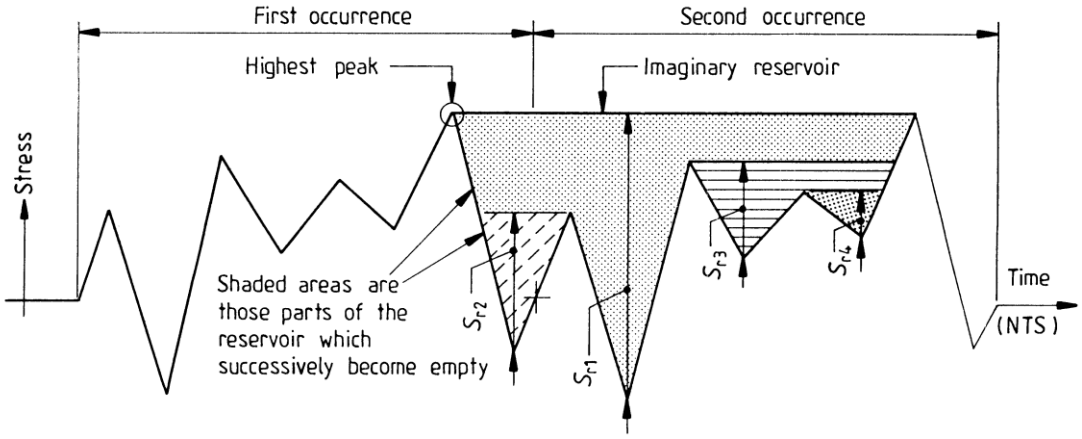

Figure 3.28: Example of cycle counting by reservoir method [BS7608, 2014]

3.3.4 Crack growth rates

Fracture mechanics often plays a role in life prediction of components that are subject to time-dependent crack growth mechanisms such as fatigue or stress corrosion cracking. The rate of cracking can be correlated with fracture mechanics parameters such as the stress-intensity factor, and the critical crack size for failure can be computed if the fracture toughness is known, the fatigue crack growth rate in metals can usually be described by the following Paris relationship:

$da/dN = A(\Delta K)^m$

where da/dN is the fatigue crack growth rate per cycle, $\Delta K = K_{max} - K_{min}$ is the stress intensity factor range during the cycle, and A and m are parameters that depend the material, environment, frequency, temperature and stress ratio. [Anderson , 2005].

BS 7910[2013] recommended A and m values tables such as Table 10.

Figure 3.29 shows a schematic log-log plot of *da/dN* versus ΔK, which illustrates typical fatigue crack growth behaviour in metals. The sigmoidal curve contains three distinct regions. At intermediate Δ*K* values, the curve is linear, but the crack growth rate deviates from the linear trend at high and low Δ*K* levels. At the low end, *da/dN* approaches zero at a threshold Δ*K*, below which the crack will not grow. In some

materials, the observed growth rate increases rapidly at high ΔK values. There are two possible explanations for the Region III behaviour. Some researchers have hypothesized that the crack growth rate accelerates as K_{max} approaches K_c, the fracture toughness of the material. According to this hypothesis, microscopic fracture events contribute to crack growth, resulting in a higher overall growth rate [Anderson, 2005].

An alternative hypothesis is that the apparent acceleration in *da/dN* is not real but is due to the influence of crack-tip plasticity on the true driving force for fatigue. At high K_{max} values, linear elastic fracture mechanics is no longer valid, and a parameter like ΔJ (ΔK) might be more appropriate to characterize fatigue. [Anderson, 2005].

There may also be an addition of stable crack growth and fatigue crack growth as described in Section 3.3.2 (above).

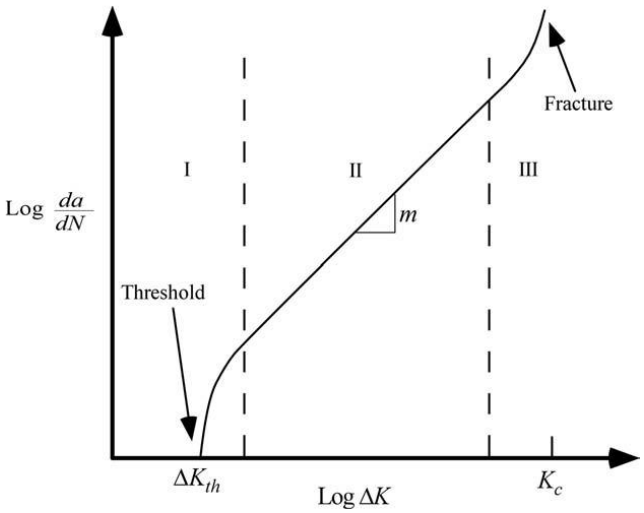

Figure 3.29: Typical fatigue crack growth behavior in metals [Anderson, 2005]

Region I: is the near threshold region and indicates a threshold value ΔKth below which there is no fatigue crack growth or the growth is too small to measure. Microstructure, mean stress, and environment mainly control region I crack growth.

Region II: shows essentially a linear relationship between log *da/dN* and log ΔK, first suggested by Paris

– *m* is the slope of the curve

– A is the coefficient found by extending the straight line to ΔK = 1 MPa√m.

– Region II (Paris region) corresponds to stable macroscopic crack growth. Microstructure and mean stress have less influence on fatigue crack growth behaviour in region II than in region I.

In region III

–the fatigue crack growth rates are very high as they approach instability

–little fatigue crack growth life is involved.

–this region is controlled primarily by fracture toughness *Kc* or *KIc* [Ralph *et. al.*, 2001].

3.3.4.1 Similitude in fatigue

The concept of similitude, when it applies, provides the theoretical basis for fracture mechanics. Similitude implies that the crack-tip conditions are uniquely defined by a single loading parameter such as the stress-intensity factor. In the case of a stationary crack, two configurations will fail at the same critical *K* value, provided an elastic singularity zone exists at the crack tip. Under certain conditions, fatigue crack growth can also be characterized by the stress-intensity factor, as discussed next.

Consider a growing crack in the presence of a constant amplitude cyclic stress intensity as shown in Figure 3.30.

A cyclic plastic zone forms at the crack tip, and the growing crack leaves behind a plastic wake. If the plastic zone is sufficiently small that it is embedded within an elastic singularity zone, the conditions at the crack tip are uniquely defined by the current *K* value, and the crack growth rate is characterized by K_{min} and K_{max} as shown in Figure 3.30 [Anderson , 2005].

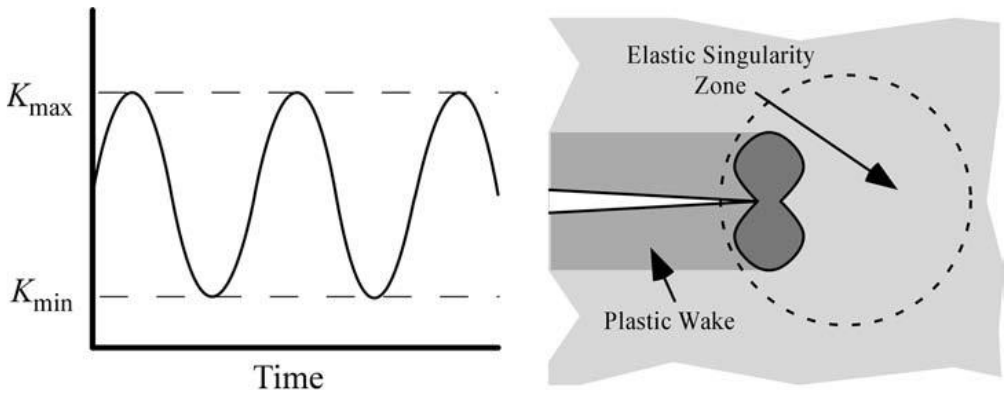

Figure 3.30: Constant amplitude fatigue crack growth under small-scale yielding conditions[Anderson , 2005]

3.4 Ratcheting

Ratcheting is one of the strain controlled low cycle fatigue responses, is defined as the accumulation of plastic strain with cycles. In other words ratcheting, a strain accumulation under stress controlled cycling with non-zero mean stress, is a predominant phenomenon in cyclic plasticity. This phenomenon is characterized by a translation of the hysteresis loop under non-symmetrical stress loading which is shown in Figure 3.31 [Verma, 2011].

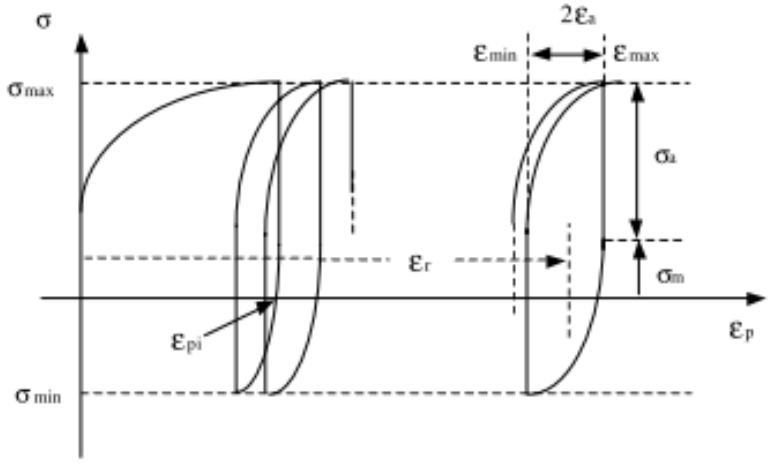

Figure 3.31: Schematic of ratcheting phenomena [Verma, 2011]

There are the two types of ratcheting: material ratcheting and structural ratcheting.

In both cases the signature (or definition) of ratcheting is the persistent movement of the hysteresis cycle to higher strains, cycle on cycle. However, there are two completely different mechanisms by which this can occur due to the material constitutive behaviour or due to a structural mechanism:

1) Material ratcheting

Ratcheting can occur in a purely uniaxial, load-controlled test under uniform (membrane) cyclic stressing. This is "material ratcheting" because, under these conditions, there is no structural mechanism which could cause the ratcheting. Material ratcheting will occur only above a certain maximum stress.

2) Structural ratcheting

If a structure exhibits ratcheting at a maximum stress below the material ratchet limit (for the relevant temperature and R-ratio) then this must be structural ratcheting. Structural ratcheting can occur under uniaxial loading [T73S04 (R5V2/3), 2013].

- Ratcheting strain (εr) increase continuously with number of cycle (N) that indicates, plastic strain accumulated with time and material is finally failed due to high plastic strain. If ratcheting strain (εr) first increase with number of cycle (N) then comes to a constant value, indicates that in first portion of the curve plastic strain accumulated with time then stops, so material don't fail due to ratcheting as reported by Satyadevi *et al.*[2007].
- Ratcheting and failure behaviours of the materials depend greatly on the cyclic hardening/softening features of the materials [Kang *et al*., 2005].
- Ratcheting can deteriorate the performances of a component by the cumulative effects of fatigue damage, which arises from alternating stress, and damage by permanent strain (ratcheting strain) accumulation in a particular direction. The latter leads to further enhancement of fatigue damage by continuous thinning of the component cross-section.

- Ratcheting strain can be defined as the position of the centre of the hysteresis loop on the strain axis [Surajit, 2010].

Yang [2005] tested the cyclic strain low cycle fatigue and cyclic stress ratcheting failure of carbon steel 45 with quenched and tempered treatment. The tests for cyclic strain low cycle fatigue with or without mean strains were carried out to investigate the effect of mean strain on low cycle fatigue (LCF) behaviour. The effects of mean stress and stress amplitude on the ratcheting failure were experimentally studied under stress controlled cycling tests also. The evolution equation of fatigue damage is proposed based on the symmetric cyclic strain LCF experimental results, and the equation is used to evaluate the effects of the fatigue damage on the ratcheting failure under different cyclic stressing.

The true strains were calculated from the measured engineering strains, and the true stress is calculated by the current load divided by the current cross-sectional area which is approximately calculated by using the plastic volume incompressibility principle based on the current engineering strain and engineering stress. If the cyclic engineering strain peak and valley are presented by ε_{enp} and ε_{env}, respectively, the true strain amplitude $\Delta\varepsilon/2$ can be calculated as:

$$\frac{\Delta\varepsilon}{2} = \frac{\ln(1+\varepsilon_{enp}) - \ln(1+\varepsilon_{env})}{2} \qquad 3.14$$

True plastic strain ε^p is

$$\varepsilon^p = \ln(1+\varepsilon_{en}) - \frac{\sigma}{E} \qquad 3.15$$

where: ε_{en} denotes engineering strain, σ is the true normal stress and E is elastic Young's modulus. True plastic strain amplitude $\varepsilon^p/2$ is obtained as:

$$\frac{\Delta\varepsilon^p}{2} = \frac{\Delta\varepsilon}{2} - \frac{\Delta\sigma}{2E} \qquad 3.16$$

where: $\Delta\sigma/2$ is true stress amplitude. True ratcheting strain ε_r is defined as:

$$\varepsilon r = (\varepsilon^p_p - \varepsilon^p_v)/2 \quad 3.17$$

Where:

ε^p_p and ε^p_v present the cyclic true plastic strain peak and valley for the cyclic stress peak and valley, respectively.

Based on the linear accumulative damage formula, Equation 3.18 can be presented as following:

$$\frac{dD}{dN} = 13.8\left(\frac{\Delta\varepsilon^p}{2}\right)^{1.8664} \quad 3.18$$

Equation 2.20 is used to evaluate the effects of the fatigue damage on the cyclic stress ratcheting failure under different cyclic stresses. Based on the evolutions of the true plastic strain amplitudes under different stress paths as shown in Figure 3.32, the LCF damage *Df* for the ratcheting failure by using Equation 3.19 can be presented as

$$D_f = \sum_{i=1}^{N_f} 13.8\left(\frac{\Delta\varepsilon^p}{2}\right)_i^{1.8664} \quad 3.19$$

In Equation 3.19, N_f presents the measured cyclic number to the stress ratcheting failure, $\Delta\varepsilon p/2$ is the true plastic strain amplitude in Cycle i under cyclic stressing paths. The LCF damages D_f calculated by Equation 3.19 for ratcheting failure under different stress paths were listed in Table 3.2.

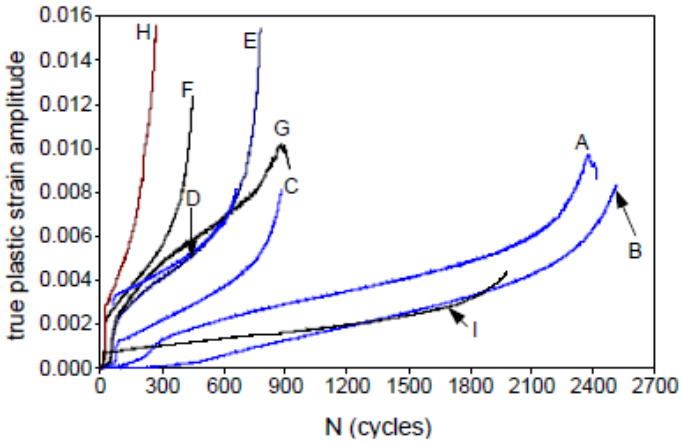

Figure 3.32: Evolution of the true plastic strain amplitudes for several stress controlled loading cases [Yang , 2005]

Table 3.2: Experimental results for the ratcheting failure under stress controlled cycling

Stress paths	Cyclic eng. Stress (MPa)	Cycles to failure	True strain limit for failure	Cyclic true stress for failure (MPa)	Maximum true stress peak for failure (MPa)	LCF D_f	Failure mode
A	40.46±407.43	2417	0.3262	56±564.6	620.6	1.21	Fracture
B	65.9±407.4	2526	0.3817	96.6±596.3	696.9	0.684	Necking
C	91.4±407.4	883	0.388	134.7±600.6	735.3	0.313	Necking
D	116.8±407.4	663	0.36376	168±585.8	753.8	0.181	Necking
E	40.5±432.9	779	0.3576	57.8±619	676.8	0.708	Necking
F	65.9±432.9	448	0.3977	98.1±664.3	762.4	0.365	Necking
G	15±458.3	942	0.16455	17.1±524.4	541.5	1.02	Fracture
H	65.9±458.4	269	0.41594	99.9±694.8	794.7	0.361	Necking
I	152.8±356.5	1994	0.3687	220.9±515.4	736.3	0.263	Necking

[Yang , 2005]

The Author found that:

- Plastic strain amplitude is the key factor causing the LCF damage. It can be assumed that the LCF damage under the large plastic strain amplitude will affect the ratcheting behavior under the subsequent asymmetric cyclic stressing.
- Large ratcheting strain should lead to the significant decrease of the cross-sectional area of the specimen so that the true stress increases under a specific load range and results in cyclic damage and small mean stresses even though

the failure modes are somewhat dominated by the ratcheting damage failure. For the loading paths of the small engineering stress amplitudes and the large engineering mean stresses, the LCF damages are relatively small.

- The LCF damage has very strong influences on the ratcheting failure under high engineering stress amplitude and small mean stress while the failure mode is dominated by the ductile localized necking under relatively small engineering stress amplitudes and large mean stresses.

The Author concluded that:

- Under symmetric strain cycling, the LCF life for the carbon steel 45 is mainly dependent on the plastic strain amplitude, which can be characterized by the Coffin-Manson formula.
- The LCF tests of the material for different mean strains indicate that under the same cyclic saturated true plastic strain amplitudes, the LCF life is not affected significantly by the mean strain, but the mean strain has the significant influence on the initial instantaneous cyclic plastic behaviour.
- Ratcheting failure life N_f decreases with the increase of mean engineering stress under the same engineering stress amplitude while the engineering stress amplitude dominates the N_f under asymmetrically cyclic stressing for the same engineering stress peak.
- When the engineering stress amplitude is very large and the mean stress is very small, the fatigue damage D_f is relatively large. When the engineering mean stress is relatively large and the engineering stress amplitude is relatively small, the fatigue damage D_f is relatively small.

3.5 Fracture mechanics Provisions in Codes and Standards

3.5.1 BS 7608: 2014

BS7608, the Code of Practice for Fatigue Design and Assessment of Steel Structures provides general recommendations for structural steel members exposed to repetitive stress fluctuations. This standard was partially replaced in 2010, in the UK, by the current Eurocode 3: Design of Steel Structures. However the Eurocode is much less detailed than BS7608, so the BS will continue in parallel with EC3. With fabricated steel structures, welds are often the source of fatigue failure. The fatigue assessment procedures embodied in these standards involve the use of various weld categories and cracking scenarios. Each scenario has its own S-N curve. The probability of failure associated with this data often varies across codes.

BS 7608 gives recommendations for the fatigue design and assessment of parts of steel structures that are subject to repeated fluctuations of stress. It is restricted to wrought structural steel with a specified minimum yield strength less than 700 MPa. The document is intended to be generic, possibly used as an adjunct to other specific structure-related design codes. As such, it is not stated to be either “limit state” or “working stress” and could take up whatever philosophy is inherent in the citing structure-specific code.

The document has four main sections dealing with: general aspects, classification of details, stress calculations and allowable fatigue stresses. The main document is supported by a number of annexes dealing with specific technical items. These include Annex A, which covers fatigue design philosophy.

Fatigue design and assessment is achieved by the standard combination of stress ranges (nominal, coupled to standard detail classification or geometric, the latter including SCFs), S-N curves for standard details, and the Palmgren-Miner linear

cumulative damage rule for joints subjected to a stress spectrum. The joint is deemed satisfactory if the cumulative damage is less than unity.

3.5.2 Fatigue damage index (EC3:BS EN 1993-1-9 : 2005) and (BS 7608:2014)

3.5.2.1 Cycles to failure

For a joint subjected to a number of repetitions *n*i of each of several stress ranges, *S*ri, the value of *n*i corresponding to each *S*ri should be determined from standard loading rules (if applicable), from stress spectra measured on a similar structural member, or by making reasonable assumptions as to the expected service history.

The number of cycles to failure *N*i at each stress range, *S*ri, should then be determined from the basic *S-N* curves, modified as necessary in accordance with effect of stress relief for welded details, for the relevant joint class at the selected probability of failure. The design should then be modified so that the cumulative damage (Miner's) summation is as follows:

$$\sum \frac{n_i}{N_i} = \frac{n_1}{N_1} + \frac{n_2}{N_2} + \frac{n_3}{N_3} + \frac{n_4}{N_4} \leq D \qquad 3.20$$

The fatigue assessment based on damage accumulation should meet the following criteria:

D = 1.0 for indicating low cycle fatigue.

3.5.2.2 Cycle counting by the reservoir method (EC3:BS EN 1993-1-9 : 2005) [BS7608, 2014]

The purpose of cycle counting is to reduce an irregular series of stress fluctuations to a simple list of stress ranges. The method, shown in Figure 3.28, is suitable when dealing with short stress histories, such as those produced by individual loading events. It consists of imagining a plot of the graph of each individual stress history as

a cross section of a reservoir, which is successively drained from each low point, counting one cycle for each draining operation. The result, after many repetitions of the loading event, will be the same as that obtainable by the rainflow method.

3.5.3 Crack growth rate BS7910 [2013] and DNV-RP-F108 [2006]

Fatigue cracks in welded joints can originate either from the toe or root of the weld, depending on the type of joint, or from planar or non-planar flaws in the weld. Cracks originating from the weld toe normally initiate at small flaws while cracks originating from the root often start from areas of deliberate lack of penetration; in both cases the initiating feature can therefore be regarded as a planar discontinuity.

In essence, therefore, most fatigue cracks in welded joints can be regarded as starting from a pre-existing planar flaw and their behaviour can be described by the use of fracture mechanics analysis.

The fracture mechanics approach assumes that a flaw may be idealized as a sharp tipped crack which propagates in accordance with the law relating the crack growth rate, da/dN, and the range of stress intensity factor, ΔK, for the material containing the flaw. The overall relationship between da/dN and ΔK is normally observed to be a sigmoidal curve in a log (da/dN) versus log (ΔK) plot.

There is a central portion for which it may be reasonable to assume a linear relationship (i.e. the Paris law) or, for greater precision, to represent the data by two or more straight lines At low values of ΔK, the rate of growth falls off rapidly, such that, below a threshold stress intensity factor range, ΔK_0, crack growth is insignificant. At high values of ΔK, when the maximum stress intensity factor in the cycle, Kmax, approaches the critical stress intensity factor for failure under static load, Kc, the rate of crack growth accelerates rapidly. A number of crack growth laws are available which describe the entire sigmoidal relationship. However, it is

often sufficient to assume that the central portion applies for all values of ΔK from ΔK_0 up to failure. The Paris law, the relevant equation is as follows:

$da/dN = A(\Delta K)^m$

where:
A and m are constants which depend on the material and the applied conditions, including environment and cyclic frequency.
For $\Delta K < \Delta K_0$, da/dN is assumed to be zero.

The stress intensity factor range, ΔK, is a function of structural geometry, stress range and instantaneous crack size and is calculated from the following equation:

$$\Delta K = Y(\Delta\sigma)\sqrt{(\pi a)} \qquad 3.21$$

The acceptability of a crack of initial size ai then depends on whether the calculated cyclic life, N, is greater or less than the required life.

$a_\circ$ is the inital crack size (The calculation life is usually very sensitive to the assumed value $a_\circ$. Therefore $a_\circ$ should be underestimated. For nominally flaw -free welded joints failing from the weld toe $a_\circ$ should be assumed to lie within the range 0.1 mm to 0.25mm unless a larger size in known to be relevant [BS 7608, 2014].)

Kc: fracture toughness = $\sqrt{}$ δcE σy
δc = G/σy , take δc = (range is 0.1 to 1mm)

3.5.3.1 Recommended fatigue crack growth laws for steels in air

The values of A and m depend upon the material and the applied conditions, such as stress ratio, environment, test frequency and waveform as shown in Table 3.3 [Table 10 BS7910, 2013]. Whenever possible, data relevant to the particular material, product form and service conditions should be used and where any doubt exists concerning the influence of the environment such data should be obtained. Provided

that sufficient data are available to enable them to be defined, the chosen values should correspond to the mean plus two standard deviations of log d*a*/d*N*.

Table 3.3: Constants A and m for fatigue crack growth laws for steels in air

R	Stage A				Stage B				Stage A/Stage B transition point ΔK N/mm$^{3/2}$	
	Mean curve		Mean + 2SD		Mean curve		Mean + 2SD			
	A [B)]	m	A [B)]	m	A [B)]	m	A [B)]	m	Mean curve	Mean + 2SD
<0.5	1.21×10^{-26}	8.16	4.37×10^{-26}	8.16	3.98×10^{-13}	2.88	6.77×10^{-13}	2.88	363	315
≥0.5	4.80×10^{-18}	5.10	2.10×10^{-17}	5.10	5.86×10^{-13}	2.88	1.29×10^{-12}	2.88	196	144

[A)] Mean + 2SD for $R \geq 0.5$ values recommended for assessing welded joints.
[B)] For da/dN in mm/cycle and ΔK in N/mm$^{3/2}$.

BS7910 [2013]

Recommendations are available in the form of simple laws [see Figure 3.34a] and more precise two-stage relationships [Figure 3.34b]. For the latter, both the mean and mean plus two standard deviations (mean + 2SD) of log (da/dN) versus log (ΔK) relationships for $R < 0.5$ and $R > 0.5$ are given. However, for conservatism and to allow for the influence of residual stresses, the mean + 2SD laws for $R \geq 0.5$ should normally be used to assess welded components.

Figure 3.33 shows completely reversed sinusoidal stress for R= -1

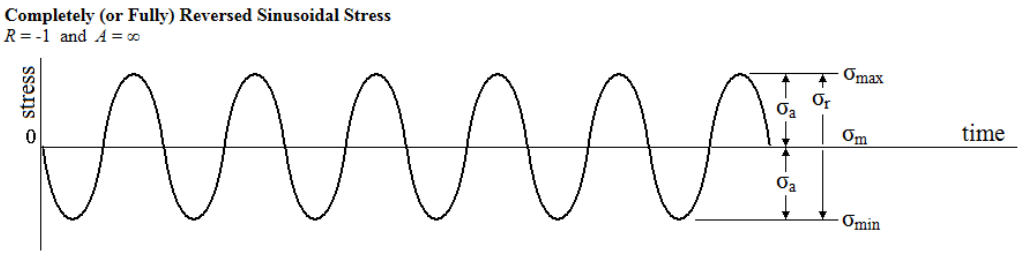

Figure 3.33 Fully reversed sinusoidal stress [Engineering Archives, 2008- 2012]

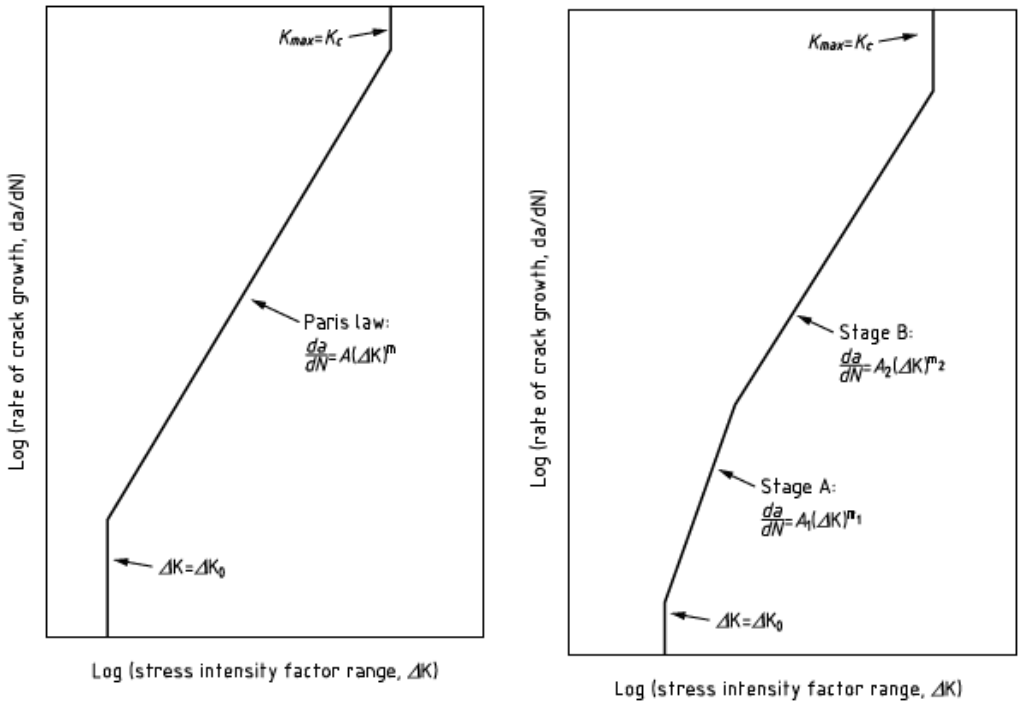

a) Simple Paris law crack growth relationship b) Two stage crack growth relationship

Figure 3.34: Shows flowchart for option 2a fracture assessment constructed by BS7910 [2013]

3.5.4 EC8 EN1998-1: 2005

Strain-hardening of the material corresponds to $f_u / f_y > 1.0$, and is a necessary property to propagate yield and to avoid yielding all taking place in narrow section where yielding first occurred. Steel conforming to EN2005 have $f_u / f_y > 1.4$.

Clause 6.5.4 (1), which refers to a Euro-code 3 rule for bars in tension, also aims at the mitigation of a localized brittle failure.

3.5.5 The failure assessment diagram (FAD) [BS 7910:2013/2005] and (FAD) [DNV-RP-F108, 2006]

These codes provide guidance on avoiding fracture. The Failure Assessment diagram provides a representation of the interaction between failure by fracture and failure by yielding. Note that the work in this thesis was based on BS 7910:2005.

3.5.5.1 Level 2- Normal assessment

Level 2 is the normal assessment route for general application. It has two methods. Each method has an assessment line given by the equation of a curve and a cut-off. If the assessment point lies within the area bounded by the axes and the assessment line, the flaw is acceptable; if it lies on or outside the line, the flaw is unacceptable. The FAD is shown in Figure 3.34 with different cut-offs for different materials.
The cut-off is to prevent localized plastic collapse and it is set at the point at which Lr = Lrmax where:

$$L_{\mathrm{rmax}} = \frac{\sigma_{\mathrm{Y}} + \sigma_{\mathrm{u}}}{2\sigma_{\mathrm{v}}} \qquad 3.22$$

For the purposes of defining the cut-off, mean rather than minimum properties may be used. For materials which exhibit a yield discontinuity in the stress-strain curve (i.e. any curve which is not monotonically increasing), or for which it cannot be assumed with confidence that no discontinuities exist, a cut-off value for Lr of 1.0 should be applied.
Assessments are based on a single value of toughness. The equations describing the assessment line are the following:

a) for Lr, Kr, and $L\mathrm{r}_{\mathrm{max}}$:

$$\sqrt{\delta_{\mathrm{r}}} \text{ or } K_{\mathrm{r}} = (1 - 0.14L_{\mathrm{r}}^{2})\{0.3 + 0.7\exp(-0.65L_{\mathrm{r}}^{6})\} \qquad 3.23$$

b) for $L_r > L_{rmax}$:

$\sqrt{\delta_r}$ or $K_r = 0$

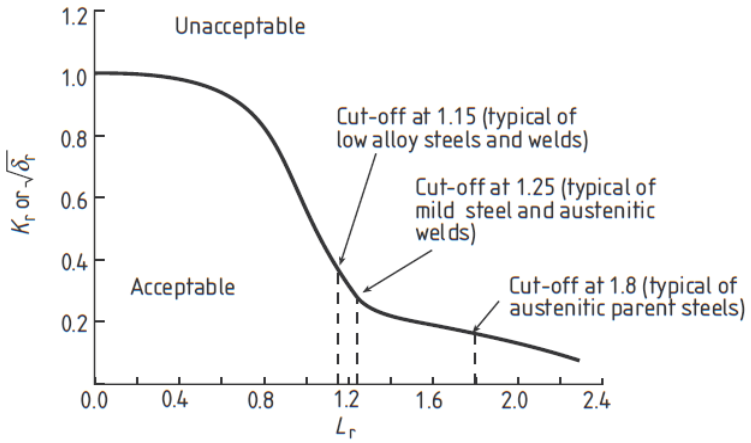

Figure 3.35:Level 2a FAD with typical cut-offs on the *L*r axis, i.e. *L*rmax, for the material being assessed [BS7910, 2013]

Definition of *Lr* and *Kr* for option 2a curve are defined by R6 and BS 7910 [2005] standards approach, and explained in Sec. 3.3.2.1.

In addition, fracture ratio *K*r is evaluated using an enhanced value of fracture toughness, *K*mat (is a measure of the initiation toughness), corresponding to the postulated amount of tearing, typically up to 1 mm, in a fracture assessment [BS 7910, 2013].

3.6 Conclusion

- There are two types of the crack, internal cracks and external cracks this classification depend on the position of crack in the metal. Danielb [1997] has stated that external crack-like defects form during the later stage of solidification. A crack occurs when the partially solidified metal is placed in tension by the constrained cooling and contraction of the surrounding welding. Campbell [2003] has stated that role of entrained oxide films as the main cause of defects in most welding, the operator during welding process

melts and moves the liquid metals using the torch or the welding machine to fill the groove between these two parts, since the liquid surface is commonly covered with an oxide film, it is entrained into the melt by a simple porosity folding action has called a "bifilm" and behaves like a crack in the liquid [Campbell, 2003].

- Fracture demands are evaluated in terms of stress intensity factor (KI) and crack tip opening displacement (CTOD) by using BS7910 [2013] standards and modern pipeline design (Det Norske Veritas DNV-RP-F108)[2006].
- Cracks can also be modelled and J-integral,G or K values directly determined from the FE analysis.
- The fatigue crack initiated in the region of stress concentration, in the transition from overall to the heat affected zone (HAZ), and developed through the HAZs coarse-grain region [Burzic *et al*., 2007].
- The FE method is the most common numerical method used in conjunction with the fracture mechanics approach.
- The maximum values of stress and strain can be predicted by the FE analyses, and can be used as a failure criterion to compare with the experimental results, it is known that these maximum predicted values are usually found very near to the singular points of the model (sharp corners or bi-material interfaces). Therefore, their magnitude strongly depends on how well the stress field around the singularity is modelled (i.e., mesh refinement).
- The maximum critical values obtained by the FE analyses are also dependent on the proximity of the critical point from the stress or strain concentrator.

  In order to overcome this problem, a common approach used by many researchers is to compare the same variables (stress or strain) between simulations of experiments and the structures to be investigated.
- Strain life method is known as low cycle fatigue failures are typically observed when the applied load cycles produce large plastic strains within the

specimen, therefore strains (displacement) must be controlled rather than stress (load) [Darrell, 2008, 2013].

- In steel welded connections, strain values can point to an earlier failure due to either weld failure or cracking in the weld area.
- Coffin and Manson [1950] first developed methods for low cycle fatigue problems associated with gas turbines and nuclear reactors [Darrell, 2008, 2013].
- Coffin-Manson strain-life formula gives better design values for the fatigue life, because Coffin-Manson strain-life formula consider both the elastic and plastic strains [Tevatia *et al.,* 2011]
- Coffin [1954] and Manson [1953] have established a mathematical relationship between the total strain amplitude $\Delta\varepsilon / 2$ and the reversals to failure cycles $2Nf$, Morrow and Smith *et al*. [1968] has established a relationship between the mean stress σ_{mean} and fatigue life $2Nf$ using Coffin -Manson formula, and Smith-Watson-Topper (SWT) [1970] have established another relationship mean stress correction model.
- Fracture toughness demands play a main role in steel connection frames subjected to cyclic loading (according to elasto-plastic regime but not linear elastic fracture mechanics).
- To calculate fracture toughness demands in welded beam-column connections finite element analyses may be used to examine how the connection details influence fracture resistance.
- Toughness had almost no influence on cyclic performance because the cyclic influences were only on the crack propagation phase [Rosien and Ostertag, 2009]. A material's fracture resistance is usually described by a single parameter, either K (Stress Intensity Factor), CTOD (crack tip opening displacement) or the J-integral. It is however known that the stress and strain state at a crack tip is not fully characterized by such a single parameter alone

but that the crack tip constraint, i.e. the degree of crack tip stress tri-axiality, will also influence the fracture resistance.

- Fracture toughness was found to have a significant effect by Righiniotis and Imam [2004] not by Kiral and Erim [2005].
- The failure assessment diagram (FAD) was used to determine if a crack may cause a structural failure or be safe, and it is defined by R6 and BS7910 standards approach.
- The failure assessment diagram (FAD) is the locus separating the acceptable and unacceptable conditions, i.e. "failure" is assumed if the assessment point falls on or outside the FAD curve while safe conditions are assumed if the assessment point falls inside the FAD curve.
- For establishing FAD and determining CTOD, the British standard [BS7910, 2005] recommended to use the total expected value of the strength for the material to be employed, which is using stress range for total cycle (σ_T) in stress time history increment, but Det Norske Veritas DNV-RP-F108[2006] recommended to use the highest expected value of the strength for the material to be employed, which is using stress range for last cycle (σ_L) in stress time history increment as recommended by DNV-RP-F108[2006].
- Fatigue damage index (FDI) is used to calculate total damage to the element due to the cyclic load using the Palmgren-Miner rule including either rainflow cycle counting method or reservoir method [BS7608, 2014].
- Fatigue damage index (FDI) gives the engineer an additional tool that can be used to better understand the performance of their design under seismic loads [Campbell *et al*.,2008].
- BS 7910 [2013] recommended to use total strain range for the determination of the applied CTOD.
- The bad effects of residual stresses on the structural performance were increasing in SIF and stress triaxiality, (a) increasing promotion of connection brittle fracture and (b) finally reducing connection ductility. These effects

depend on weld joint geometry, welding process, restraint conditions, basic and weld material properties [Hedayat and Celikag, 2009].

- Large panel zone deformations in connections with weak joint panels, showed a roughly double fracture toughness demand compared with connections with strong panels zones [Chi *et al*., 2000].
- A weaker panel zone can significantly increase the potential for ductile fracture of the connection [Ricles *et al*., 2004]
- Strain hardening increased the material strength (stiffness) but decreased the plastic deformation capacity (Toughness) [Björk *et al*., 2006].
- Ratcheting failure life N_f decreases with the increase of cyclic mean engineering stress under the same engineering stress amplitude while the engineering stress amplitude dominates the N_f under asymmetrically cyclic stressing for the same engineering stress peak.
- Material don't fail due to ratcheting as reported by Satyadevi *et al.*[2007].
- Ratcheting is a strain accumulation under stress controlled cycling with non-zero mean stress as reported by Verma [2011]. Displacement ratcheting does not occur in the experiments owing to the deflection control. However material ratcheting does occurs as shown in Figure 3.23.
- The joint behaviour depended on the loading history, and geometric section properties [Carlo and Castiglioni, 2005].
- Strain hardening increased the material strength but decreased the plastic deformation capacity and led to brittle fracture [Björk *et al*., 2006].
- An estimation of the remaining life of a member is important as this allows the engineer to predict the cumulative effect of multiple earthquakes over the life of a structure [Campbell *et al*.,2008].
- Current investigations showed that the maximum stress distribution for the base model concentrate in the area of penal zone. By adding two flange gussets more support will be provide to the T-connection by distributing the load, so reducing the value of the maximum stress and making the connection

have a greater deformation capacity that contributes to the overall safety of the structure. Also results shows that the maximum principle stress and the maximum principle strain in the critical point have been reduced.

There was quite a lot of work has been done on increasing load to fracture but not so much on low-cycle fatigue in earthquakes, also there was not enough work done in fully welded steel connection considering low cycle fatigue. Because of the lack of investigation on beam-column welded connection LCF behavior, further investigations are needed to determine the general LCF behavior, therefore low cycle fatigue concept has been adopted and conducted on the beam-column welded connection LCF strength life.

Model test data was available from data from Mele *et al.* [2003], but there was no fracture toughness data, therefore I decided to primarily use and compare LCF approaches. Fracture mechanics methods were also tried (with estimated fracture toughness values).

Parametric study can adopt the FEA for researching in order to characterize the LCF fatigue behaviour of steel connections. Models will be used in conjunction with moderately detailed elasto-plastic finite element analysis (FEA) models to investigate how well Mele's experimental data could be predicted.
A validated, or at least calibrated, numerical model will be established to model four cases and also will be used to modify the four cases to include the following:

1. Fully welded beam to column connection with four column web double plates (base model).
2. Fully welded beam to column connection with four column web bracing plates and beam flange bracing gussets (improved model).

The following chapter will be showing the application of finite element modeling analysis with LCF prediction, model comparison/validation, and discussion.

CHAPTER 4
FE MODELLING AND MODEL VALIDATION

4.1 Introduction

The behaviour of beam-to-column connections was studied by finite element simulations. The primary objectives of this analytical study were: (a) to investigate the effect of low cycle fatigue on the steel connection considering the stress and strain environment at the locations where fracture initiated in the test specimens, (b) to study the effectiveness of finite element simulation to evaluate the performance of the connection, (c) to investigate the effects of other variables which were not considered in the experimental program; and (d) to aid in the development of further improved connections.

The correlation between simulations and experimental observations was a primary interest of this study.
The majority of beam-column connection specimens failed due to fracture of the beam flange just above the weld.

Finite element simulation of the specimens provided detailed information on the stress and strain environment at local regions of concern. Therefore, although the initiation and propagation of fracture was not modelled, the likelihood of fracture was considered based on the computed stress and strain distribution. The primary focus of this study was the effect of geometric configurations on the performance of beam-to-column connections.
Section 4.2 outlines the finite element analysis procedure.
Section 4.3 modification of stress strain curve.
Section 4.4 comparison/validation model result with experimental data
Section 4.5 panel zone under shear, and
Section 4.6 discussion

4.2 Description of the finite element analysis

4.2.1 Finite element models

The general purpose finite element analysis program ANSYS Workbench version 14.5 was used to perform nonlinear three-dimensional (3-D) finite element simulations of beam-column connection test specimens. ANSYS was run using Microsoft windows 2007 as the operating system.

Four models of BCC5 (BCC5A, BCC5B, BCC5C and BCC5D) [Mele *at el*., 2003] have been modelled. All models have the same dimensions and experimental data except the displacement loading history. The finite element analysis of the steel connection model (base model), represents one type of steel frame connection.

Figure 4.1 shows the 3-D solid model included details of the column stiffeners (10mm thickness continuity bracing in the column web, two in each side). The goal of including such bracing is to increase the rotational stiffness of the connection, decreasing the concentrated stress value and overall controlling of the stress distribution [Trajanoska, 2000].

The 3-D solid model was made using Solid Works version 13 software program, and then exported as STEP files into ANSYS workbench where the structural analysis was made.

Nonlinear 3-D finite element models (base models) were developed to represent the beam-column specimen, the analysis was carried out including engineering data: multilinear isotropic hardening, non linear material, non linear geometry, and displacement loading.

The base model represents the fully welded connection design of a beam to column connection with chosen profiles; the beam profile is an IPE300 and the column has a HE160B profile; data is shown in Table A.1 Appendix A.

The nominal specimen dimensions and experimental data by Mele *at el.*[2003] were used to define the model geometry.

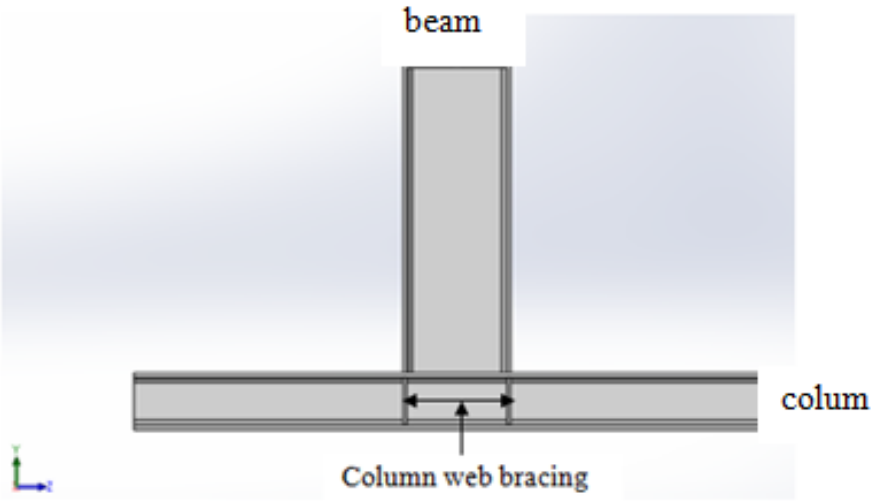

Figure 4.1: Column web bracing plates (10mm thickness)

The definition of the environment of the model, the mesh generation and the load implementation is done in the ANSYS program.

4.2.1.1 Element type

In this work solid 186 and solid 187 elements are used as element type. Solid 186 is well suited to modelling irregular meshes. The element may have any work orientation. In this work solid 186 structural solid is used for meshing of double plates steel. A solid 187 element is a higher order 3-D, 10-node element and it has a quadratic displacement behaviour and is well suited to modelling irregular meshes. In this work solid 187 is used for meshing of beam and column.

Solid187 element description

Solid187 element is a higher order 3-D, 10-node element. Solid187 has a quadratic displacement behaviour and is well suited to modelling irregular meshes (such as those produced from various CAD/CAM systems).

The element is defined by 10 nodes having three degrees of freedom at each node: translations in the nodal x, y, and z directions. The element has plasticity, hyper-elasticity, creep, stress stiffening, large deflection, and large strain capabilities. It also has mixed formulation capability for simulating deformations of nearly incompressible elasto-plastic materials, and fully incompressible hyper-elastic materials.

The geometry, node locations, and the coordinate system for this element are shown in Figure 4.2 [ANSYS release 14.5, 2012].

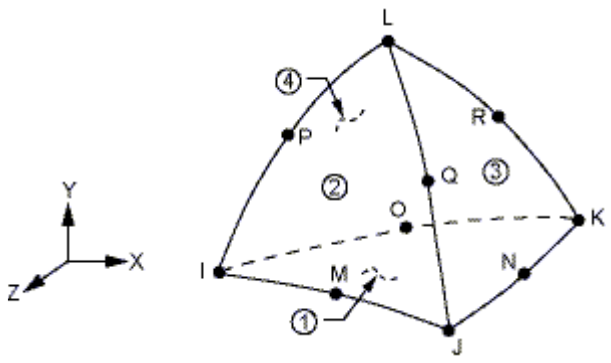

Figure 4.2: Solid187 geometry [ANSYS release 14.5, 2012]

Solid186 element description

Soild186 is a higher order 3-D 20-node solid element that exhibits quadratic displacement behaviour. The element is defined by 20 nodes having three degrees of

freedom per node: translations in the nodal x, y, and z directions. The element supports plasticity, hyper-elasticity, creep, stress stiffening, large deflection, and large strain capabilities. It also has mixed formulation capability for simulating deformations of nearly incompressible elasto-plastic materials, and fully incompressible hyper-elastic materials.

SOLID186 homogeneous Structural Solid is well suited to modelling irregular meshes (such as those produced by various CAD/CAM systems). The element may have any spatial orientation. The geometry, node locations, and the coordinate system for this element are shown in Figure 4.3 [ANSYS release 14.5, 2012].

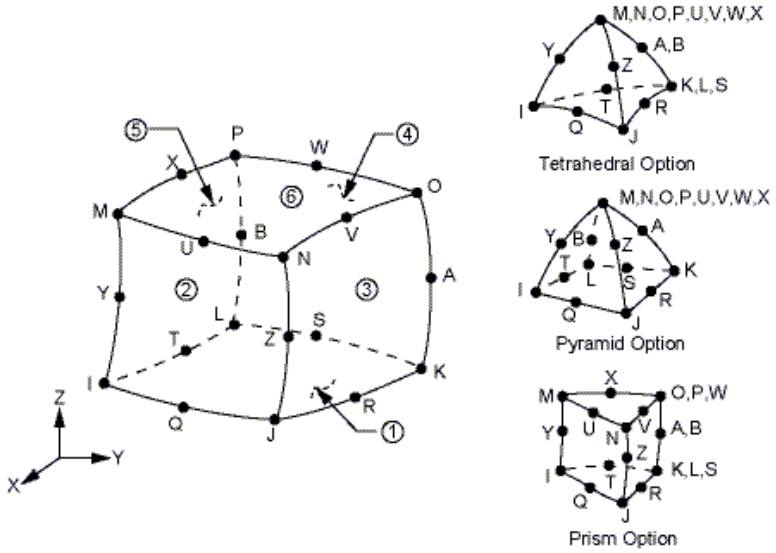

Figure 4.3: Solid 186 homogenous structural solid geometry
[ANSYS release 14.5, 2012]

4.2.2 Connection

4.2.2.1 Automatically generated connections

The connections folder is the container for all types of connection objects except for the three types that can be automatically generated (contact, Joint, and Mesh

connection). The objects of each of these three types are placed in a sub-folder called the connection group folder as illustrated in Figure 4.4, the details view of the connections folder provides the following two properties [ANSYS release 14.5, 2012]

4.2.2.2 Auto detection

Common connections folder operations for auto generated connections can automatically generate supported connections for a group of bodies in a model and use a separate tolerance value for that group as shown in Figure 4.5.

If applicable, set the auto detection properties. Note that these properties will be applied only to scoped geometries for this connection group.
Choose create automatic connections from the context menu (right mouse click) for the connection group [ANSYS release 14.5, 2012].

4.2.2.3 Generate automatic connection on refresh

In this work, automatically generate connections for a group of bodies is chose, insert a connection group object under the connections folder from the toolbar button by choosing insert from the context menu (right mouse click) for this folder.

Generate automatic connection on refresh: options are *yes* (default). This is a setting to turn on for auto generation of connection objects when the geometry is refreshed. The process of automatically creating the contact as follows and as shown in Figure 4.6.

Connections: connection group

Connection type: contact

Geometry: all bodies

Face/Face: yes

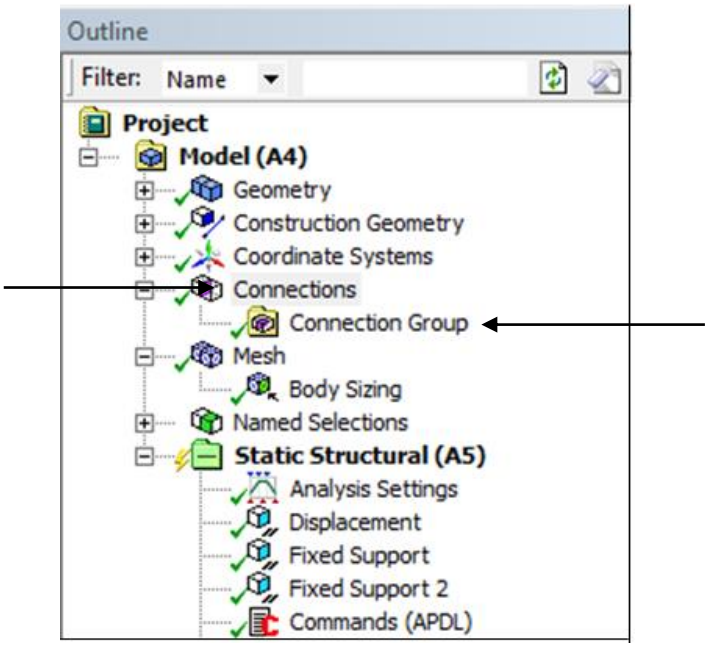

Figure 4.4: Toolbar outline connections [ANSYS release 14.5, 2012]

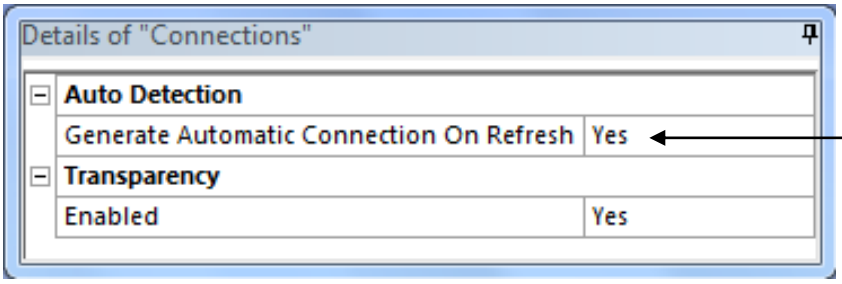

Figure 4.5: Toolbar details of connections (Auto detection)

[ANSYS release 14.5,2012]

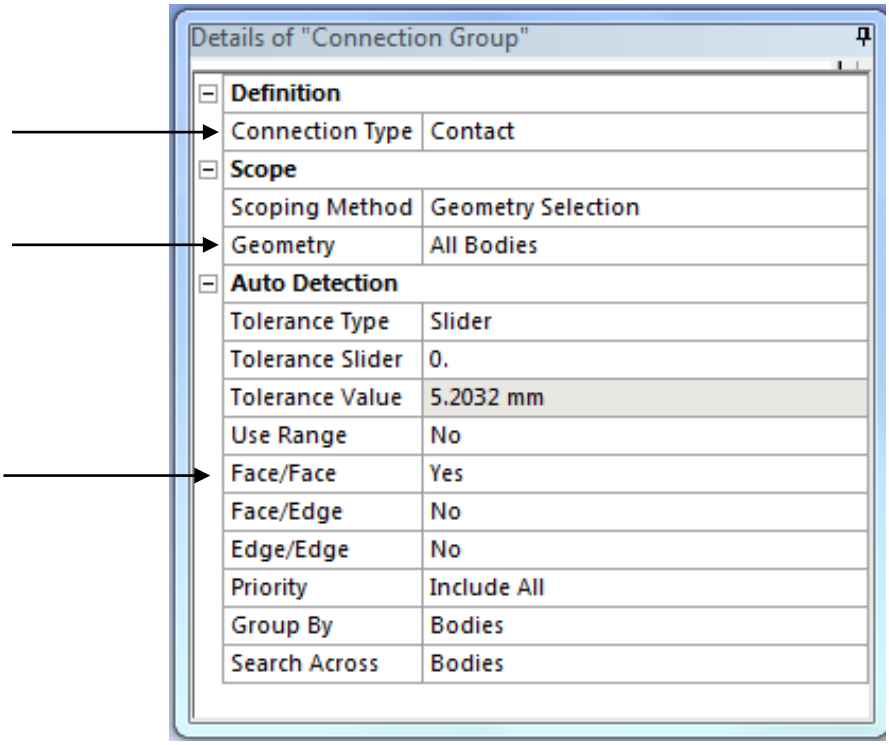

Figure 4.6: Toolbar details of connection group
[ANSYS release 14.5, 2012]

4.2.3 Meshing

Meshing is an integral part of the computer-aided engineering simulation process. The mesh influences the accuracy, convergence and speed of the solution.

From easy, automatic meshing to a highly crafted mesh, ANSYS provides the ultimate solution (according to ANSYS release 14.5 [2012]). Powerful automation capabilities ease the initial meshing of a new geometry by keying off physics preferences and using smart defaults so a mesh can be obtained upon first try. Therefore, the better and more automated the meshing tools, the better the solution [ANSYS release 14.5, 2012].

For solid models, meshing technologies from ANSYS provide robust, well-shaped quadratic tetrahedral meshing on even the most complicated geometries. With automatic contact detection and setup [ANSYS release 14.5, 2012].
The mesh is consistent for all of the models, it is made using the method mesh/all as shown in Figure 4.7.

To obtain good accuracy in regions a large number of small elements must be used (refine meshing), with a specific contact sizing type in the welded zone (sphere size), the radius of sphere is 300mm with sizing 10 mm, due to defining the contact of the welded parts as shown in Figure 4.8, and Figure 4.9 shows section in considered connection with refine meshing. Therefore all elements are assembled together and the requirements of continuity and equilibrium are satisfied between neighbouring elements is explained by Becker [2004].

The fracture mechanics methods are based on a small initial crack. Typical value in a weld, that I used, is 0.2mm. This is discussed further in Section 5.2.1

It should be noted however that this mesh does not include a model of the welds the fine detail of the weld shape, the fine detail of the intersections between the plates and the welds or the different stress-strain properties of the weld metal, HAZ and parent plate. It might be regarded as a possible engineering model that could be used by designers (it runs in 24 hours on a present-day PC) rather than a model that might be used by researchers that would take many days to run or require advanced computing hardware and so would probably not be used by designers.

Non-linear numerical models can give detailed information at any location in a structure. Numerical models are still time consuming to set up and run but increases in computer power mean that runs can be made in short enough time for the methods to be used within design or within the development of design codes. In design it is now possible for the designer to improve the design with this type of model.

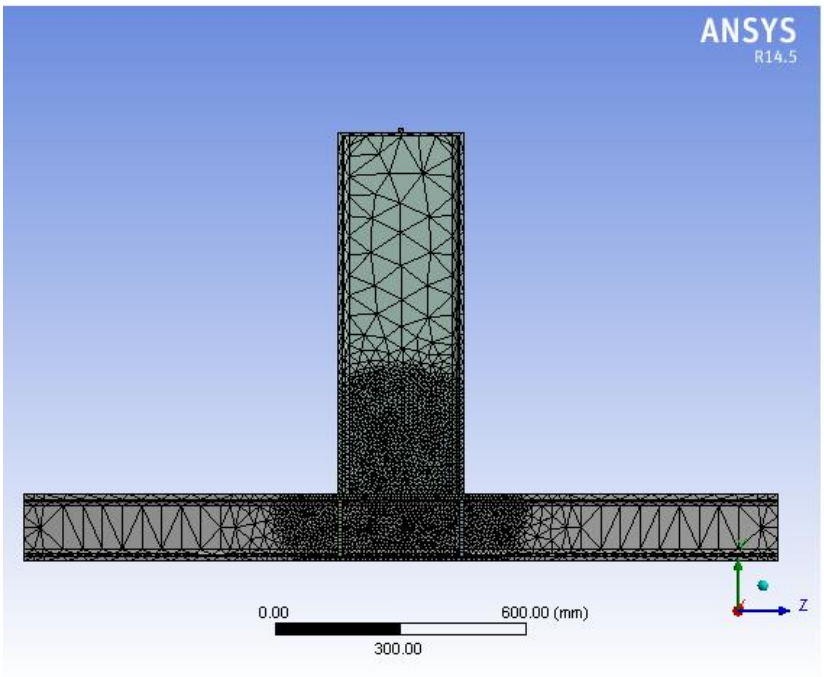

Figure 4.7: Meshing and fine meshing using Ansys release 14.5

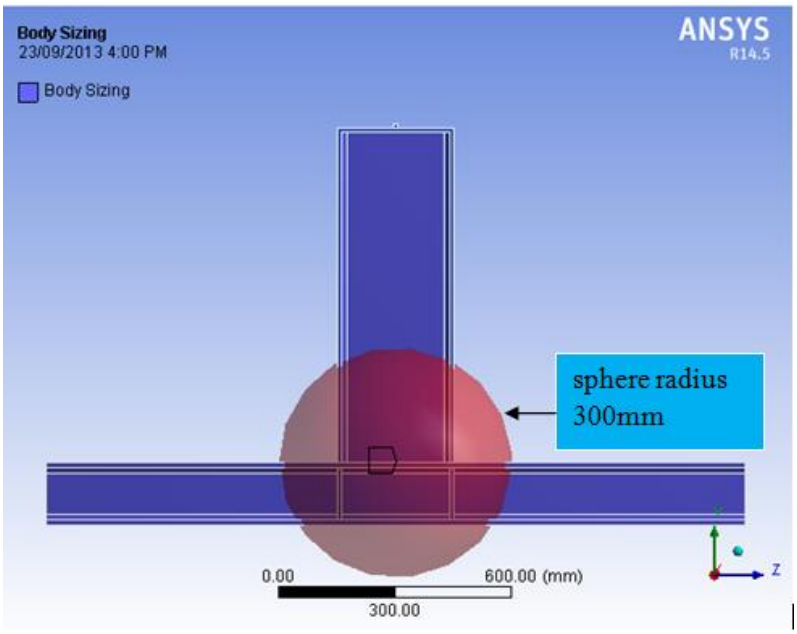

Figure 4.8: Refine mesh in welded joint sphere radius is 300mm with 10mm sizing

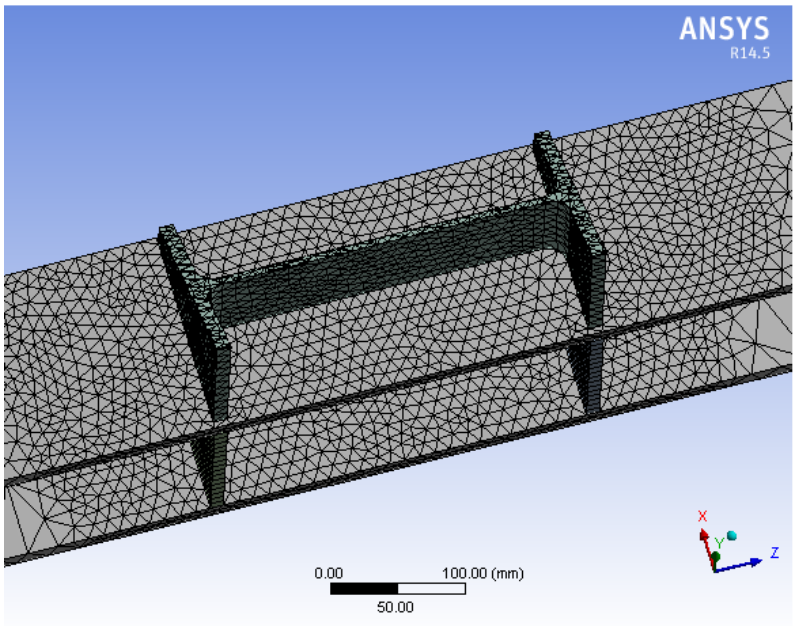

Figure 4.9: Section in considered connection with refine meshing

4.2.4 Cyclic displacement loading and supports

The cyclic displacement loading is applied to the beam in the horizontal direction, in-plane, Z direction, the column is fixed at both ends, that sets the translation at zero as shown in Figure 4.10 [Calado, 2010-2014, per. comm.]. Note however the initial FE results suggested some support flexibility and so the FE model was adjusted (by modifying the Young's modulus E to get elastic deformation correct and then plastic deformation correct) to match the actual measured force deflection plots in the elastic region. A possibly better alternative would have been to use elastic spring supports but the behaviour of primary interest was the large plastic strain that is largely determined by the bending moment in the beam and is not too affected by the support conditions.

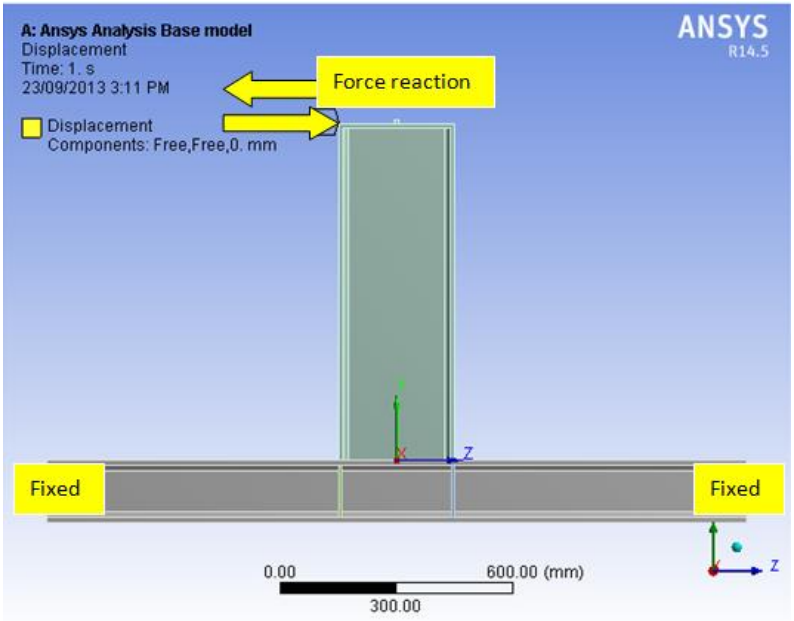

Figure 4.10: Location of displacement and force reaction in Z direction

The displacement was applied 862.5mm distance from the column top flange, as shown in Figure A.3 Appendix A, as input to the ANSYS non-linear analysis.

Figure 4.11 shows displacement vs. number of substeps applied to BCC5A model; this displacement history is obtained from the experimental test. The other BCC5 displacement vs. number of substeps graphs are shown in Figure B.1 Appendix B.

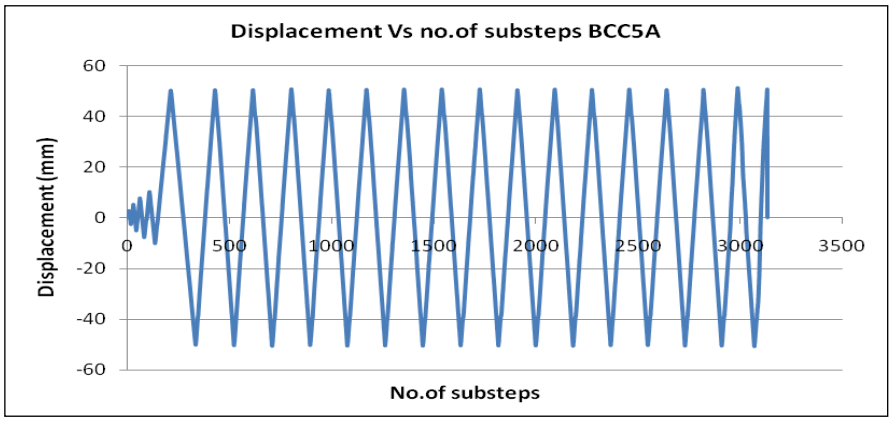

Figure 4.11: Time-displacement loading applied to the model

Table 4.1 shows number of substeps, number of iteration and time of running computer analysis for each model is set as one second (one step), which is different than the test time as explained in Sec.A.3.2.1. Appendix A.

Table 4.1: Number of substeps, time run the analysis and number of iteration of BCC5 models

Case no.	No. of cycles	No. of substeps	Time running the analysis (second)	No. of iteration
BCC5A	16	3134	77862	6608
BCC5B	5	1526	34809	3189
BCC5C	18	2595	61847	5549
BCC5D	23	3366	80296	7192

The displacement convergence value = 0.2038E-01 criterion = 0.1954E-04, force convergence value = 895.4 criterion = 27.40, Displacement convergence value = 0.5165E-05 criterion= 0.1954E-04 <<< Converged equil iter 2 completed. New triang matrix. Max dof inc= -0.9273E-07 force convergence value = 0.4005E-03 criterion = 28.03 <<< Converged.

Number of total nodes = 75811, number of contact elements = 0, number of spring elements = 0, number of bearing elements = 0, number of solid elements = 40185, number of total elements = 40185 and mesh size is 10mm. There are no degradation . (Note: all other related information are shown in CD attached to this thesis).

To assist other analysts I note that it was difficult to get total strain and normal stress expressions from the solution using the ANSYS Workbench. After extensive investigation: searching papers, contacting the IDAC ANSYS company and google

searching, it was found that by clicking on solution and using worksheet in the main bar it is possible to get them through user defined result expressions. Table 4.2 shows the quick user defined result expressions symbols in (X,Y,Z,XY,YZ and XZ directions), where EPTO is total strain, EPPL is plastic strain, EPEL is elastic strain, U is displacement, S is stress and F is Force.

Table 4.2: Quick user defined result expressions

Type	Component	Output unit
EPTO	X,Y,Z,XY,YZ,XZ	total strain
EPPL	X,Y,Z,XY,YZ,XZ	plastic strain
EPEL	X,Y,Z,XY,YZ,XZ	elastic strain
U	X,Y,Z,XY,YZ,XZ	displacement
S	X,Y,Z,XY,YZ,XZ	stress
F	X,Y,Z	Force

4.2.5 Nonlinear analysis

Material nonlinearity was considered using the von Mises yield criterion which is the default options adopted by ANSYS. Hardening was modelled by an isotropic hardening rule.

The constitutive rule of the isotropic hardening material was modelled by a multi-linear rule (The multilinear mathematical model was derived in order to obtain a better representation of the nonlinear behaviour of connections when the linear range of response is exceeded). The most basic form of the multilinear model is bilinear model [Cafer, 2009]). The A36 steel model represented the beam was a vertical I-beam (a typical European beam section IPE300, which is considered equivalent to W12330 U.S. wide flange section), and the column is a horizontal I-beam (HE160B possibly equivalent to W8324 U.S) as shown in Table A.1.

The residual stresses arising from the steel manufacturing process and fabrication process were not accounted for in material modelling. Material properties of BCC5 models are:

- Modulus of elasticity, E_{steel}= 200 x 10^3 MPa
- Yield stress of A36 steel, σ_y= 274.88 MPa
- Ultimate Stress of A36 steel, σ_u= 404.6 MPa

Stress-strain tension test data applied to the BCC5 FE ANSYS models is shown in Figure 4.12 and Table 4.3.

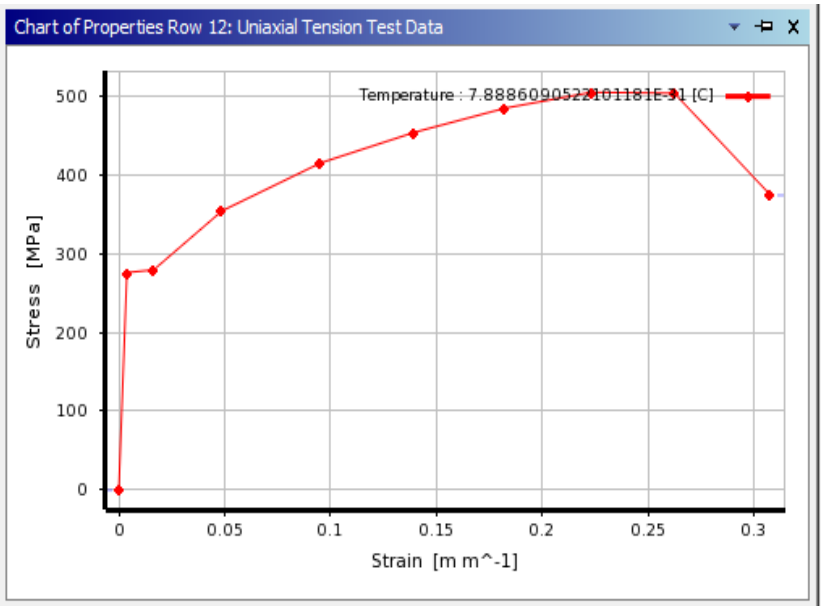

Figure 4.12: Stress-strain curve uniaxial tension test data

Table 4.3: Stress- strain uniaxial tension test data

	B	C
1	Strain (m m^-1)	Stress (MPa)
2	0	0
3	0.0038172	275.83
4	0.016464	279.34
5	0.04879	354.38
6	0.09531	415.25
7	0.13976	454.25
8	0.18232	484.8
9	0.22314	505
10	0.26236	503.75
11	0.30785	374.14
*		

4.3 Modification of stress strain curve

Analysis was done to the base model using ANSYS release 14.5, applied stress-strain experimental curve in engineering data as input in "Multilinear Isotropic Hardening", the hysteresis loops force displacement was obtained from FE analysis as shown in Figure 4.13, which looks like linear shape without nonlinearity, it is the first validation analysis process (for BCC5A), and it is not match with the experimental work hysteresis loops.

After further investigation, it was discovered that there was a difference in the force-displacement curve in the elastic zone as shown in Figure 4.14 and Figure 4.15, it is likely however that the elastic strains are overestimated by this procedure. Initially poor agreement between elastic analysis and experiment, this was traced to measured stress strain data not including a point corresponding to commencement of yield (yield point is missing in experimental test).

The stress strain curve used was corrected correspond to the young modulus of steel of 200 Gpa and this resulted in a reasonable agreement between experimental work and FE analysis.

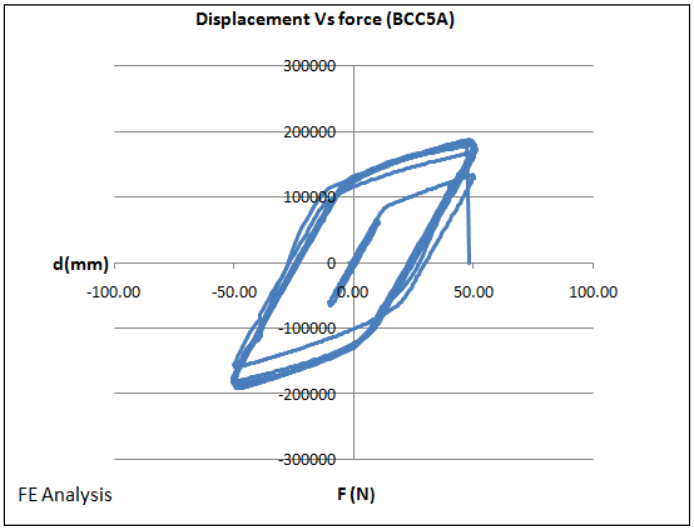

Figure 4.13: Force vs. displacement hysteresis loops

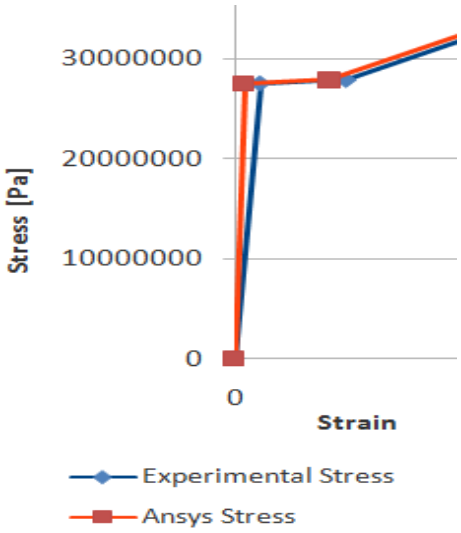

Figure 4.14: Difference in elastic stress-strain curve between experiment and steel British standard in linear zone

In this work, where plastic strains are most important, it was compensated for by adjusting the E value, the yield point was setting to zero and subtracting 0.0038172 from each strain from Table 4.3, to get the new plastic stress-strain curve and data and applied to the Multilinear Isotropic Hardening as shown in Figure 4.16 and Table 4.4.

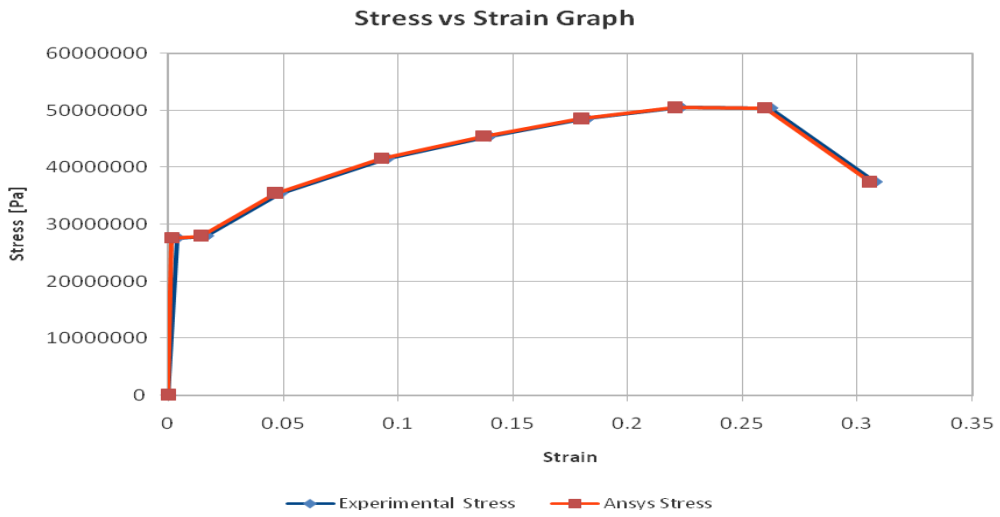

Figure 4.15: Combine stress vs. strain graphs (experiment and steel British standard)

FE force-displacement hysteresis loops (for all base models) look close to the experimental hysteresis loops as shown in Figures 4.17-4.20, which means the base models should predict the maximum normal stress and strain locations in the experimental work at the fracture location as explained in Sec.4.4.2.

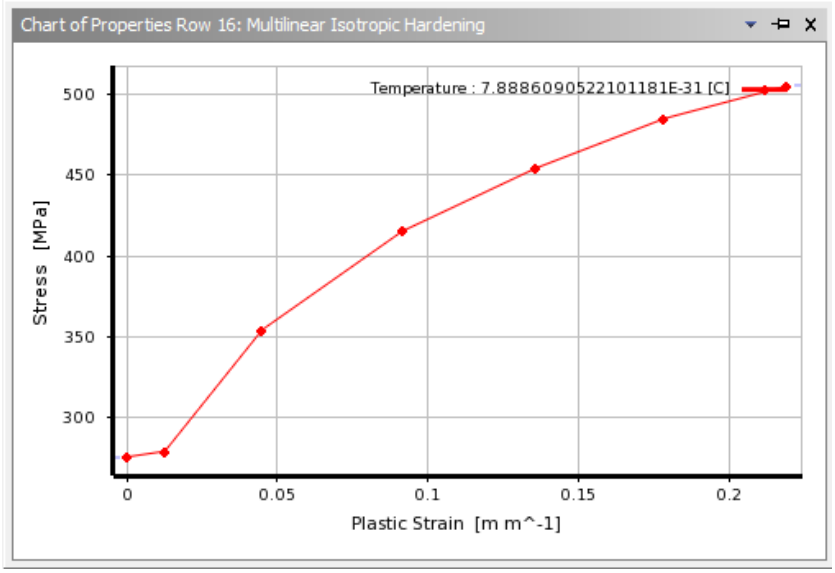

Figure 4.16: Multilinear Isotropic Hardening plastic stress-strain curve

Table 4.4: Multilinear Isotropic Hardening plastic stress-strain data

	B	C
1	Plastic Strain (m m^-1)	Stress (MPa)
2	0	275.83
3	0.012647	279.34
4	0.044973	354.38
5	0.091493	415.25
6	0.13594	454.25
7	0.1785	484.8
8	0.21933	505
*		

A simple calculation was done using MathCAD programme is shown in Sec.C.6 Appendix C, to investigate the stiffness in the joint, it was found that:

- Joint in actual test sample (steel joint) is more stiff than the FE base model joint.

- Panel zone in experiment had higher stress than FE
- Maximum strain location in FE has the same location in experiment

4.4 Validation of model result with experimental data

A comparison /validation process for the base model has been done by comparing the FE results with the experimental data.

4.4.1 Hysteresis loops

Hysteresis loops of load displacement were considered for the validation process. Numerical force reaction history was obtained by applying the experimental load displacement history and consequently numerical hysteresis loops were constructed in Sec. B.2 Appendix B.

Figures 4.17-4.20 show displacement vs. force reaction hysteresis loops for experimental test (blue) and FE ANSYS programme (red), and as these figures demonstrated also throughout the experimental program, the number of cycles to failure and the failure modes behaviour for each specimen are shown in Table A.3 Appendix A. All BCC5 specimens are characterised by a great regularity and stability of the force displacement hysteresis loops up to failure, with no deterioration of stiffness and strength properties. In the last cycle the BCC5 specimens collapsed with a sudden and sharp reduction of strength, due to brittle fracture initiated in the beam flange and propagated also in the web during the test, significant distortion of the joint panel zone has been observed, while no remarkable plastic deformation in the beam occurred.

By comparing the data between the experimental force-displacement hysteresis loops which are subjected to the cyclic load with the FE analysis force-displacement hysteresis loops which were presented in Figures 4.17-4.20, it can be seen that

maximum and minimum values of the applied force were close to each other and ranged between +190000 to -190000N. Moreover, the experimental and the numerical values of displacement were close to each other, that means the FE base model was (after some elastic calibration described above) able to predict the force reaction at the same position as the cyclic force was applied in the experiment of steel joint, with an acceptable range of accuracy.

In the initial linear zone it can be noticed (from the hysteresis loops) that in the experiment the joint is a little stiffer than the FE joint. However the general behaviour is very similar in all the experiments, except the FE model does not fracture and result in the irregular parts of the experimental traces.

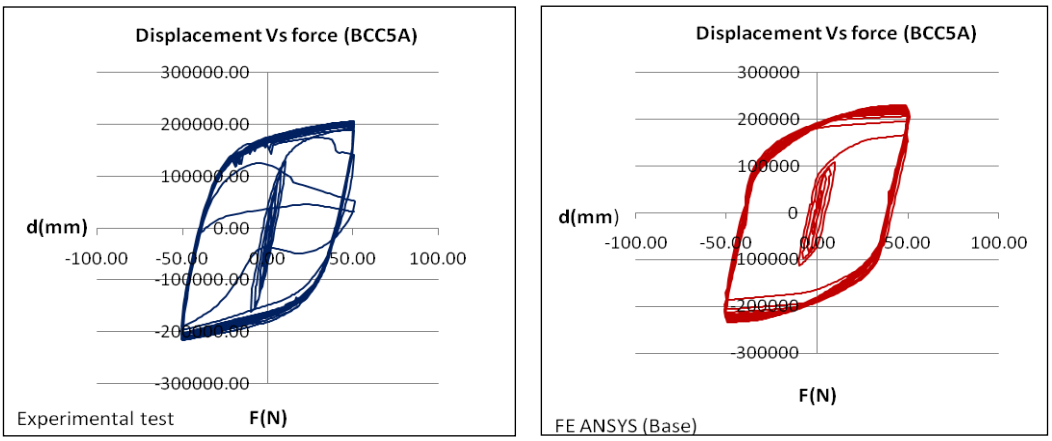

Figure 4.17: Displacement vs. force-reaction hysteresis loops for experimental test and FE ANSYS of BCC5A

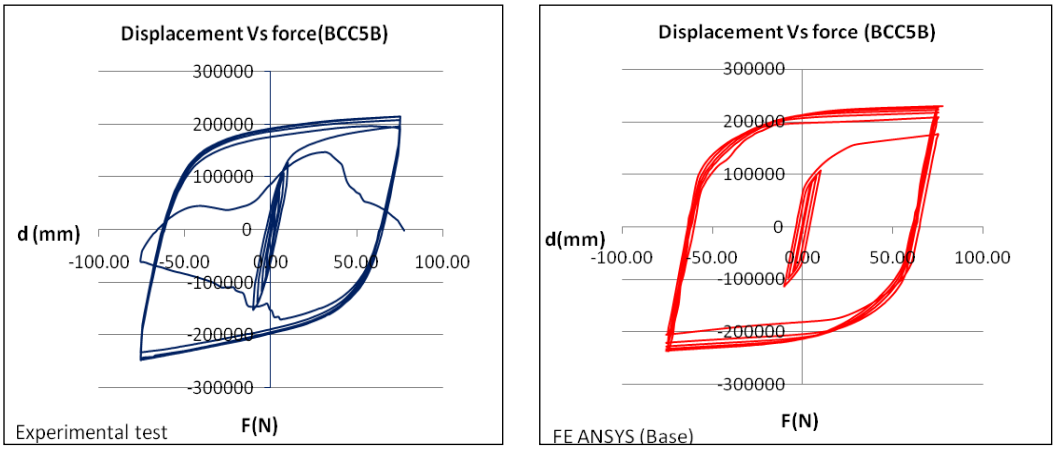

Figure 4.18: Displacement vs. force hysteresis loops for experimental test and FE ANSYS of BCC5B

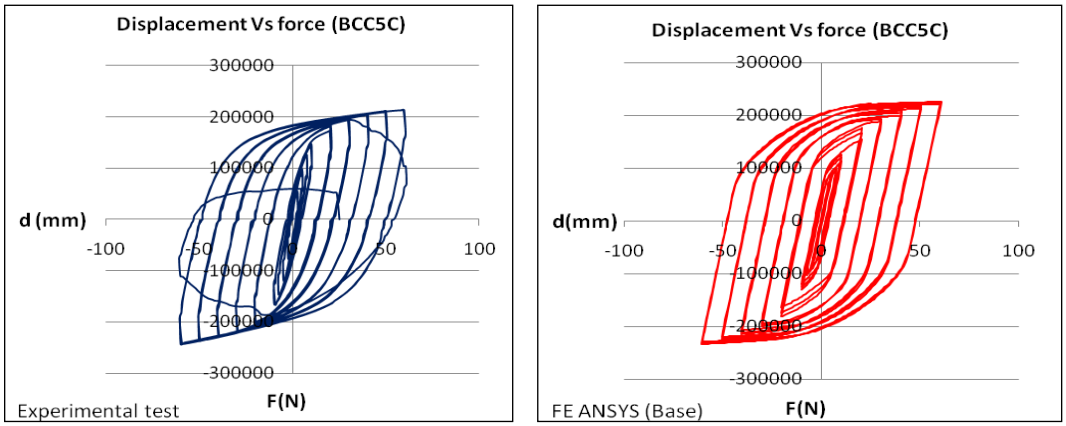

Figure 4.19: Displacement vs. force-reaction hysteresis loops for experimental test and FE ANSYS of BCC5C

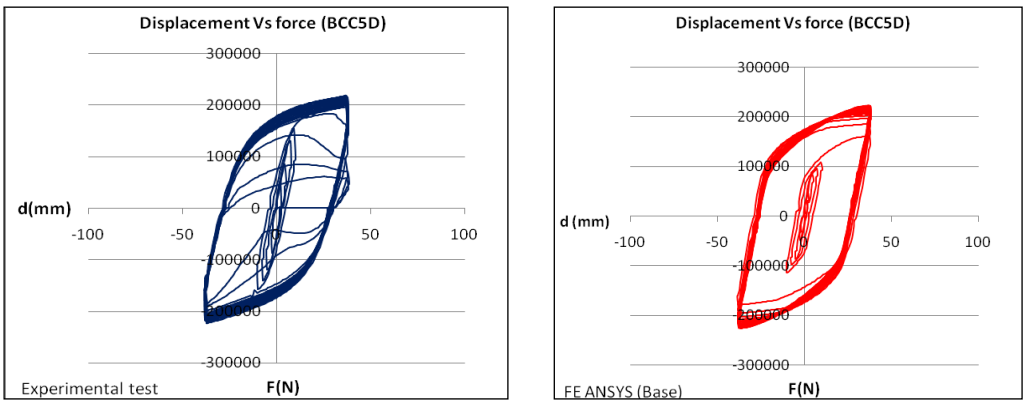

Figure 4.20: Displacement vs. force-reaction hysteresis loops for experimental test and FE ANSYS of BCC5D

4.4.2 Failure Location

Figure 4.21 and Figures D1-D3 Appendix D show the maximum normal stress and maximum total strain of FE analysis for BCC5A and BCC5B, BCC5C and BCC5D base models respectively, occurred in the same location as experimental work. Therefore the FE analysis base model can represent the experimental work.

Table 4.5 shows maximum total strain (maximum principle strain) and maximum normal stress (maximum principle stress) at critical point where the failure occurred for BCC5A, BCC5B, BCC5C and BCC5D models.

Table 4.5: Maximum total strain and maximum normal stress at critical point where the failure occurred for BCC5 models

Case No.	Maximum total strain at critical point (mm/mm) at last substep before end	Maximum normal stress at critical point (MPa) at last substep before end
BCC5A	0.019617	606.45
BCC5B	0.022179	611.8
BCC5C	0.010972	553.6
BCC5D	0.01533	294.05

Table 4.5 shows that increasing the maximum total strain (0.010972 - 0.01533) in the case BCC5C and BCC5D respectively is due to the effect of ratchetng strain which occurs due to more cycles. And the maximum normal stress decreases (553.6 - 294.05) for BCC5C and BCC5D respectively is due to related displacement-time history (see Appendix B Figure B.1(b) and (c)).

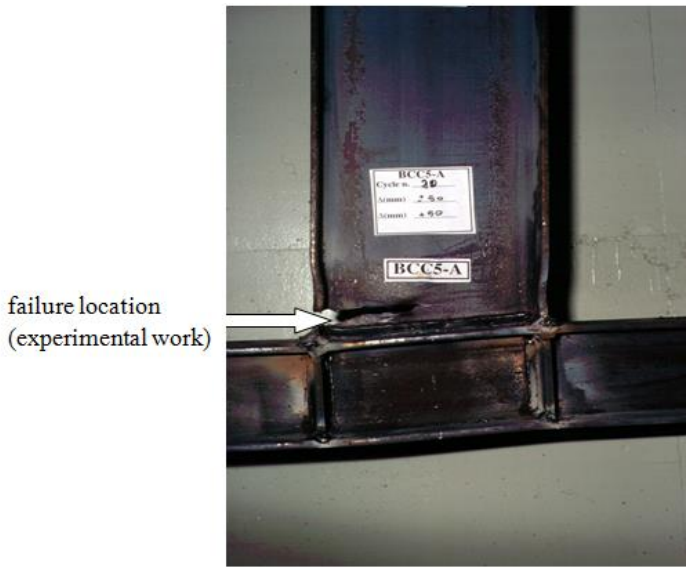

(a) [Calado, 2010-2014, per. comm.]

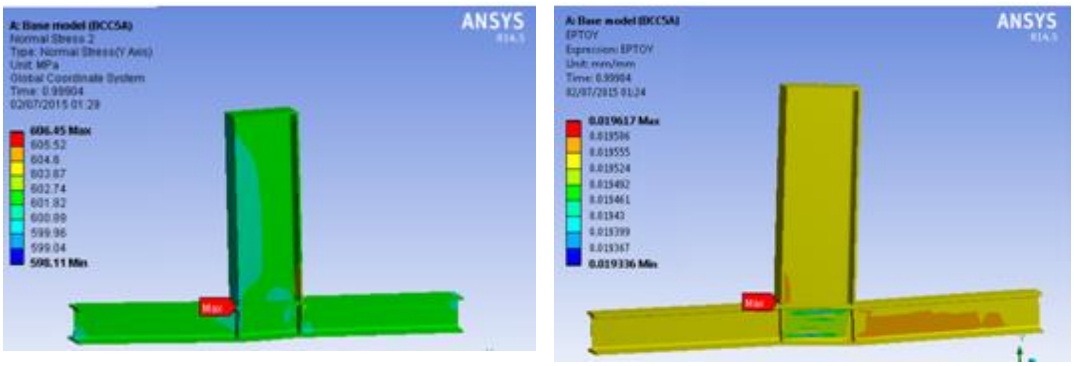

(b) (c)

Figure 4.21: (a) Specimen location failure (b) FE maximum normal stress location (c) FE maximum total strain location for BCC5A base model

4.5 Panel zone under shear

The panel zone is described to be an element mainly subjected to shear stresses and therefore its failure mode is governed by shear yielding. In steel connection the stiffness and resistance due to load are developed through the transfer of bending moment (in shear) between beam and column connection. The characteristics of the joint behaviour are therefore related to the column, beam and connection properties.

As part of the connection the panel zone plays an important role in terms of strength, stiffness and ductility, for the overall behaviour of the frame structure.

A moment will developed due to applied displacement load and this moment produces a shear stress distribution in the panel zone where the higher stresses concentrate at the middle of the panel zone and reduce reasonably towards the corners. A simplified methodology for the shear stress distribution is to assume a constant shear stress throughout the panel zone, and the bending moment (*Mb*) (which is produced by the applied horizontal displacement force times distance between the force applied to the centre of column web) is transmitted into the joint through a couple of forces concentrated at the centroid of the flanges of the beams, although axial stresses and bending stresses are also present, the principal stress regime that develops in the panel zone is due to the shear imposed by the force pair (*Vb1&Vb2*) as shown in Figure 4.22. A simple calculation for joint stiffness related work has been done in MathCAD in Sec.C.6 Appendix C.

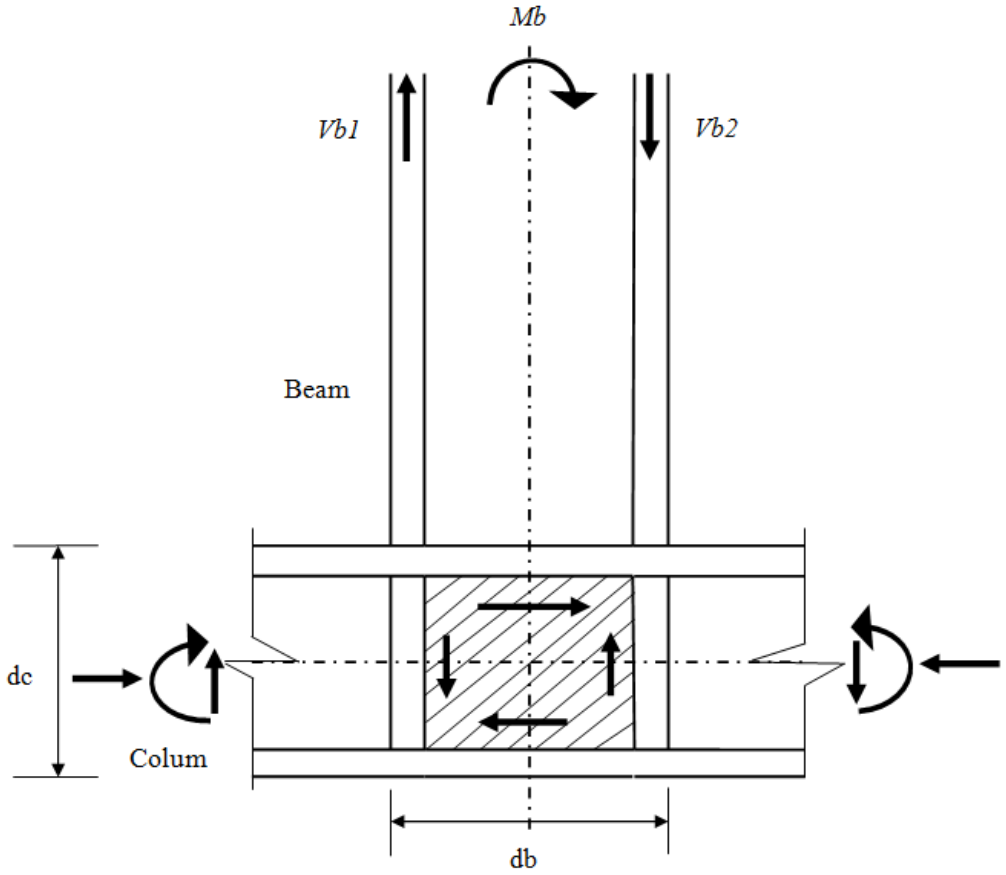

Figure 4.22: Shearing force in the beam-column connection (panel zone)

4.6 Discussion

Displacement loading was applied to the FE base model to get a force reaction as output in the same place where the displacement was applied as shown in Figure 4.10. There was a difference between the measured and calculated force-displacement curve as shown in Figure 4.11, the difference is probably due to the boundary conditions.

By assignment doubler plates in the panel zone, increasing panel zone rigidity reduces deformations of this element and develops it's performance level. It is useful to include doubler plates in the panel zone. The goal of including doubler plates is to

increase the rotational stiffness of the connection, decreasing the concentrated stress value and overall controlling of the stress distribution.

It is very important to investigate the first point of failure when analysing the numerical model, in order to record the right location for starting crack when simulating with test specimen.

According to the simple calculation using MathCAD programme as shown in Sec. C.6 Appendix C, it was found that the joint stiffness in actual test specimen is stiffer than FE base model joint, it means that the experiment has more flexibility in the support than FE base model.

The FE results and the experimental results are compared to examine the validity and the predictability of the proposed model (base model). After some calibration, the FE results have satisfactory agreement with the experimental work at different stages of loading.

A low cycle fatigue displacement was applied to the FE base model and validated against physical tests. The test results shows that the cyclic behaviour of the specimens BCC5 are characterised by a great regularity and stability of the hysteresis loops up to failure in the very last cycle as shown in Figures 4.17- 4.20, without warning signs, owing to a crack either at the weld toes or in the base material and with no deterioration of stiffness and strength properties.

The specimens have collapsed with a sudden and sharp reduction of strength, due to fracture initiated in the beam flange and propagated also in the web. During the tests, significant distortion of the joint panel zone has been observed, while there was no remarkable plastic deformation in the beam, as reported by Mele *et al*. [2003].

Panel zone rigidity has an important effect on other elements of structure like a beam, and its performance level is more critical than other elements.

The effect of panel zone strength was not considered explicitly in the experimental program, finite element simulations were conducted to provide information on possible effects associated with panel zone yielding.

Shear yielding in the column panel zone is an efficient energy dissipation mechanism for moment resistance frames (MRFs), while also cautioning that excessive panel zone deformation can cause kinks in the column flanges, and consequently generate large strain demands in the region of the beam flange welds. The high strains imposed by these kinks can lead to premature fracture of the beam flange welds. Nonetheless, the notion of beneficial panel zone yielding led to a relaxed panel zone strength requirement in the code provisions prior to the Northridge Earthquake, to permit substantial inelastic deformation in the panel zone and to provide savings by reducing the need for column web doubler plates.

The location of fracture inferred from the simulation results did not necessarily agree with the observed fracture behaviour for all BCC5 specimens. Figure 4.23 and Figures D4-D6 Appendix D, FE analysis contours show the highest strain location in the middle of the left beam flange due to imposed displacement applied at the same beam flange where the highest strain occurred. Figure A.6 Appendix A for BCC5 specimen photos shows that the fracture occurred at the edge of the left beam flange, and this might be due to simulation analysis:

- The difference in material properties between the weld, HAZ and plate was not taken into account.
- The possible presence of weld defects were not accounted for.
- The local thickening in the vicinity of welds was not included in the analysis.

- The plastic strain and stress may not provide sufficient information to predict fracture behaviour, for instance the direction relative to the weld toe is probably important.
- The initiation, growth, and propagation of fracture was not explicitly modelled.
- In the analysis, the stress concentration in the middle of the flange greater than that at the edge. However the weld shape and some undercut around the edge of the flange may mean that in practice the stress concentration is greater at the edge more than the stress at the edge of the flange.

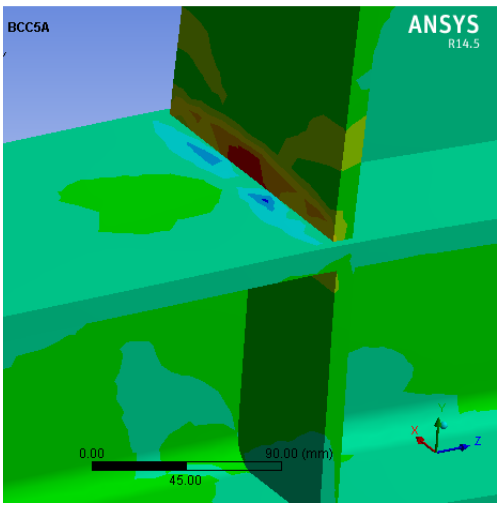

(a) left beam flange at 0.25s

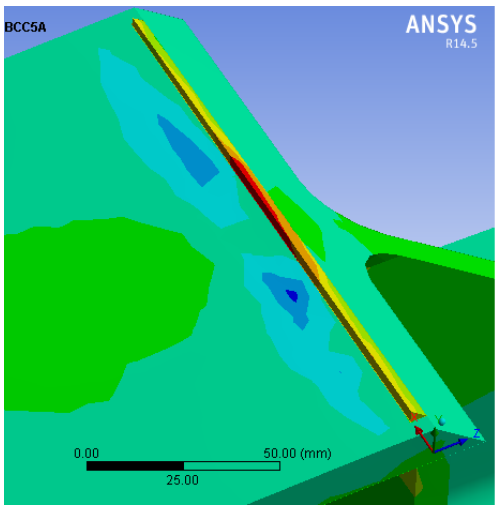

(b) section at left beam flange at 0.25s

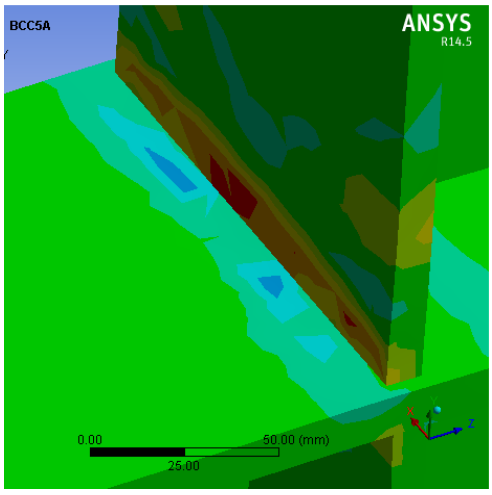

(c) left beam flange at 0.5s

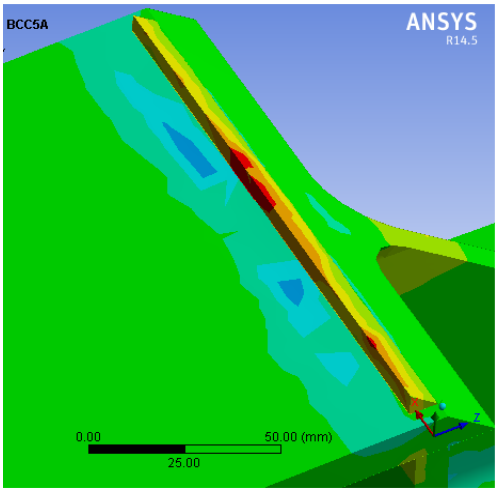

(d) section at left beam flange at 0.5s

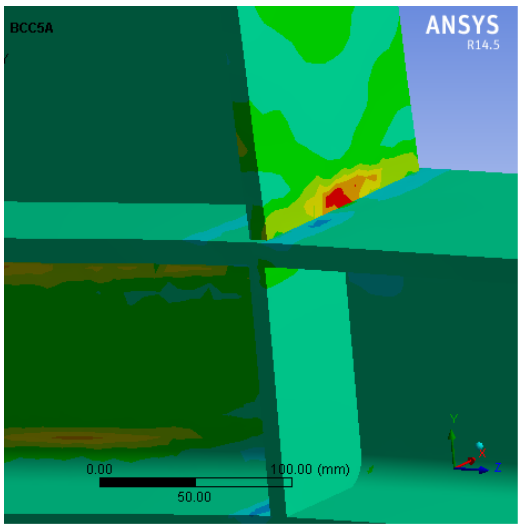

(e) right beam flange at 0.75s

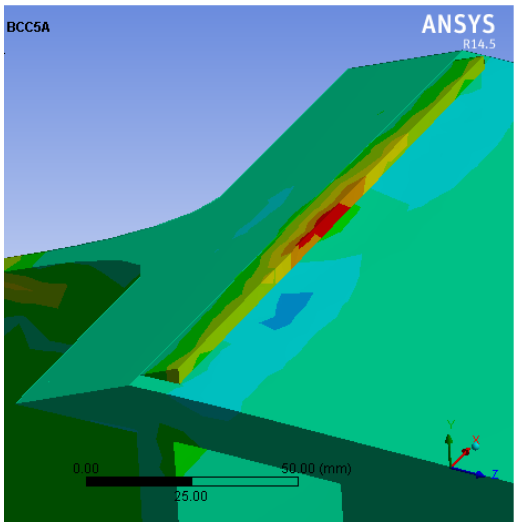

(f) section at right beam flange at 0.75s

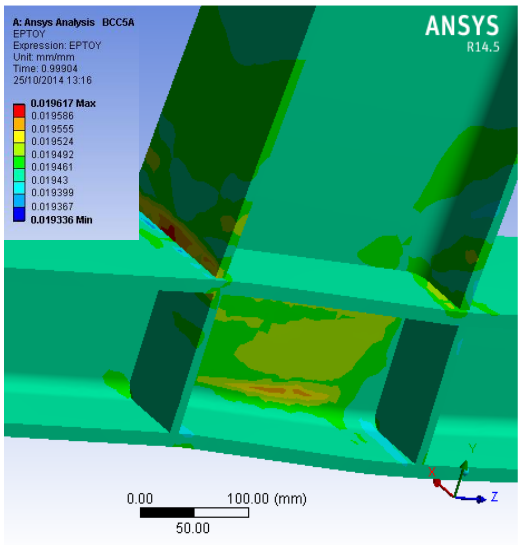

(g) left beam flange at 0.99904 s

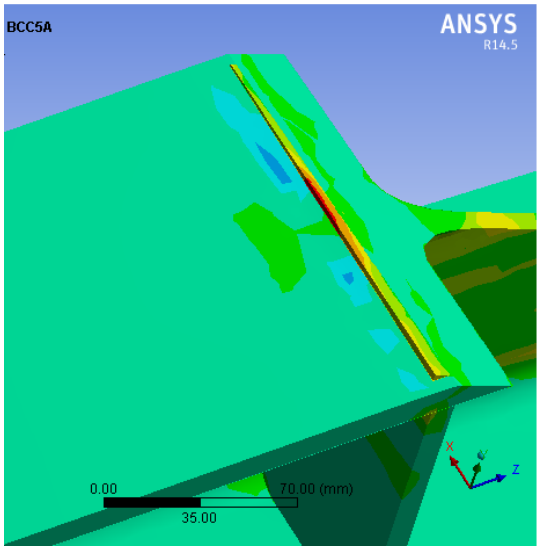

(h) section at left beam flange at 0.99904s

Figure 4.23: (a) Left beam flange at 0.25second, (b) section at left beam flange at 0.25second, (c) left beam flange at 0.5 second, (d) section at left beam flange at 0.5 second, (e) right beam flange at 0.75 second, (f) section at right beam flange at 0.75 second, (g) left beam flange at 0.99904 second and (h) section at left beam flange at 0.99904 second for BCC5A

4.6.1 Ratcheting

Even though the displacements applied in the experiments were symmetrical with a zero mean the strains in the (vertical) beam flanges were found to ratchet upwards in the finite element analysis (for example see Figure 4.25). For an applied moment the compressive and tension flange forces will be equal and opposite but at large strain this is achieved at a lower absolute value of compressive than tensile strain.

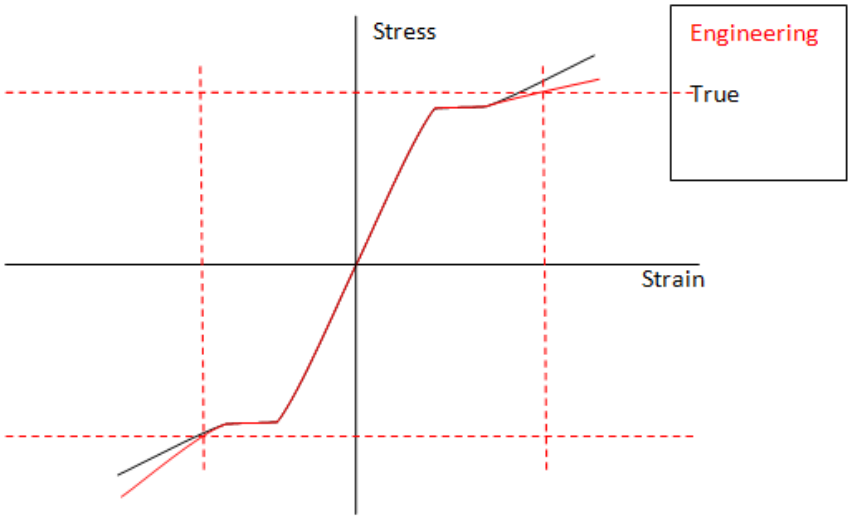

Figure 4.24: Difference between true and engineering stress-strain curve [Barltrop, 2009-2014, per.comm.]

The true stress strain curve is assumed anti-symmetric. However the engineering stress strain curve is not anti-symmetric and results in a smaller absolute strain for the same absolute engineering stress in the compression than tension plastic regime. So on large strain cycling equal and opposite tension and compression flange forces there will be a ratcheting effect to positive tensile strains in both flanges, See Figure 4.24, [Barltrop, 2009-2014, per.comm.].

In this work, plastic strain vs. number of substeps graph was used to calculate ratcheting for each cycle by using Equation 3.17 Sec.3.4.

$$\varepsilon r = (\varepsilon^{p}_{p} - \varepsilon^{p}_{v})/2 \quad 3.17$$

where: ε^{p}_{p} and ε^{p}_{v} present the cyclic true plastic strain peak and valley for the cyclic stress peak and valley, respectively.

Figure 4.25 shows plastic strain vs. number of substeps for BCC5A FE ANSYS. Figures B.4 Appendix B show plastic strain vs. number of substeps for other BCC5 FE ANSYS graphs.

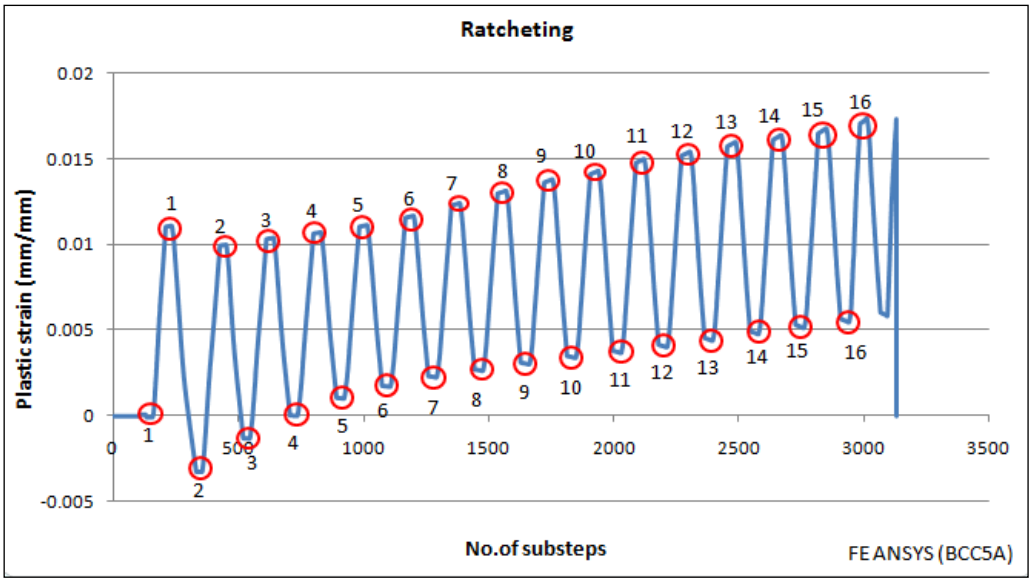

Figure 4.25: Plastic strain vs. no. of substeps for BCC5A FE ANSYS

Table 4.6 shows ratcheting results for each cycles and total ratcheting for each model for all BCC5 FE ANSYS models.

Table 4.6 shows that the BCC5D model has 23 life cycles with total ratcheting (εr) 0.074, and BCC5B model has 5 life cycles with total ratcheting (εr) 0.04266. Therefore, the results indicate that there is a linear relationship between ratcheting strain and number of cycle.

Table 4.6: Ratcheting results for each cycle and total ratcheting for each model for all BCC5 FE ANSYS models

No.of cycles	BCC5A	BCC5B	BCC5C	BCC5D
1	0.00541	0.00846	0.00002	0.00385
2	0.00635	0.00915	0.00001	0.00475
3	0.005535	0.0082	0.0000102	0.00385
4	0.005045	0.0082	0.001445	0.00345
5	0.00471	0.00865	0.0022	0.00325
6	0.00475		0.00175	0.0031
7	0.0048		0.00245	0.003
8	0.0051		0.0026	0.003
9	0.0051		0.00225	0.00305
10	0.0053		0.00285	0.003
11	0.0053		0.0034	0.00305
12	0.00555		0.00335	0.0031
13	0.00555		0.00429	0.003
14	0.00555		0.00495	0.0032
15	0.00555		0.005	0.00325
16	0.00565		0.0061	0.0034
17			0.00697	0.00335
18			0.007215	0.0033
19				0.00325
20				0.00345
21				0.00195
22				0.002
23				0.0034
Total (εr)=	0.08525	0.04266	0.0568602	0.074

4.7 Summary

The finite element analysis for welded T- steel connection was investigated under the effect of low cycle fatigue including; the finite element results were compared with experimental data. The plastic behavior was well represented by the finite element analysis but the experimental elastic behavior was more flexible than the finite element analysis, probably as a result of support flexibility. However the plastic behaviour was most important for this work so the elastic stiffness was simply reduced in order to match the experimental data.

The following chapter will show the prediction of cracking using fracture mechanics including: failure assessment diagram (FAD), fatigue damage index (FDI), crack growth calculations and strain life formulas.

CHAPTER 5
PREDICTION OF CRACKING

5.1 Introduction

All structures and mechanical components that are cyclically loaded can fail by fatigue. For steel structures, data from constant amplitude loading fatigue testing is usually used, with Miner's rule to account for variable amplitude loading, to make a simple and quick estimate of the likely fatigue performance or durability.

In many structural failures, a fatigue crack growth process occurs until the crack reach a critical size for final fracture. Cracks may grow slowly over the service life from various crack growth mechanisms such as fatigue and creep. Each of these cracking mechanisms has certain characteristic features that are used in failure analysis to determine the cause of cracking or crack growth. The majority of final structural failures are brittle fractures and these almost invariably initiate at defects, notches, or discontinuities as reported by Hoeppner [1981].

Brittle fracture is the fast (almost instantaneous) growth of a crack or cracks in the body. Metals which are usually ductile can behave in a brittle manner, leading to fast crack propagation, when cyclic loading has been applied and fatigue has resulted in small cracks that, through a combination of crack size and applied load, become unstable. It is possible in some cases to have limited plasticity near the crack tip, and such failures are referred to as quasi-brittle failures. Brittle materials show very limited plasticity at the crack tip.

The strength in the joint decreases with cyclic load and progressively the joint becomes weak. The stiffness of the structure decreases as the cracks grow, but the change in stiffness may not be noticeable until the structure is close to failing.

Outline of this chapter; various methods are applied to determine their usefulness in the prediction of the VLCF reported in Mele's [2003] experimental work.

Different methods have been investigated in this chapter of looking at the results. Sections are included in this chapter as follows:

Section 5.2 applies fracture mechanics, particularly the failure assessment diagram (FAD), to investigate the applicability of this method to the assessment. Whereas much conventional fracture assessment is done using elastic with the FAD that methodology is not appropriate to the very large strains associated with this low cycle fatigue problem. However non-linear structural analysis is used and the stress intensity values are calculated on the basis of the non-linear stress, strain*E and the geometric mean of stress and strain*E, and fatigue damage index (FDI).
Section 5.3 applies low cycle fatigue methods (Coffin Manson and modifications of this basic methodology).
Section 5.4 applies fracture mechanics crack growth calculations based on stress, strain*E, and the geometric mean of stress and strain*E
Section 5.5 simple comparison of elasto-plastic stress and strain in comparison with Ultimate tensile strength (UTS), the related strain and elongation at failure in simple test specimens.
Section 5.6 is the strain rate estimation
Section 5.7 is the conclusion to this Chapter.

5.2 Fracture mechanics

The fracture mechanics field of interest is the analysis of the mechanisms of the crack propagation and instability in materials. Usually, two categories are identified: the linear-elastic fracture mechanics (LEFM) and the elastic-plastic fracture mechanics (EPFM). The LEFM theory, which is governed by brittle fracture, is reasonably well established, and the stress intensity factor (SIF or *K*) approach is the

most widely employed. EPFM is applied when ductility affects the crack behaviour and uses approaches such as the crack-tip opening displacement (CTOD), and the failure assessment diagram (FAD). The Mele *et al.* [2003] experiments demonstrated extensive plasticity so EPFM, rather than LEFM methods are appropriate for their analysis.

5.2.1 Failure assessment diagram (FAD)

To determine if a crack may cause a structural failure, computing the FAD point is necessary to evaluate an existing crack found during inspection, or to evaluate the end-of-life critical crack size for a fatigue crack growth analysis. Using ANSYS is needed for the calculation of the reference stress and stress intensity for the specific crack location and the specific structural component geometry. The failure assessment diagram is explained in Sec.3.3.2.1.

5.2.1.1 Failure assessment diagram (FAD) based on cumulative stress increments

The application of the FAD will be based on cumulative stress (σ_T) which is recommended by BS7910 [2005], and last half cycle stress range which is recommended by DNV-RP-F108[2006].

In order to establish failure assessment diagram (FAD) curve the following equation is used:

$$K_r = \left(1 - 0.14L_r^2\right) \cdot \left[0.3 + 0.7\, exp\left(-0.65L_r^6\right)\right]$$

where:

Lr is the load ratio, which is the ratio between the reference stress and the material yield strength, it is plot in x-axis.

Kr is the toughness ratio, which is the ratio of the stress intensity factor, it is plot in y-axis.

Figure 5.1 shows normal stress vs. no. of substeps for BCC5A model, it is an analysis output evaluated at left beam flange in critical point in y- direction. It is used to calculate stress ranges. The other related figures for BCC5 models are shown in Sec.B.5 Appendix B.

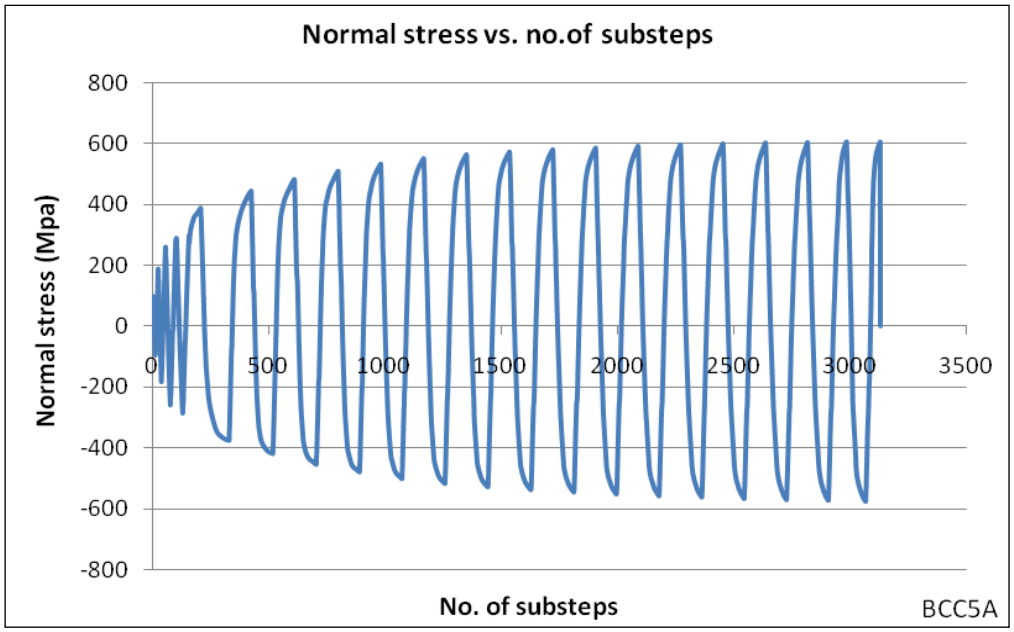

Figure 5.1: Normal stress vs. no. of cycles for BCC5A model analysis

To calculate *Lr* and *Kr* for BCC5A model, the following procedure explained using cumulative stress (σ_T):

$Lr_{max} = \sigma_u/\sigma_y = 404.6/274.8 = 1.5$

$Lr = \sigma_{max} / \sigma_y = 16321.07 /274.8 = 59$

where:

σ_y is yeild stress for flange (experimental test)= 274.8MPa

$Kr = Kf / Kc,$ 5.1

where:

Kf is stress intensity factor = $\sigma_T \sqrt{\pi a_\circ}$

$a_\circ$ is initial crack depth take it 0.2mm [BS 7608, 2014]

Kc: fracture toughness = $\sqrt{\delta c E \sigma y}$

$\delta c = G/\sigma y$, take δc = (range is 0.1 to 1mm) [DNV-RP-F108, 2006]

Kc(same for all specimens) = $\sqrt{(0.1 * 200000 * 274.8)}$ to $\sqrt{(1 * 200000 * 274.8)}$

= 2344MPa $mm^{½}$ to 7413MPa $mm^{½}$

$Kf = \sigma_T \sqrt{\pi a_\circ}$ = 16321.07 $\sqrt{(3.14 * 0.2)}$= 12893 MPa $mm^{½}$

Kr = *Kf* / *Kc* = 12893/2344 = 5.4

So the point (*Lr*,*Kr*,) is (59,5.4)

Sec.C.7 shows *Lr* and *Kr* calculations for BCC5B, BCC5C AND BCC5D models respectively.

Table 5.1 shows (*Lr*, *Kr*) points for all BCC5 models by using maximum stress, cumulative stress (σ_T) and last half cycle stress range.

Table 5.1: (*Lr*, *Kr*) results using maximum stress, cumulative stress (σ_T) and last half cycle stress range for CTOD = 0.1mm (Kr values would be 0.31 times these values for CTOD = 1mm)

Case No.	Maximum stress (σ_{max}) MPa	Max stress (Lr,Kr)	Cumulative stress ranges (σ_T) MPa	Cumulative stress ranges (Lr,Kr)	Last half cycle stress range (σ_L) MPa	Last half cycle stress range (Lr, Kr)
BCC5A	606.45	(2.2, 0.19)	16321.07	(59, 5.4)	1158.49	(4.2, 0.37)
BCC5B	611.8	(2.2, 0.2)	4646.31	(17, 1.5)	1129.12	(4.1, 0.38)
BCC5C	553.6	(2.0, 0.18)	15038.51	(55, 5.0)	1154.37	(4.2, 0.39)
BCC5D	294.05	(1.07, 0.09)	22606.32	(82, 7.0)	1123.52	(4.1, 0.37)

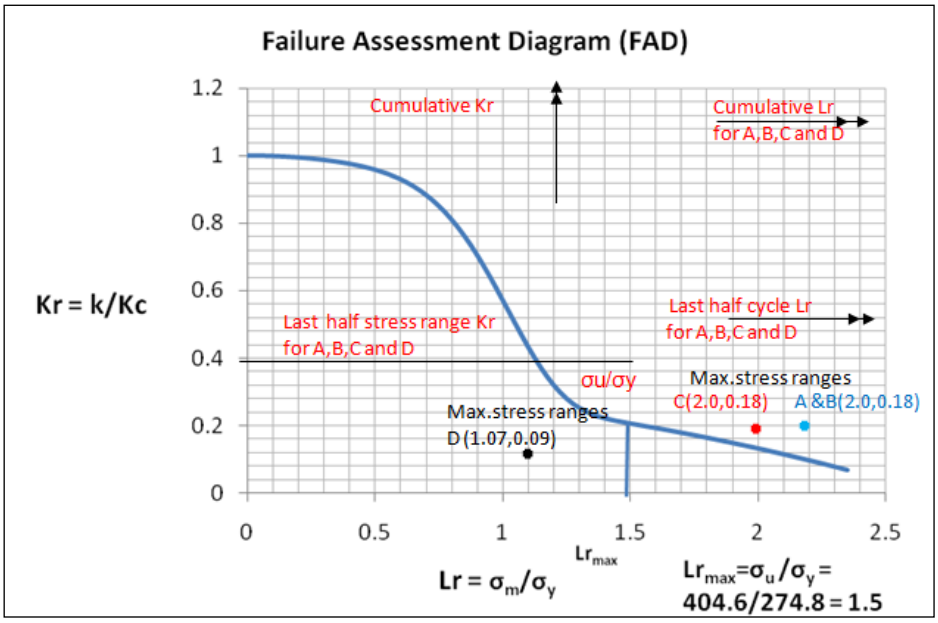

Figure 5.2: Results plotted on BS7910 Level 2a FAD for CTOD = 0.1

Discussion

These results suggest that, if a FAD is to be used to indicate failure, then both *Lr* and *Kr* should be based on the maximum stress. The cumulative value gives *Lr* and *Kr* that are extremely large. The last stress range could be consistent with the FAD if the CTOD of the test specimen was about 1 rather than 0.1 (DNV-RP-F108 [2006], recommended that CTOD should be between 0.1mm to 1mm).

Although a value of 1 is quite high it is possible that it might have been achieved as a result of the heating effect of the large stress ranges.

Note that σu has been exceeded in three numerical models (BCC5A, BCC5B and BCC5C) and it is clear in Figure 5.2.

σu is an engineering stress (based on the forces and the initial dimensions). The results calculated by the FE software are true stresses (based on the forces and the reduced thicknesses that result from large tensile strains). Therefore the calculated

(true) stresses can exceed the engineering value of σu. Cyclic loading can also shift the stress strain curve and increase or decrease the true σu.

This is possible as a result of the applied displacement rather than applied force in the experiments. The dynamic response in a real earthquake could be somewhere between that from an applied displacement and an applied force, so it would not be sensible to design for strains larger than those recommended in BS7910 for ordinary loading without studying this in more detail.

Note that no allowance for increase in crack size caused by static load stable crack growth or fatigue has been taken into account. These effects would increase the *Kr* value. Also, no increase in *Kc* as a result of stable crack growth has been estimated, this would decrease the *Kr* value.
This calculation should be performed in addition to the fatigue calculations (Coffin Manson or crack growth) to ensure that the structure does not fail by fast fracture before the number of cycles predicted by the fatigue analysis is achieved.
If sufficient information was available about the J-R performance of the steel then the fatigue crack growth, table crack growth and FAD calculations could be integrated.

5.2.1.2 Failure assessment diagram (FAD) using strain increments based on stress modified based on strain*E

The application of the FAD will be based on stress modified on strain*E using cumulative (strain*E) ranges (reservoir method) which is recommended by BS7910 [2013], last half cycle (strain*E) range which is recommended by DNV-RP-F108[2006], overall (strain*E) ranges and up & down (strain*E) ranges.

Table 5.2 shows modified stress on (strain*E) using reservoir method, last half cycle (strain*E) range, overall (strain*E) ranges and up & down (strain*E) ranges methods to calculate different values of stress ranges as shown in Figure 5.3.

Table 5.3: shows calculations of stress intensity factor K_f using Table 5.2 to get (*Lr*, *Kr*) as shown in Table 5.4.

Figure 5.2 shows the failure assessment diagram curve, and Table 5.4 shows FAD points (*Lr*, *Kr)* for all BCC5 models.

Table 5.2: Shows (ε*E) ranges for four options applied on FAD to get (*Lr*,*Kr*)

Case No.	ε*E ranges (Maximum) (MPa)	reservoir method ε*E ranges (MPa)	last half cycle (ε*E range) (MPa)	over all (ε*E ranges) (MPa)	cumulative up and down (ε*E ranges) (MPa)
BCC5A	3840	46162	3100	2885.15	92324
BCC5B	3706.2	17047.5	3435.8	3409.5	34095
BCC5C	3460	34636	3706	1924.2222	69272
BCC5D	3240	49618.38	2246	2157.32087	99236.76

Table 5.3: Shows calculations of stress intensity factor K_f using Table 5.2

Case No.	ε*E ranges (Maximum) (MPa)	reservoir method $Kf = \sigma_T \sqrt{\pi a_o}$ (MPa mm^{½})	last half cycle $Kf = \sigma_T \sqrt{\pi a_o}$ (MPa mm^{½})	over all $Kf = \sigma_T \sqrt{\pi a_o}$ (MPa mm^{½})	cumulative up and down $Kf = \sigma_T \sqrt{\pi a_o}$ (MPa mm^{½})
BCC5A	3840	36560	2455	2285	73120
BCC5B	3706.2	13501	2721	2700	27003
BCC5C	3460	27431	2935	1523	54863
BCC5D	3240	39297	2835	1708	78595

Table 5.4: Shows (*Lr, Kr*) results for each BCC5 model using four methods (ε*E ranges) reservoir count method, last half cycle range, over all ranges and up and down ranges)

Case No.	Lr.Kr (reservoir count method) (ε*E ranges)	Lr.Kr (last half cycle) (ε*E range)	Lr.Kr (over all) (ε*E ranges)	Lr.Kr cumulative (up and down) (ε*E ranges)
BCC5A	(13,15)	(13,1.0)	(13,0.97)	(13,31)
BCC5B	(13,5.75)	(13,1.16)	(13,1.15)	(13,11.5)
BCC5C	(12,11.7)	(12,1.25)	(12,0.65)	(12,23)
BCC5D	(11,16)	(11,0.75)	(11,0.72)	(11,33)

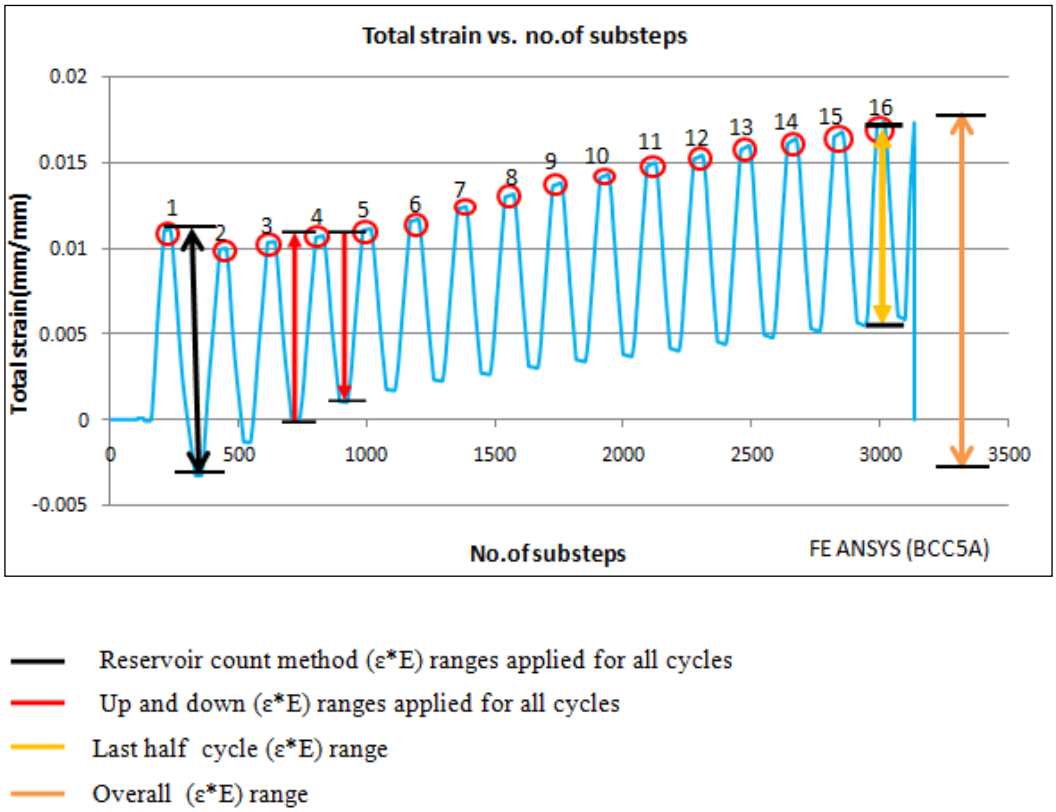

Figure 5.3: Shows four options applied to calculate (*Lr, Kr*) using 16 cycles for BCC5A models and applied for all BCC5 models

Table 5.4 shows calculation of *Kr* and *Lr* for each case using four methods (ε*E ranges) reservoir count method, last half cycle range, over all ranges and up and down ranges)

Figure 5.2 shows the axis of the FAD chart use the non-dimensional ratios *Lr* (plastic collapse ratio) on the x-axis, and *Kr* (brittle fracture ratio) on the y-axis. The evaluation points (for the four methods) illustrated in Table 5.4 show that all points lie above the FAD curve which indicate unacceptable cracks that indicate a predicted structural failure, which can be useful to determine predicted critical crack sizes at failure.

The crack length was growing fast, so it was anticipated that the crack length would be the larger crack dimension, and is likely to be the worst case.
Since the beam flange crack evaluation points still lie above the FAD curve, therefore the beam flange crack is at risk for sudden rupture.

Discussion

This work was based on an estimate of CTOD, however the results will not be too sensitive to the precise value so the general conclusions are probably reasonable.
The values of Lr and Kr lie considerably outside the FAD curve, it is therefore clear that an artificial stress corresponding to the elasto-plastic strain*E is not relevant for use in the FAD.

Overall from this work it would appear that using the maximum value of stress to calculate Lr and Kr provides the best fit with the experiments.

Conclusion

The following conclusions can be drawn:

- Applying a BS7910, 2014 FAD to the maximum stress for the Kr (Ka applied / K critical) calculation appears to work well. In the experiments large values of Lr (Applied stress / Yield stress) were obtained but these are probably a result of the displacement controlled experiment, so in the absence of further information Lr should be limited in the way specified by BS7910.
- An initial defect size is required for the calculation. 0.2mm was used for this work. Depending on the fatigue calculations it is possible to update this cycle by cycle. In that case the maximum Kr could occur later in a time history with a larger crack size da a smaller stress than the maximum stress.
- Table 5.4 shows (*Lr*, *Kr*) results for each BCC5 model using four methods (ε*E ranges) reservoir count method, last half cycle range, over all ranges and up and down ranges), all the points were lying outside FAD curve. By using the last cycle highest stress with the FAD and if the crack had grown from 0.2mm to a few mm in length during the cyclic loading then the FAD might represent the final failure, although it would be difficult to use it in a predictive manner. So the low cycle fatigue method seems to be a much better option. It probably also better represents the structural behaviour.
- In this work, the computed reference stress is used to obtain the plastic collapse ratio (*Lr*), and the analysis is used to obtain the stress intensity to obtain the brittle fracture ratio (*Kr*). These ratios give the location of the evaluation point on the FAD to indicate structural failure or safety.

  Computing the FAD point is necessary to evaluate an existing crack found during inspection, or to evaluate the end-of-life critical crack size for a fatigue crack growth analysis. Engineers benefit from using ANSYS which computes CTOD needed for the calculation of the reference stress and stress intensity for the specific crack location and the specific structural component geometry.

- It would be expected that the CTOD to be in the range 0.1 to 1mm. Even still the DET NORSKE VERITAS (DNV) [2012] pipeline assessment method is very pessimistic in comparison with the option 2 curve.
- Failure assessment diagram (FAD) curve to classify situation of structure safe or unsafe. The evaluation points inside the FAD curve indicate acceptable cracks, and the evaluation points above the FAD curve are unacceptable cracks that indicate a predicted structural failure. An evaluation point on the FAD curve is a critical crack on the verge of failure, which can be useful to determine predicted critical crack sizes.

5.2.2 Fatigue damage index (FDI) (Coffin-Manson + Reservoir count)

FDI is a method can be used to predict the damage to steel frame structures subjected to earthquakes and helps the engineer to better understand the performance of their design under seismic loads.

The application of the *FDI* will be based on plastic strain ranges and approximately for total strain ranges to calculate *FDI*. In this work total strain range used to calculate *FDI* by using cycle counting by the reservoir method as explained in Sec.3.3.3, and it is shown in Figure 3.28 [BS7608, 2014] , it is easy to apply by hand and suitable when dealing with short stress histories.

FDI calculated using total strain vs. number of substeps graphs. Figures 5.3 & B.3 Appendix B are shown total strain vs. number of substeps for BCC5A and BCC5B, BCC5C and BCC5D respectively. Calculating fatigue damage index using MathCAD is shown in Sec.C.4 using Coffin-Manson relation Appendix C. Calculation details are shown in Table C.3 Appendix C, and the final results are illustrated in Table 5.5. It is not as straight forward to calculate damage from the Coffin-Manson type of equations as from an ordinary S-N curve as an iteration is required (I used the MathCAD root function).

Calculating fatigue damage index using MathCAD (including n') for BCC5A as follows:

$Ncyc := 16$ ORIGIN ≡ 1

$ie := 1..Ncyc$

$\sigma f := 724$

$\varepsilon f := \frac{0.218}{Fac}$

$b := -.150$

$c := -.699$

$E := 200 \times 10^3$ $E = 2 \times 10^5$

$\varepsilon fe_{ie} :=$

0.014
0.014
0.014
0.014
0.0146
0.0146
0.015
0.015
0.015
0.01508
0.01508
0.01508
0.01508
0.01508
0.01508
0.0157

$\varepsilon fe_{ie} =$

0.014
0.014
0.014
0.014
0.0146
0.0146
0.015
0.015
0.015
0.0151
0.0151
0.0151
0.0151
0.0151
0.0151
0.0157

$Nf := 5$

$$Nfe_{ie} := root\left[1 - \left[\frac{\sigma f}{E}\cdot(2\cdot Nf)^b + \varepsilon f\cdot(2\cdot Nf)^c\right] - \frac{\varepsilon fe_{ie}}{2}, Nf\right]$$

$Nfe =$

	1
1	39.703
2	39.703
3	39.703
4	39.703
5	36.807
6	36.807
7	35.065
8	35.065
9	35.065
10	34.733
11	34.733
12	34.733
13	34.733
14	34.733
15	34.733
16	32.328

$\varepsilon fe \cdot E =$

	1
1	$2.8\cdot10^3$
2	$2.8\cdot10^3$
3	$2.8\cdot10^3$
4	$2.8\cdot10^3$
5	$2.92\cdot10^3$
6	$2.92\cdot10^3$
7	$3\cdot10^3$
8	$3\cdot10^3$
9	$3\cdot10^3$
10	$3.016\cdot10^3$
11	$3.016\cdot10^3$
12	$3.016\cdot10^3$
13	$3.016\cdot10^3$
14	$3.016\cdot10^3$
15	$3.016\cdot10^3$
16	$3.14\cdot10^3$

$$D := \sum_{ie} \frac{1}{Nfe_{ie}} \qquad D = 0.44$$

Predicted cycles to failure

$$\frac{Ncyc}{D} = 36.01$$

$$Fac \equiv 2$$

Calculating fatigue damage index using MathCAD (excluding n') for BCC5A as follows:

$$Ncyc := 16 \qquad ORIGIN \equiv 1$$

$$ie := 1..Ncyc$$

$$\sigma f := 724$$

$$\varepsilon f := \frac{0.218}{Fac}$$

$$b := -.066$$

$$c := -.492$$

$$E := 200 \times 10^3 \qquad E = 2 \times 10^5$$

$\varepsilon fe_{ie} :=$

0.014
0.014
0.014
0.014
0.0146
0.0146
0.015
0.015
0.015
0.01508
0.01508
0.01508
0.01508
0.01508
0.01508
0.0157

$\varepsilon fe_{ie} =$

0.014
0.014
0.014
0.014
0.0146
0.0146
0.015
0.015
0.015
0.0151
0.0151
0.0151
0.0151
0.0151
0.0151
0.0157

$$Nf := 5$$

$$Nfe_{ie} := root\left[1 \cdot \left[\frac{\sigma f}{E} \cdot (2 \cdot Nf)^b + \varepsilon f \cdot (2 \cdot Nf)^c\right] - \frac{\varepsilon fe_{ie}}{2}, Nf\right]$$

$$D := \sum_{ie} \frac{1}{Nfe_{ie}} \qquad D = 0.061$$

Predicted cycles to failure

$$\frac{Ncyc}{D} = 262.76$$

$Fac \equiv 2$

Nfe =

	1
1	307.049
2	307.049
3	307.049
4	307.049
5	272.376
6	272.376
7	252.361
8	252.361
9	252.361
10	248.618
11	248.618
12	248.618
13	248.618
14	248.618
15	248.618
16	222.185

εfe·E =

	1
1	$2.8 \cdot 10^3$
2	$2.8 \cdot 10^3$
3	$2.8 \cdot 10^3$
4	$2.8 \cdot 10^3$
5	$2.92 \cdot 10^3$
6	$2.92 \cdot 10^3$
7	$3 \cdot 10^3$
8	$3 \cdot 10^3$
9	$3 \cdot 10^3$
10	$3.016 \cdot 10^3$
11	$3.016 \cdot 10^3$
12	$3.016 \cdot 10^3$
13	$3.016 \cdot 10^3$
14	$3.016 \cdot 10^3$
15	$3.016 \cdot 10^3$
16	$3.14 \cdot 10^3$

Table 5.5: Final results of fatigue damage index (*FDI*) for BCC5 FE base models, and predicted cycles to failure excluding and including cyclic strain hardening (n`) and considering ($\varepsilon' f$ /2) the difference between welded and un-welded

Case No.	No. of cycle to failure (experimental work)	Fatigue Damage Index. *FDI* (Accumulated Damage) $=\sum \frac{1}{Nfe(ie)}$		Predicted cycles to failure =Ncyc/D	
		Excluding strain hardening exponent	Including strain hardening exponent	Excluding strain hardening exponent	Including strain hardening exponent
BCC5A	16	0.061	0.444	262	36
BCC5B	5	0.044	0.237	115	21
BCC5C	18	0.035	0.272	521	66
BCC5D	23	0.035	0.357	666	64

Tables 5.5 shows fatigue damage index (*FDI*) for BCC5A is 0.061 for excluding (n') and predicted cycles to is failure is 262, but if strain hardening will be used in the

experimental test (including n') for the same model, the model will be stiff ,less toughness then less cycle to failure as shown in Table 5.5, and the *FDI* will be 0.444 and predicted cycles to failure will be 36, (The strain hardening of material is defined as strain increases further with the increase of stress).

Therefore these results gave indication that there is an inverse relationship between *FDI* results and the predicted cycles to failure. The more damage in structure the less life cycle.
Another indication established that using cyclic strain hardening with constant amplitude displacement cause the stress to be higher, force to be bigger, structure will be stiffer and fatigue will be expected more quickly with fewer cycles to failure.

Table 5.5 is not showing the value of *FDI* is greater than or equal 1.0 to indicate a low-cycle fatigue fracture of the member as reported by Campbell *et al.* [2008], therefore modification factor has been calculated using low cycle fatigue formulas to get *FDI* is equal to 1.0 for BCC5 models, and fatigue ductility coefficient (ε'f) should be divide by the modification factor as shown in Table 4.6.

In order to obtain the observed cycles to failure in the BCC5 tests it was necessary to modify the fatigue ductility exponent ($\varepsilon' f$) by divided by a factor in order to use the low cycle fatigue formulas. The required modification is shown in Table 5.6.

Note that the version of the formula that includes (n') provides a much more constant modification.

Table 5.6 shows the final results of fatigue damage index (FDI) for BCC5 FE base models, and predicted cycles to failure excluding and including cyclic strain hardening (n`) and considering modification factor ($\varepsilon' f$ /Fac.). For excluding strain hardening (n'), the factor is about ($\varepsilon' f$ /10) but if strain hardening will be used in the tests, the factor will be about ($\varepsilon' f$ /5), and the influence of these factors is giving exact

cycles to failure by using Coffin-Manson formula which makes good agreement with the experimental tests.

Table 5.6: Final results of fatigue damage index (*FDI*) for BCC5 FE base models, and predicted cycles to failure excluding and including cyclic strain hardening (n`) and considering modification factor ($\varepsilon' f$ /Fac.) the difference between welded and un-welded

Case No.	No. of cycle to failure (experimental work)	Factor to be used by divide (ε'f) / Fac. in strain life formula		Fatigue Damage Index. *FDI* (Accumulated Damage) $=\sum \frac{1}{Nfe(ie)}$		Predicted cycles to failure =Ncyc/D	
		Factor Exc. (n')	Factor Inc. (n')	Excluding strain hardening exponent	Including strain hardening exponent	Excluding strain hardening exponent	Including strain hardening exponent
BCC5A	16	8.8	3.7	1.005	1.003	15.922	15.955
BCC5B	5	10.2	5.9	1.012	1.015	4.938	4.923
BCC5C	18	12	5.4	1.005	1.0	17.919	18.18
BCC5D	23	12.77	4.47	1.008	1.01	22.815	22.963

Table 5.7 shows comparison of number of cycles to failure between strain life formulas and experimental work for BCC5 models considering strain hardening exponent(n') and including (ε'f/2).

Table 5.7: Compares number of cycles between strain life formulas and experimental findings considering strain hardening exponent(n') and including (ε'f/2)

Case No.	Experimental cycles to failure	Coffin and Manson no. of cycles to failure	Morrow &Smith *et al.* no. of cycles to failure	Smith -Watson - Topper (SWT) no. of cycles to failure
BCC5A	16	36	36	20
BCC5B	5	21	21	12
BCC5C	18	66	66	39
BCC5D	23	64	64	86

Table 5.8 shows comparison of number of cycles to failure between strain life formulas and experimental work for BCC5 models considering strain hardening exponent(n') and including modification factor (ε'f/Fac.).

Table 5.8: Compares number of cycles between strain life formulas and experimental findings considering strain hardening exponent(n') including modification factor (ε'f/Fac.) (see Table 5.6)

Case No.	Experimental cycles to failure	Coffin and Manson no. of cycles to failure	Morrow &Smith *et al.* no. of cycles to failure	Smith -Watson - Topper (SWT) no. of cycles to failure
BCC5A	16	16	16	14
BCC5B	5	5	5	8
BCC5C	18	18	18	21
BCC5D	23	23	23	55

5.2.2.1 Discussion

These calculations in Tables 5.5 and 5.7 are giving overestimates of cycles to failure higher than observed in the tests. If compared with the modification factor Tables 5.6 and 5.8 which indicate a remarkably good result.

However the calculated results make no particular allowance for weld defects that would decrease the life and they make no allowance for the interaction with any stable crack growth and final fracture.

5.2.2.2 Conclusion

- The fatigue damage index (FDI) calculation is based on total strain increments obtained from analysis for all BCC5 models. The calculation provides information for fatigue damage for each BCC5 model allowing to predict the life cycles of structures as shown in Table 5.5.
- Predicted cycles to failure and the fatigue damage index are affected by cyclic strain hardening exponents, the strain hardening increases stiffness and leads to brittle failure with a short fatigue life (predicted cycles to failure) as shown in Table 5.5.
- Fatigue damage index (FDI) can be used to predict the damage in steel structures and helps the engineer to better understand the performance of their design under seismic loads. Values of *FDI* greater than or equal to 1.0 indicates a low-cycle fatigue fracture of the member as reported by Campbell *et al.* [2008], therefore using strain life formulas to get FDI for BCC5 models, it should be divide (ε'f) by Factor as shown in Table 5.6.
- The fatigue damage index (FDI) gives the engineer an additional tool that can be used to better understand the performance of their design under seismic loads.

5. 3 Low cycle fatigue methods (Coffin Manson and modifications of this basic methodology)

The fatigue analysis is based on strain-life method (ε-*N*), using Coffin-Manson relationship [Coffin,1954] and [Manson, 1953], Morrow mean stress correction Morrow [1968] and Smith *et al*. [1970] to determine the strain amplitude as shown in Sec.C.1 Appendix C.

Strain amplitude calculations for BCC5A model is shown as follow using strain life formulas. Strain amplitude calculation for BCC5B, BCC5C and BCC5D are shown in Sec.C.1 Appendix C.
Strain life formulas as explained in Sec.3.1.2.2 chapter 3, are used to calculate strain amplitude according to the number of cycles, results are illustrated in Table 5.9.
Strain life formulas are including fatigue exponents as illustrated in Table C.2.
Strain life formulas are:

Coffin-Manson formulas:

$$\frac{\Delta\varepsilon}{2} = \frac{\sigma_f^{'}}{E}\left(2N_f\right)^b + \varepsilon_f^{'}\left(2N_f\right)^c$$

Morrow and Smith *et al.*:

$$\varepsilon_a = \frac{\sigma_f^{'} - \sigma_{mean}}{E}\left(2N_f\right)^b + \varepsilon_f^{'}\left(2N_f\right)^c$$

Smith-Watson-Topper (SWT):

$$\sigma_{max}\,\varepsilon_a E = \left(\sigma_f^{'}\right)^2\left(2N_f\right)^{2b} + \sigma_f^{'}\varepsilon_f^{'}E\left(2N_f\right)^{b+c}$$

Difference among these formulas is that Morrow and Smith *et al*. is including stress mean (σ_{mean}) and Smith-Watson-Topper (SWT) is including maximum stress (σ_{max}).

These formulas are calculating strain amplitude due to cyclic loading for plain steel member, but in this work, they are used to calculate strain amplitude for T-steel welded connection.

The strain amplitude of the FE base model can be determined by using either Total strain or Plastic strain [Kyungkoo and Bozidar, 2004], in the current investigation, the total strain- time history was considered. The maximum stress was obtained from normal stress-time history. All the results were taken from FE analysis for the four cases at the critical point (known area of failure) in the model.

Table 5.9 shows calculating results for strain amplitude using strain life formulas is for BCC5 FE models not considering cyclic strain hardening (n`), and is shown in Sec.C.1 Appendix C.

Calculating strain amplitude using strain life formulas for BCC5A (without using n`) as follows:

$\frac{\Delta\varepsilon}{2}$ = εa = Total Strain amplitude, which is half strain range Δε to be compared with total strain amplitude FE Analysis in critical point in Y-direction.

σ`f ,ε`f, b and c are obtained from Table C.2

Nf = 16 cycles Table C.1

b= -0.066 and *C*= -0.492

Including factor divide fatigue ductility coefficient by2 (ε'*f* /2) for difference between welded and un-welded [Almar,1985].

Solution:

$$\frac{\Delta\varepsilon}{2} = \frac{\sigma'f}{E}(2Nf)^b + \varepsilon'f(2Nf)^c$$

$$\frac{\Delta\varepsilon}{2} = \frac{\sigma'f}{E}(2Nf)^b + (\varepsilon'f/2)(2Nf)^c$$

$$\frac{\Delta\varepsilon}{2} = \frac{724}{200e3}(32)^{-0.066} + (\frac{0.218}{2}) \text{ x } (32)^{-0.492}$$

$$\frac{\Delta\varepsilon}{2} = 0.0226$$

Morrow and Smith

$$\varepsilon a = \frac{\sigma' f - \sigma mean}{E}(2Nf)^b + \varepsilon' f(2Nf)^c$$

$$\varepsilon a = \frac{\sigma' f - \sigma mean}{E}(2Nf)^b + (\varepsilon' f/2)(2Nf)^c$$

where: σ_{mean} =0

$$\varepsilon a = \frac{724-0}{200e3}(32)^{-0.066} + (\frac{0.218}{2}) \text{ x } (32)^{-0.492}$$

$$\varepsilon a = 0.0226$$

Smith-Watson-Topper (SWT)

$$\sigma max\ \varepsilon a = \sigma max\ \frac{\Delta\varepsilon}{2} = \frac{(\sigma' f)^2}{E}(2Nf)^{2b} + \sigma' f\varepsilon' f\ (2Nf)^{b+c}$$

$$\sigma max\ \varepsilon a = \sigma max\ \frac{\Delta\varepsilon}{2} = \frac{(\sigma' f)^2}{E}(2Nf)^{2b} + \sigma' f(\varepsilon' f/2)\ (2Nf)^{b+c}$$

$$\sigma max\ \varepsilon a = \frac{(724)^2}{200e3}(32)^{-0.132} + 724\ x\ (\frac{0.218}{2})(32)^{-0.558}$$

σ_{max} is taken from normal stress in Y-direction obtained from FE ANSYS

σ_{max} = 606.45MPa obtained from Table 6.1

$$\varepsilon a = \frac{(724)^2\ (32)^{-0.132} + 724\ x\ (\frac{0.218}{2}) \text{ x } 200e3\ (32)^{-0.558}}{606.45x\ 200e3}$$

$\varepsilon a = 0.0215$

Cyclic and fatigue properties of base ($\sigma`f$ ,$\varepsilon`f$, b ,c and n'), weld, and heat affected materials for ASTM A36/E60S-3 welds are illustrated in Table C.2.
Nf cycles are taken from Table C.1

b= -0.066 and C= -0.492

Including factor divide fatigue ductility coefficient by 2(ε′f/2) for difference between welded and un-welded structure [Almar,1985] as mentioned in Sec.3.1.2.2.

Table 5.9: Strain amplitude final results of BCC5 FE models using the strain life formulas considering factor (ε′f/2), excluding cyclic strain hardening exponent (n`)

Case No.	No. of cycles to failure	Maximum stress (σmax) MPa	Total strain amplitude Base model $\varepsilon a=\frac{\Delta\varepsilon}{2}$	Coffin and Manson $\varepsilon a=\frac{\Delta\varepsilon}{2}$	Morrow &Smith *et al.* $\varepsilon a=\frac{\Delta\varepsilon}{2}$	Smith -Watson - Topper (SWT) $\varepsilon a=\frac{\Delta\varepsilon}{2}$
BCC5A	16	606.45	0.0074	0.0226	0.0226	0.0215
BCC5B	5	611.8	0.0100	0.0382	0.0382	0.0388
BCC5C	18	553.6	0.0048	0.0215	0.0215	0.0222
BCC5D	23	294.05	0.0053	0.0193	0.0193	0.0370

Table 5.10 shows calculating results for strain amplitude using strain life formulas is for BCC5 FE models excluding cyclic strain hardening (n`), and considering modification factor (ε′f/Fac.).

Table 5.10: Strain amplitude final results of BCC5 FE models using the strain life formulas considering modification factor (ε′f/Fac.) (see Table 5.6), excluding cyclic strain hardening exponent (n`)

Case No.	No. of Cycles to failure	Maximum stress (σmax) MPa	Total strain amplitude Base model $\varepsilon a=\frac{\Delta\varepsilon}{2}$	Coffin and Manson $\varepsilon a=\frac{\Delta\varepsilon}{2}$	Morrow & Smith *et al.* $\varepsilon a=\frac{\Delta\varepsilon}{2}$	Smith -Watson - Topper (SWT) $\varepsilon a=\frac{\Delta\varepsilon}{2}$
BCC5A	16	606.45	0.0074	0.00738	0.00738	0.007
BCC5B	5	611.8	0.0100	0.0099	0.0099	0.01
BCC5C	18	553.6	0.0048	0.005	0.005	0.006
BCC5D	23	294.05	0.0053	0.0054	0.0054	0.010

Table 5.11 shows total strain amplitude (final results), using FE analysis to calculate strain amplitude and by inputting the observed cycles to failure into the strain-life formulas and considering factor (ε′f/2), including cyclic strain hardening exponent (n`).

Calculating strain amplitude for BCC5A using strain life formulas (using n`) as follows:

There have been attempts to relate the Coffin-Manson exponent *C* with the cyclic strain hardening exponent *n`* based on certain energy criterion. Morrow has shown that the exponents *C* and *b* can be related to *n`* by:

$C = -1/(1+5n`)$ and

$b = -n`/(1+5n`)$

Tomkins has given the above relations as:

$C = -1/(1+2n`)$ and

$b = -n`/(1+2n`)$, therefore

$b = -0.150$ and $C = -0.699$

Including factor divide Fatigue ductility coefficient by2 ($\varepsilon' f$ /2) for difference between welded and un-welded [Almar,1985].

Coffin and Manson (BCC5A)

$$\frac{\Delta\varepsilon}{2} = \frac{\sigma' f}{E}(2Nf)^b + \varepsilon' f(2Nf)^c$$

$\frac{\Delta\varepsilon}{2}$ = εa = Total Strain amplitude ,which is half strain range Δε to be compared with Total strain amplitude FE Analysis in critical point in Y-direction.

where:

σ`f ,ε`f,b and c are taken from Table C.2

Nf = 16 cycles taken from Table C.1

where:

n`= 0.215 (Table C.2)

C = -1/(1+2*n`*) and *b* = -n`/ (1+2*n`*) ,therefore

b= -0.150 and *C*= -0.699

Solution:

$$\frac{\Delta\varepsilon}{2} = \frac{\sigma' f}{E}(2Nf)^b + (\varepsilon' f/2)(2Nf)^c$$

$$\frac{\Delta\varepsilon}{2} = \frac{724}{200e3}(32)^{-0.150} + (\frac{0.218}{2}) \text{ x } (32)^{-0.699}$$

$$\frac{\Delta\varepsilon}{2} = 0.0118$$

Morrow and Smith

$$\varepsilon a = \frac{\sigma' f - \sigma mean}{E}(2Nf)^b + (\varepsilon' f/2)(2Nf)^c$$

where: $\sigma_{mean} = 0$

$$\varepsilon a = \frac{\Delta\varepsilon}{2} = \frac{724 - 0}{200e3}(32)^{-0.150} + (\frac{0.218}{2})\ \text{x}\ (32)^{-0.699}$$

$$\varepsilon a = \frac{\Delta\varepsilon}{2} = 0.0118$$

Smith-Watson-Topper (SWT)

$$\sigma max\ \varepsilon a = \sigma max\ \frac{\Delta\varepsilon}{2} = \frac{(\sigma' f)^2}{E}(2Nf)^{2b} + \sigma' f(\varepsilon' f/2)\ (2Nf)^{b+c}$$

$$\sigma max\ \varepsilon a = \frac{(724)^2}{200e3}(32)^{-0.3} + 724\,x\,(\frac{0.218}{2})(32)^{-0.849}$$

σ_{max} is taken from normal stress in Y-direction obtained from FE ANSYS

σ_{max} = 606.45 MPa taken from Table 6.1

$$\varepsilon a = \frac{(724)^2\,(32)^{-0.3} + 724\,x\,(\frac{0.218}{2})\ \text{x}\ 200e3\ (32)^{-0.849}}{606.45x\ 200e3}$$

$$\varepsilon a = 0.0088$$

Table 5.11: Strain amplitude final results of BCC5 FE models using the strain life formulas considering factor (ε′f/2), including cyclic strain hardening exponent (n`)

Case No.	No. of Cycles to failure	Maximum stress (σmax) MPa	Total strain amplitude Base model $\varepsilon a=\frac{\Delta\varepsilon}{2}$	Coffin and Manson $\varepsilon a=\frac{\Delta\varepsilon}{2}$	Morrow & Smith *et al.* $\varepsilon a=\frac{\Delta\varepsilon}{2}$	Smith -Watson - Topper (SWT) $\varepsilon a=\frac{\Delta\varepsilon}{2}$
BCC5A	16	606.45	0.0074	0.0118	0.0118	0.0088
BCC5B	5	611.8	0.0100	0.0243	0.0243	0.0253
BCC5C	18	553.6	0.0048	0.0110	0.0110	0.0225
BCC5D	23	294.05	0.0053	0.0095	0.0095	0.0132

Tables 5.12 shows total strain amplitude (final results), using FE analysis to calculate strain amplitude and by inputting the observed cycles to failure into the strain-life formulas and modification factor (ε′f/Fac.), including cyclic strain hardening exponent (n`).

Tables 5.9 and 5.11 considering (ε′f/2) for excluding (n') and if including (n') in experimental tests previously, showed less strain amplitude and overestimate number of cycles to failure when using strain life formulas in comparison with base model analysis.

Tables 5.10 and 5.12 considering (ε′f/Fac.) (see Table 5.6), for excluding (n') and if including (n') in experimental tests previously, showed close strain amplitude values and exact number of cycles to failure when using strain life formulas in comparison with base model analysis.

Table 5.12: Strain amplitude final results of BCC5 FE models using the strain life formulas considering modification factor (ε′f/Fac.) (see Table 5.6), including cyclic strain hardening exponent (n`)

Case No.	No. of Cycles to failure	Maximum stress (σmax) MPa	Total strain amplitude Base model $\varepsilon a=\frac{\Delta\varepsilon}{2}$	Coffin and Manson $\varepsilon a=\frac{\Delta\varepsilon}{2}$	Morrow & Smith *et al.* $\varepsilon a=\frac{\Delta\varepsilon}{2}$	Smith -Watson - Topper (SWT) $\varepsilon a=\frac{\Delta\varepsilon}{2}$
BCC5A	16	606.45	0.0074	0.0073	0.0073	0.005
BCC5B	5	611.8	0.0100	0.0099	0.0099	0.008
BCC5C	18	553.6	0.0048	0.005	0.005	0.004
BCC5D	23	294.05	0.0053	0.0053	0.0053	0.0074

The following can be concluded:

- The absolute results and trends of fatigue life can be compared between the various analyses and experiments. There was no agreement between the absolute results of three equations with base model as shown in Table 5.9. For the trend of total strain amplitude result; Coffin-Manson formula and Morrow-Smith formula showed similar trend with the experiments while the SWT formula was different, because of the maximum stress included in SWT formula, and this gave a poorer result.
- By using modification factor, there was good agreement between the results and trends of fatigue life between the various analyses and experiments as shown in the Table 5.10, except BCC5D model when using SWT formula, the Fatigue ductility coefficient should be divided by 10 to match experiment strain amplitude.
- Calculating strain amplitude for BCC5 FE models using strain life formulas by considering strain hardening exponent (*n`*) uses the same procedure as without considering cyclic strain hardening (n`), the only difference is *b* and *c*

values, which is mentioned above and explained in Sec.C.2. Excel 2007 was used to calculate strain amplitude for the strain life formulas.

- Smith-Watson-Topper (SWT) shows different results than the other LCF formulas because of maximum stress involves in this formula as shown in Table 5.11. However, the relationship between *c*, *b*, and (*n`*) can be obtained purely based on geometry.
- By using modification factor, strain amplitude for Coffin-Manson formula and Morrow-Smith formula showed good agreement in comparison with experimental test strain amplitude as shown in Table 5.12, except Smith-Watson-Topper (SWT) showed a little difference in strain amplitude in comparison with experimental work strain amplitude for all BCC5 models, the Fatigue ductility coefficient should be divided by 5 to match experiment strain amplitude.
- There is an inverse proportion relationship between strain amplitude and number of cycles, which is clear in BCC5B and BCC5D as shown in Tables 5.9 &5.11.
- There is a difference between Tables 5.9 & 5.11, in comparison of strain amplitude for FE base model and strain amplitude which are calculated using strain life formulas.
- Table 5.9 shows the strain amplitude for BCC5 FE base models, should be multiplied by factor 4 to be close to strain amplitude from strain life formulas, but in Table 5.11 the strain amplitude for BCC5 FE base models should be multiplied by factor 2 to be close to strain amplitude from strain life formulas. This has a large error in comparison between two Tables 5.9 & 5.11 and this error is due to using the cyclic strain hardening exponent (*n`*) as shown in Table 5.11.
- The results of Coffin-Manson and Morrow & Smith *et al.* are close to each other but the results of Smith -Watson-Topper (SWT) are different as that depends on the stress at the critical point which is included in SWT formula.

- Figures 5.4 (a, b, c and d) show total strain amplitude variation as a function of number of life cycles representing Smith *et al.* relationship for BCC5 FE ANSYS base models.

  The relationship is plotted in Figures 5.4 (a, b, c and d) on (log-log scales) with the red curve (considering strain hardening exponent n`) and blue curve (not considering strain hardening exponent n`). The curves show that the slope of the Smith *et al.* relationship considering strain hardening exponent (n`) is greater than the slope of the Morrow & Smith *et al.* relationship without considering cyclic strain hardening exponent (n`). Including cyclic strain hardening exponent (n`) increase stiffness joint and reduces the number of predicted cycle life.

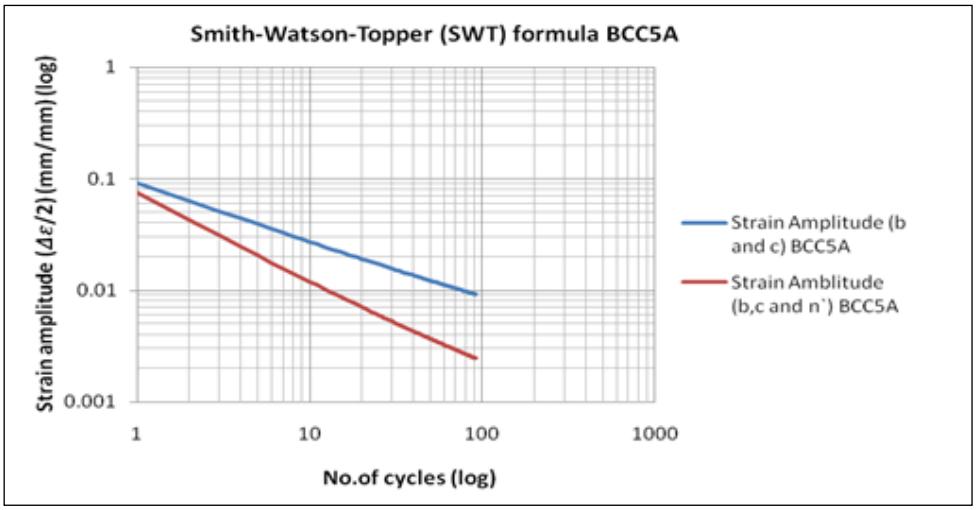

(a)

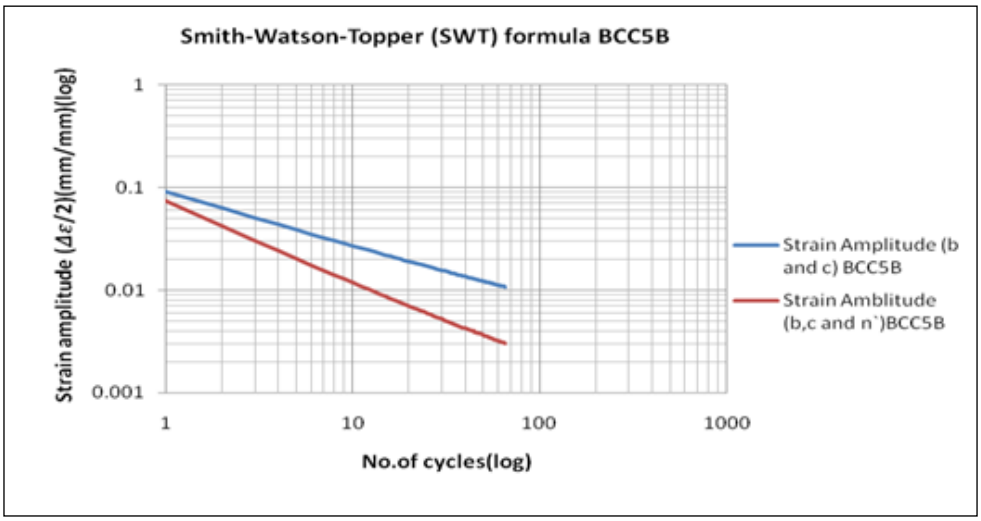
Smith-Watson-Topper (SWT) formula BCC5B
Strain amplitude (Δε/2)(mm/mm)(log)
1
0.1
0.01
0.001
1
10
100
1000
No.of cycles(log)
Strain Amplitude (b and c) BCC5B
Strain Amblitude (b,c and n`)BCC5B

(b)

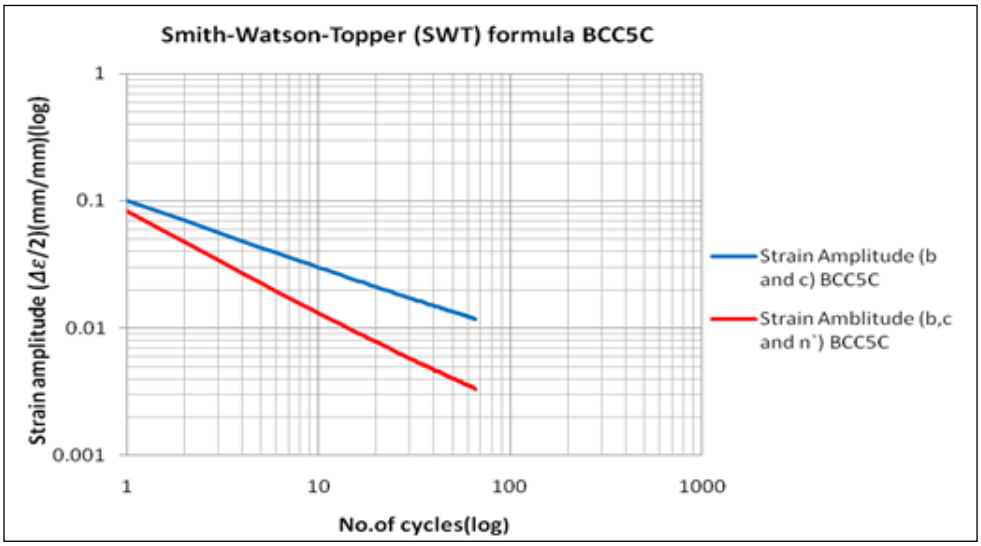
Smith-Watson-Topper (SWT) formula BCC5C
Strain amplitude (Δε/2)(mm/mm)(log)
1
0.1
0.01
0.001
1
10
100
1000
No.of cycles(log)
Strain Amplitude (b and c) BCC5C
Strain Amblitude (b,c and n`) BCC5C

(c)

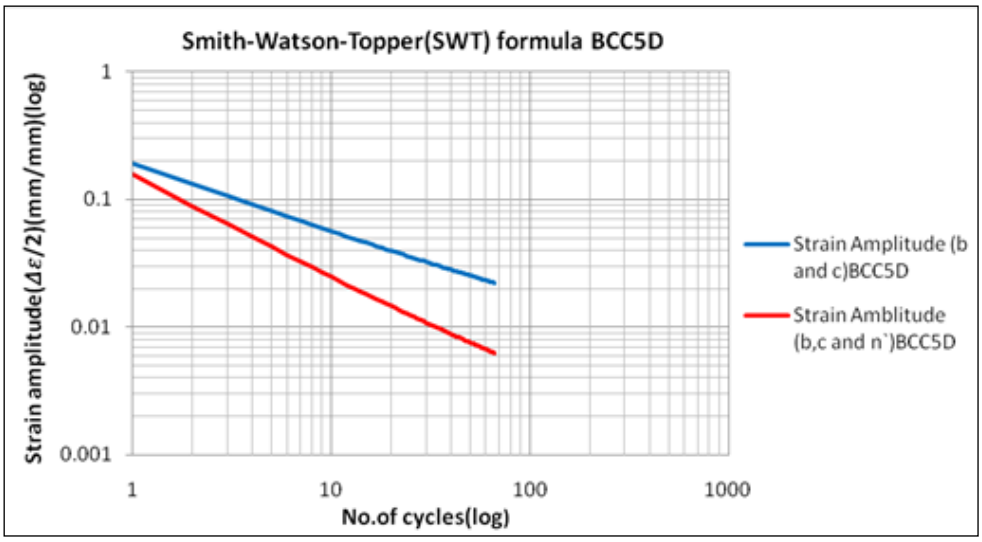

(d)

Figure 5.4: Shows the effect of strain hardening exponent (n') by plotting strain amplitude vs. no. of cycles (log -log scale) using Smith-Watson-Topper (SWT) relationship for FE ANSYS base models:(a) BCC5A, (b) BCC5B, (c) BCC5C and (d) BCC5D

- The fatigue life can be estimated using Coffin Manson type equations. It is recommended that the variant by (ε′f/2) is used and that the coefficients are modified (un-welded describe modification welded) (as reported by Almar [1985]) in order to increase the calculated damage rate. This modification may allow for stable crack growth at the higher strain cycles and for the steel surfaces being less perfect than in the original Coffin Manson experiments.
- It appears that low cycle fatigue formulas can be used but they need to be modified as calculated in this thesis and as shown in Tables 5.10 & 5.12.
- Coffin-Manson formula is used for plain bars the fatigue tests sample were circular bars in cross section having an hourglass-shaped test section with a minimum diameter of 0.25 inch as reported in Coffin and Manson [1954], but in this work Coffin -Manson equation has been used for a welded structure.

- Tables 5.13 & 5.15 show that welded joint had less life cycles than un-welded joint, that's because welded joint has defects due to solidification process or Hydrogen porosity as explained in chapter 3. Therefore, fatigue ductility coefficient should be divided by 2 ($\varepsilon'_f/2$) when apply strain life formulas in order to allow for difference between welded and un-welded structure as mentioned in chapter 3 in Sec.3.1.2.2 [Almar,1985], and the results of life cycles in strain life formulas were not match the life cycle of experimental tests.
- Modification factor has been calculated in this thesis for BCC5 models as shown in Table 5.6, and applied to low cycle fatigue formulas. Life cycle results showed a good agreement with the experimental tests as shown in Tables 5.14 & 5.16.
- Tables 5.13 & 5.15 show number of cycles to failure using strain life formulas and fatigue damage index, considering strain hardening exponents (n') and considering strain hardening exponents respectively for all BCC5 models. Number of cycle to failure by using cyclic strain hardening exponent (n') in strain life formulas are less than number of cycle to failure without using cyclic strain hardening exponent (n'), because strain hardening make the joint increase stiffness joint and decrease toughness joint, therefore the life cycles will be less.
- Tables 5.14 & 5.16 considering strain hardening exponents (n') and considering strain hardening exponents respectively for all BCC5 models. Number of cycle to failure by using cyclic strain hardening exponent (n') in strain life formulas are equal to the number of cycle to failure without using cyclic strain hardening exponent (n'), because of the modification factors are different (see Table 5.6).

Table 5.13: Shows number of cycles to failure considering strain hardening exponents (n') using strain life formulas and fatigue damage index , for all BCC5 models , welded and un-welded joints

Case No.	CTF (Experimental test)	CTF Coffin- Manson		CTF Morrow &Smith *et al.*		CTF Smith-Watson-Top (SWT)		CTF (FDI)	
		εf '/2	**εf '**	**εf '/2**	**εf '**	**εf '/2**	**εf '**	**εf '/2**	**εf '**
BCC5A	16	36	90	36	90	20	40	36	91
BCC5B	5	21	54	21	54	12	26	21	54
BCC5C	18	66	268	66	268	39	81	66	165
BCC5D	23	64	163	64	163	86	171	64	156

where:

CTF is number of cycles to failure

εf ' is fatigue ductility coefficient used in strain life formulas

εf '/2 is fatigue ductility coefficient divided by 2 (difference between welded and un-welded joint)

Table 5.14: Shows number of cycles to failure considering strain hardening exponents (n') using strain life formulas and fatigue damage index , for all BCC5 models, welded and un-welded joints modification factor (ε'f/Fac.)

(see Table 5.6)

Case No.	CTF (Experimental test)	CTF Coffin- Manson		CTF Morrow &Smith *et al.*		CTF Smith-Watson-Top (SWT)		CTF (FDI)	
		εf '/Fac	**εf '**	**εf '/Fac**	**εf '**	**εf '/Fac**	**εf '**	**εf '/Fac**	**εf '**
BCC5A	16	16	90	16	90	14	40	15.955	91
BCC5B	5	5	54	5	54	8	26	4.923	54
BCC5C	18	18	268	18	268	21	81	18.18	165
BCC5D	23	23	163	23	163	55	171	22.963	156

Table 5.15: Shows number of cycle to failure not considering cyclic strain hardening component (n') using strain life formulas and fatigue damage index , for all BCC5 models, for welded and un-welded joints

Case No.	CTF (Experimental test)	CTF Coffin- Manson		CTF Morrow &Smith *et al.*		CTF Smith-Watson-Top (SWT)		CTF (FDI)	
		εf '/2	**εf '**	**εf '/2**	**εf '**	**εf '/2**	**εf '**	**εf '/2**	**εf '**
BCC5A	16	262	989	262	989	151	477	262	992
BCC5B	5	115	443	115	443	75	246	115	443
BCC5C	18	922	3515	922	3515	533	1588	521	1959
BCC5D	23	675	2586	675	2586	2358	6390	666	2432

Table 5.16: Shows number of cycle to failure not considering cyclic strain hardening component (n') using strain life formulas and fatigue damage index , for all BCC5 models, welded and un-welded joints modification factor (ε'f/Fac.)
(see Table 5.6)

Case No.	CTF (Experimental test)	CTF Coffin- Manson		CTF Morrow &Smith *et al.*		CTF Smith-Watson-Top (SWT)		CTF (FDI)	
		εf '/Fac	**εf '**	**εf '/Fac**	**εf '**	**εf '/Fac**	**εf '**	**εf '/Fac**	**εf '**
BCC5A	16	16	989	16	989	14	477	15.922	992
BCC5B	5	5	443	5	443	5	246	4.938	443
BCC5C	18	18	3515	18	3515	37	1588	17.919	1959
BCC5D	23	23	2586	23	2586	230	6390	22.815	2432

- Applying fatigue cyclic exponents *c* and *b* with and without the cyclic strain hardening exponent (*n`*) in strain life formulas in order to calculate strain amplitude results in a large difference in the results. The FE analysis strain amplitude should be multiplied by factor 4 to be close to strain life formulas, strain amplitude for non (n`) as shown in Table 4.9, but the FE analysis models strain amplitude results should be multiplied by factor 2 to be close to strain life formulas strain amplitude with (n`) as shown in Table 5.11.

Table 5.7 shows for these experiments the Smith-Watson-Topper (SWT) method performed best. However it still overestimated the cycles to failure approximately by 2 times.

Table 5.8 shows for these experiments the coffin-Manson and Morrow & Smith *et.al* method performed best. But SWT formula shows a difference in life cycle in comparison with the experimental tests because of maximum stress is included in this formula.

The use of strain hardening option increasing joint stiffness and decreasing joint toughness, therefore decrease in fatigue life resulting from the welds [Björk *et al*., 2006].

Table 5.17 shows ssummary of experiments and calculation results based on computer Analysis output for all LCF methods

Table 5.17: Summary of experiments and calculation results based on computer Analysis output for all LCF methods, using (ε'f/2)

Case No.	CTF experiment	FDI		FAD	Crack growth (mm)	Ratcheting (mm)
		CTF (with n')	CTF (without n')	(Kr,Lr)		
BCC5A	16	36	262	(0.37, 2.2)	0.00232	0.143
BCC5B	5	21	115	(0.38, 2.2)	0.00057	0.0706
BCC5C	18	80	959	(0.39, 2.0)	0.0016	0.130
BCC5D	23	66	704	(0.37, 1.07)	0.0030	0.158

- Coefficient of variation is the percentage variation in mean, standard deviation being considered as the total variation in the mean. Using the coefficient of variation to compare the variability of strain life formulas based on number of cycles to failure.
- Tables 5.18, 5.19, 5.20 and 5.21 show number of cycles to failure for welded joint considering (n') for BCC5A, BCC5B, BCC5C and BCC5D respectively. Comparing the coefficient of variation values from the methods indicates that Smith-Watson-Topper method (SWT) had the highest coefficient of variation while the Coffin-Manson and Morrow & Smith *et al.* have same values. The coefficient of variation for SWT formula is the largest in all BCC5 calculations which indicates that this formula is more variable and it is less stable or less uniform, but same tables show that the coefficient of variation for Coffin-Manson and Morrow & Smith *et al* are smaller than SWT which indicate that these formulas are less variable and it is more stable or more uniform.

Table 5.18: Shows number of cycles to failure for welded joint using (ε'f/2), including mean value, standard deviation and coefficient of variation for BCC5A model

Method	CTF including (n')	CTF excluding (n')	Mean	Standard deviation	Coefficient of variation	Chapter/section reference/Appendix
Experimental test	16					Appendix A
Coffin-Manson	36	262	149	159.80	1.07	4/Sec.4.3 / C,Sec.C.1
Morrow &Smith *et al.*	36	262	149	159.80	1.07	4/Sec.4.3/ C,Sec.C.1
Smith-Watson-Topper (SWT)	20	151	85.5	92.63	1.08	4/Sec.4.3 / C,Sec.C.1
Fatigue damage index (FDI)	36	262	149	159.80	1.07	4/Sec.4.2.2 / C, Sec.C.3

Table 5.19: Shows number of cycles to failure for welded joint, using (ε'f/2), including mean value, standard deviation and coefficient of variation for BCC5B model

Method	CTF including (n')	CTF excluding (n')	Mean	Standard deviation	Coefficient of variation	Chapter/section reference/Appendix
Experimental test	5					Appendix A
Coffin-Manson	21	115	68	66.46	0.97	4/Sec.4.3 / C,Sec.C.1
Morrow &Smith *et al.*	21	115	68	66.46	0.97	4/Sec.4.3/ C,Sec.C.1
Smith-Watson-Topper (SWT)	12	75	43.5	44.54	1.02	4/Sec.4.3 / C,Sec.C.1
Fatigue damage index (FDI)	21	115	68	66.46	0.97	4/Sec.4.2.2 / C, Sec.C.3

Table 5.20: Shows number of cycles to failure for welded joint, using (ε'f/2), including mean value, standard deviation and coefficient of variation for BCC5C model

Method	CTF including (n')	CTF excluding (n')	Mean	Standard deviation	Coefficient of variation	Chapter/section reference/Appendix
Experimental test	18					Appendix A
Coffin-Manson	66	922	501	595.38	1.188	4/Sec.4.3 / C,Sec.C.1
Morrow &Smith *et al.*	66	922	501	595.38	1.18	4/Sec.4.3/ C,Sec.C.1
Smith-Watson-Topper (SWT)	39	533	286	349.31	1.22	4/Sec.4.3 / C,Sec.C.1
Fatigue damage index (FDI)	66	521	293.5	321.73	1.09	4/Sec.4.2.2 / C, Sec.C.3

Table 5.21: Shows number of cycles to failure for welded joint, using (ε'f /2), including mean value, standard deviation and coefficient of variation for BCC5D model

Method	CTF including (n')	CTF excluding (n')	Mean	Standard deviation	Coefficient of variation	Chapter/section reference/Appendix
Experimental test	23					Appendix A
Coffin-Manson	64	675	370.5	430.62	1.16	4/Sec.4.3 / C,Sec.C.1
Morrow &Smith *et al.*	64	675	370.5	430.62	1.16	4/Sec.4.3/ C,Sec.C.1
Smith-Watson-Topper (SWT)	86	2358	1222	1606.54	1.31	4/Sec.4.3 / C,Sec.C.1
Fatigue damage index (FDI)	64	666	365	425.67	1.16	4/Sec.4.2.2 / C, Sec.C.3

5.4 Crack growth calculations

A prerequisite for accurate fatigue life predictions is to have reliable fatigue data at hand. From the *damage-tolerant* point of view this means to have a proper description of the relation between the applied load at the crack tip and the corresponding measured fatigue crack growth rate. The purpose of conducting fatigue crack growth calculation is to establish this relationship.

Fatigue crack propagation behaviour is typically described in terms of crack growth rate or crack length extension per cycle of loading, which is commonly described by the crack growth equation proposed by Paris and Erdogan [Alam,2005], and popularly known as the Paris law, as given below:

$da/dN = A(\Delta K)^m$

The application of the crack growth rates will be based on cumulative stress increments, however I am going to assume that a small crack of length $a_\circ$ is already exist inside the material. British standards BS7910 [2013] will be followed to carry out crack growth calculations.

Crack growth is explained in Sec. 3.3.4, and methodology of calculation as follows:

ΔK: stress intensity factor range = K_{max} - K_{min}

K_{max} = $\sigma_{max} \sqrt{\pi a_{\circ}}$ (using σ_{max} for each cycle in increment stress- time history)

Kmin = $\sigma_{min} \sqrt{\pi a_{\circ}}$ (using σ_{min} for each cycle in increment stress- time history)

$a_{\circ}$= crack length

Values of the constants A and m for fatigue crack growth laws for steels in air are recommended in BS 7910 [2013] Table 5.22.

Table 5.22: Constants A and m for fatigue crack growth laws for steels in air

R	Stage A				Stage B				Stage A/Stage B transition point ΔK N/mm$^{3/2}$	
	Mean curve		Mean + 2SD		Mean curve		Mean + 2SD			
	A [B)]	m	A [B)]	m	A [B)]	m	A [B)]	m	Mean curve	Mean + 2SD
<0.5	1.21×10^{-26}	8.16	4.37×10^{-26}	8.16	3.98×10^{-13}	2.88	6.77×10^{-13}	2.88	363	315
≥0.5	4.80×10^{-18}	5.10	2.10×10^{-17}	5.10	5.86×10^{-13}	2.88	1.29×10^{-12}	2.88	196	144

A) Mean + 2SD for $R \geq 0.5$ values recommended for assessing welded joints.

B) For da/dN in mm/cycle and ΔK in $N/mm^{3/2}$.

[BS 7910, 2013]

(Note: According to the Table 5.22, I should take the value of R <0.5 according to sinusoidal graph below, therefore A= 3.98×10^{-13} , and m=2.88, but because of the crack keep open by ratcheting positive strain and plasticity keep the crack open, I have chose, A= 5.86×10^{-13} , and m=2.88).

Table 5.23 shows results of crack growth rates calculations based on stress ranges, stress modified by (strain*E) and Geometric mean of stress and (strain*E) for BCC5A model, the other related tables for BCC5B, BCC5C and BCC5D are shown in Sec.C.8, Tables C.4, C.7and C.10 Appendix C, respectively.

(Note: According to the Table 5.22, I should take the value of R <0.5 according to sinusoidal graph below, therefore A= 3.98×10^{-13} , and m=2.88, but because of the

crack keep open by ratcheting positive strain and plasticity keep the crack open, I have chose, A= 5.86×10^{-13} , and m=2.88).

Figures 5.5, C.2,C.3 and C.4 represents Tables 5.23, C.4,C.7 and C.10 respectively

A=5.86*10^-13 Table 4.22 [BS7910, 2013]

m=2.88 Table 5.22 [BS7910, 2013]

$a_{\circ}$ (estimate) = crack length = 0.2mm

5.4.1 Crack growth calculations based on stress modified (strain*E) and (geometric mean of stress and strain*E)

In this section applies fracture mechanics crack growth calculations based on stress modified so that they are based on strain*E, and also modified so that they are based on geometric mean of stress and strain*E.

Table 5.23: shows results of crack growth rates calculations based on stress ranges, stress modified by (strain*E) and Geometric mean of stress and (strain*E) for BCC5A, all other related tables for BCC5 models are shown in Sec.C.8

Table 5.23: Shows results of crack growth rates calculations based on stress ranges, stress modified by (strain*E) and Geometric mean of stress and (strain*E) for BCC5A

Cycle no.	Stress ranges da/dN(mm/cycle)=A ΔK^m	Modified stress by strain*E da/dN(mm/cycle)=A ΔK^m	Geometric mean of stress and strain*E da/dN(mm/cycle)=A ΔK^m	Mean of stress and strain*E da/dN(mm/cycle)=A ΔK^m
1	3.41283E-05	0.002187184	0.000273212	0.000546748
2	6.68735E-05	0.003657442	0.000493898	0.000942506
3	8.33983E-05	0.002989462	0.000498531	0.00084225
4	0.000108438	0.00259493	0.000529468	0.000804212
5	0.00012385	0.002395773	0.000543486	0.000783893
6	0.000147331	0.002434962	0.000597335	0.000830889
7	0.000146323	0.002599889	0.000614791	0.000869667
8	0.000162336	0.002799435	0.000671598	0.00094373
9	0.000167488	0.003215393	0.000730672	0.001053022
10	0.000171964	0.00315982	0.000733504	0.001046561
11	0.000175764	0.003588743	0.000789809	0.001155798
12	0.000183341	0.003713429	0.00082003	0.001198063
13	0.000187604	0.00411746	0.000872898	0.001300873
14	0.000193076	0.004079766	0.000880883	0.001301064
15	0.000196042	0.004188224	0.000898727	0.001331429
16	0.00020322	0.004636859	0.000962121	0.00144916

Table 5.24: Shows calculations of stress intensity factor using modification stress by (ε*E) for BCC5A

No. of cycles	εmax	εmin	εrange	εmax*E	εmin*E	Kmax=σmax √π a	Kmin=σmin √π a
1	0.0122	-0.0011	0.0133	2440	-220	1932.48	-174.24
2	0.0115	-0.0043	0.0158	2300	-860	1833.072254	-685.4096253
3	0.012	-0.0026	0.0146	2400	-520	1929.993936	-418.1653527
4	0.0125	-0.0013	0.0138	2500	-260	2024.956225	-210.5954474
5	0.013	-0.00034	0.01334	2600	-68	2118.998159	-55.41995186
6	0.0136	0.00026	0.01334	2720	52	2229.322335	42.61939757
7	0.0142	0.00063	0.01357	2840	126	2340.890647	103.856416
8	0.0149	0.00106	0.01384	2980	212	2471.007373	175.7897863
9	0.0157	0.00127	0.01443	3140	254	2620.277834	211.9587802
10	0.0161	0.00186	0.01424	3220	372	2706.455448	312.6712505
11	0.0167	0.00192	0.01478	3340	384	2826.971827	325.0171202
12	0.0173	0.00246	0.01484	3460	492	2951.494009	419.6922117
13	0.0179	0.00264	0.01526	3580	528	3078.240672	453.997507
14	0.0181	0.00302	0.01508	3620	604	3139.745763	523.8691826
15	0.0185	0.00341	0.01509	3700	682	3236.355213	596.5389878
16	0.0192	0.0037	0.0155	3840	740	3387.570726	652.8131086

Table 5.25: Shows calculations of stress intensity factor using stress ranges for BCC5A

No. of cycles	Normal stress MPa (min)	Normal stress MPa (max)	Kmax=σmax √π a	Kmin=σmin √π a	ΔK=Kmax-Kmin
1	-261.59	365.79	289.70568	-207.17928	496.88496
2	-356.2	435.51	345.2431869	-282.3715257	627.6147126
3	-387.96	466.7	370.0303689	-307.6001326	677.6305015
4	-440.17	495.87	393.2401799	-349.0683647	742.3085446
5	-459.42	520.56	412.9319053	-364.4328722	777.3647775
6	-482.22	558.33	443.0296993	-382.6371171	825.6668164
7	-488.37	549.32	436.0405315	-387.659496	823.7000275
8	-512.9	562.5	446.6654281	-407.2794632	853.9448913
9	-518.57	568.12	451.3105133	-411.9483435	863.2588568
10	-528.4	567.83	451.2681559	-419.9321867	871.2003427
11	-530.84	573.27	455.7862631	-422.0517032	877.8379662
12	-540.02	579.9	461.2588659	-429.5378733	890.7967392
13	-548.06	580.32	461.8030051	-436.1313672	897.9343723
14	-547.4	591.77	471.1336974	-435.8088209	906.9425183
15	-553.46	591.21	470.9130185	-440.8442334	911.7572519
16	-551.6	606.89	483.6370881	-439.5758998	923.2129879

Figure 5.5: shows crack growth represents stress ranges , modified stress by strain*E, Geometric mean of stress and strain*E and mean of stress and strain*E ranges) vs. no. of cycles which is represented in Table 5.23 for BCC5A model, the other related charts are shown in Sec.C.8 Figures C.2,C.3 and C.4 Appendix C.

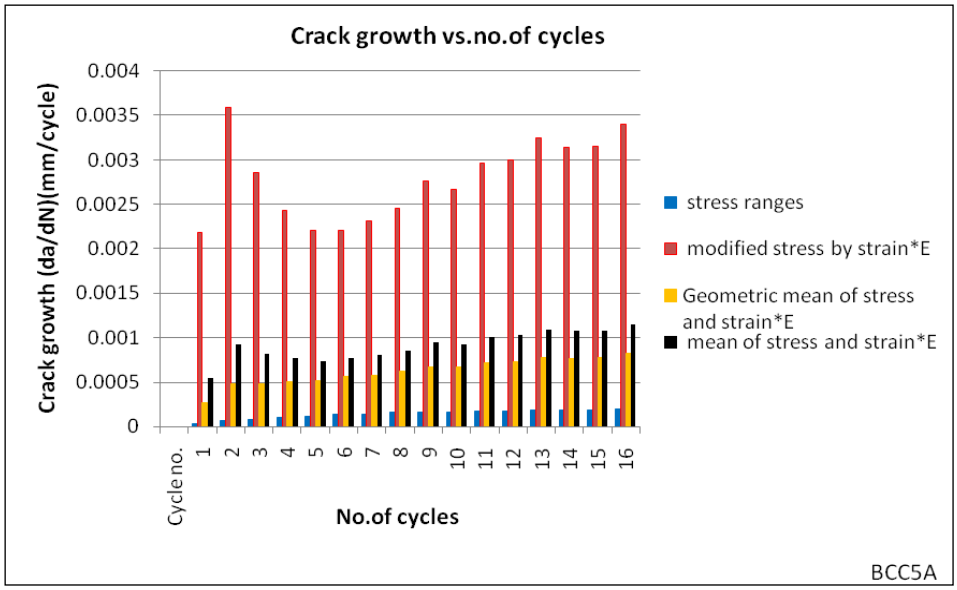

(a)

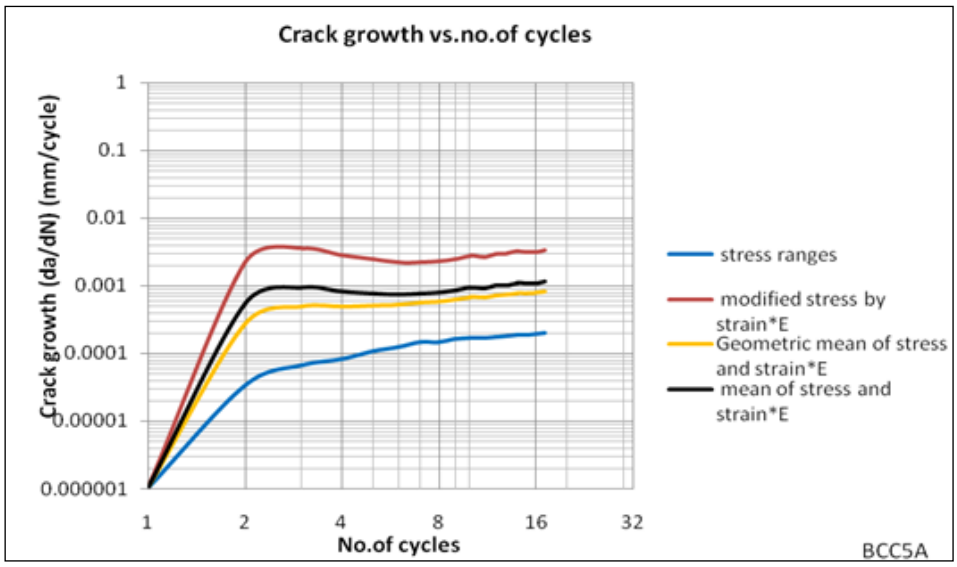

(b)

Figure 5.5: (a) Chart and (b) log- log crack growth vs. no. of cycles for BCC5A model represent crack growth represents stress ranges , modified stress by strain*E, Geometric mean of stress and strain*E and mean of stress and strain*E ranges, related to Table 5.23

Figure 5.5 (a) shows a chart of the crack growth rate as a function of number of cycle, higher values were obtained from of modified stress by strain*E (red colour) compared to geometric mean of stress and strain*E (orange colour) and mean of stress and strain*E ranges (black colour), while the lowest values obtained by using the stress ranges method (blue colour).

Figure 5.5 shows that the crack growth for cycle nº 2 is higher than cycle nº 16, and this is depends on plastic strain ranges value for each cycle, the plastic strain ranges value of cycle no.2 is more than plastic strain ranges of cycle no. 16, therefore the crack growth for cycle nº 2 is higher than the crack growth in cycle nº 16.
Different results of crack growth based on the four option calculation (stress ranges, modified stress by strain*E, Geometric mean of stress and strain*E and mean of stress and strain*E ranges).

Figure 5.5 (b) shows the crack growth rate as a function of number of cycle, four different methods were considered to evaluate the crack growth of a BCC5A model. All the considered methods of crack growth calculations showed a similar trend, where during the first cycle 1 to 2 there is a steep increment in the crack growth and then nearly constant crack growth from cycle 2 to 16. The obtained crack growth values were slightly different from method to other, higher values were obtained from the modified stress by strain*E (red colour) compared to geometric mean ranges (orange colour) and mean of stress and strain*E ranges (black colour), while the lowest values obtained by using the stress ranges method (blue colour).

Overall methodology for fatigue life calculation

1- Four steel connection models have been analysis using ANSYS 14.5 Workbench. All models have same materials type (A36) for beams and columns.
2- Displacement cyclic loading - time history were applied at the cantilever beam.

3-Stress range is obtained from computer analysis to use it in crack growth calculations and also modified stress by strain*E, Geometric mean of stress and strain*E and mean of stress and strain*E ranges were used to calculate crack growth.
4- The fatigue crack growth rate is calculated using Paris equation.
5- Calculations were based on Mode 1(Figure 3.26), Region II **(**Figure 3.29).
6- Failure occurs when the crack attains a critical size which is recommended by BS7910 [2013] and DNV-RP-F108 [2006], that the total crack extension during the whole installation process shall be less than 1 mm. Table 5.26 shows four different methods to calculate crack size for BCC5 models, crack size for each BCC5 model was more than 1 mm except BCC5B model the crack size was about 1mm.

Table 5.26: Shows total crack size for all BCC5 models considering stress ranges , modified stress by strain*E, Geometric mean of stress and strain*E and mean of stress and strain*E ranges

Case no.	Crack size (stress range) (mm)	Crack size (modified stress by strain*E) (mm)	Crack size (geometric mean of stress and strain*E) (mm)	Crack size (mean of stress and strain*E) (mm)
BCC5A	3.216474776	3.562198114	3.275108391	3.313181759
BCC5B	1.00135869	1.070220903	1.009275383	1.01792057
BCC5C	3.60995647	3.714175324	3.631852952	3.642083324
BCC5D	4.629806903	4.924973867	4.694885227	4.722696484

Conclusion

Crack growth calculation using fracture mechanics is another method that might give a reasonable comparison with the tests and, on the face of it, is worth investigating when we apply it to both high cycle fatigue and fracture. Using modified stress by strain*E, Geometric mean of stress and strain*E and mean of stress and strain*E ranges. Overall this work showed that all methods give overestimated for cycle to failure in comparison to the tests, similar results. And crack extension during the whole installation process for BCC5 models are not showing less than 1 mm as

recommended by BS7910 [2013] and DNV-RP-F108 [2006]. All BCC5 models were more than 1 mm except BCC5B model the crack size was about 1mm.

- Paris' law gives the advancement d*a* of fatigue crack per unit cycle d*N*, as a function of the amplitude of stress intensity factor Δ*K*, and shows material's constants *A* and *m* with applied stress range in a simple manner using the Wöhler S-N curve.
- In this thesis, FEM has been used to analyse the steel connection, meshing and refined meshing has been created in order to evaluate the crack by using maximum principle strain (total strain) and maximum principle stress (normal stress) criteria and these criteria have been compared with experimental results.
- Calculating crack tip opening displacement (CTOD) measures the resistance of a material to growing a crack, which indicates the toughness of the material which indicates that the fracture will occur at the critical value of CTOD.
- The purpose of conducting fatigue crack growth calculation is to establish relationship between the applied load at the crack tip and the corresponding measured fatigue crack growth rate.

5.5 Simple summation of plastic stress and strain in comparison with Ultimate tensile strength (UTS), the related strain and elongation at failure in simple test specimens.

Table 5.27 shows a simple summation cumulative stress ranges, last cycle stress ranges, cumulative (ε*E) ranges and last cycle (ε*E) ranges in comparison with ultimate tensile strength (obtained from test). It is showing that cumulative stress ranges, last cycle stress ranges and cumulative cycle (ε*E) ranges and the last cycle (ε*E) ranges for all BCC5 values are over the limit of ultimate tensile strength.

Table 5.27: Simple summation of plastic stress and strain in comparison with Ultimate tensile strength (UTS), the related plastic stress at failure in simple test specimens

Case No.	UTS (test) (MPa)	Cumulative σ ranges(analysis) (MPa)	last cycle σ range (analysis) (MPa)	Cumulative (ε*E) ranges (analysis) (MPa)	last cycle (ε*E) ranges (analysis) (MPa)
BCC5A	404.6	16321.07	1158.49	46162	3100
BCC5B	404.6	4646.31	1129.12	17047.5	3435.8
BCC5C	404.6	15038.51	1154.37	34262	3332
BCC5D	404.6	22606.32	1123.52	49516.38	2144

where: UTS is the Ultimate tensile strength which is the maximum stress that a material can withstand while being stretched or pulled before failing or breaking (test measurement).

Table 5.28 shows a simple summation cumulative strain ranges, last cycle strain ranges, over all strain ranges and up and down strain ranges in comparison with true strain ranges (obtained from test). It is showing that the cumulative (ε) ranges, the last cycle (ε) ranges and the overall (ε) ranges for all BCC5 models within the limit of true strain ranges and up & down strain ranges values over the limit of true strain ranges except BCC5B model.

Table 5.28: Simple summation of strain in comparison with true strain, the related strain and elongation at failure in simple test specimens

Case No.	True strain range at failure (material test)	Cumulative ε ranges (analysis)	last cycle ε ranges (analysis)	over all ε ranges (analysis)	Cumulative up and down ε ranges (analysis)
BCC5A	0.31	0.230	0.015	0.014	0.461
BCC5B	0.31	0.085	0.017	0.017	0.170
BCC5C	0.31	0.173	0.018	0.009	0.346
BCC5D	0.31	0.248	0.011	0.010	0.496

5.5.1 Conclusion

Using the UTS based on the true stress may also be a reasonable predictor of fracture but that cannot be confirmed again owing to the displacement control of the tests.

Using the maximum strain at failure 0.31.

Table 5.28 shows that stress ranges and stress modified by ε*E ranges for cumulative ranges and last cycle range are exceed Ultimate limit strength which is indicate that the failure occurred when stress exceed UTS.

5.6 Strain rate estimation for BCC5 models

The estimation of strain rate is as follow:

BCC5A

Strain/displacement approx. 0.01/100mm = 0.0001/mm (100mm from Figure 4.17, 0.01 strain from Figure 4.25)

Displacement rate max = 2mm/sec (from test see Sec. A.3.2.1)

Therefore strain rate = 0.0001/mm *2mm/sec = 0.0002/sec

BCC5B

Strain/displacement approx. 0.017/126mm = 0.00013/mm (126mm from Figure 4.18, 0.017 strain from Figure B.4(a))

Displacement rate max = 2mm/sec (from test see Sec. A.3.2.1)

Therefore strain rate = 0.00013/mm *2mm/sec = 0.00027/sec

BCC5C

Strain/displacement approx. 0.015/100mm = 0.00015/mm (126mm from Figure 4.19, 0.015 strain from Figure B.4(b))

Displacement rate max = 2mm/sec (from test see Sec.A.3.2.1)

Therefore strain rate = 0.00015/mm *2mm/sec = 0.0003/sec

BCC5D

Strain/displacement approx. 0.013/50mm = 0.00026/mm (126mm from Figure 4.20, 0.015 strain from Figure B.4(c))

Displacement rate max = 2mm/sec (from test see Sec.A.3.2.1)
Therefore strain rate = 0.00026/mm *2mm/sec = 0.00052/sec

Table 5.29 shows final results for strain rate estimation using displacement approximation from hysteresis loops from experimental tests and strain range from FE graph analysis.

Table 5.29: Summary for strain rate estimation using displacement approximation from hysteresis loops and strain range from FE graph

Case No.	Strain (mm/mm)	displacement approx.(mm)	Strain rate	Strain Reference	Displacement Reference chapter 3
BCC5A	0.01	100	0.0002/sec	Fig.3.25, Chapter 3	Fig.3.17
BCC5B	0.017	126	0.00027/sec	Fig.B.4(a) App. B	Fig.3.18
BCC5C	0.015	100	0.0003/sec	Fig.B.4(b) App. B	Fig.3.19
BCC5D	0.013	50	0.00052/sec	Fig.B.4(c) App. B	Fig.3.20

Table 5.29 shows there was inverse relationship between displacement and strain rate. The strain rate is quite low for all BCC5 models and may be lower than in real earthquakes (see Table 5.30 of Loading rate). Stable crack growth ratcheting.

There is a possibility that there is some stable crack growth ratcheting. However I do not have the material property data to investigate this.

Table 5.30: Typical loading rates in some engineering components

Application	***Symbol.1.*, s^{-1}**	***Symbol.2.*, MPa $\sqrt{m}$ $^{0.5}s^{-1}$**
Storage tanks, pressure vessels	10^{-6} to 10^{-4}	10^{-2} to 1
Bridges, cranes earthmoving	10^{-2} to 0.1	10 to 10^{3}
Earthquake loading Marine collisions	0.1 to 10	100 to 10^{4}
Land transport, aircraft undercarriage	10 to 1000	10^{3} to 10^{6}
Explosion, ballistics	10^{4} to 10^{6} plus	10^{7} to 10^{10} plus

[Wiesner and MacGillivray, 1999]

5.7 Conclusion for this chapter

The following conclusions can be drawn that are based on using non-linear FEA in conjunction with a FAD, Coffin Manson very low cycle fatigue calculations, Paris Law crack growth calculations, the UTS (based on true stress) , the ultimate true strain and strain rate estimation:

1. This work is based on 4 experiments, so only preliminary conclusions can be drawn.
2. It is necessary to calculate the resistance of the connection to fracture and to very low cycle fatigue during earthquake induced elasto-plastic cycling.
3. Using Non-linear FEA in conjunction with Stress intensity Factor calculation based on linear fracture mechanics, a failure assessment diagram and either a

Coffin-Manson or Paris Law may be a reasonable basis for the assessment of fatigue and fracture.

4. The prediction of the fatigue life of steel structures can be carried out in a number of different ways considering British standards BS 7910[2013], and DNV-RP-F108 [2006]:

- Failure assessment diagram (FAD) curve to classify situation of structure safe or unsafe. The evaluation points inside the FAD curve indicate acceptable cracks, and the evaluation points above the FAD curve are unacceptable cracks that indicate a predicted structural failure. An evaluation point on the FAD curve is a critical crack on the verge of failure, which can be useful to determine predicted critical crack sizes.
- Fatigue damage index (FDI) can be used to predict the damage in steel structures and helps the engineer to better understand the performance of their design under seismic loads. Values of *FDI* greater than or equal to 1.0 indicates a low-cycle fatigue fracture of the member as reported by Campbell *et al.* [2008], therefore using strain life formulas to get FDI for BCC5 models, it should be divide (ε'f) by Factor as shown in Table 5.6.

5. Applying a BS7910 FAD to the maximum stress for the Kr (Ka applied / K critical) calculation appears to work well. In the experiments large values of Lr (Applied stress / Yield stress) were obtained but these are probably a result of the displacement controlled experiment, so in the absence of further information Lr should be limited in the way specified by BS7910.
6. An initial defect size is required for the calculation. 0.2mm was used for this work. Depending on the fatigue calculations it is possible to update this cycle by cycle. In that case the maximum Kr could occur later in a time history with a larger crack size da a smaller stress than the maximum stress.
7. Using the UTS based on the true stress may also be a reasonable predictor of fracture but that cannot be confirmed again owing to the displacement control of the tests.

8. The fatigue life can be estimated using Coffin Manson type equations. It is recommended that the variant by ($\varepsilon'f/2$) is used and that the coefficients are modified (un-welded describe modification welded) (as reported by Almar [1985]) in order to increase the calculated damage rate. This modification may allow for stable crack growth at the higher strain cycles and for the steel surfaces being less perfect than in the original Coffin Manson experiments.
10. It appears that low cycle fatigue formulas can be used but they need to be modified as calculated in this thesis and as shown in Tables 5.10 & 5.12

The use of strain hardening option increasing joint stiffness and decreasing joint toughness, therefore decrease in fatigue life resulting from the welds [Björk *et al*., 2006].

Table 5.7 shows for these experiments the Smith-Watson-Topper (SWT) method performed best. However it still overestimated the cycles to failure approximately by 2 times.

A reason for this might be that the Coffin-Manson and other equations do not distinguish between:

1) Properties of parent plate, weld metal and HAZ.
2) Cracks growing from weld defects and cracks growing from surfaces with smaller defects.

The reasons are:

- Coffin-Manson and other formulas are used for plain bars as reported in Coffin and Manson [1954], but in this work strain life formulas have been used for T- steel welded connection.
- All welded structures contain defects at some level of examination, and the joint itself is a discontinuity in the structure [ASM, Vol19].

The low cycle fatigue formula overestimated the cycles to failure as shown in Table 5.5.

The reasons for this are unclear but may include :

1) That weld defects were not included in the tests on which the low cycle fatigue formulae were based.
2) The strain ranges in the BCC5 tests were much higher than those on which the low cycle fatigue formulae were based.

CHAPTER 6
DESIGN MODELLING IMPROVEMENT AND DATA OUTPUT

6.1 Introduction

In the previous work there were no bracing gussets plates connection in the column-beam flanges area. Gussets are now added. Their function is to increase the connection overall stiffness and stress distribution control. Figure 6.1 shows the connection model with bracing gussets. A fully welded connection it included two welded gussets 125x125x10mm thickness as flange bracing that is aligned with the webs of the beam and column. The gussets are defined as solid parts with same material properties as the other elements of the connection.

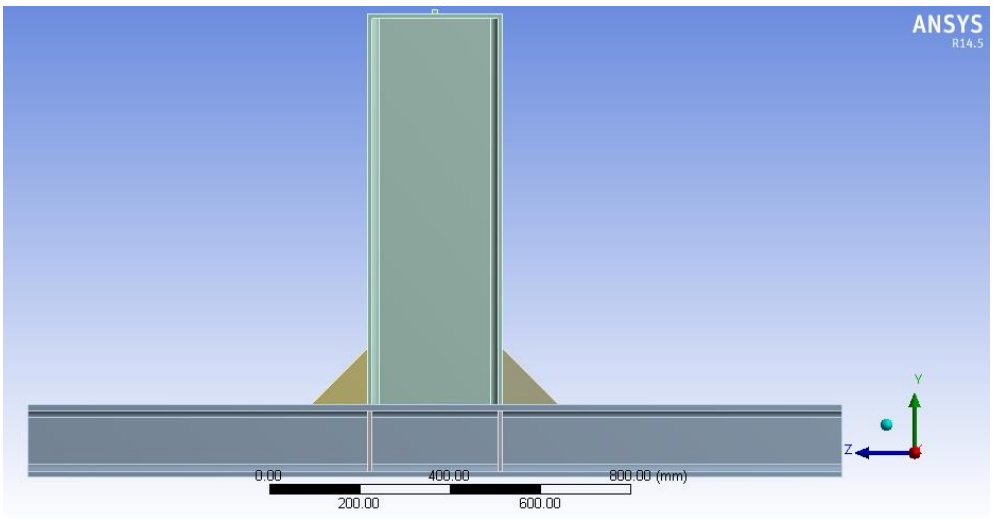

Figure 6.1: Flange bracing and four column web bracing gussets (improved model)

Analysis has been done in ANSYS 14.5 Workbench for BCC5 FE improved models. Table 6.1 shows total strain amplitude and maximum normal stress results for BCC5 base and improved models.

Table 6.1 indicates that total strain amplitude and maximum normal stress results decreased in improved models which means that life cycles of improved models are more than life cycles of base models as shown in Table 6.2.

Table 6.1: Total strain amplitude and maximum normal stress results for base and improved models for BCC5 FE models

Case No.	Total strain amplitude using Coffin -Manson formula $\varepsilon a=\frac{\Delta\varepsilon}{2}$		Maximum normal stress (MPa)	
	base	improved	base	improved
BCC5A	0.0074	0.0043	606.45	470.19
BCC5B	0.0100	0.0039	611.8	371.34
BCC5C	0.0048	0.0022	553.6	430.1
BCC5D	0.0053	0.0028	294.05	242.57

Table 6.2 shows number of cycles to failure for base and improved models using strain life formulas with strain hardening (n`) and factor (ε'f/2), which is the difference between welded and un-welded structure[Almar,1985], as calculated using MathCAD Sec.C.4 Appendix C.

Table 6.3 shows number of cycles to failure for base and improved models using strain life formulas with strain hardening (n`) and modification factor ($\varepsilon' f$ / Fac.) (see Table 5.6).

Table 6.2: Number of cycles to failure for BCC5 base and improved models using strain life formulas including (ε'f/2) considering strain hardening exponent (n`)

Case No.	No. of Cycles to failure Experimental test	No. of Cycles to failure Coffin and Manson		No. of Cycles to failure Morrow &Smith *et al.*		No. of Cycles to failure Smith -Watson - Topper (SWT)	
		Base	Improved	Base	Improved	Base	Improved
BCC5A	16	36	100	36	100	20	40
BCC5B	5	21	123	21	123	12	46
BCC5C	18	66	472	66	472	39	127
BCC5D	23	64	258	64	258	86	243

Table 6.3: Number of cycles to failure for BCC5 base and improved models using strain life formulas including (ε'f/Fac) (see Table 5.6), considering strain hardening exponent (n`)

Case No.	No. of Cycles to failure Experimental test	No. of Cycles to failure Coffin and Manson		No. of Cycles to failure Morrow &Smith *et al.*		No. of Cycles to failure Smith -Watson - Topper (SWT)	
		Base	Improved	Base	Improved	Base	Improved
BCC5A	16	16	46	16	46	14	32
BCC5B	5	5	33	5	33	8	35
BCC5C	18	18	168	18	168	21	77
BCC5D	23	23	103	23	103	55	173

Outline of this chapter:
Section 6.2 displacement vs. force reaction hysteresis loops for FE ANSYS base and improved models
Section 6.3 strain amplitude comparison for BCC5 FE base and improved models measured in critical point.
Section 6.4 normal stress comparison for BCC5 FE base and improved models measured in critical point.
Section 6.5 discussion
Section 6.6 results and conclusion
Section 6.7 summary

6.2 Displacement vs. force reaction hysteresis loops for FE ANSYS base and improved models

Figures 6.2-6.5 show displacement vs. force reaction hysteresis loops for FE ANSYS base model (red) and FE ANSYS improved model (black).

By comparing the data between the FE ANSYS base models force-displacement hysteresis loops which are subjected to the cyclic load with the FE ANSYS improved models force-displacement hysteresis loops which were presented in Figures 6.2-6.5, it can be seen that maximum and minimum values of the applied force for the base model were close to each other and ranged between +190000 to -190000N. But the maximum and minimum values of the applied force for the improved model were close to each other and ranged between +207000 to -207000N. which is 17000N more than value of base model.

The 17000N additional force is a result of the increased stiffness in the connection and the prescribed displacement time history remaining the same. (In real earthquake conditions the increase in stiffness will probably reduce the deflections slightly).

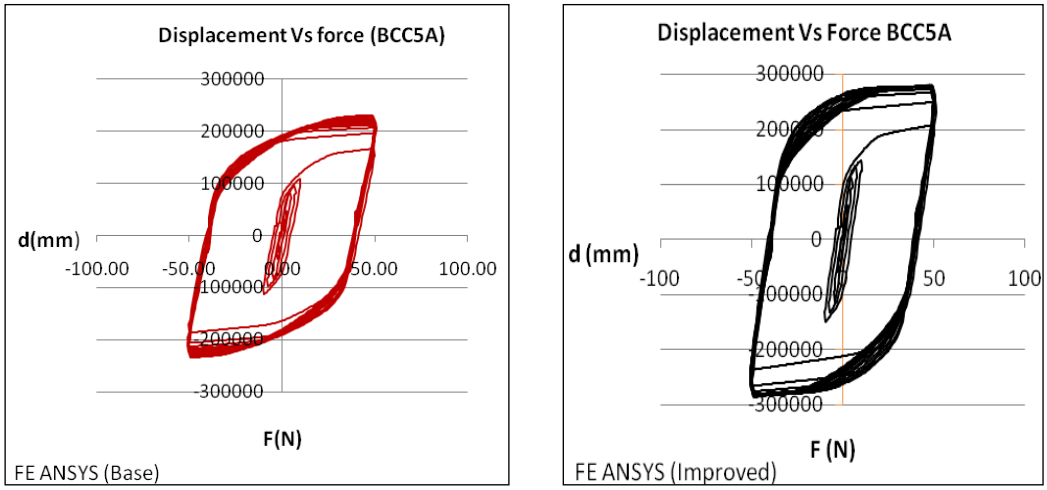

(a) (b)

Figure 6.2: Displacement vs. force reaction hysteresis loops for BCC5A, FE ANSYS (a) base model and (b) improved model

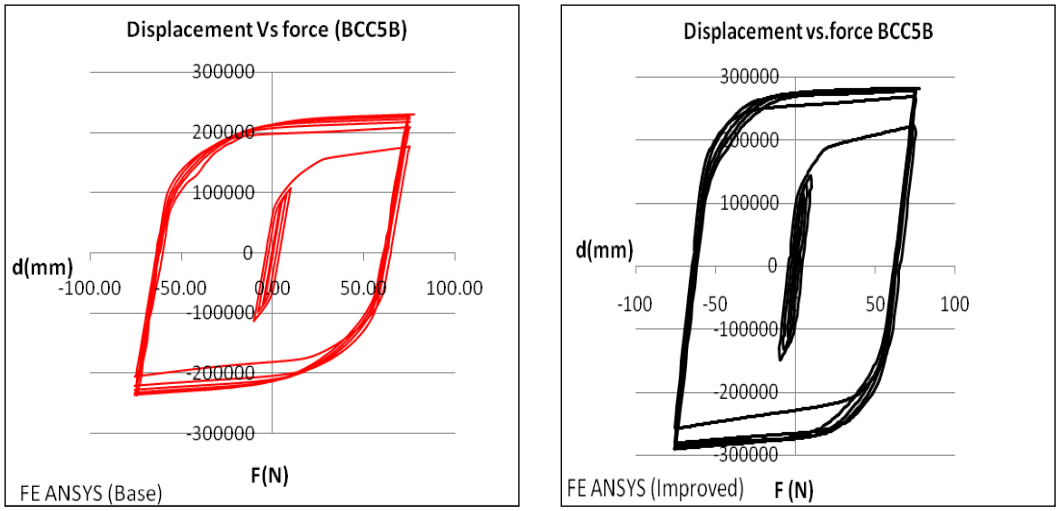

(a) (b)

Figure 6.3: Displacement vs. force reaction hysteresis loops for BCC5B, FE ANSYS (a) base model and (b) improved model

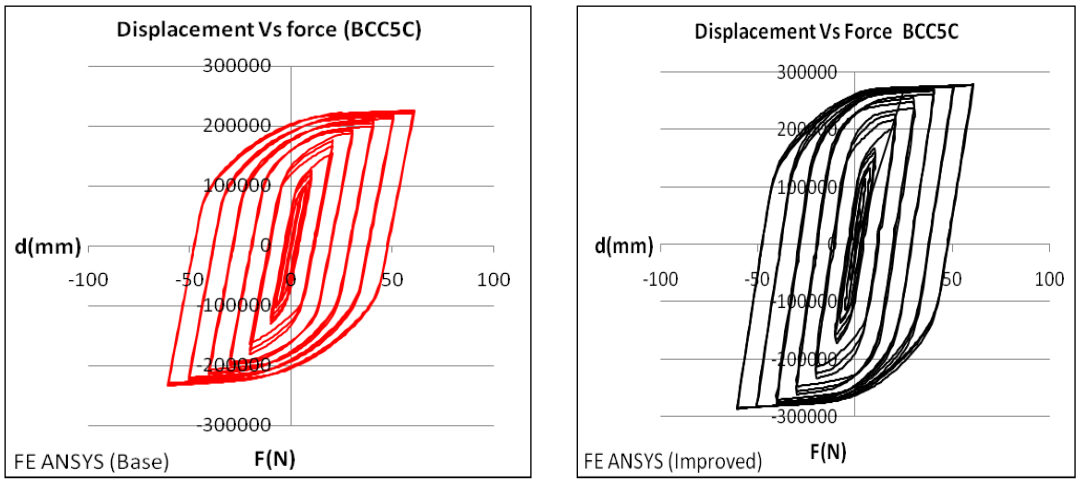

(a) (b)

Figure 6.4: Displacement vs. force reaction hysteresis loops for BCC5C, FE ANSYS (a) base model and (b) improved model

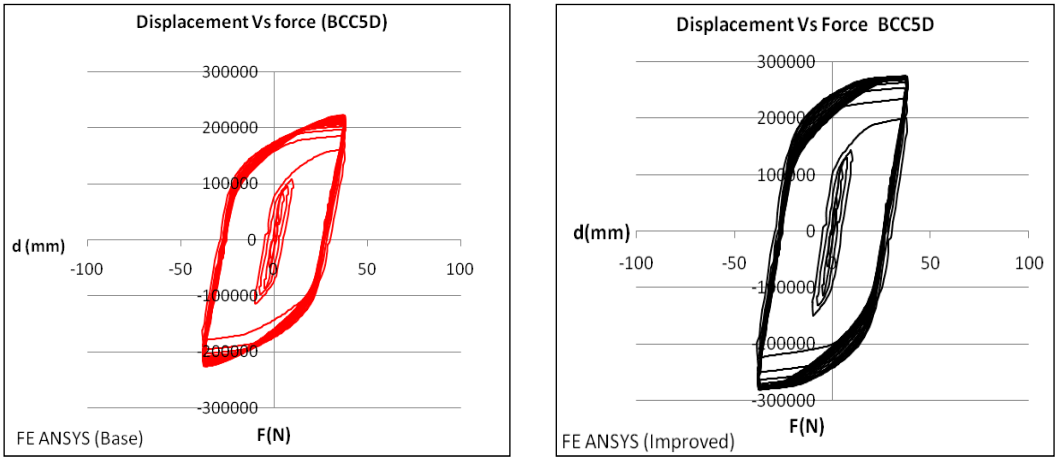

(a) (b)

Figure 6.5: Displacement Vs force reaction hysteresis loops for BCC5D, FE ANSYS (a) base model and (b) improved model

6.3 Strain amplitude comparison for BCC5 FE base and improved models measured in critical point

Table 6.4 shows total strain amplitude for the base models and the improved models, and indicates that failure occurred in the base model when total strain amplitude reached the maximum value of (0.0073) at cycle 16 for BCC5A model. Also from the same table it can be seen that the total strain amplitude of the improved model has a lower value (0.0043) compared to the base model and it's a strong indication that the improved model will survive better in an earthquake for longer (more than 16 cycles).

Table 6.4 shows the same finding as BCC5A model, that the maximum total strain amplitude for BCC5 FE ANSYS base and improved models.

Table 6.4: Shows the difference of strain amplitude for base and improved models output from FE analysis for all BCC5 models

Case No.	No. of cycle to failure (Experiment)	Strain amplitude (base)	Strain amplitude (improved)
BCC5A	16	0.007386875	0.00431875
BCC5B	5	0.01003	0.003992
BCC5C	18	0.004844722	0.002243222
BCC5D	23	0.00532913	0.002821304

6.4 Normal stress comparison for BCC5 FE base and improved models measured in critical point

Table 6.1, indicates that failure occurred in the base model of BCC5A when normal stress reached the maximum value of (606.45 MPa) at cycle 16. Also from the same table it can be seen that the normal stress of the improved model has a lower value (470.19 MPa) compared to the base and it's a strong indication that the improved

model has a longer working life (more than 16 cycles), same finding and indication applied to BCC5B, BCC5C and BCC5D.

Table 6.2 shows the number of cycles to failure, for the BCC5 FE base and improved models. The results indicate that as a result of total strain and normal stresses decreasing in the improved model, the number of cycles to failure have increased, therefore the connection has been improved.

6.5 Discussion

The solution shows that using bracing gussets causes an increase in stiffness, which results in additional forces under prescribed displacement conditions. Nevertheless there is an overall decrease of the total strain amplitude and normal stress as shown in Table 6.1. As a result the number of cycles to failure have increased for all improved models, in comparison with the base models, for all strain life formulas as shown in Table 6.2.

Table 6.3 shows number of cycles to failure for BCC5 base and improved models using strain life formulas including (ε'f/Fac) (see Table 5.6), considering strain hardening exponent (n`), Coffin-Manson and Morrow & Smith *et.al.* showed reasonable results for both BCC5 base and improved models.

Table 6.4 shows a difference of strain amplitude for base and improved models, which indicate that the improved model is not reach the strain amplitude for base model at the end of cycle life, which means that the cycle life for the improved model is longer than the cycle life of the base model for all improved models.
It was noticed for all BCC5 models that the maximum high stress occurs in the panel zone, and that occurs due to shear stresses in the panel zone as discussed in Sec.4.5 and shown in chapter 4, Figure 4.22.

The connection deformation for the improved model under the cyclic displacement loading gives the presented connection high rotational stiffness as a rigid type of connection [Trajanoska *et al.*, 2000].

6.6 Results and conclusion

Based on results, many points can be concluded as follows:

- The advantage of bracing gussets is that they reduce the stresses and strains as shown in Tables 6.1 & 6.4, and move the highest strains away from panel zone (bracing gussets as shown in Figures 6.6 & 6.7 that is not affected by welding defects or heating so it should also be better) to be able to resist high cyclic strains.
- Improved model showed that the maximum strain is less than the maximum strain in base model as shown in Table 6.4, and location of maximum strain is moved to guess plate rather than weld zone as shown in Figure 6.6. Therefore the guess plate make the joint in improved model more ductile than the joint in base model. Life cycles to failure for improved model are more than life cycles to failure base model.
- The plastic hinges occur in the members framing into the joint and is moved away from the beam end.
- The connection is more rigid and this can be beneficial.
- Rigid connections are needed when higher stiffness is required and in structures where additional bracing of the frame may be avoid by including this type of connection. And regardless of the fact of the difficulties that may occur during manufacture, this is usually a designer's choice for connection in cases where greater rotational stiffness, shear capacity and deformation capacity are needed [Trajanoska *et al.*, 2000].
- The fully welded connections can give different characteristics that can change significantly if bracings or additional stiffeners added. The numerical

analysis makes it easier for the designers to explore the connections characteristics and make new connection designs.

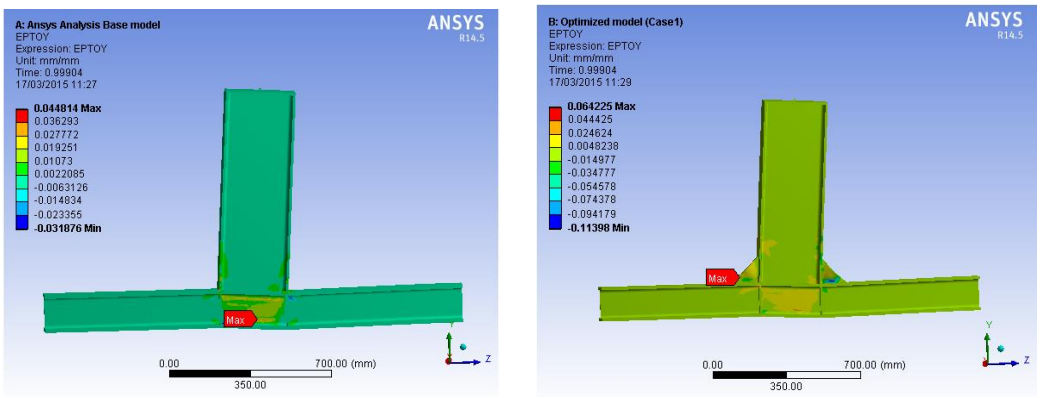

Figure 6.6: (a) Base model strain distribution, (b) improved model strain distribution for BCC5A

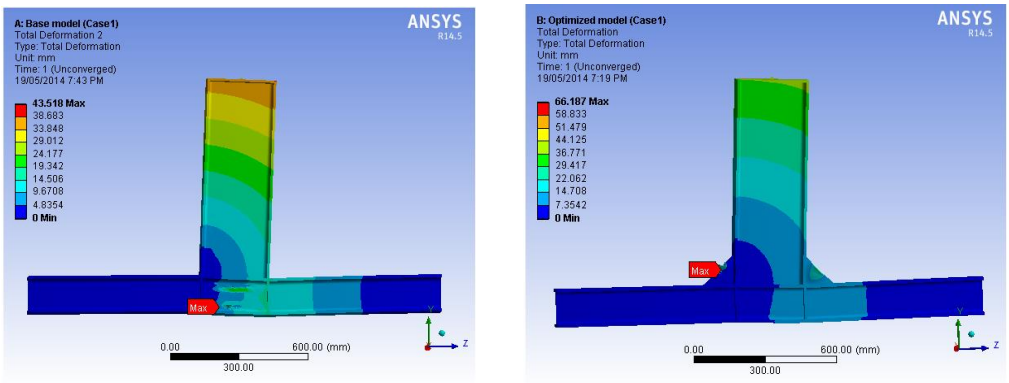

(a) (b)

Figure 6.7: (a) Base model total deformation distribution, (b) improved model deformation distribution for BCC5A

6.7 Summary

Modelling improvement for T-steel welded connection was improved using finite element analysis: displacement vs. force reaction hysteresis loops for FE ANSYS base and improved model, total strain amplitude vs. no. of cycles log-log graphs for base and improved models measured in critical point, normal stress comparison for BCC5 FE base and improved models measured in critical point, discussion, results and conclusion.

Following chapter will be include: conclusions for this study and recommendation for future work.

CHAPTER 7
CONCLUSION AND RECOMMENDATION FOR FUTURE WORK

7.1 Conclusion

7.1.1 General

The steel-T connection is a common type of structural component in most frame structures. In earthquakes these connections may be subjected to cyclic loading that involves large plastic strains. Physical modelling of a cyclically loaded, steel welded connections is expensive and time consuming in both building and laboratory time.

Modelling the connection using FE analysis is becoming fast and low-cost but it is not clear what is the most effective way of setting up the analysis and interpreting the results in conjunction with low cycle fatigue (LCF) formulas or fracture mechanics models.

However failure criteria under the very high strain-range cyclic loads that occur in earthquakes are not well understood.

This thesis has investigated this problem by comparing published experimental work with finite element structural analysis and applied low cycle fatigue (LCF), fracture mechanics and simple stress and cumulative strain limit methodologies.

Physical experiments published by Mele *et al.* [2003] (experiments BCC5A, BCC5B, BCC5C and BCC5D) were used as a basis for the FE modelling and comparison with calculated cycles to failure in this thesis.

7.1.2 Finite element analysis

The finite element modelling used ANSYS V 14.5 with non-linear geometry and non-linear material solid elements of type S 235 JR (EN 10025: 1993), which is equivalent to the U.S. steel grade ASTM A36.

The size of the elements, in the vicinity of the large strains was about 0.5 times the plate thickness with 2 elements through the plate thickness. The material stress strain curve was measured for the material used in the experiments and was provided by Mele *et al.* [2003] .

The results showed that the plastic part of the experimental force time history was predicted well when the experimental displacements were applied to the finite element model. The elastic part was poorer, this was traced to measured stress strain data not including a point corresponding to commencement of yield (the yield point is missing in the reported experimental test results).

The finite element analysis also identified a strain ratcheting effect, even under the applied displacement loading condition, which was explained in terms of the material stress-strain properties.

Failure was not found to occur where the FE analysis predicted the highest strains. The highest strains occurred in panel zone. Shear stress reduces the yield stress in panel zone and may reduce the fracture risk as shown in Sec.4.5.

Stresses, strains and artificial stresses equal to Youngs modulus*total strain and the geometric and arithmetic mean of true stress and artificial stress were calculated, to be used in fatigue, crack growth and failure assessment calculations.

A damage summation method corresponding to reservoir counting and Miner's rule was applied to the strain time histories predicted by the finite element analysis.

Note that σu, from tension tests, has been exceeded in three numerical models (BCC5A, BCC5B and BCC5C).

7.1.3 Applicability of Low Cycle Fatigue equations

The major conclusion of this work is that the Coffin-Manson and Morrow-Smith low cycle fatigue formulas and parameters estimate too many cycles to failure in this region of very low cycle fatigue and are therefore unsafe to apply to earthquake responses without modification. It is possible that they could be used with modified coefficients as calculated in this thesis: the standard value of $\varepsilon' f$ should be divided by about 5 (if the strain hardening version of the formula is used) and about 10 (if the strain hardening version of the formula is not used). See Tables 5.10 and 5.12. However recommending constants at this stage would be premature as more testing and comparison work will be needed; the results obtained (Table 5.6) showed moderate variability but these results are only for a limited range of plastic strain and the contributions from the effects of welds versus plain steel and very low cycle fatigue against the larger numbers of cycles considered in ordinary low cycle fatigue are not yet clear.

- Different LCF life equations by Coffin-Manson, Morrow & Smith *et.al* and SWT were compared with the experimental results. There was no agreement between the absolute results of the three equations. For the trend of total strain amplitude result; Coffin-Manson formula and Morrow-Smith formula showed similar trend with the experiments while the SWT formula was different, because the maximum stress was included in SWT formula, and this gave a poorer result. Comparing the coefficient of variation values from the methods indicates that Smith-Watson-Topper method (SWT) had the

highest coefficient of variation while the Coffin-Manson and Morrow & Smith *et al.* have the same, lower, values. This also indicates that modified Coffin-Manson and Morrow & Smith methods are more applicable to estimating low cycle fatigue in earthquake conditions.

7.1.4 Use of cumulative failure strain to determine cycles to failure

In three of the four tests (A, C and D) the cumulative true strain (summing both increasing and decreasing strain increments) in comparison with the true strain on failure in a simple tension test experiment was a safe failure criterion.

7.1.5 Fracture mechanics crack growth

Crack growth was calculated using the Paris Equation to give the advancement da of crack per unit cycle dN, as a function of the amplitude of stress intensity factor ΔK with material constants A and m from BS7910 and with applied stress ranges from the non-linear analysis. However, the predicted crack growth was too small to explain the observed failures using ordinary Paris Law coefficients and the true stress ranges.

In order to investigate whether the plastic strain might result in a better fit the stress used in the Paris equation was modified to strain*E (and the geometric and arithmetic mean of stress and strain*E). However none of the methods showed a large total crack extension during the whole cyclic loading process. It is possible that these results are correct and that the crack extension per cycle is very small with the final failure being a result of fast fracture.

It is also possible that there is some stable crack growth during the increasing tensile strain part of each cycle. To estimate this requires a knowledge of the "R curve" for the region of crack extension, which I do not have (and which a designer would not usually be able to estimate).

7.1.6 Use of cumulative failure strain to determine cycles to failure

In three of the four tests (A, C and D) the cumulative true strain (summing both increasing and decreasing strain increments) in comparison with the true strain on failure in a simple tension test experiment was a safe failure criterion.

7.1.7 Applicability of Fracture Mechanics Failure Assessment Diagram (FAD)

The applicability of the FAD (which usually is used as a predictor of failure under a single application of load) was examined.

The detailed material properties required for a fracture mechanics assessment (toughness, R-curve and initial defect size data) were not available and a robust fracture mechanics analysis would require very much more modelling and computer run time. Also for practical application, that would require the fracture mechanics data that is typically not available to the designer, so this thesis has applied some simplified fracture mechanics, which could also be more easily used by designers.

The application of a fracture mechanics failure assessment diagram (*Lr, Kr*) using maximum stress, cumulative stress (σ_T) and last half cycle stress range was investigated.
(DNV-RP-F108 [2006], recommended that CTOD should be between 0.1mm to 1mm). For CTOD = 0.1mm (Kr values would be 0.31 times these values for CTOD = 1mm).

The cumulative stress gives Lr and Kr that are extremely large and so predict failure to early. With the CTOD of the test specimen assumed to be about 1mm rather than 0.1 it was found that, if a FAD is to be used to indicate failure, then both Lr and Kr should be based on the maximum stress, with no allowance for cumulative cycles and no increase based on increasing the stress to represent the plastic strains.

So it appears that the FAD methodology does help to predict the final failure (which is its usual application) but it does not help to predict the number of cycles to failure under very low cycle fatigue.

7.1.8 Use of measured UTS as a fracture criterion

Using the UTS based on the true stress may be a reasonable predictor of fracture in realistic conditions but it is difficult to confirm this owing to the displacement control used in these tests that may have allowed the structure to survive for longer and at higher strain levels than in real dynamic earthquake conditions. However for these tests a safe failure criterion would be that failure occurred when the true stress range in the earthquake exceeded twice the true failure strain in a simple tension test experiment.

7.1.9 Overall conclusion and tentative recommendation for fracture assessment

From this research, for the very low cycle fatigue and/or fracture in earthquakes:

1) Conventional Coffin Manson equations can be applied but need a large correction factor of 5 to 10 depending on the particular formula.
2) Fracture mechanics based on crack growth under cyclic loads grossly over-predicted the observed lives.
3) Calculating the cumulative true strain (up and down going) and comparing with the true failure strain in a tensile test could also allow an estimate of the number of cycles to failure.
4) The BS7910 failure assessment diagram, using true peak stress and with typical weld defects was possibly a reasonable indicator of failure, however the appropriate fracture toughness to use in the method will not usually be known.
5) Comparing half the true cyclic stress range with true ultimate tensile stress in a conventional tensile test provided a safe estimate of failure in these tests.

6) The fatigue assessment by using reservoir method based on damage accumulation when D=1.0 which is recommended by [EC3:1993-1-9:2005] and [BS7608, 2014] as explained in Sec.3.5.3 chapter 3. Table 5.5 chapter 5 shows the damage for all BCC5 models are less than 1.0.

7.2 Recommendation for future work

- This work was based on existing experimental data and adds to the existing comparisons of experimental and calculated low cycle fatigue data. However, future experimental work should ensure that the material properties near the heat affected zone of welds are better characterized. Realistic modelling of these properties is essential for the finite element simulations to reliably estimate the fracture behaviour of welded beam-to-column moment connections.
- To understand the importance of different toughness in the weld metal, heat affected zone and parent steel a set of tests with different combinations of these properties should be performed and analysed.
- The toughness of the steel and welds should be measured to determine the Kc value for use with the FAD.
- J-R curves should also be measured in future experiments and used to investigate whether stable tearing might occur.
- Loading rate and temperature effects on toughness and the J-R curves should be considered.
- To understand the importance of different initial defects in the welded connections a set of tests, on simple geometry, with different manufactured imperfections should be performed.
- To characterize the low cycle fatigue with different numbers of cycles to failure, similar T-steel connections could be subject to different forced deflections, to obtain failure in 1 to 1000 cycles.

- An experimental and numerical modelling protocol and data that should be presented should be defined.
- Scale effects should be assessed by performing full-scale and small scale tests.
- Further numerical and experimental models investigation are needed to study different failure modes for joints with different proportions, for instance cracking starting in the "panel zone".
- The FE models, with some experimental verification, should be extended to include different connection geometry.
- To establish an overall, FE-based, design tool for joints in earthquake prone structures, the connection analysis methodology needs to predict the low-cycle rotational capacity and material force-deflection characteristics that can be input into a global analysis.
- Once a good methodology has been achieved then FE based investigations could be used to increase the fatigue life of steel joints, possibly by increasing material toughness and reducing strain concentrations and by controlling initial defects. This should enhance existing design and detailing procedures for welded steel connections that encourage the connection to fail in a ductile manner.
- The costs and benefits of improved welding processes, that for instance reduce slag inclusions and porosity and increase toughness, should be assessed.
- If toughness is found to be important then suitable, cost-effective, methods for the quality control of toughness need to be determined.
- Whole structure seismic damage evaluation is needed to verify and demonstrate the application of LCF life prediction. Note that the evaluation may need to consider a sequence of large earthquakes during the required life of the structure.

- The applicability to other branches of structural engineering should be considered, for instance explosions in chemical works and offshore platforms and structural response to military or terrorist explosions.
- More comparison of experimental and FEA models of steel connections are needed, particularly to assess the accuracy of the combination of particular FEA models and LCF models.
- Finite element results corresponding to very low cycle fatigue experiments (by others).
- A demonstration of strain ratcheting even under displacement controlled cyclic displacement loading.

APPENDIX A
EXPERIMENT SETUP AND DATA COLLECTION

A.1 Introduction

Experimental data related to this investigation was obtained from literature [Mele *et al*.,2003]. During my study at the University of Strathclyde, there was, unfortunately, no fund available for me to carry out any experimental work, as well as there being no suitable experimental facilities available inside the University. However after a full consideration and deep discussion with my supervisor we have agreed to use experimental data available from literature, this also helped me to save time toward finishing my PhD work.

This Appendix summarises: connection description, welding, test program, test setup, test procedure and standards including: welded connection type, beam and column length, and loading protocol.

A.2 Scope of the study (this section is closely based on Mele *et al.* 2003)

A.2.1 Connection description

A crack's strength and propagation path depend on residual stresses. These residual stresses are generated by the welding process as a result of the temperature gradients and metallurgical modifications. To reflect the impact of these values, the computation of the residual stresses was performed by modelling the welding process. However, this is a difficult task because it is necessary to consider many physical phenomena that occur during the welding process. Thus, the goal of this Appendix part was to compute a 3D balanced residual stress field generated by the welding process to enter at the beginning of the simulation of a cycle large scale beam-to-column test.

The structure under investigation, described in Figure A.1, was a fully welded connection between a beam and a column. The beam was a horizontal I-beam (a typical European beam section IPE300, which is considered equivalent to W12x30 U.S. wide flange section), and the column is a vertical I-beam (HE160B possibly equivalent to W8x24 U.S) Table A.1.

Table A.1: Beam and column sections of specimens and comparison to U.S equivalent profiles

Element section	h (mm)	b_f (mm)	t_w (mm)	t_f (mm)	h_w/t_w	$b_f/2t_f$	Mass per length (kg/m)	I_{xx} (cm^4)	Z_x (cm^3)
Beam									
IPE	300	150	7.1	10.7	39.2	7.0	42.2	8356	628
U.S section									
W 12X6.5X30	313	166	6.6	11.2	44.03	7.41	44.5	9934	708
W 12X6.5X26	310	165	5.8	9.7	50.10	8.51	39.0	8527	612
W 10X8X33	247	202	7.4	11.0	30.41	9.18	49.0	7097	
Column BCC5									
HE 160 B	160	160	8	13	16.75	6.15	42.6	2492	354
U.S section									
W6X6X25	162	154	8.1	11.6	17.14	6.64	37.1	2220	310
W8X6.5X24	210	165	6.2	10.2	29.13	8.09	36	3438	379

[Mele *et al*., 2003]

The beam section is typically welded to the column; complete joint penetration welds are applied at the beam flanges and fillet welds are applied at both sides of the beam web. Flange continuity plates are commonly utilized for stiffening the column panel zone and to transfer the bending moments, as shear forces, into the panel zone (PZ). The highly stressed panel zone can make a substantial contribution to the overall deformation of the connection

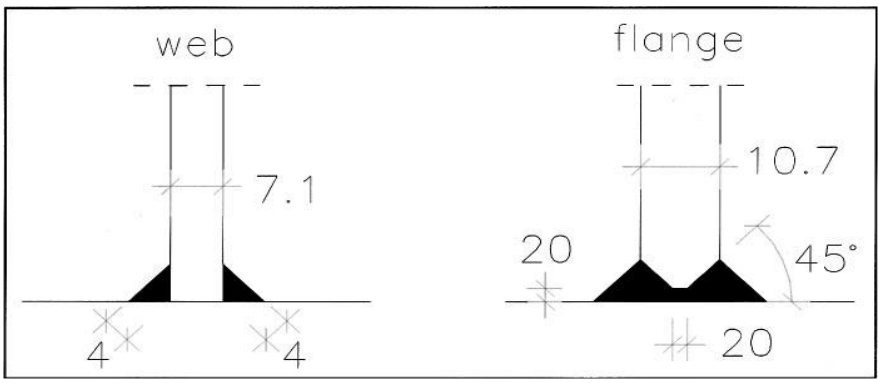

Figure A.1: Welded beam-to-column connection with dimensions in millimetres [Mele *et al*. 2003]

A.2.2 Welding

The specimens are T-shaped beam-column sub assemblages, consisting of a 1,000 mm long beam and a 1,800 mm long column. The beam flanges have been connected to the column flange by means of complete joint penetration (CJP) double bevel vee groove welds, while fillet welds have been applied between both sides of the beam web and the column flange as shown in Figure A.1 . The manual metal-arc welding MMAW, also known as shielded metal arc welding (SMAW) process has been used for the specimens with E7018-1 electrodes. Typically metal inert gas and flux cored arc welding, are gradually superseding metal arc (MMA) welding for reasons of productivity and cost effectiveness Steel Construction Institute, 1992), [Mele *et al*., 2003].

A specific procedure for minimizing defects in the welds is often implemented: After having welded the beam flanges from the top, the root opening is back-gouged (i.e. cleaned of impurities from the bottom) and the opening is filled by means of fillet welds. This procedure, minimizing the defects that may result at the bottom of the flange and reduces the potential of crack formation.

All welds have been made in the horizontal position, no special access holes have been necessary to make the connection, and no weld runoff tabs have been used to

make the CJP welds. In the welding process, special care has been paid in order to minimize porosity and defects, thus reducing the potentials of crack formation.
The control of the welds has been made through non destructive tests using ultrasonic equipment. The continuity of the connection through the column has been ensured by horizontal 10 mm thick plate stiffeners, fillet welded to the column web and flanges.

This experiment describes fully welded of beam to column connections of a wide experimental program carried out at the Material and Structures test Laboratory of the Instituto Superior Tecnico of Lisbon [Mele *et al*., 2003].

A.3 Test Program

The test program by Mele *et al*. [2003] was carried out with the aim of defining the effects of the column size, and the loading history on the connection behaviour. The following section discusses: the design of the specimen, the experimental setup, and the loading histories which have been utilized in the tests. The experimental results are presented through hysteresis loops, global performance parameters and the major factors affecting the cyclic behaviour: the failure modes and moment-rotation are considered.
It should be noted that the BCC5 specimens are characterized by a weak column since the nominal plastic moment of the column is slightly larger than half of the nominal plastic moment of the beam.

A.3.1 Experimental set-up, instrumentation plan

The test setup, represented in Figure A.2(a), mainly consisted in a foundation, a supporting girder, a reaction RC wall, a power jackscrew, and a lateral frame at Figure A.2(b). Due to the characteristics of the test setup the column was the horizontal element while the beam was the vertical one. The power jackscrew (capacity 1,000 kN, stroke 6400 mm) is attached to a specific frame, prestressed

against the reaction wall, and designed to accommodate the screw backward movement.

The power jackscrew is connected to the end of the beam through a pinned connection in order to avoid the introduction of moments. The specimen is connected to the supporting girder through two steel elements Figure A.2(a) end supports (A and B). The connections between the ends of the column and the steel elements (A and B) are a fixed type [Calado, 2010-2014, per. comm.].

The supporting girder is fastened to the reaction wall and to the foundation by means of prestressed bars. The lateral frame was designed to prevent specimen' lateral displacement and is located at the end of the beam Figure A.2(b). An automatic testing technique was developed to allow computerized control of the power jackscrew, of the displacement, and of the transducer used to monitor the specimen during the testing process Figure A.2(b).

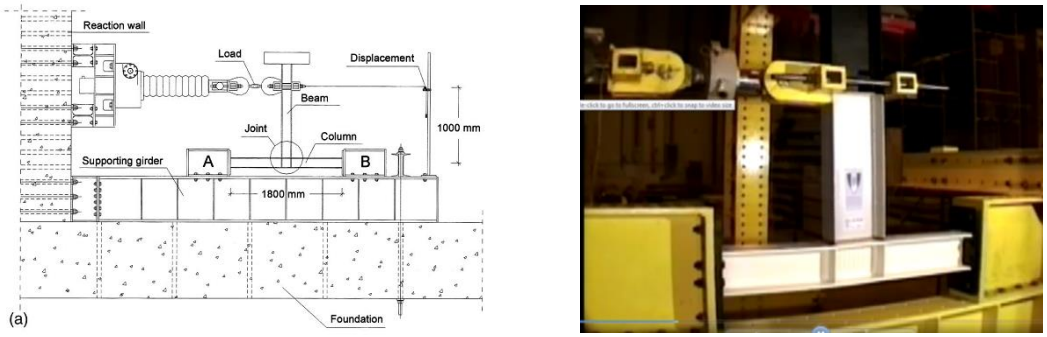

(a) (b)

Figure A.2: (a) Consists in a foundation, supporting girder, reaction RC wall and power jackscrew (b) a lateral frame [Calado, 2010-2014, per. comm.]

Specimen has been instrumented with electrical displacement transducers (LVDTs), which record the displacement history at the point when the load applied in order to obtain a careful documentation of the various phenomena occurring during the test as show in Figure A.3. The specimen has been tested up to failure under cyclic loading

histories. This latter test type has been carried out according to the basic loading history recommended in ECCS [1986] [Mele *et al.*, 2003].

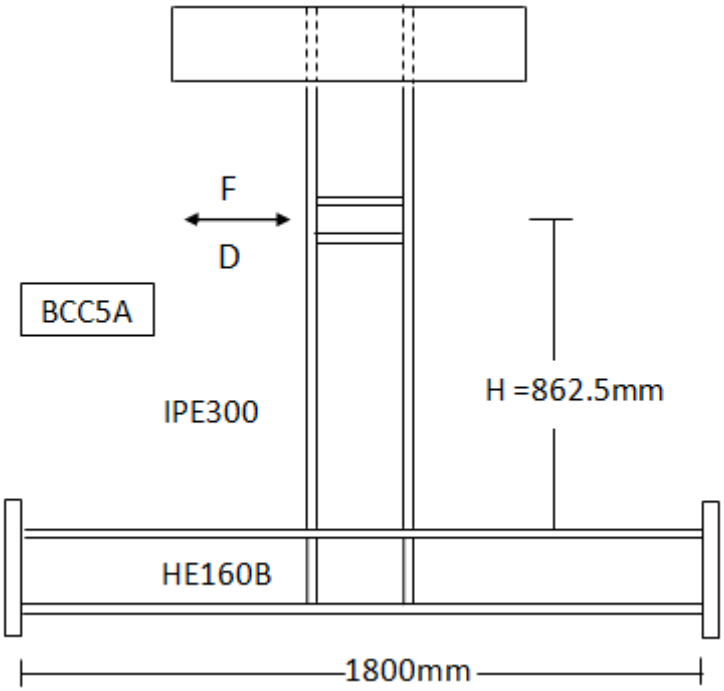

Figure A.3: Specimen instrumentation

A.3.2 Loading History

In particular, details are reported about the loading history, the total number of cycles performed during the tests, N_{tot}, and the number of cycles to conventional failure, N, which has been evaluated in accordance with the approach presented in the following. Moreover, the type of failure is reported, too. As a general remark, it should be mentioned that the spread of plasticity was observed only in the nodal zone, while beam and column remained in the elastic range in the other parts of the specimen. As a consequence, joint behaviour is herein presented with reference to the global response of the specimen, i.e., by considering the relationship between the force applied at the beam free end, F, and the associated displacement, Table A.2 provides the test loading history, defined in terms of cyclic amplitude of the applied beam tip displacement (*d*); cyclic amplitude of the applied beam tip displacement

normalized to theoretical value of the specimen yielding displacement (*dy)* (*d*/*dy*); cyclic amplitude of the applied interstory drift angle (*d*/*H*), i.e., *d* normalized to the distance *H* between the beam tip and the column centre line (H). The stepwise increasing amplitude was been carried out according to the basic loading history recommended in ECCS [1986], which is sketched in Figure A.4. This basic loading history is divided into steps, with three symmetrical cycles repeated in each step *j* at a peak deformation *dj*. The increase of the peak deformation per step is defined as a multiplier of the theoretical value of the yielding displacement of the specimen, *dy*.

Table A.2: Loading history test

Case No.	d(mm)	d/dy	d/H (%)
BCC5A	C. type ±50	C. type ±5	C. type ±5
BCC5B	C. type ±75	C. type ±7.5	C. type ±7.5
BCC5C	S.I type (ECCS)		
BCC5D	C. type ±37.5	C. type ±37.5	C. type ±37.5

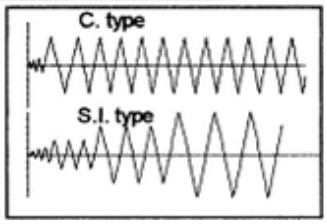

Legend: C. type = cyclic constant amplitude loading history
S.I. type = cyclic stepwise increasing amplitude loading history

[Mele *et al*. 2003]

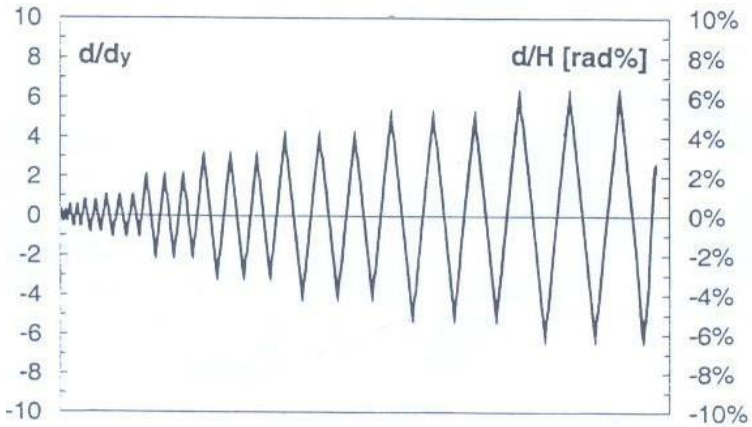

Figure A.4: ECCS cyclic stepwise increasing amplitude loading history

[Mele *et al*. 2003]

Accordance to the ECCS [1986] procedure, specimen response was not affected by remarkable deterioration of strength, stiffness and for energy absorption capability. Collapse was sudden, without warning signs, owing to a crack either at the weld toes or in the base material as shown in Figure A.5. Furthermore, in case of brittle collapse, the failure mode was observed, which was due to a crack formed in the centre of the weld between the beam flange and the column and propagated toward the edges, was observed in all the types of considered rigid joints.

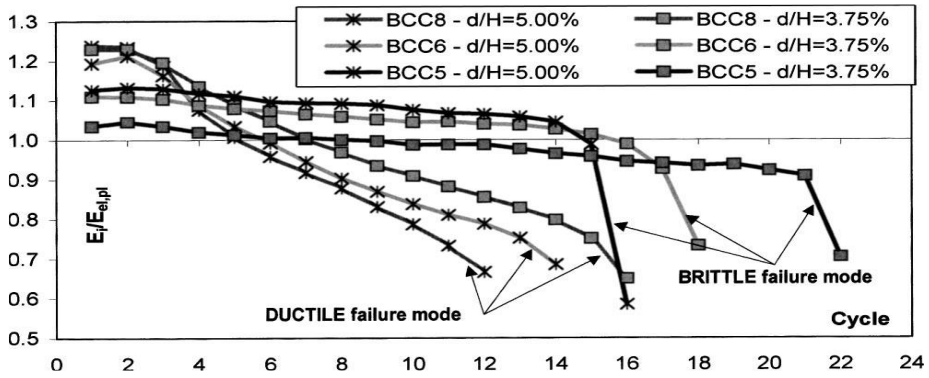

Figure A.5: Normalised cyclic energy [Mele et al., 2003]

A.3.2.1 Data acquisition is variable during the test

It is not possible to give a value because the data acquisition is variable during the test.

The actuator that applies the displacement and the force is electric and has variable speed of 0.1 mm / sec and 2 mm / sec.

The data acquisition is made at the end of each increment of displacement.

However it is taking into account that the criterion of reading (data acquisition) is based on two conditions: maximum increment of displacement or maximum increment of force. When the increment of displacement or force exceeds the maximum values the acquisition of data is performed.

To illustrate: in the elastic range if the increment of force that governs the data acquisition while in plastic range is the displacement.

As an order of magnitude, Calado says that the maximum increments of the force are normally of the order of 25 kN-50 kN while for the displacements are of the order of 0.2 mm to 2 mm [Calado, 2010-2014, per. comm.].

A.3.3 Experiment results

As can be derived from the *M-d*/*H* curves, the cyclic behaviour of specimens BCC5 is characterized by a great regularity and stability of the hysteresis loops up to failure, with no deterioration of stiffness and strength properties at an increasing number of cycles. The very last cycle in this test presents a sudden and sharp reduction of strength, corresponding to the physical collapse of the specimen.

A summary of the number of complete plastic cycles to collapse and failure mode of all four BCC5 specimens is shown in Table A.3.

The collapse has always occurred in a brittle mode, due to a fracture close to the weld, initiated in the beam flange and propagated also in the web. This collapse mode is related to the significant distortion of the joint PZ, which gives rise to high stress and strain concentrations at weld locations. While considerable distortion of PZ occurred during all test, no large plastic deformation in the beam was observed.

Figure A.6 shows photos of specimens test BCC5 at the end of the test. This failure mode is representative of what was observed for the BCC5 specimens, i.e., visible PZ distortion; brittle failure mode with cracks either at or close to the beam-to-column weld locations, and no plastic hinge in the beam was expected such behaviour one by Mele *et al*. [2003], on the basis of the relative strength values provided in the section ‘‘specimen properties.’’

Figure A.6: BCC5 specimens at the end of the test [Calado, 2010-2014, per. comm.]

The rigid joint with the weaker column (BCC5) exhibited a very stable behaviour, in terms of force-displacement hysteresis loops as shown in Figure A.7, with a very limited deterioration of stiffness, strength and energy absorption capability. Collapse was due to the fracture of the (IPE300) beam flange in the vicinity of the welded connections.

In the case of small amplitude cycles, brittle failure was observed with cracking in the welds. On the contrary, in the case of a weaker column (BCC5), the plastic hinge was not so evident, the plastic deformation of beam flanges was small, and the failure occurred due to cracking at the welds.

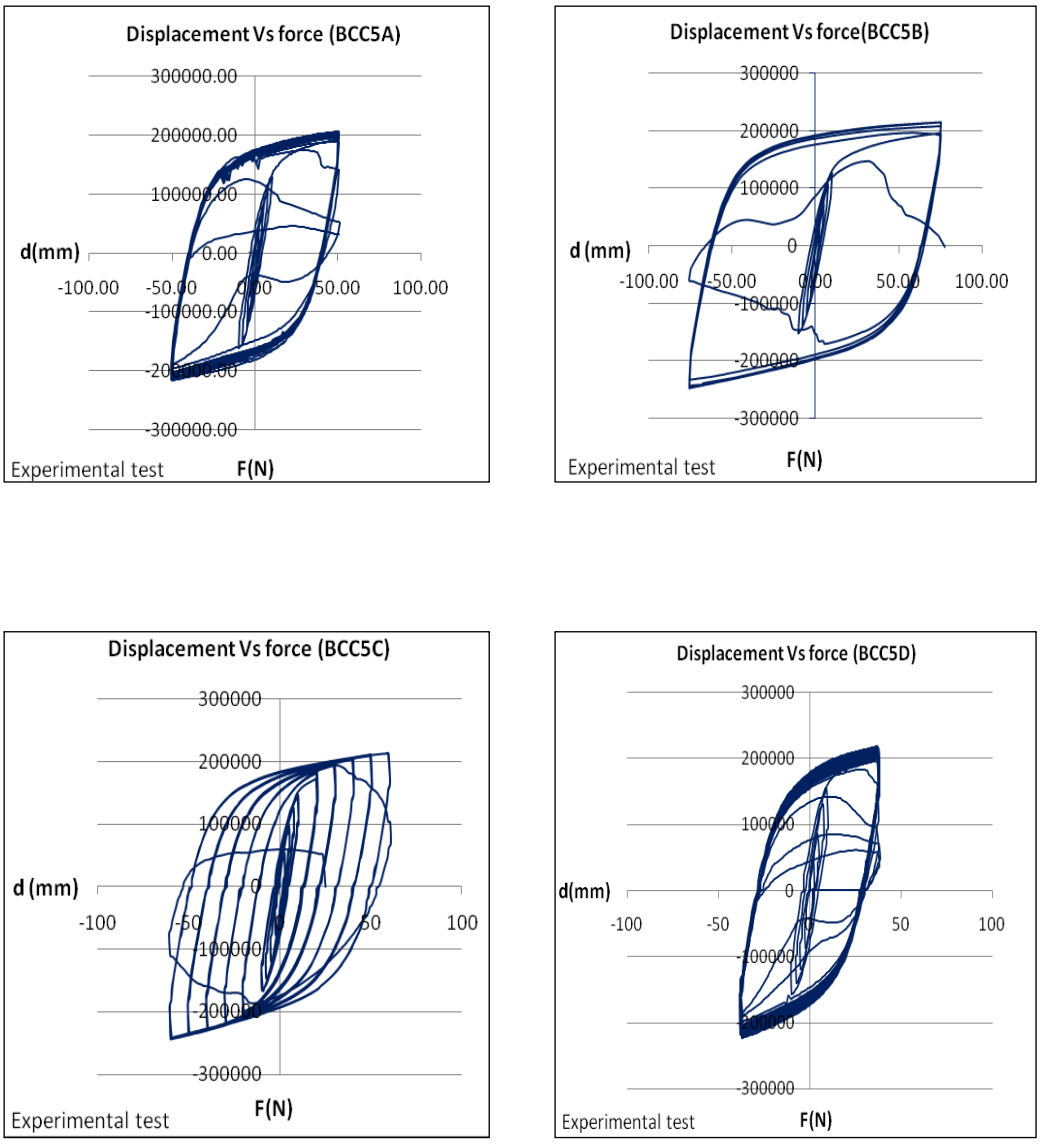

Figure A.7: BCC5 hystrises loops force-displacement tests

[Calado, 2010-2014, per. comm.]

Table A.3: Number of plastic cycles and failure modes of BCC5 specimens

Case No.	No. cycles	Failure modes
BCC5A	16	Crack on the beam flange close to the weld, propagated in the beam web.
BCC5B	5	Fracture of the beam flange near the weld.
BCC5C	18	Crack on the beam flange close to the weld, propagated in the beam web.
BCC5D	23	Fracture of the beam flange.

[Mele *et al*., 2003]

Table A.3 shows the failure mode of each specimen. It seems to be that the overall behaviour of all BCC5 tests was similar, but the difference was related to the appearance or not of a small crack before the collapse in cases BCC5A and BCC5C the failure started with a crack but cases BCC5B and BCC5D without crack [Calado, 2010-2014, per. comm.].

Table A.4 shows average of actual yield stress and ultimate stress measured for beam and column properties.

Table A.4: Average of actual measured properties of BCC5

	Beam IPE300		Column HE160B	
Variable	Flange	Web	Flange	Web
f_y (MPa)	274.8	305.5	323.1	395.6
f_u (MPa)	404.6	412.6	460.2	490.1
YR	1.47	1.35	1.42	1.24

[Mele *et al*., 2003]

A.3.3.1 Effect of panel zone on cyclic behaviour and failure mode

The BCC5 specimens, even though able to experience high plastic deformation levels, have shown sudden failure modes in all cyclic tests, with hysteresis loops practically overlaid and no degradation of the flexural strength up to the very last cycle, where a sharp decay of the load carrying capacity occurred due to fracture that generally developed in the proximity of the weld and the buckled zones of the beam flanges. These aspects are more deeply analyzed in the next subsection.

A.3.3.2 Effect of loading history on failure mode

No significant effect of the loading history on the failure mode of the BCC5 specimens was observed throughout the experimental program.

A.3.3.3 Effect of loading history on hysteretic behaviour

In Figure A.5 the normalized cyclic energy, i.e., Ei /Eel,pl , defined as the ratio between the absorbed energy in the single plastic cycle Ei and the energy that might be absorbed in the same cycle if it had an elastic-perfectly plastic behaviour Eel,pl is plotted against the number of cycle subjected to the tests at d/H53.75% and d/H55.0%.

The sudden decay, due to brittle failure mode, of the normalized cyclic energy for the BCC5 specimens, the first kind of trend can be derived, while in the case of d/H53.75% (brittle failure mode), the behaviour is close to the one observed for the BCC5 specimens.

Therefore, it can be concluded that, in the case of ‘‘brittle’’ failure mode, the behaviour of the different specimens show large scatters in the number of cycles to collapse and in the values of the cycle energy at collapse.

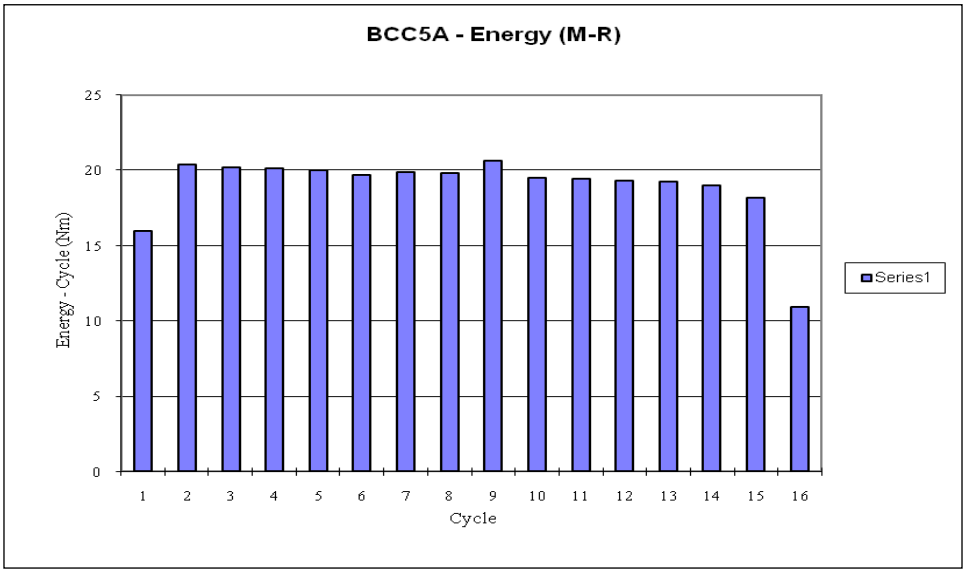

Figure A.8: Energy - cycle chart [Calado, 2010-2014, per. comm.]

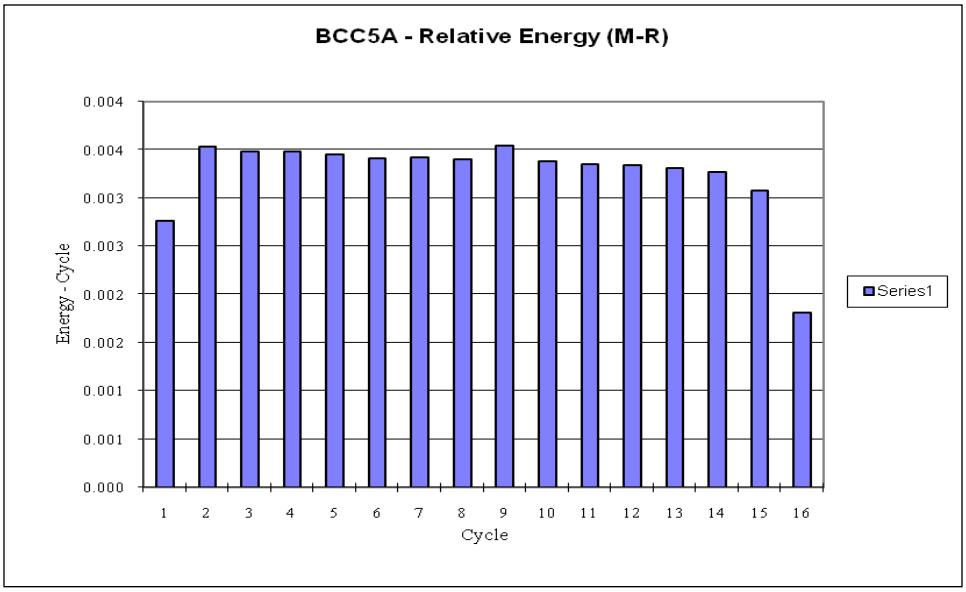

Figure A.9: Energy - Cycle chart [Calado, 2010-2014, per. comm.]

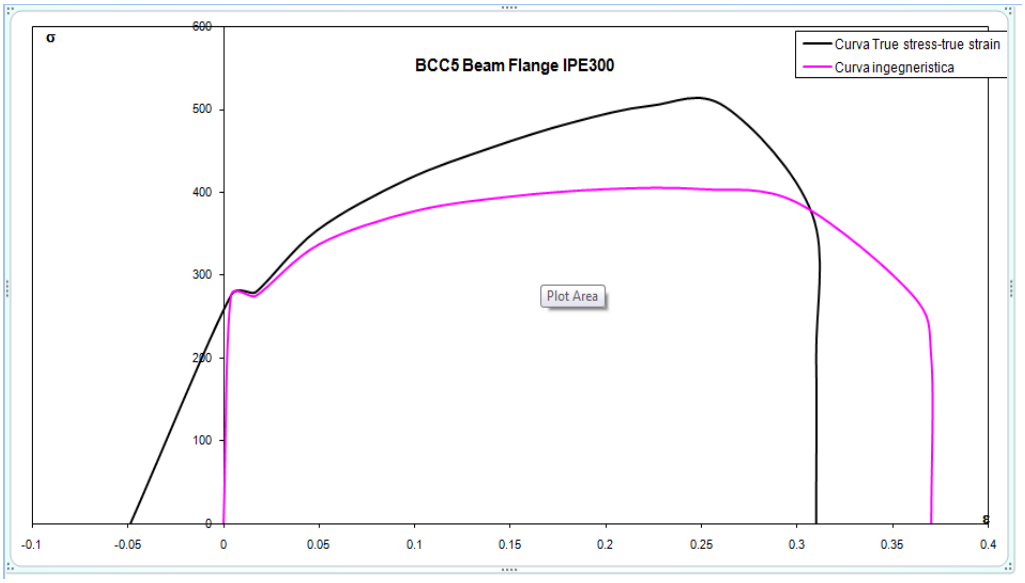

Figure A.10: Beam flange true stress- strain (black) and engineering stress- strain (purple) curves [Calado, 2010-2014, per. comm.]

Table A.5: Beam flange stress-strain

Beam Flange				TRUE STRESS		TRUE STRAIN	
	0		0		0		0
f_y^*	274.78	ε_y^*	0.0038245	f_y^{**}	275.8259	$\varepsilon_{y^*}^*$	0.003817
f_{y1}^*	274.78	ε_{1^*}	0.0166	$f_{y1^{**}}$	279.3363	$\varepsilon_{1^{**}}$	0.016464
f_{y2}^*	337.5	ε_2^*	0.05	$f_{y2^*}^*$	354.3750	ε_2^{**}	0.04879
f_{y3}^*	377.5	ε_{3^*}	0.1	$f_{y3^*}^*$	415.2500	$\varepsilon_{3^{**}}$	0.09531
f_{y4}^*	395.00	ε_{4^*}	0.15	$f_{y4^*}^*$	454.2500	$\varepsilon_{4^{**}}$	0.139762
f_{y5}^*	404	ε_{5^*}	0.2	$f_{y5^*}^*$	484.8000	$\varepsilon_{5^{**}}$	0.182322
f_{y6}^*	404	ε_{6^*}	0.25	$f_{y6^*}^*$	505.0000	$\varepsilon_{6^{**}}$	0.223144
f_{y7}^*	387.5	ε_{7^*}	0.3	$f_{y7^*}^*$	503.7500	$\varepsilon_{7^{**}}$	0.262364
f_u^*	275	ε_{u^*}	0.3605	$f_{u^*}^*$	374.1375	$\varepsilon_{u^{**}}$	0.307852

[Calado, 2010-2014, per. comm.]

A.4 Summary

Appendix A was focused on experiment setup case study and data collection by Mele et al.[2003] and Calado [2010-2014, per.comm.], including: connection description, welding, test program, test setup, test procedure and standards including: welded connection type, beam and column length, and loading protocol.

Following Appendix B is focusing on finite element input and output including: displacement vs. number of substeps graphs for base and improved models (input), displacement vs. force reaction hysteresis loops for base models (output), total strain vs. number of substeps for BCC5 FE ANSYS models, reservoir method (calculating FDI) and plastic strain vs. number of substeps for BCC5 FE ANSYS models (calculating ratcheting strain).

APPENDIX B
FINITE ELEMENT INPUT AND OUTPUT

This Appendix is showing the finite element input and output, the outline of this Appendix summarises:

Section B.1 displacement vs. number of substeps graphs for base and improved models.

Section B.2 displacement vs. force reaction hysteresis loops for base models.

Section B.3 total strain vs. number of substeps for BCC5 FE ANSYS models, and reservoir method (calculating FDI)

Section B.4 plastic strain vs. number of substeps for BCC5 FE ANSYS models (calculating ratcheting strain).

Section B.5 Normal stress vs. no. of substeps for BCC5 FE ANSYS models (calculating FAD and crack growth rates)

B.1 Displacement vs. number of substeps graphs for base and improved models (input)

Applying cyclic displacement loading is explained in Sec.4.2.4 chapter 4.

Figures 4.11 and B.1 show displacement vs. number of substeps for base and improved models for BCC5A, BCC5B, BCC5C and BCC5D respectively.

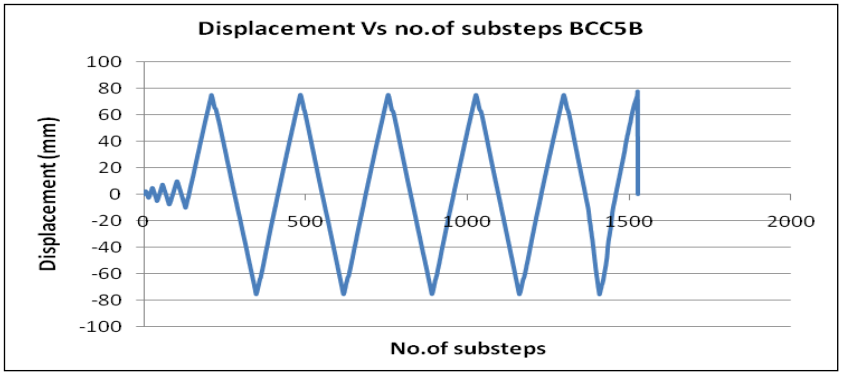

(a)

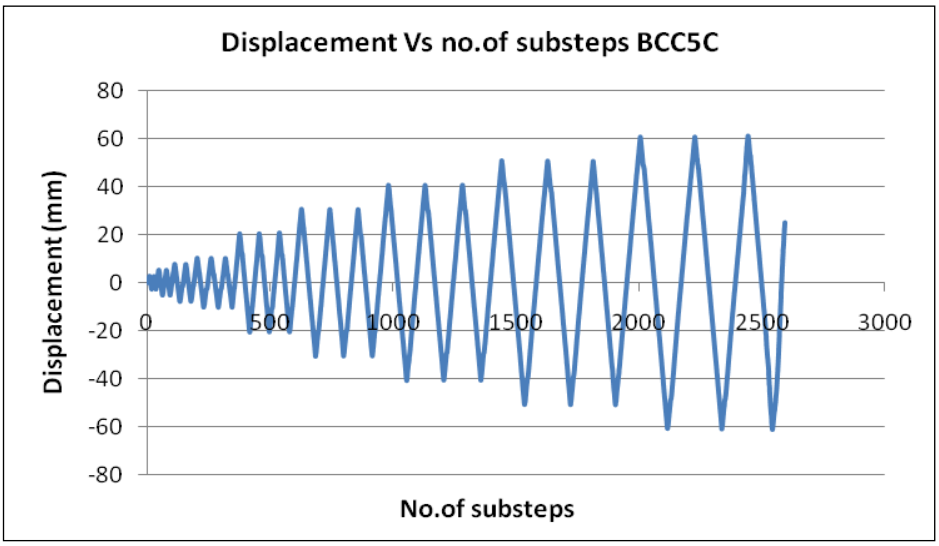

(b)

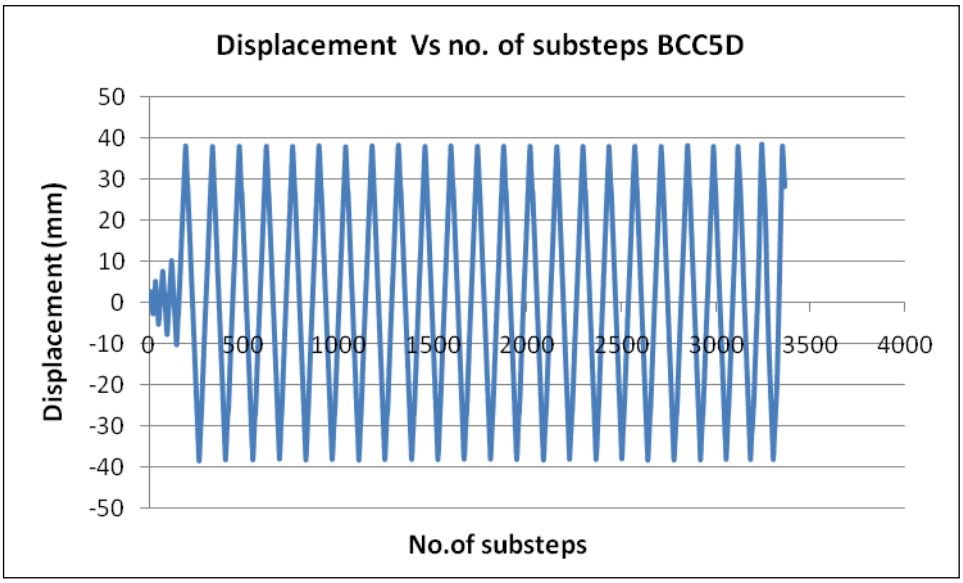

(c)

Figure B.1: Displacement vs. number of substeps for base and improved models input;(a) (BCC5B),(b) (BCC5C) and (c) (BCC5D)

B.2 Displacement vs. force reaction hysteresis loops for base models (output)

Validation model results using FE model hysteresis loops are explained in Sec.4.4.1 and shown in Figures 4.17-4.20.

Figure B.1 shows displacement vs. force reaction hysteresis loops for FE ANSYS models output for BCC5A, BCC5B, BCC5C) and BCC5D respectively.

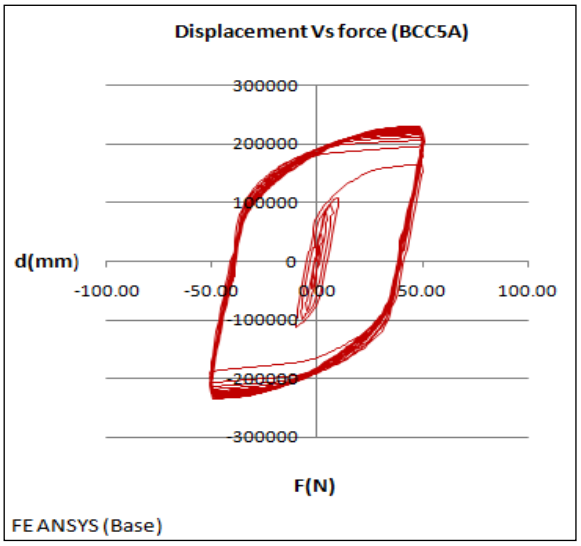

(a)

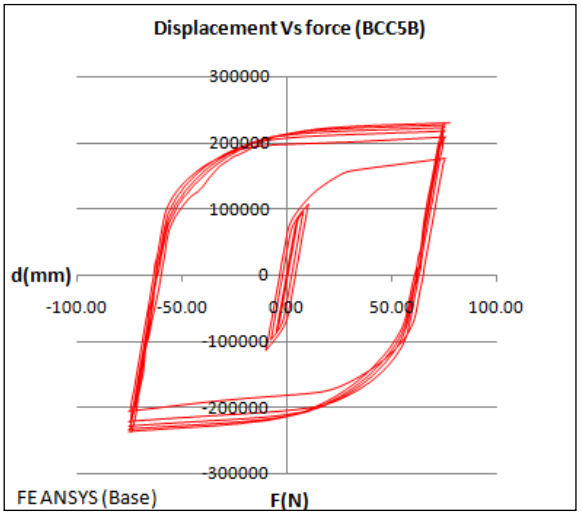

(b)

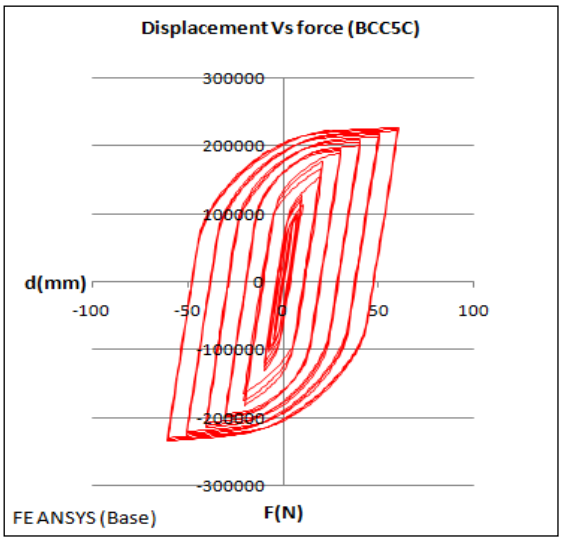

(c)

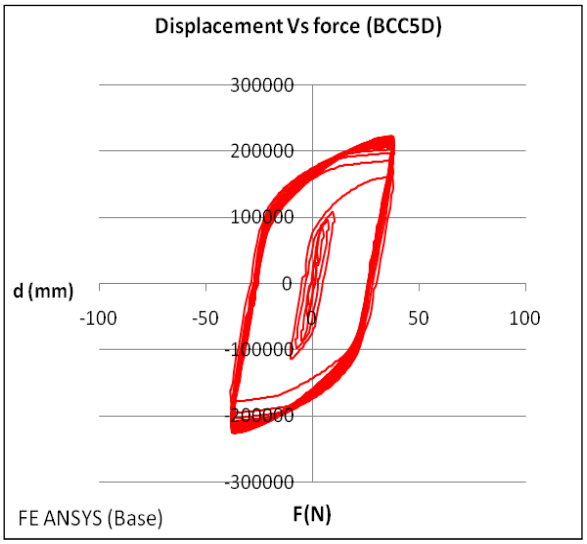

(d)

Figure B.2: Displacement vs. force reaction hysteresis loops for FE ANSYS models output;(a) (BCC5A),(b) (BCC5B),(c) (BCC5C) and (d) (BCC5D)

B.3 Total strain vs. no. of substeps for BCC5 FE ANSYS models, reservoir method (calculating FDI)

Figures 5.3 and B.3 show total strain vs. no. of substeps is measured in the highest strain location , reservoir method is been used to calculate fatigue damage index as explained in Sec.5.2.2 and FDI results are illustrated in Table 5.5.
Plot contours for critical location are shown in Figures D.4-D.7 Appendix D.

It was difficult to get total strain from FE ANSYS output as explained in Sec.4.2.4.

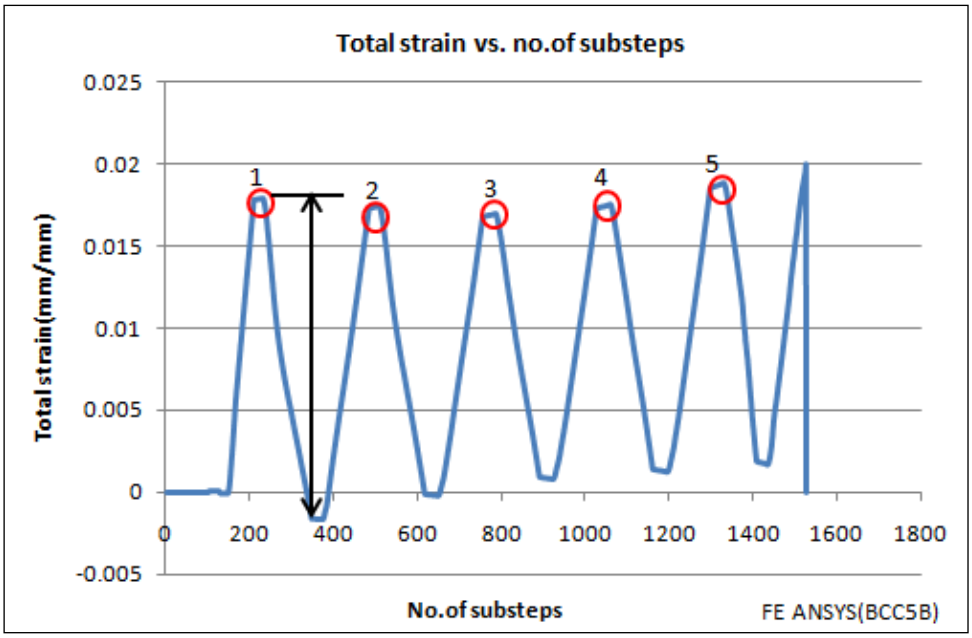

(a)

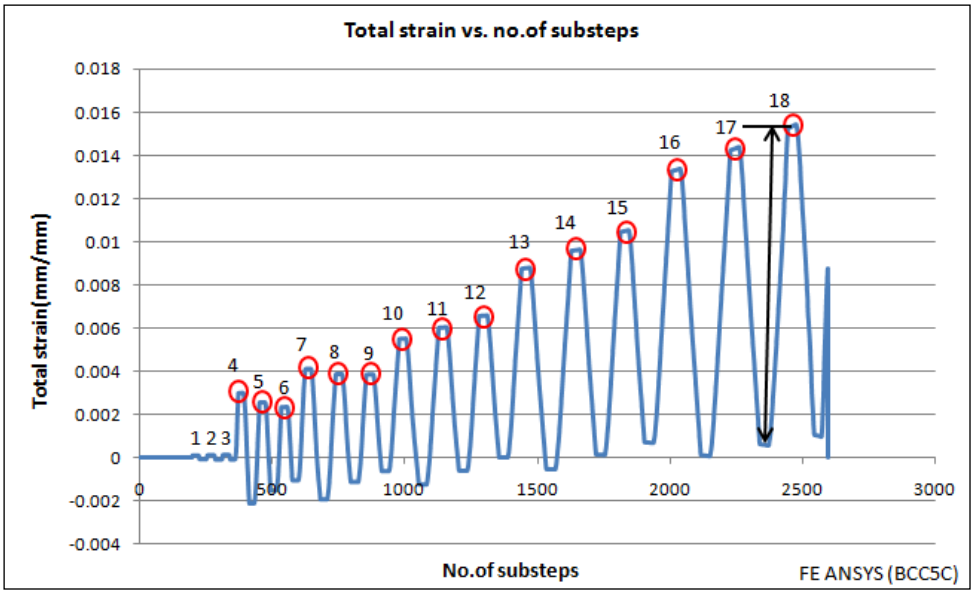

(b)

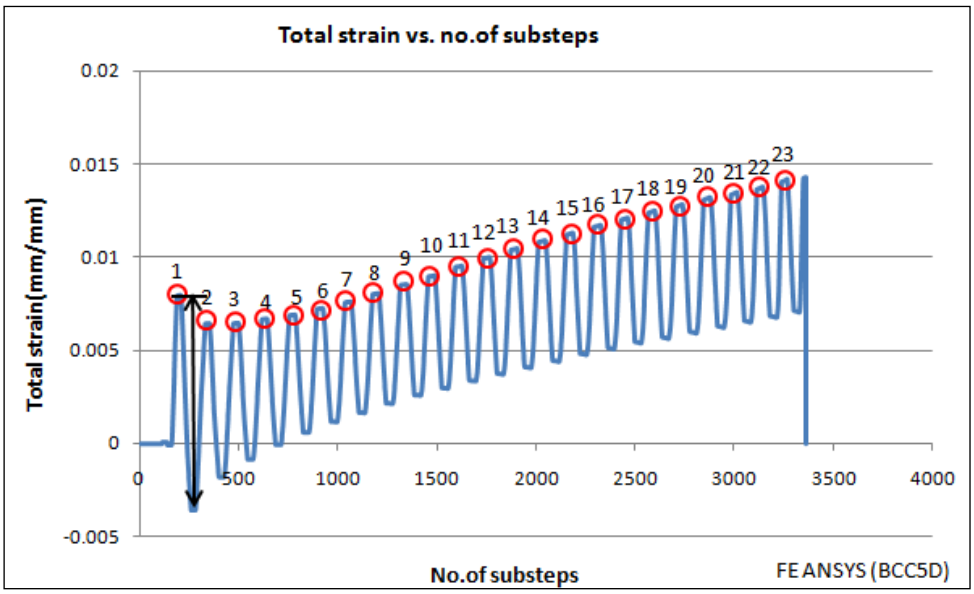

(c)

Figure B.3: Total strain vs. no. of substeps for FE ANSYS models (output);(a) (BCC5B),(b) (BCC5C), and (C) (BCC5D)

B.4 Plastic strain vs. no. of substeps for BCC5 FE ANSYS models (calculating ratcheting strain)

Figure B.4 shows plastic strain vs. no. of substeps is measured in the highest strain location , plastic strain graphs are used to calculate ratcheting strain as explained in Sec.4.6.1 and ratcheting results are illustrated in Table 4.6. Plastic strain vs no.of substeps for BCC5A is shown in Figure 4.25.

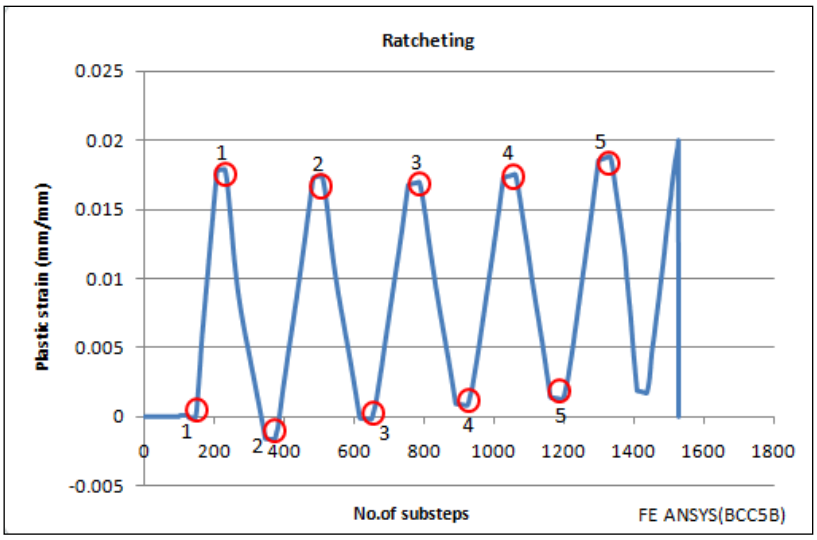

(a)

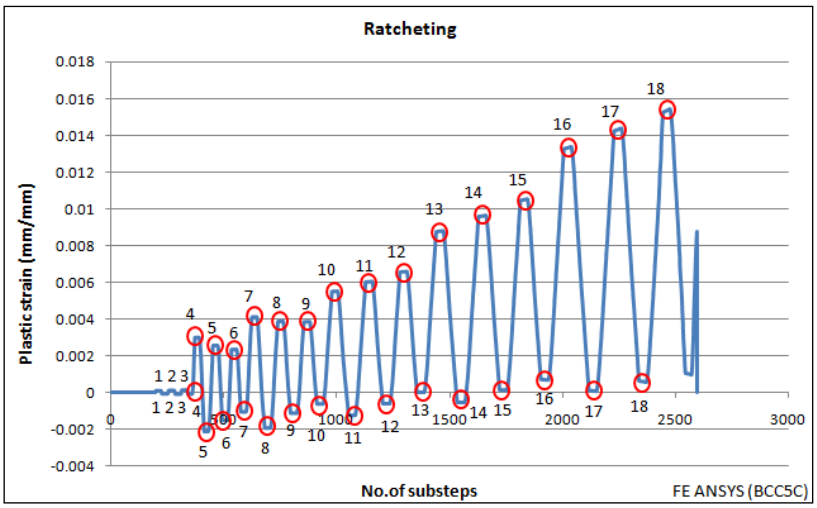

(b)

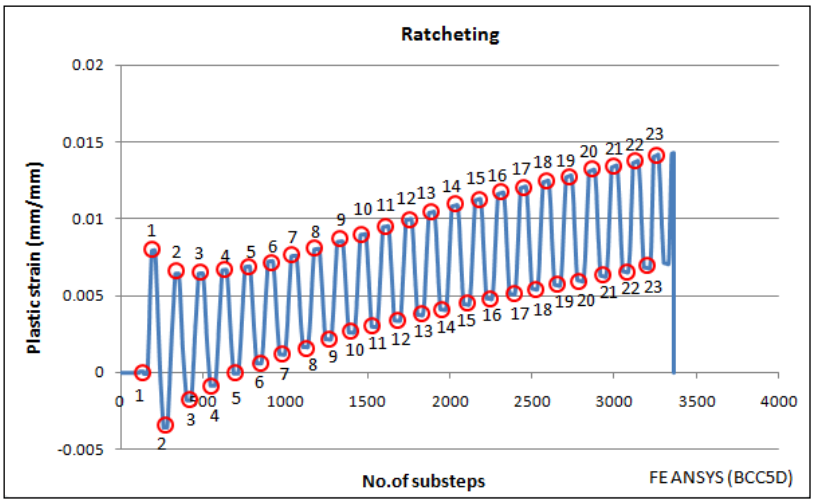

(c)

Figure B.4: Plastic strain vs. no. of substeps for FE ANSYS models (output);(a) (BCC5B),(b) (BCC5C), and (C) (BCC5D)

B.5 Normal stress vs. no. of substeps for BCC5 FE ANSYS models (calculating FAD and crack growth rates)

Figure B.5 shows normal stress vs. no. of substeps is measured in the highest strain location , normal stress graphs are used to calculate crack growth rates as explained in Sec.5.4 and illustrated in Tables 5.23 and shown in Figure 5.5 for BCC5A model.

Tables 5.23, C.4,C.7 and C.10 show results of crack growth rates calculations based on stress ranges, stress modified by (strain*E) and Geometric mean of stress and (strain*E) for BCC5A, BCC5B,BCC5C and BCC5D respectively.

Figures 5.5, C.2,C.3 and C.4 represents Tables 5.23, C.4,C.7 and C.10 respectively, which are show crack growth represents stress ranges , modified stress by strain*E, Geometric mean of stress and strain*E and mean of stress and strain*E ranges) vs. no. of cycles. Normal stress vs. no. of substeps for BCC5A is shown in Figure 5.1. Sec.5.2.1.1.

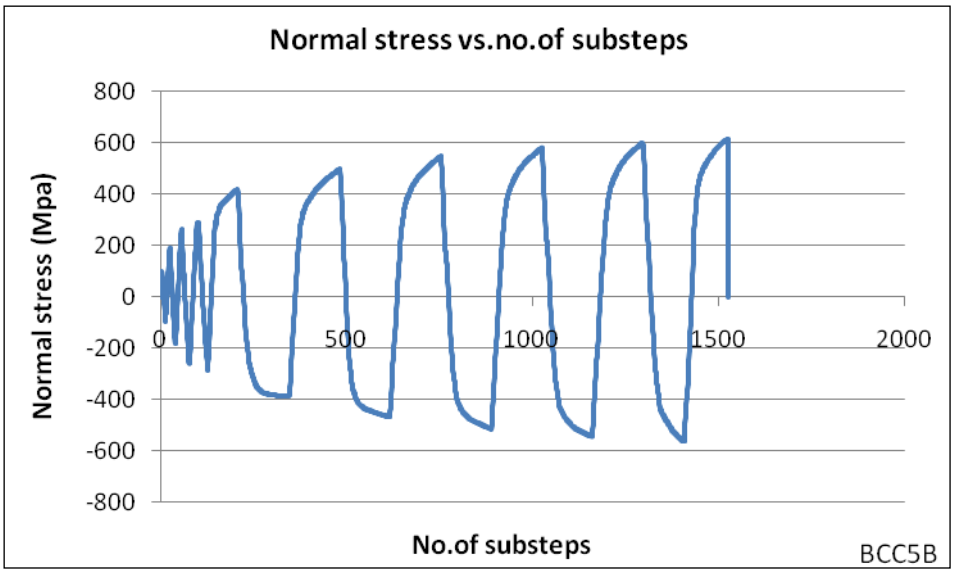
Normal stress vs.no.of substeps
Normal stress (Mpa)
800
600
400
200
0
-200
-400
-600
-800
0
500
1000
1500
2000
No.of substeps
BCC5B

(a)

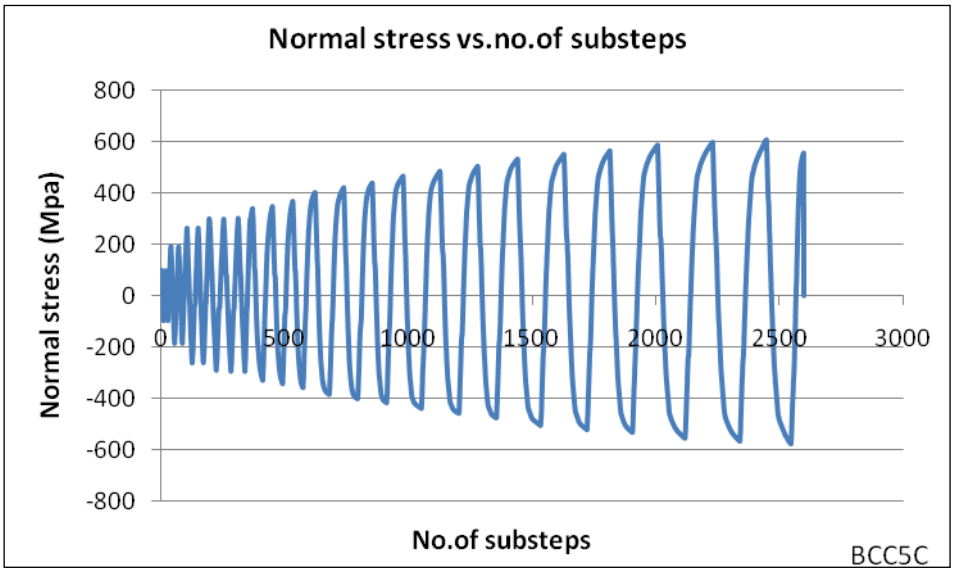
Normal stress vs.no.of substeps
Normal stress (Mpa)
800
600
400
200
0
-200
-400
-600
-800
0
500
1000
1500
2000
2500
3000
No.of substeps
BCC5C

(b)

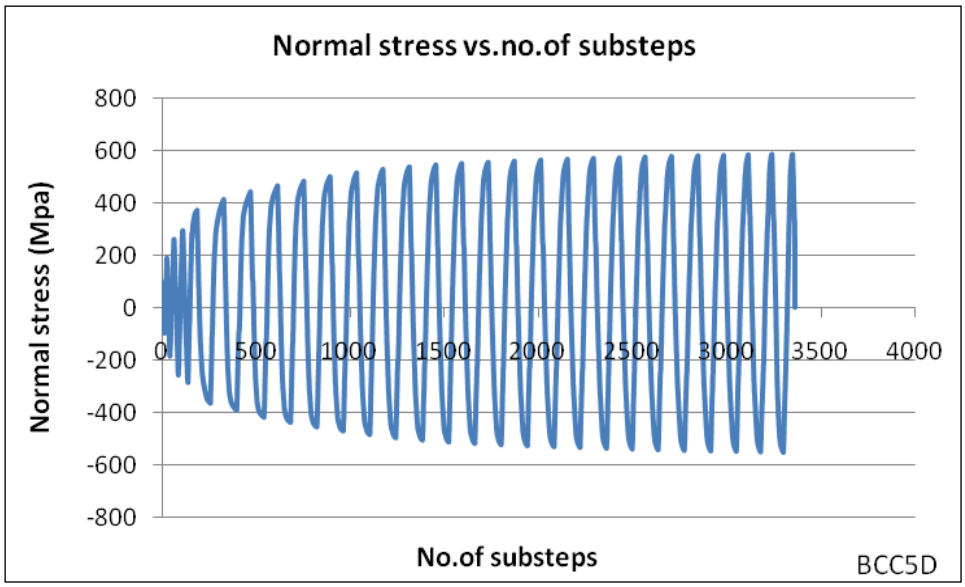

(c)

Figure B.5: : Normal stress vs. no. of substeps for FE ANSYS models (output);(a) (BCC5B),(b) (BCC5C), and (C) (BCC5D)

B.6 Summary

Appendix B was focused on finite element input and output including: displacement vs. number of substeps graphs for base and improved models , displacement vs. force reaction hysteresis loops for base models, total strain vs. number of substeps for BCC5 FE ANSYS models, reservoir method (calculating FDI) and plastic strain vs. number of substeps for BCC5 FE ANSYS models (calculating ratcheting strain).

Following Appendix C is showing calculation of strain amplitude and fatigue damage index including: strain life formulas (strain amplitude calculation without using n`), relation among b,c and n` (strain amplitude calculation using n`), fatigue damage index, calculating fatigue damage index using MathCAD (including n'), calculating fatigue damage index using MathCAD (excluding n'), panel zone stiffness MathCAD calculations (stress-strain graph correction), failure assessment diagram (FAD) calculation and crack growth rates.

APPENDIX C
CALCULATING STRAIN AMPLITUDE AND FATIGUE DAMAGE INDEX

The strain amplitude, calculated by the ANSYS FE analysis, may be the maximum or directional components of total strain, plastic strain or elastic strain. In this work the critical location was in the beam. At that location the total strain results used are those in the direction parallel to the beam's axis. The maximum stress is also the stress in the direction of the beam's axis. All the results are taken from the FE ANSYS at the critical point. in Y-direction.

There were four experiments that were subject to FE analysis. These were given letter and case numbers as shown in Table C.1.

Table C.1: Number of plastic cycles and failure modes of BCC5 specimens

Case No.	No. cycles
BCC5A	16
BCC5B	5
BCC5C	18
BCC5D	23

[Mele *et al*., 2003]

Table C.2: Cyclic and fatigue properties of base ,weld, and heat affected materials for ASTM A36/E60S-3 welds

Material	A36-HAZ
Cyclic strain hardening exponent, n`	0.215
Fatigue strength cofficient, σ`f	724Mpa
Fatigue ductility cofficient, ε`f	0.218
Fatigue strength exponent,b	-0.066
Fatigue ductility exponent,c	-0.492

[Higashida *et al*., 1978]

Outline of this Appendix summarises:

Section C.1 strain life formulas (strain amplitude calculation without using n`)

Section C.2 relation among b,c and n` (strain amplitude calculation using n`)

Section C.3 fatigue damage index

Section C.4 calculating fatigue damage index including (n') using MathCAD

Section C.5 calculating fatigue damage index excluding (n') using MathCAD

Section C.6 panel zone stiffness MathCAD calculations (stress-strain graph correction)

Section C.7 failure assessment diagram (FAD) calculation, and

Section C.8 crack growth rates

C.1 Strain life formulas (strain amplitude calculation without using n`)

Strain life formulas are explained in Sec.3.1.2.2 chapter 3, and Sec.5.3 chapter 5. Calculating results for strain amplitude using strain life formulas is illustrated in Table 5.9 Sec.5.3 using (ε'f/2), for BCC5 FE models without considering cyclic strain hardening (n`), and Table 5.10 using modification factor (ε'f/ Fac.).

Cyclic and fatigue properties of base, weld, and heat affected materials for ASTM A36/E60S-3 welds are illustrated in Table C.2.

Strain life formulas are:

Coffin-Manson formulas:

$$\frac{\Delta\varepsilon}{2} = \frac{\sigma_f'}{E}(2N_f)^b + \varepsilon_f'(2N_f)^c$$

Morrow and Smith *et al.*:

$$\varepsilon_a = \frac{\sigma_f' - \sigma_{mean}}{E}(2N_f)^b + \varepsilon_f'(2N_f)^c$$

Smith-Watson-Topper (SWT):

$$\sigma_{max}\,\varepsilon_a E = (\sigma_f')^2(2N_f)^{2b} + \sigma_f'\varepsilon_f' E(2N_f)^{b+c}$$

Difference among these formulas is that Morrow and Smith *et al*. is including stress mean (σ_{mean}) and Smith-Watson-Topper (SWT) is including stress maximum (σ_{max}). These formulas are calculating strain amplitude due to cyclic loading for plain steel member, but in this work, they are used to calculate strain amplitude for T-steel welded connection.

C.1.1 BCC5B Coffin and Manson

$\frac{\Delta\varepsilon}{2}$ = εa = Total Strain amplitude, which is half strain range Δε to be compared with total strain amplitude FE Analysis in critical point in Y-direction.

σ`f ,ε`f, b and c are obtained from Table C.2

Nf = 5 cycles Table C.1

b= -0.066 and *C*= -0.492

Including factor divide fatigue ductility coefficient by2 ($\varepsilon' f/2$) for difference between welded and un-welded [Almar,1985].

$$\frac{\Delta\varepsilon}{2} = \frac{\sigma' f}{E}(2Nf)^b + \varepsilon' f(2Nf)^c$$

Solution:

$$\frac{\Delta\varepsilon}{2} = \frac{\sigma' f}{E}(2Nf)^b + \varepsilon' f(2Nf)^c$$

$$\frac{\Delta\varepsilon}{2} = \frac{\sigma' f}{E}(2Nf)^b + (\varepsilon' f/2)(2Nf)^c$$

$\frac{\Delta\varepsilon}{2}$ = Total Strain amplitude, to be compare it with Total Strain amplitude from FE analysis in Y-direction

Nf = 5 cycles (Table C.1)

Solution:

$$\frac{\Delta\varepsilon}{2} = \frac{\sigma' f}{E}(2Nf)^b + (\varepsilon' f/2)(2Nf)^c$$

$$\frac{\Delta\varepsilon}{2} = \frac{724}{200e3}(10)^{-0.066} + \left(\frac{0.218}{2}\right) \mathrm{x}\, (10)^{-0.492}$$

$$\frac{\Delta\varepsilon}{2} = 0.0382$$

C.1.1.1 Morrow and Smith

$$\varepsilon a = \frac{\sigma' f - \sigma mean}{E}(2Nf)^b + \varepsilon' f(2Nf)^c$$

$$\varepsilon a = \frac{\sigma' f - \sigma mean}{E}(2Nf)^b + (\varepsilon' f/2)(2Nf)^c$$

where: σ_{mean} =0

$$\varepsilon a = \frac{724-0}{200e3}(10)^{-0.066} + (\frac{0.218}{2}) \text{ x } (10)^{-0.492}$$

$$\varepsilon a = 0.0382$$

C.1.1.2 Smith-Watson-Topper (SWT)

$$\sigma max\ \varepsilon a = \sigma max\ \frac{\Delta\varepsilon}{2} = \frac{(\sigma' f)^2}{E}(2Nf)^{2b} + \sigma' f \varepsilon' f\ (2Nf)^{b+c}$$

$$\sigma max\ \varepsilon a = \sigma max\ \frac{\Delta\varepsilon}{2} = \frac{(\sigma' f)^2}{E}(2Nf)^{2b} + \sigma' f (\varepsilon' f/2)\ (2Nf)^{b+c}$$

$$\sigma max\ \varepsilon a = \frac{(724)^2}{200e3}(10)^{-0.132} + 724\ x\ (\frac{0.218}{2})(10)^{-0.558}$$

σ_{max} is taken from normal stress in Y-direction obtained from FE ANSYS

σ_{max} = 611.8 MPa obtained from Table 6.1

$$\varepsilon a = \frac{(724)^2\ (10)^{-0.132} + 724\ x\ (\frac{0.218}{2}) \text{ x } 200e3\ (10)^{-0.558}}{611.8x\ 200e3}$$

$$\varepsilon a = \frac{\Delta\varepsilon}{2} = 0.0388$$

C.1.2 BCC5C Coffin and Manson

$$\frac{\Delta\varepsilon}{2} = \frac{\sigma' f}{E}(2Nf)^b + \varepsilon' f(2Nf)^c$$

$Nf = 18$ taken from Table C.1

$$\frac{\Delta\varepsilon}{2} = \frac{\sigma' f}{E}(2Nf)^b + (\varepsilon' f/2)(2Nf)^c$$

$$\frac{\Delta\varepsilon}{2} = \frac{724}{200e3}(36)^{-0.066} + (\frac{0.218}{2}) \text{ x } (36)^{-0.492}$$

$$\varepsilon a = \frac{\Delta\varepsilon}{2} = 0.0215$$

C.1.2.1 Morrow and Smith

$$\varepsilon a = \frac{\sigma' f - \sigma mean}{E}(2Nf)^b + \varepsilon' f(2Nf)^c$$

$$\varepsilon a = \frac{\sigma' f - \sigma mean}{E}(2Nf)^b + (\varepsilon' f/2)(2Nf)^c$$

$$\varepsilon a = \frac{724 - 0}{200e3}(36)^{-0.066} + (\frac{0.218}{2}) \text{ x } (36)^{-0.492}$$

$$\varepsilon a = 0.0215$$

C.1.2.2 Smith-Watson-Topper (SWT)

$$\sigma max\ \varepsilon a = \sigma max\ \frac{\Delta\varepsilon}{2} = \frac{(\sigma' f)^2}{E}(2Nf)^{2b} + \sigma' f \varepsilon' f\ (2Nf)^{b+c}$$

σ_{max} is taken from normal stress in Y-direction obtained from FE ANSYS

σ_{max} = 553.6 MPa taken from Table 5.1

$$\sigma max\ \varepsilon a = \sigma max\ \frac{\Delta\varepsilon}{2} = \frac{(\sigma' f)^2}{E}(2Nf)^{2b} + \sigma' f(\varepsilon' f/2)\ (2Nf)^{b+c}$$

$$\varepsilon a = \frac{(724)^2\,(36)^{-0.132} + 724\,x\,(\frac{0.218}{2}) \text{ x } 200e3\,(36)^{-0.558}}{553.6\,x\,200e3}$$

$$\varepsilon a = 0.0222$$

C.1.3 Coffin and Manson (BCC5D)

$$\frac{\Delta\varepsilon}{2} = \frac{\sigma' f}{E}(2Nf)^b + \varepsilon' f(2Nf)^c$$

$Nf = 23$ taken from Table C.1

$$\frac{\Delta\varepsilon}{2} = \frac{\sigma'f}{E}(2Nf)^b + (\varepsilon'f/2)(2Nf)^c$$

$$\frac{\Delta\varepsilon}{2} = \frac{724}{200e3}(46)^{-0.066} + (\frac{0.218}{2}) \text{ x } (46)^{-0.492}$$

$$\frac{\Delta\varepsilon}{2} = 0.0193$$

C.1.3.1 Morrow and Smith

$$\varepsilon a = \frac{\sigma'f - \sigma mean}{E}(2Nf)^b + \varepsilon'f(2Nf)^c$$

$$\varepsilon a = \frac{\sigma'f - \sigma mean}{E}(2Nf)^b + (\varepsilon'f/2)(2Nf)^c$$

$$\varepsilon a = \frac{724 - 0}{200e3}(46)^{-0.066} + (\frac{0.218}{2}) \text{ x } (46)^{-0.492}$$

$$\frac{\Delta\varepsilon}{2} = \varepsilon a = 0.0193$$

C.1.3.2 Smith-Watson-Topper (SWT)

$$\sigma max\ \varepsilon a = \sigma max\ \frac{\Delta\varepsilon}{2} = \frac{(\sigma'f)^2}{E}(2Nf)^{2b} + \sigma'f\varepsilon'f(2Nf)^{b+c}$$

σ_{max} is taken from normal stress in Y-direction obtained from FE ANSYS

σ_{max} = 294.05 MPa taken from Table 6.1

$$\sigma max\ \varepsilon a = \sigma max\ \frac{\Delta\varepsilon}{2} = \frac{(\sigma'f)^2}{E}(2Nf)^{2b} + \sigma'f(\varepsilon'f/2)\ (2Nf)^{b+c}$$

$$\varepsilon a = \frac{(724)^2\,(46)^{-0.132} + 724\,x\,(\frac{0.218}{2}) \text{ x } 200e3\,(46)^{-0.558}}{294.05\,x\,200e3}$$

$$\frac{\Delta\varepsilon}{2} = \varepsilon a = 0.0370$$

C.2 Relation among b,c and n` (strain amplitude calculation using n`)

There have been attempts to relate the Coffin-Manson exponent *C* with the cyclic strain hardening exponent *n`* based on certain energy criterion. Morrow has shown that the exponents *C* and *b* can be related to *n`* by:

$C = -1/(1+5n`)$ and

$b = -n`/(1+5n`)$

Tomkins has given the above relations as:

$C = -1/(1+2n`)$ and

$b = -n`/(1+2n`)$, therefore

$b = -0.150$ and $C = -0.699$

Including factor divide Fatigue ductility coefficient by2 ($\varepsilon'f$ /2) for difference between welded and un-welded [Almar,1985].

In the above relations ,both exponents are independently related to *n`*, therefore any change in (*n`*) will affect the values of both *C* and *b* as explained in Sec.3.1.2.2.1[Raman and Radhakrishnan, 2002].

Table 5.11 Sec.5.3 using (ε'f/2) shows strain amplitude for BCC5 results using strain life formulas considering strain hardening exponent (n`) and Table 5.12 using modification factor (ε'f/Fac).

Calculating strain amplitude for BCC5 using relation among *b,c* and n` as follows, the calculation has done using Excel 2007.

C.2.1 Coffin and Manson (BCC5B)

$$\frac{\Delta\varepsilon}{2} = \frac{\sigma'f}{E}(2Nf)^b + \varepsilon'f(2Nf)^c$$

$\frac{\Delta\varepsilon}{2}$ = εa = Total Strain amplitude ,which is half strain range Δε to be compared with Total strain amplitude FE Analysis in critical point in Y-direction.

where:

σ`f ,ε`f,b and c are taken from Table C.2

Nf = 5 cycles taken from Table C.1

where:

n`= 0.215 (Table C.2)

C = -1/(1+2*n`*) and *b* = -n`/ (1+2*n`*) ,therefore

b= -0.150 and *C*= -0.699

Solution:

$$\frac{\Delta\varepsilon}{2} = \frac{\sigma' f}{E}(2Nf)^b + (\varepsilon' f/2)(2Nf)^c$$

$$\frac{\Delta\varepsilon}{2} = \frac{724}{200e3}(10)^{-0.150} + (\frac{0.218}{2}) \text{ x } (10)^{-0.699}$$

$$\frac{\Delta\varepsilon}{2} = 0.0243$$

C.2.1.1 Morrow and Smith

$$\varepsilon a = \frac{\sigma' f - \sigma mean}{E}(2Nf)^b + (\varepsilon' f/2)(2Nf)^c$$

where: $\sigma_{mean} = 0$

$$\varepsilon a = \frac{\Delta\varepsilon}{2} = \frac{724-0}{200e3}(10)^{-0.150} + (\frac{0.218}{2}) \text{ x } (10)^{-0.699}$$

$$\varepsilon a = \frac{\Delta\varepsilon}{2} = 0.0243$$

C.2.1.2 Smith-Watson-Topper (SWT)

$$\sigma max\ \varepsilon a = \sigma max\ \frac{\Delta\varepsilon}{2} = \frac{(\sigma' f)^2}{E}(2Nf)^{2b} + \sigma' f(\varepsilon' f/2)\ (2Nf)^{b+c}$$

$$\sigma max\ \varepsilon a = \frac{(724)^2}{200e3}(10)^{-0.3} + 724\,x\,(\frac{0.218}{2})(10)^{-0.849}$$

σ_{max} is taken from normal stress in Y-direction obtained from FE ANSYS

σ_{max} = 611.8 MPa taken from Table 5.1

$$\varepsilon a = \frac{(724)^2\,(10)^{-0.3} + 724\,x\,(\frac{0.218}{2})\,\text{x}\,200e3\,(10)^{-0.849}}{611.8x\,200e3}$$

$$\varepsilon a = 0.0253$$

C.2.2 Coffin and Manson (BCC5C)

Nf = 18 cycles taken from Table C.1

$$\frac{\Delta\varepsilon}{2} = \frac{\sigma' f}{E}(2Nf)^b + (\varepsilon' f/2)(2Nf)^c$$

$$\frac{\Delta\varepsilon}{2} = \frac{724}{200\text{e}3}(36)^{-0.150} + (\frac{0.218}{2})\,\text{x}\,(36)^{-0.699} = 0.0110$$

C.2.2.1 Morrow and Smith

$$\varepsilon a = \frac{\sigma' f - \sigma mean}{E}(2Nf)^b + (\varepsilon' f/2)(2Nf)^c$$

where: σ_{mean} = 0

$$\varepsilon a = \frac{\Delta\varepsilon}{2} = \frac{724-0}{200\text{e}3}(36)^{-0.150} + (\frac{0.218}{2})\ \text{x}\,(36)^{-0.699}$$

$$\varepsilon a = \frac{\Delta\varepsilon}{2} = 0.0110$$

C.2.2.2 Smith-Watson-Topper (SWT)

$$\sigma max\ \varepsilon a = \sigma max\ \frac{\Delta\varepsilon}{2} = \frac{(\sigma' f)^2}{E}(2Nf)^{2b} + \sigma' f(\varepsilon' f/2)\ (2Nf)^{b+c}$$

$$\sigma max\ \varepsilon a = \frac{(724)^2}{200e3}(36)^{-0.3} + 724\,x\,(\frac{0.218}{2})(36)^{-0.849}$$

σ_{max} is taken from normal stress in Y-direction obtained from FE ANSYS

σ_{max} = 553.6 MPa taken from Table 6.1

$$\varepsilon a = \frac{(724)^2\,(10)^{-0.3} + 724\,x\,(\frac{0.218}{2})\,\text{x}\,200e3\,(10)^{-0.849}}{553.6x\ 200e3}$$

$$\varepsilon a = 0.0225$$

C.2.3 Coffin and Manson (BCC5D)

Nf = 23 cycles taken from Table C.2

$$\frac{\Delta\varepsilon}{2} = \frac{\sigma' f}{E}(2Nf)^b + (\varepsilon' f/2)(2Nf)^c$$

$$\frac{\Delta\varepsilon}{2} = \frac{724}{200\text{e}3}(46)^{-0.150} + (\frac{0.218}{2})\,\text{x}\,(46)^{-0.699}$$

$$\frac{\Delta\varepsilon}{2} = 0.0095$$

C.2.3.1 Morrow and Smith

$$\varepsilon a = \frac{\sigma' f - \sigma mean}{E}(2Nf)^b + (\varepsilon' f/2)(2Nf)^c$$

where: σ_{mean} = 0

$$\varepsilon a = \frac{\Delta\varepsilon}{2} = \frac{724-0}{200e3}(46)^{-0.150} + (\frac{0.218}{2})\ \text{x}\ (46)^{-0.699}$$

$$\varepsilon a = \frac{\Delta\varepsilon}{2} = 0.0095$$

C.2.3.2 Smith-Watson-Topper (SWT)

$$\sigma max\ \varepsilon a = \sigma max\ \frac{\Delta\varepsilon}{2} = \frac{(\sigma' f)^2}{E}(2Nf)^{2b} + \sigma' f(\varepsilon' f/2)\ (2Nf)^{b+c}$$

$$\sigma max\ \varepsilon a = \frac{(724)^2}{200e3}(46)^{-0.3} + 724\,x\,(\frac{0.218}{2})(46)^{-0.849}$$

σ_{max} is taken from normal stress in Y-direction obtained from FE ANSYS

σ_{max} = 294.05 MPa taken from Table 6.1

$$\varepsilon a = \frac{(724)^2\,(46)^{-0.3} + 724\,x\,(\frac{0.218}{2})\ \text{x}\ 200e3\ (46)^{-0.849}}{294.05x\ 200e3}$$

$$\varepsilon a = 0.0132$$

Figure 5.4 shows strain amplitude vs. number of cycles (log -log scale) for Smith-Watson-Topper (SWT) relationship for FE ANSYS base models:(a) BCC5A, (b) BCC5B, (c) BCC5C and (d) BCC5D. Same indication of Figures 3.12 & 3.13, when applying Coffin-Manson and Morrow &Smith formulas.

C.3 Fatigue damage index

Table 5.5 using (ε'f/2) shows calculation of fatigue damage index for cycling based on typical strain amplitude measured (considering cyclic strain hardening exponent *n`*) and using fatigue ductility coefficient factor by 2 (ε'f/2) for the difference between welded and un-welded and Table 5.6 using modification factor (ε'f/Fac). Cycle counting by reservoir method [BS 7608, 2014].

See Sec. 5.2.2 chapter 5 and Sec. 3.3.3 chapter 3.

Table C.3: Fatigue damage index and number of cycles to failure calculation based on typical strain amplitude considering cyclic strain hardening (n`)

Case No.	Number of cycles at constant Amplitude =*ni*	Cycles to failure at constant amplitude *Ni* (using coffin Manson Equation graph (*n`*)	Damage at constant Amplitude=*ni/Ni*
BCC5A	4 cycles @0.007	39	4/39
	2 cycles @0.0073	36	2/36
	3 cycles @0.0075	34	3/34
	6 cycles @0.00754	35	6/35
	1 cycles @0.00785	32	1/32
	Fatigue Damage Index.*FDI* (Accumulated Damage)		45 %
	Ncyc to failure		16/0.45= 36
BCC5B	2 cycle @0.0097	22	2/22
	1cycle @0.00995	21	1/21
	1 cycles @0.0102	20	1/20
	1 cycle@0.0106	19	1/19
	Fatigue Damage Index.FDI (Accumulated Damage)		24.1%
	Ncyc to failure		5/0.241= 21

Case No.	Number of cycles at constant Amplitude =*ni*	Cycles to failure at constant amplitude *Ni* (using coffin Manson Equation graph (*n`*)	Damage at constant Amplitude=*ni/Ni*
BCC5C	3 cycle @0.00105	5222	3/5222
	1 cycles @0.0027	272	1/272
	1 cycle @0.00354	148	1/148
	1 cycle @0.00323	181	1/181
	1 cycles @0.00391	120	1/120
	1 cycle @0.0043	99	1/99
	1 cycle @0.00392	120	1/120
	1 cycle @0.00466	84	1/84
	1 cycle @0.00524	67	1/67
	1 cycle @0.00532	65	1/65
	1 cycle @0.0062	48	1/48
	1 cycle @0.0069	40	1/40
	1 cycle @0.007185	38	1/38
	1 cycle @0.00833	29	1/29
	1 cycle @0.00915	25	1/25
	1 cycle @0.00947	23	1/23
	Fatigue Damage Index.*FDI* (Accumulated Damage)		27%
	Ncyc to failure		18/0.27= 66

Case No.	Number of cycles at constant Amplitude =*ni*	Cycles to failure at constant amplitude *Ni* (using coffin Manson Equation graph (*n`*)	Damage at constant Amplitude=*ni/Ni*
BCC5D	1 cycle @0.00506	72	1/72
	1 cycles @0.0051	70	1/70
	1 cycle @0.0052	68	1/68
	1 cycle @0.00527	66	1/66
	4 cycles @0.00529	66	4/66
	10 cycle @0.00531	65	10/65
	2 cycle @0.00533	65	2/65
	1 cycle @0.00563	59	1/59
	1 cycle @0.00568	57	1/57
	1 cycle @0.00571	56	1/56
	Fatigue Damage Index.*FDI* (Accumulated Damage)		35.5%
	Ncyc to failure		23/0.355= 64

C.4 Calculating fatigue damage index using MathCAD (including n')

The Palmgren-Miner rule is used to predict the damage per cycle as reported in Miner [1945] as explained in Sec.3.3.3 and Sec.5.2.2. Adopting Miner's rule that

accumulates damage induced by cycles of constant strain range linearly, a damage index *D*, can be expressed in Equation 3.13 as follows:

$$FDI = \sum_{i}^{n} ni/Ni \qquad 3.13$$

where: *FDI* is the fatigue damage index, or total damage to the element due to the cyclic load, ni is the number of different cycle amplitudes in the loading history, and *Ni* is the number of cycles at amplitude i. Values of *FDI* greater than or equal to 1.0 indicate a low-cycle fatigue fracture of the member as reported in Campbell *et al.* [2008]. Using cycle counting by the reservoir method as shown in Figure 3.28 [BS7608, 2014].

In this work total strain range is using to calculate *FDI* by using Cycle counting by the reservoir method as explained in Sec.3.3.3, and it is shown in Figure 3.28 [BS7608, 2014], it is easy to apply by hand and suitable when dealing with short stress histories.

FDI calculation using total strain vs. number of substeps is shown in Figure B.3 Appendix B. Calculating failure damage index using MathCAD is explained in Sec. C.4 using Coffin-Manson relation Appendix C. Calculation details are shown in Table C.3 Appendix C, and the final results are illustrated as shown in Table 5.5.
Considering cyclic strain hardening exponent (n`) and using fatigue ductility coefficient factor by 2 ($\varepsilon' f /2$) for the difference between welded and un-welded, and Table 5.6 using modification factor (ε'f/Fac).

Using cyclic strain hardening (n`) to calculate FDI and predicted cycles to failure as shown in Table 5.5, the following Tomkins relations has been used ;
$C = -1/(1+2n`) = -0.699$ and $b = -n`/(1+2n`) = -0.150$, and MathCAD calculation as follows:

C.4.1 BCC5B

$Ncyc := 5$ $ORIGIN \equiv 1$

$ie := 1..Ncyc$

$\sigma f := 724$

$\varepsilon f := \frac{0.218}{Fac}$

$b := -.150$

$c := -.699$

$E := 200 \times 10^3$ $E = 2 \times 10^5$

$\varepsilon fe_{ie} :=$

0.0194
0.0194
0.0199
0.0204
0.0212

$\varepsilon fe_{ie} =$

0.0194
0.0194
0.0199
0.0204
0.0212

$Nf := 5$

$$Nfe_{ie} := root\left[1 \cdot \left[\frac{\sigma f}{E} \cdot (2 \cdot Nf)^b + \varepsilon f \cdot (2 \cdot Nf)^c\right] - \frac{\varepsilon fe_{ie}}{2}, Nf\right]$$

$$Nfe = \begin{pmatrix} 22.353 \\ 22.353 \\ 21.4 \\ 20.513 \\ 19.216 \end{pmatrix}$$

$$\varepsilon fe \cdot E = \begin{pmatrix} 3.88 \times 10^3 \\ 3.88 \times 10^3 \\ 3.98 \times 10^3 \\ 4.08 \times 10^3 \\ 4.24 \times 10^3 \end{pmatrix}$$

$$D := \sum_{ie} \frac{1}{Nfe_{ie}} \qquad D = 0.237$$

Predicted cycles to failure

$$\frac{Ncyc}{D} = 21.098$$

$Fac \equiv 2$

C.4.2 BCC5C

$Ncyc := 18$ $ORIGIN \equiv 1$

$ie := 1..Ncyc$

$\sigma f := 724$

$\varepsilon f := \frac{0.218}{Fac}$

$b := -.150$

$c := -.699$

$E := 200 \times 10^3$ $E = 2 \times 10^5$

$\varepsilon fe_{ie} :=$

0.0021
0.0021
0.0021
0.0054
0.00708
0.00646
0.00782
0.0086
0.00784
0.00932
0.01048
0.01064
0.0124
0.0138
0.01437
0.01666
0.0183
0.01894

$\varepsilon fe_{ie} =$

$2.1 \cdot 10^{-3}$
$2.1 \cdot 10^{-3}$
$2.1 \cdot 10^{-3}$
$5.4 \cdot 10^{-3}$
$7.08 \cdot 10^{-3}$
$6.46 \cdot 10^{-3}$
$7.82 \cdot 10^{-3}$
$8.6 \cdot 10^{-3}$
$7.84 \cdot 10^{-3}$
$9.32 \cdot 10^{-3}$
0.0105
0.0106
0.0124
0.0138
0.0144
...

$Nf := 5$

$$Nfe_{ie} := root\left[1 \cdot \left[\frac{\sigma f}{E} \cdot (2 \cdot Nf)^b + \varepsilon f \cdot (2 \cdot Nf)^c\right] - \frac{\varepsilon fe_{ie}}{2}, Nf\right]$$

$$D := \sum_{ie} \frac{1}{Nfe_{ie}} \qquad D = 0.272$$

Predicted cycles to failure

$$\frac{Ncyc}{D} = 66.06$$

$Fac \equiv 2$

$Nfe =$

	1
1	$5.716 \cdot 10^3$
2	$5.716 \cdot 10^3$
3	$5.716 \cdot 10^3$
4	282.165
5	151.963
6	186.009
7	122.918
8	100.975
9	122.261
10	85.872
11	68.221
12	66.256
13	49.606
14	40.754
15	37.874
16	...

$\varepsilon fe \cdot E =$

	1
1	420
2	420
3	420
4	$1.08 \cdot 10^3$
5	$1.416 \cdot 10^3$
6	$1.292 \cdot 10^3$
7	$1.564 \cdot 10^3$
8	$1.72 \cdot 10^3$
9	$1.568 \cdot 10^3$
10	$1.864 \cdot 10^3$
11	$2.096 \cdot 10^3$
12	$2.128 \cdot 10^3$
13	$2.48 \cdot 10^3$
14	$2.76 \cdot 10^3$
15	$2.874 \cdot 10^3$
16	...

C.4.3 BCC5D

$Ncyc := 23$ $\quad ORIGIN \equiv 1$

$ie := 1..Ncyc$

$\sigma f := 724$

$$\varepsilon f := \frac{0.218}{Fac}$$

$b := -.150$

$c := -.699$

$E := 200 \times 10^3$ $\quad E = 2 \times 10^5$

$\varepsilon fe_{ie} :=$

0.01012
0.0102
0.0104
0.01054
0.01058
0.01058
0.01058
0.01058
0.01062
0.01062
0.01062
0.01062
0.01062
0.01062
0.01062
0.01062
0.01062
0.01062
0.01062
0.01066
0.01066
0.01126
0.01136
0.0142

$\varepsilon fe_{ie} =$

0.0101
0.0102
0.0104
0.0105
0.0106
0.0106
0.0106
0.0106
0.0106
0.0106
0.0106
0.0106
0.0106
0.0106
0.0106
0.0106
...

$$Nf := 5$$

$$Nfe_{ie} := root\left[1 \cdot \left[\frac{\sigma f}{E} \cdot (2 \cdot Nf)^{b} + \varepsilon f \cdot (2 \cdot Nf)^{c}\right] - \frac{\varepsilon fe_{ie}}{2}, Nf\right]$$

Nfe =

	1
1	73.009
2	71.898
3	69.239
4	67.473
5	66.982
6	66.982
7	66.982
8	66.982
9	66.496
10	66.496
11	66.496
12	66.496
13	66.496
14	66.496
15	66.496
16	...

εfe·E =

	1
1	$2.024 \cdot 10^3$
2	$2.04 \cdot 10^3$
3	$2.08 \cdot 10^3$
4	$2.108 \cdot 10^3$
5	$2.116 \cdot 10^3$
6	$2.116 \cdot 10^3$
7	$2.116 \cdot 10^3$
8	$2.116 \cdot 10^3$
9	$2.124 \cdot 10^3$
10	$2.124 \cdot 10^3$
11	$2.124 \cdot 10^3$
12	$2.124 \cdot 10^3$
13	$2.124 \cdot 10^3$
14	$2.124 \cdot 10^3$
15	$2.124 \cdot 10^3$
16	...

$$D := \sum_{ie} \frac{1}{Nfe_{ie}} \qquad D = 0.357$$

Predicted cycles to failure

$$\frac{Ncyc}{D} = 64.42$$

$$Fac \equiv 2$$

C.5 Calculating fatigue damage index using MathCAD (excluding n')

Not considering cyclic strain hardening exponent (n`) and using fatigue ductility coefficient factor by 2 ($\varepsilon' f/2$) for the difference between welded and un-welded.

C.5.1 BCC5B

$Ncyc := 5$ $ORIGIN \equiv 1$

$ie := 1..Ncyc$

$\sigma f := 724$

$\varepsilon f := \frac{0.218}{Fac}$

$b := -.066$

$c := -.492$

$E := 200 \times 10^3$ $E = 2 \times 10^5$

$\varepsilon fe_{ie} :=$

0.0194
0.0194
0.0199
0.0204
0.0212

$\varepsilon fe_{ie} =$

0.0194
0.0194
0.0199
0.0204
0.0212

$$Nfe = \begin{pmatrix} 125.661 \\ 125.661 \\ 117.579 \\ 110.24 \\ 99.829 \end{pmatrix} \qquad \varepsilon fe \cdot E = \begin{pmatrix} 3.88 \times 10^3 \\ 3.88 \times 10^3 \\ 3.98 \times 10^3 \\ 4.08 \times 10^3 \\ 4.24 \times 10^3 \end{pmatrix}$$

$Nf := 5$

$$Nfe_{ie} := root\left[1 - \left[\frac{\sigma f}{E} \cdot (2 \cdot Nf)^b + \varepsilon f \cdot (2 \cdot Nf)^c\right] - \frac{\varepsilon fe_{ie}}{2}, Nf\right]$$

$$D := \sum_{ie} \frac{1}{Nfe_{ie}} \qquad D = 0.044$$

Predicted cycles to failure

$$\frac{Ncyc}{D} = 114.919$$

$Fac \equiv 2$

C.5.2 BCC5C

$Ncyc := 18$ $ORIGIN \equiv 1$

$ie := 1..Ncyc$

$\sigma f := 724$

$\varepsilon f := \frac{0.218}{Fac}$

$b := -.066$

$c := -.492$

$E := 200 \times 10^3$ $E = 2 \times 10^5$

$\varepsilon fe_{ie} :=$

0.0021
0.0021
0.0021
0.0054
0.00708
0.00646
0.00782
0.0086
0.00784
0.00932
0.01048
0.01064
0.0124
0.0138
0.01437
0.01666
0.0183
0.01894

$\varepsilon fe_{ie} =$

$2.1 \cdot 10^{-3}$
$2.1 \cdot 10^{-3}$
$2.1 \cdot 10^{-3}$
$5.4 \cdot 10^{-3}$
$7.08 \cdot 10^{-3}$
$6.46 \cdot 10^{-3}$
$7.82 \cdot 10^{-3}$
$8.6 \cdot 10^{-3}$
$7.84 \cdot 10^{-3}$
$9.32 \cdot 10^{-3}$
0.0105
0.0106
0.0124
0.0138
0.0144
...

$Nf := 5$

$$Nfe_{ie} := root\left[1 \cdot \left[\frac{\sigma f}{E} \cdot (2 \cdot Nf)^b + \varepsilon f \cdot (2 \cdot Nf)^c\right] - \frac{\varepsilon fe_{ie}}{2}, Nf\right]$$

$$D := \sum_{ie} \frac{1}{Nfe_{ie}} \qquad D = 0.035$$

Predicted cycles to failure

$$\frac{Ncyc}{D} = 521.485$$

$Fac \equiv 2$

$Nfe =$

	1
1	$8.056 \cdot 10^7$
2	$8.056 \cdot 10^7$
3	$8.056 \cdot 10^7$
4	$1.033 \cdot 10^4$
5	$3.025 \cdot 10^3$
6	$4.443 \cdot 10^3$
7	$2.05 \cdot 10^3$
8	$1.446 \cdot 10^3$
9	$2.03 \cdot 10^3$
10	$1.092 \cdot 10^3$
11	739.866
12	704.717
13	438.56
14	320.051
15	284.954
16	...

$\varepsilon fe \cdot E =$

	1
1	420
2	420
3	420
4	$1.08 \cdot 10^3$
5	$1.416 \cdot 10^3$
6	$1.292 \cdot 10^3$
7	$1.564 \cdot 10^3$
8	$1.72 \cdot 10^3$
9	$1.568 \cdot 10^3$
10	$1.864 \cdot 10^3$
11	$2.096 \cdot 10^3$
12	$2.128 \cdot 10^3$
13	$2.48 \cdot 10^3$
14	$2.76 \cdot 10^3$
15	$2.874 \cdot 10^3$
16	...

C.5.3 BCC5D

$Ncyc := 23$ $\qquad ORIGIN \equiv 1$

$ie := 1..Ncyc$

$\sigma f := 724$

$$\varepsilon f := \frac{0.218}{Fac}$$

$b := -.066$

$c := -.492$

$E := 200 \times 10^3$ $\qquad E = 2 \times 10^5$

$\varepsilon fe_{ie} :=$

0.01012
0.0102
0.0104
0.01054
0.01058
0.01058
0.01058
0.01058
0.01062
0.01062
0.01062
0.01062
0.01062
0.01062
0.01062
0.01062
0.01062
0.01062
0.01062
0.01066
0.01066
0.01126
0.01136
0.0142

$\varepsilon fe_{ie} =$

0.0101
0.0102
0.0104
0.0105
0.0106
0.0106
0.0106
0.0106
0.0106
0.0106
0.0106
0.0106
0.0106
0.0106
0.0106
...

$Nf := 5$

$$Nfe_{ie} := \text{root}\left[1 \cdot \left[\frac{\sigma f}{E} \cdot (2 \cdot Nf)^{b} + \varepsilon f \cdot (2 \cdot Nf)^{c}\right] - \frac{\varepsilon fe_{ie}}{2}, Nf\right]$$

Nfe =

	1
1	828.879
2	807.804
3	758.403
4	726.392
5	717.607
6	717.607
7	717.607
8	717.607
9	708.976
10	708.976
11	708.976
12	708.976
13	708.976
14	708.976
15	708.976
16	...

$\varepsilon fe \cdot E =$

	1
1	$2.024 \cdot 10^3$
2	$2.04 \cdot 10^3$
3	$2.08 \cdot 10^3$
4	$2.108 \cdot 10^3$
5	$2.116 \cdot 10^3$
6	$2.116 \cdot 10^3$
7	$2.116 \cdot 10^3$
8	$2.116 \cdot 10^3$
9	$2.124 \cdot 10^3$
10	$2.124 \cdot 10^3$
11	$2.124 \cdot 10^3$
12	$2.124 \cdot 10^3$
13	$2.124 \cdot 10^3$
14	$2.124 \cdot 10^3$
15	$2.124 \cdot 10^3$
16	...

$$D := \sum_{ie} \frac{1}{Nfe_{ie}} \qquad D = 0.035$$

Predicted cycles to failure

$$\frac{Ncyc}{D} = 666.519$$

Fac ≡ 2

C.6 Panel zone stiffness MathCAD calculations (stress-strain graph correction)

The hysteresis loops force displacement was obtained from FE ANSYS as shown in Figure 4.13, which looks like linear shape without nonlinearity, and that was not satisfactory with experimental work hysteresis loops as explained in Sec.4.3.

A simple calculation was done using MathCAD programme to investigate the stiffness in the joint.

$E := 200 \cdot 10^3 \cdot \frac{N}{mm^2}$ $\mu := 0.3$

$Lc := 1800\,mm$ $dc := 160 \cdot mm$ $G := \frac{E}{2 \cdot (1 + \mu)}$

$Ic := 2492\,cm^4$ $db := 300 \cdot mm$

$Lb := 955.5\,mm$ $twc := 8 \cdot mm$

$Ib := 8356\,cm^4$

$Kcr := \frac{16E \cdot Ic}{Lc}$ $Kcr = 4.43 \times 10^4 \cdot \frac{kN \cdot m}{rad}$

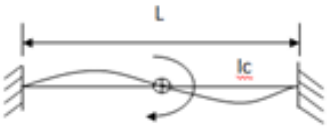

$Kb := \frac{3E \cdot Ib}{Lb^3}$ $Kb = 5.747 \times 10^7 \cdot \frac{N}{m}$

$Kc := \frac{Kcr}{Lb^2}$ $Kc = 4.852 \times 10^7 \cdot \frac{N}{m}$

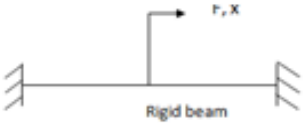

$Ksh := \frac{db \cdot dc \cdot twc G}{Lb^2}$ $Ksh = 3.235 \times 10^7 \cdot \frac{N}{m}$

$Ko := \left(\frac{1}{Kb} + \frac{1}{Kc} + \frac{1}{Ksh} \right)^{-1}$ $Ko = 1.451 \times 10^7 \cdot \frac{N}{m}$

$Kex := \frac{127517N}{9.94\,mm}$ $Kex = 1.283 \times 10^7 \cdot \frac{N}{m}$

$Kfe := \frac{63271N}{9.15mm}$ $Kfe = 6.915 \times 10^6 \cdot \frac{N}{m}$

Calculation of Ksh (stiffness of panl zone)

$$x = \alpha\, Lb$$

$$\alpha = \frac{shear\ stress}{G}$$

$$\text{shear stress} = \frac{shear\ flow}{twc}$$

$$\text{shear flow} = \frac{flange\ force}{dc}$$

$$\text{flange force} = \frac{Moment}{db}$$

$$Moment = F\, Lb$$

$$x = \frac{F.Lb.Lb}{db.dc.twc.G}$$

Therefore ;

$$\frac{F}{x} = \frac{db.dc.twc.G}{Lb^2} = Ksh$$

$$Ksh = stiffness\ of\ PZ.$$

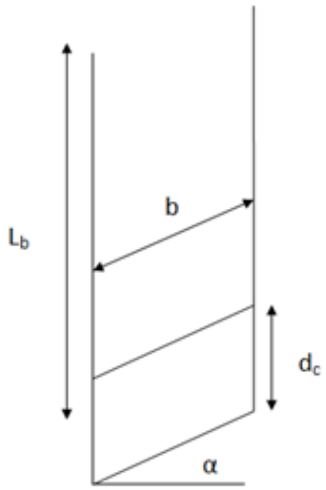

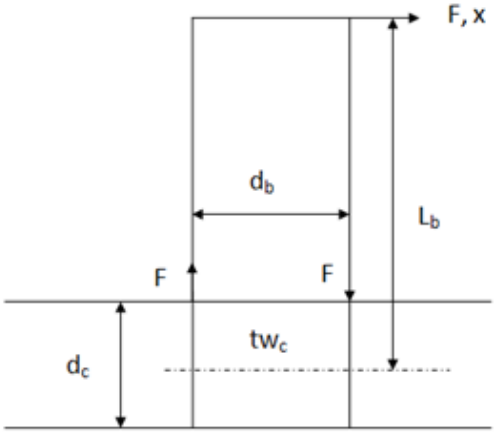

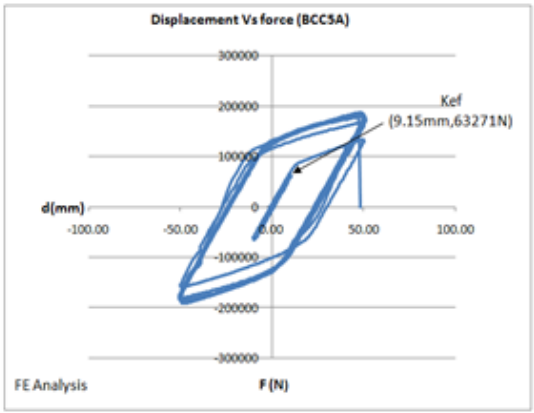

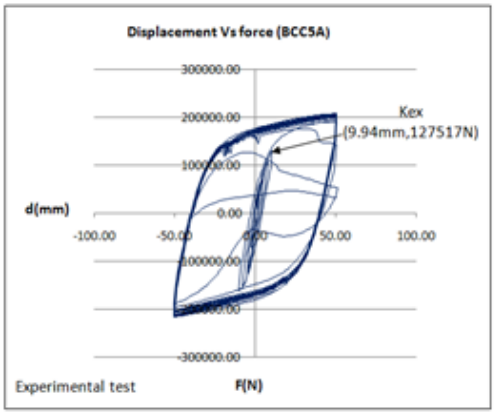

where:

Kcr is stiffness of column rotation M-θ at the connection associated with the horizontal members, *Kc* is stiffness of column converts that to a linear stiffness at the top of the vertical member, *Ko* is an estimate of the overall stiffness at the top of the vertical member, Ksh is stiffness of panel zone, Kex is stiffness of the joint (experimental test), and Kef is stiffness of the joint (FE analysis).

- Joint in actual test sample (steel joint) is more stiff than the FE base model joint (Kex = 1.283×10^7 N/m > Kfe = 6.915×10^6 N/m), it means that the experiment has more flexibility in the support than the FE base model.
- Panel zone in experiment had higher stress than FE.

After further investigation, it was discovered that there was a difference in the force-displacement curve in the Elastic zone. In this work, where plastic strains are most important, it was compensated for by adjusting the E value and it the support was modelled as fixed rather than flexible as shown in Figure 4.14 and Figure 4.15.

MathCAD calculation for stress-strain correction was done, by setting yield point to zero and subtracting 0.0038172 from each strain from Table 4.3, to get the new plastic stress-strain curve and data and applied to the Multilinear Isotropic Hardening as shown in Figure 4.16 and Table 4.4.

C.7 Failure assessment diagram (FAD) calculation

The failure assessment diagram principle is based on the interaction between fracture and collapse in a structural component including a crack as explained in Sec. 3.3.2.1. BS 7910 [2005] and Sec.3.3.2.2 DNV-RP-F108 [2006].

BS7910 FAD provides a method of checking the possibility of fracture This ignores the effect of the cyclic load, which will probably make the failure more likely, so the

check, based on initial defect size and maximum stresses, should be regarded as a minimum additional requirement.

The choice of the level depends on the amount of input data available and the desired degree of precision of the results. This work uses the "option 2", defined as the "normal assessment" which is require to have stress-strain data input.

The failure assessment diagram (FAD) is the locus separating the acceptable and unacceptable conditions, i.e. "Failure" is assumed if the assessment point falls on or outside the FAD curve while safe conditions are assumed if the assessment point falls inside the FAD-curve.

The FAD cannot be extended to arbitrarily large plastic deformations and a cut-off limit for *Lr* ($Lr = \sigma_{ref} / \sigma_Y$) must be defined.

For displacement controlled or displacement restricted situations, such as reeling, it is acceptable to increase the cut-off level in the FAD, Lr_{max}, (from $Lr_{max} = \sigma flow / \sigma Y$ as suggested in BS 7910:2005) provided there is experimental support for such an extension.

DNV-RP-F108 [2006] recommended that the FAD shall be representative for the higher end of the pipe strengths, i.e. representing a pipe with high yield strength and low strain hardening. e.g. mean plus two standard deviations or "highest expected value" of the strength for the material to be employed.

In lieu of such experimental results it is acceptable to determine Lr_{max} as:

$Lr_{max} = \sigma_U / \sigma_Y$

where: σ_U is ultimate stress and σ_Y is yield stress

$Kr = K_f/Kc$, where K_f : stress intensity factor = $\sigma T \sqrt{\pi a_\circ}$

$a_{\circ}$ is crack depth take it 0.2mm

Note: $a_{\circ}$ assumed in order to calculate stress intensity factor (K_f) and calculate *Kr* to establish the failure assessment diagram according to [BS 7608, 2014].

Kc: Fracture Toughness = $\sqrt{\delta c E \sigma y}$

$\delta c = G/\sigma y$, $\delta c = 0.1mm$

$Kr = K_f/Kc$

So the point (Lr,Kr,)

Table 5.1 shows (*Lr*, *Kr*) points for all BCC5 models by using the total stress(σ_T), see Sec. 5.2.1.1.

DNV-RP-F108 [2006] recommended that the FAD shall be representative for the higher end of the pipe strengths, i.e. representing a pipe with high yield strength and low strain hardening. e.g. mean plus two standard deviations or "highest expected value" of the strength for the material to be employed, therefore when calculating stress intensity factor (K*f*), σ_T should be the stress range of the last cycle obtained from FE ANSYS when plotting normal stress time history.

$Lr_{max} = \sigma_u / \sigma_y = 404.6 / 274.8 = 1.5$

where:

σ_u is Ultimate stress for beam flange obtained from experiment and

σ_y is Yielding stress for beam flange obtained from experiment

From Normal stress graph (FE Analysis)

σ_{max} and σ_T have been obtained from normal stress time history graph (FE Analysis) where: σ_{max} is the maximum stress in the graph, and σ_T is the total stress range in the graph.

Using the following Equation 3.10 to draw the FAD in Excel as shown in Figure C.1.

$$K_r = \left(1 - 0.14L_r^2\right) \cdot \left[0.3 + 0.7\,exp\left(-0.65L_r^6\right)\right] \qquad 3.10$$

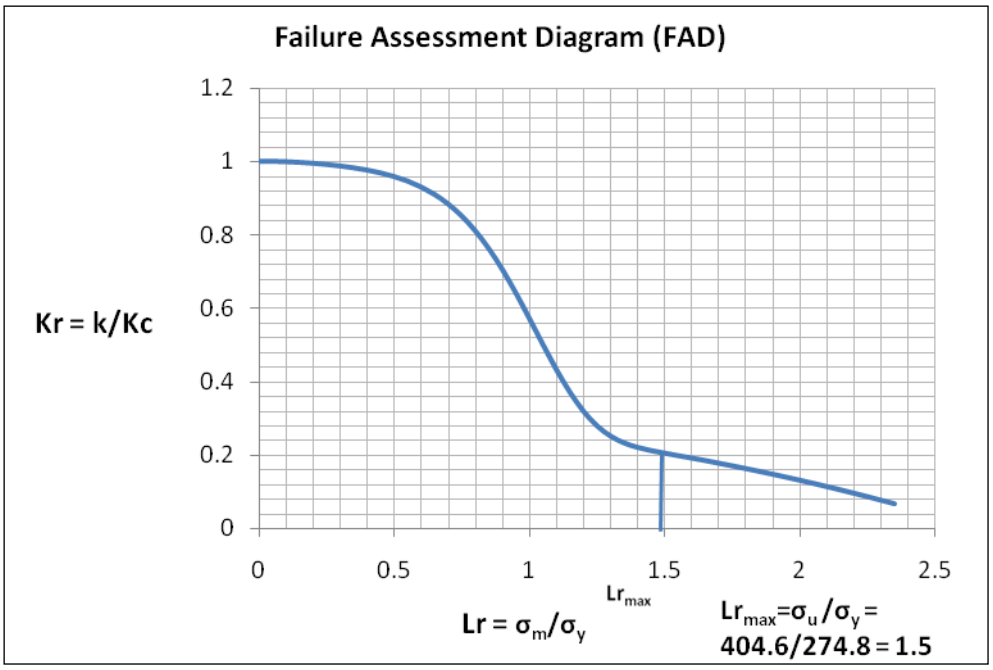

Figure C.1: Failure assessment diagram (FAD)

Calculating ((Lr,Kr,) for BCC5A is shown in Sec.5.2.1.1.

C.7.1 BCC5B

Lr = σmax/σy = 4646.31 /274.8 = 17

where σy is yield stress for flange (Exp.)= 274.8MPa

Kr = Kf/Kc

where :

Kf : stress intensity factor = σT √ π $a_{\circ}$

$a_{\circ}$ is crack depth take it 0.2mm

Kc: Fracture Toughness = √ δcE σy

δc = G/σy , take δc = 0.1mm

Kc(same for all specimens) = √(0.1* 200000* 274.8)

= 2344.35MPa mm½

Kf = σT √ π $a_{\circ}$ = 4646.31 √(3.14* 0.2)= 3670.58 Mpa mm½

Kr = Kf/Kc = 3670.58 /2344.35 = 1.5

So the point (Lr,Kr) is (17,1.5)

C.7.2 BCC5C

Lr = σmax/σy = 15038.51 /274.8 = 55

where σy is yeild stress for flange (Exp.)= 274.8MPa

Kr = Kf/Kc

where Kf : stress intensity factor = σT √ π $a_{\circ}$

$a_{\circ}$ is crack depth take it 0.2mm

Kc: Fracture Toughness = √ δcE σy

δc = G/σy , take δc = 0.1mm

Kc(same for all specimens) = √(0.1* 200000* 274.8)

= 2344.35MPa mm½

Kf = σT √ π $a_{\circ}$ = 15038.51 √(3.14* 0.2)= 11880.4 Mpa mm½

Kr = Kf/Kc = 11880.4 /2344.35 = 5

So the point (Lr,Kr,) is (55,5.0)

C.7.3 BCC5D

Lr = σmax/σy = 22606.32 /274.8 = 82

where σy is yeild stress for flange (Exp.)= 274.8MPa

Kr = Kf/Kc

where Kf : stress intensity factor = σT √ π $a_{\circ}$

$a_{\circ}$ is crack depth take it 0.2mm

Kc: Fracture Toughness = √ δcE σy

δc = G/σy , take δc = 0.1mm

Kc(same for all specimens) = √(0.1* 200000* 274.8)

= 2344.35MPa mm½

Kf = σT √ π $a_{\circ}$ = 22606.32 √(3.14* 0.2)= 17858.9 Mpa mm½

Kr = Kf/Kc = 17858.9 /2344.35 = 7

So the point (Lr,Kr,) is (82,7.0)

C.8 Crack growth rates

Crack growth rates calculation is explained in Sec. 3.3.4 chapter 3 and calculation for BCC5A is shown in Sec. 5.4 chapter 5.

Kmax=σmax √ π $a_{\circ}$ where σmax (positive value) from normal stress time history (for each cycle) ANSYS output

Kmin=σmin √ π $a_{\circ}$ where σmin (negative value) from normal stress time history (for each cycle) ANSYS output

ΔK=Kmax-Kmin

A=5.86*10^-13 Table 4.22 [BS7910, 2013]

m=2.88 Table 4.22 [BS7910, 2013]

$a_{\circ}$= crack length = 0.2mm

Tables 5.23, C.4,C.7 and C.10 show results of crack growth rates calculations based on stress ranges, stress modified by (strain*E) and Geometric mean of stress and (strain*E) for BCC5A, BCC5B,BCC5C and BCC5D respectively.

Figures 5.5, C.2,C.3 and C.4 represents Tables 5.23, C.4,C.7 and C.10 respectively, which are show crack growth represents stress ranges , modified stress by strain*E, Geometric mean of stress and strain*E and mean of stress and strain*E ranges) vs. no. of cycles.

Tables 5.24 and 5.25 related to Table 5.14

Tables C.5 and C.6 related to Table C.4

Tables C.8 and C.9 related to Table C.7

Tables C.11 and C.12 related to Table C.10

Table C.4: Shows results of crack growth rates calculations based on stress ranges, stress modified by (strain*E) and Geometric mean of stress and (strain*E) for BCC5B

Cycle no.	Stress ranges da/dN(mm/cycle)=A ΔK^m	Modified stress by strain*E da/dN(mm/cycle)=A ΔK^m	Geometric mean of stress and strain*E da/dN(mm/cycle)=A ΔK^m	Mean of stress and strain*E da/dN(mm/cycle)=A ΔK^m
1	3.76045E-05	0.004974966	0.000432529	0.001097541
2	8.20607E-05	0.005678011	0.000681682	0.001398283
3	0.000119157	0.004199377	0.000706219	0.001187607
4	0.000151427	0.004024752	0.000779063	0.001215468
5	0.000186375	0.005217257	0.000983513	0.001555662

Table C.5: Shows calculations of stress intensity factor using modification stress by (ε*E)

No. of cycles	εmax	εmin	εrange	εmax*E	εmin*E	Kmax=σmax $\sqrt{\pi a_c}$	Kmin=σmin $\sqrt{\pi a_c}$
1	0.01777	0.000078	0.017692	3554	15.6	2814.768	12.3552
2	0.01714	-0.0011414	0.0182814	3428	-228.28	2750.845257	-183.186393
3	0.01673	0.00049	0.01624	3346	98	2721.978391	79.72321646
4	0.01717	0.0013249	0.0158451	3434	264.98	2821.274122	217.6998302
5	0.018531	0.001352	0.017179	3706.2	270.4	3073.292932	224.2238435

Table C.6: Shows calculations of stress intensity factor using stress ranges

.

No. of cycles	Normal stress MPa (min)	Normal stress MPa (max)	Kmax=σmax $\sqrt{\pi a_c}$	Kmin=σmin $\sqrt{\pi a_c}$	ΔK=Kmax-Kmin
1	-253.37	395.5	313.236	-200.66904	513.90504
2	-382.21	467.8	370.8437606	-302.9931461	673.8369066
3	-452.2	515.14	408.455825	-358.5505378	767.0063628
4	-492.29	558.68	443.1106637	-390.4541932	833.5648568
5	-517.32	611.8	485.4256283	-410.4615659	895.8871942

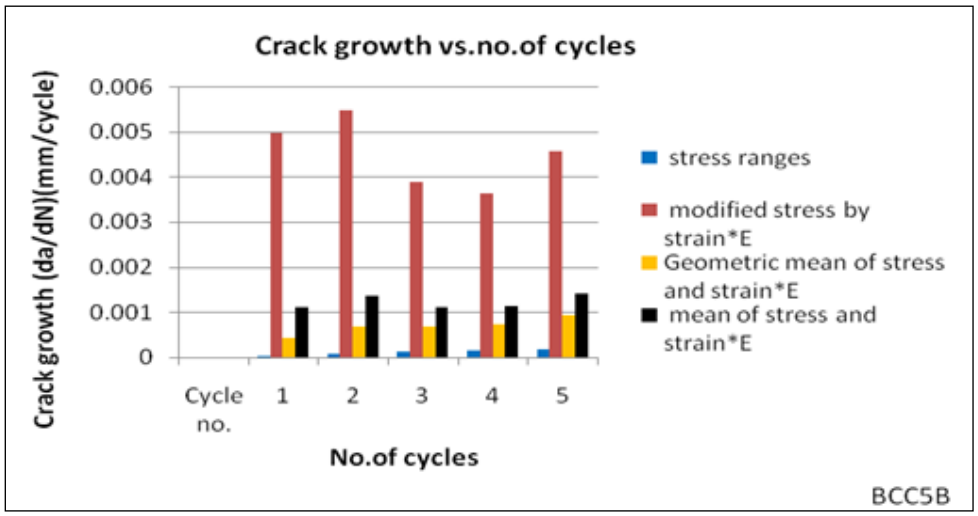

(a)

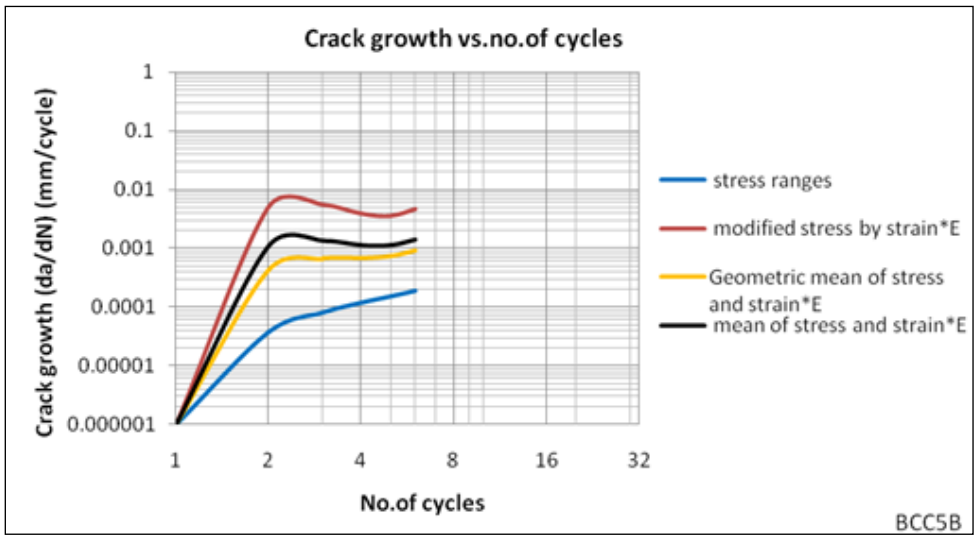

(b)

Figure C.2: (a) Chart and (b) log- log crack growth vs. no. of cycles for BCC5B model represent crack growth represents stress ranges , modified stress by strain*E, Geometric mean of stress and strain*E and mean of stress and strain*E ranges, related to Table C.4 values

Table C.7: Shows results of crack growth rates calculations based on stress ranges, stress modified by (strain*E) and Geometric mean of stress and (strain*E) for BCC5C

Cycle no.	Stress ranges da/dN(mm/cycle)=A ΔK^m	Modified stress by strain*E da/dN(mm/cycle)=A ΔK^m	Geometric mean of stress and strain*E da/dN(mm/cycle)=A ΔK^m	Mean of stress and strain*E da/dN(mm/cycle)=A ΔK^m
1	2.385E-05	7.81209E-06	1.36499E-05	1.44034E-05
2	2.23669E-05	1.10692E-05	1.57144E-05	1.60522E-05
3	2.71752E-05	1.33087E-05	1.89914E-05	1.94117E-05
4	3.15865E-05	0.000145082	6.75955E-05	7.47125E-05
5	3.73602E-05	0.000357185	0.000115335	0.000143196
6	4.38666E-05	0.000276259	0.000109895	0.000127052
7	5.38116E-05	0.000477758	0.000160039	0.000196032
8	6.41284E-05	0.000632511	0.000200983	0.000251045
9	7.09804E-05	0.000514186	0.000190603	0.000225403
10	8.46828E-05	0.000731463	0.000248246	0.000302648
11	9.38352E-05	0.001132141	0.000325005	0.0004225
12	0.000106754	0.001195317	0.000356077	0.000456046
13	0.000116412	0.00174453	0.000449037	0.000611361
14	0.000156938	0.00256643	0.000632108	0.000877671
15	0.000152205	0.002819161	0.000652068	0.000931941
16	0.000163564	0.004580851	0.000861189	0.001364123
17	0.000183348	0.0061903	0.001059306	0.00176446
18	0.000200122	0.006682021	0.001149063	0.00190886

Table C.8: Shows calculations of stress intensity factor using modification stress by (ε*E)

No. of cycles	εmax	εmin	εrange	εmax*E	εmin*E	Kmax=σmax $\sqrt{\pi a}$	Kmin=σmin $\sqrt{\pi a}$
1	0.00108	-0.0008	0.00188	216	-160	171.072	-126.72
2	0.00122	-0.0009	0.00212	244	-180	193.4141494	-142.6825693
3	0.00123	-0.00103	0.00226	246	-206	195.0049072	-163.2967922
4	0.00408	-0.0011	0.00518	816	-220	646.8670652	-174.4004342
5	0.00378	-0.0033	0.00708	756	-660	599.5206062	-523.3910054
6	0.00367	-0.0028	0.00647	734	-560	582.5933177	-444.485365
7	0.00544	-0.00238	0.00782	1088	-476	864.1661954	-378.0727105
8	0.00537	-0.00324	0.00861	1074	-648	854.0605688	-515.2991142
9	0.00548	-0.00252	0.008	1096	-504	872.9235668	-401.4174067
10	0.00701	-0.00202	0.00903	1402	-404	1118.062122	-322.1805258
11	0.00781	-0.00268	0.01049	1562	-536	1247.906821	-428.218986
12	0.00844	-0.00222	0.01066	1688	-444	1352.322458	-355.7056701
13	0.0106	-0.00152	0.01212	2120	-304	1703.375782	-244.2576593
14	0.0115	-0.0023	0.0138	2300	-460	1855.829701	-371.1659403
15	0.0124	-0.00177	0.01417	2480	-354	2013.420975	-287.3996069
16	0.0154	-0.00126	0.01666	3080	-252	2517.282829	-205.9595042
17	0.0164	-0.0019	0.0183	3280	-380	2709.466301	-313.9015837
18	0.0173	-0.00123	0.01853	3460	-246	2898.598837	-206.0853509

Table C.9: Shows calculations of stress intensity factor using stress ranges

.

No. of cycles	Normal stress MPa (min)	Normal stress MPa (max)	Kmax=σmax √ π a_c	Kmin=σmin √ π a_c	ΔK=Kmax-Kmin
1	-255.02	298.96	236.77632	-201.97584	438.75216
2	-248.68	292.6	231.9477421	-197.1317994	429.0795416
3	-285.72	293.39	232.5869882	-226.5065417	459.0935299
4	-278.14	331.98	263.1973575	-220.5124195	483.709777
5	-310.48	336.21	266.5719876	-246.1713533	512.7433409
6	-326.71	356.99	283.0743199	-259.0638703	542.1381902
7	-344.17	389.72	309.0613549	-272.9386393	581.9999942
8	-367.36	412.51	327.1785734	-291.3682595	618.5468329
9	-382.44	425.28	337.3609916	-303.3773929	640.7383845
10	-401.52	457.1	362.6670184	-318.5693748	681.2363932
11	-417.49	472.09	374.6393518	-331.3100955	705.9494474
12	-440.12	489.99	388.9353627	-349.3504599	738.2858226
13	-443.34	514.91	408.8246723	-352.0000198	760.8246921
14	-488.06	574.61	456.3571833	-387.6188839	843.9760671
15	-503.61	547.41	434.9247332	-400.125034	835.0497672
16	-509.7	567.51	451.0651996	-405.116971	856.1821706
17	-539.51	580.81	461.8239433	-428.9847551	890.8086984
18	-549.77	604.6	480.959209	-437.3419523	918.3011613

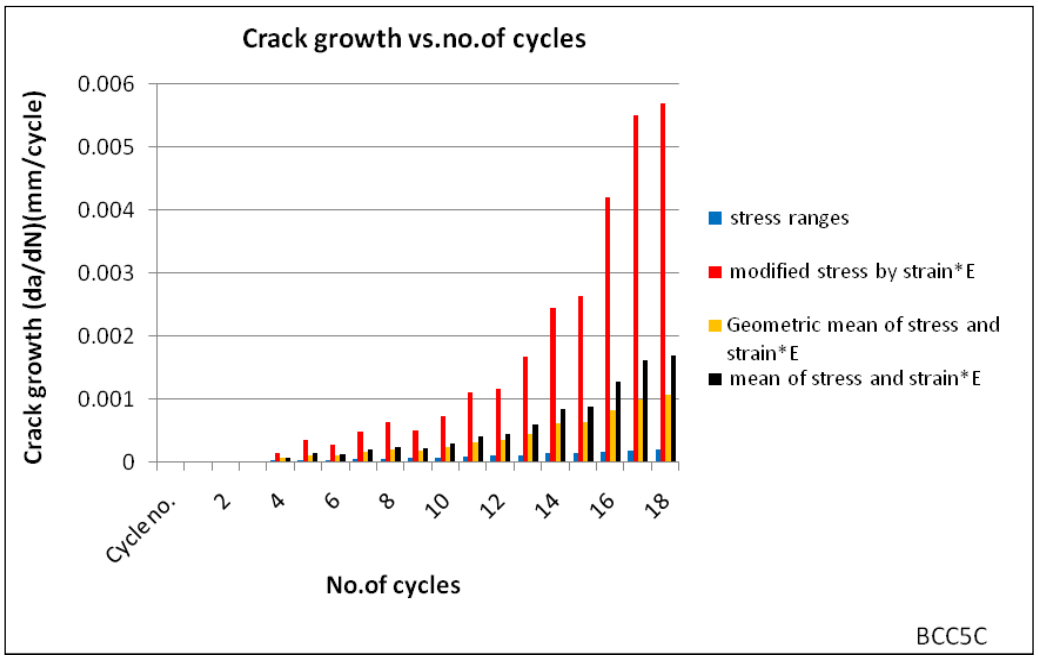

(a)

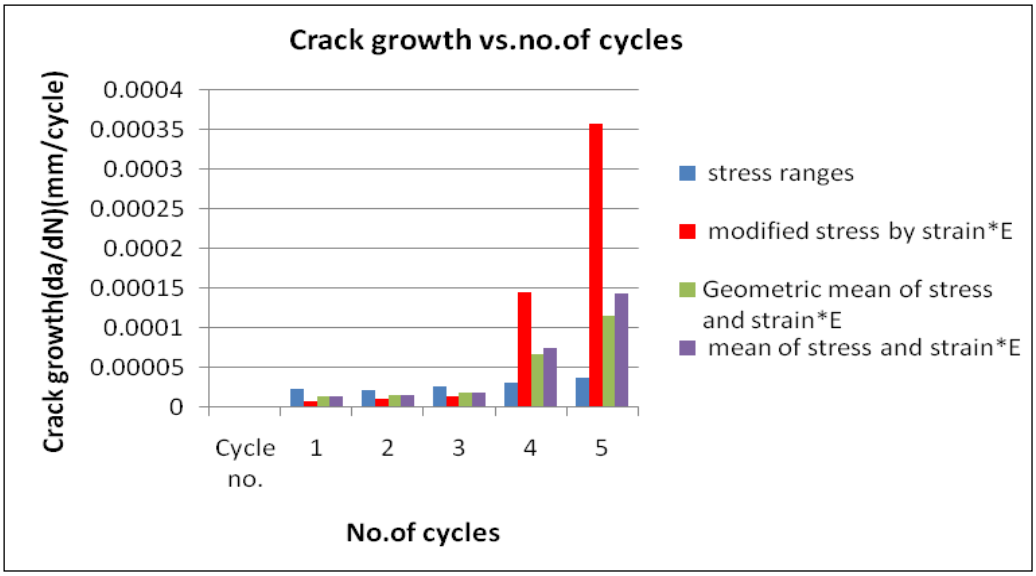

(b)

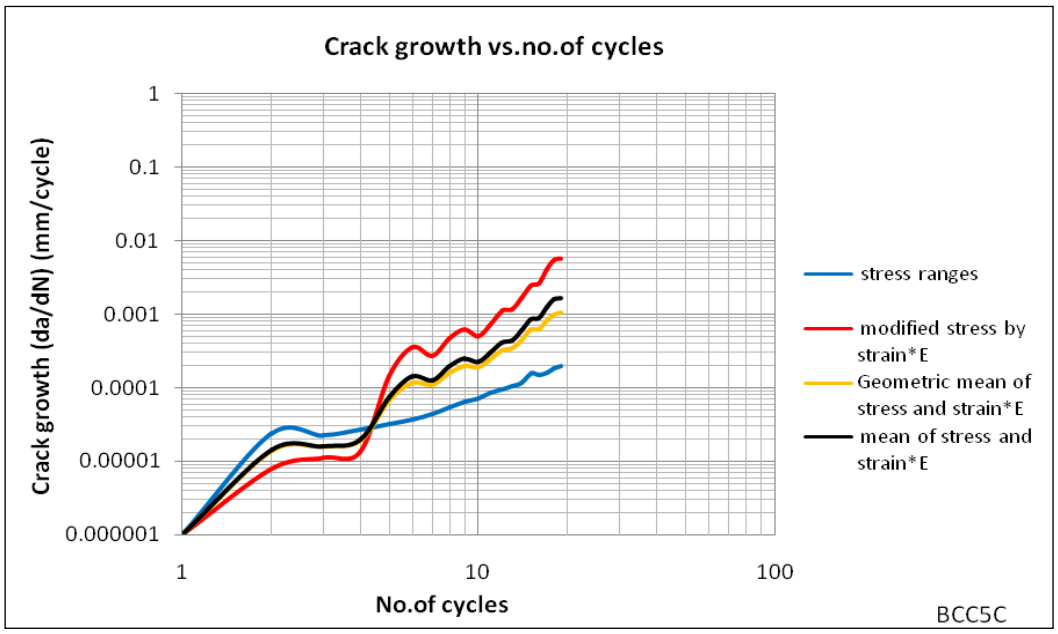

(c)

Figure C.3: (a) Chart for 18 cycles, (b) chart for first five cycles and (c) log- log crack growth vs. no. of cycles for BCC5C model represent crack growth represents stress ranges , modified stress by strain*E, Geometric mean of stress and strain*E and mean of stress and strain*E ranges, related to Table C.7 values

Table C.10: Shows results of crack growth rates calculations based on stress ranges, stress modified by (strain*E) and Geometric mean of stress and (strain*E) for BCC5D

Cycle no.	Stress ranges da/dN(mm/cycle)=A ΔK^m	Modified stress by strain*E da/dN(mm/cycle)=A ΔK^m	Geometric mean of stress and strain*E da/dN(mm/cycle)=A ΔK^m	Mean of stress and strain*E da/dN(mm/cycle)=A ΔK^m
1	3.43843E-05	0.001015627	0.000186873	0.000299372
2	3.7152E-05	0.00189007	0.000264637	0.000494211
3	6.92965E-05	0.001336735	0.000303907	0.000437883
4	7.09021E-05	0.001217579	0.000293314	0.000411385
5	9.37104E-05	0.001073374	0.000316529	0.000407035
6	9.43149E-05	0.001045062	0.000313227	0.000400193
7	0.00011688	0.0009907	0.000339384	0.000412379
8	0.000118847	0.001032381	0.000349207	0.000426243
9	0.000134903	0.001118707	0.000387125	0.000468709
10	0.000131699	0.001110978	0.000380992	0.000462761
11	0.00014284	0.00120562	0.000413141	0.000501943
12	0.000143231	0.001255952	0.000422037	0.000516367
13	0.000151678	0.001304782	0.000442438	0.000539563
14	0.000153407	0.001344699	0.000451462	0.000552544
15	0.000161593	0.001313866	0.000457758	0.000552905
16	0.000161801	0.00133608	0.000461642	0.000559231
17	0.000168332	0.001548843	0.000506681	0.000626039
18	0.000167976	0.001466543	0.000492219	0.000602493
19	0.000172718	0.001563441	0.000515034	0.000634727
20	0.000175462	0.001670196	0.000536211	0.000667177
21	0.000179427	0.00161684	0.00053317	0.000656831
22	0.00017885	0.001604458	0.000529932	0.00065246
23	0.000186994	0.001637523	0.00054707	0.000670756

Table C.11: Shows calculations of stress intensity factor using modification stress by (ε*E)

No. of cycles	εmax	εmin	εrange	εmax*E	εmin*E	Kmax=σmax √ π a	Kmin=σmin √ π a
1	0.00916	-0.00103	0.01019	1832	-206	1450.944	-163.152
2	0.00786	-0.00474	0.0126	1572	-948	1249.229952	-753.3524135
3	0.008	-0.00312	0.01112	1600	-624	1277.444496	-498.2033535
4	0.00841	-0.00232	0.01073	1682	-464	1347.329797	-371.6771852
5	0.00867	-0.00157	0.01024	1734	-314	1393.117293	-252.2715283
6	0.00915	-0.000969	0.010119	1830	-193.8	1474.080353	-156.1075259
7	0.00946	-0.000448	0.009908	1892	-89.6	1527.872794	-72.35592091
8	0.01	-0.0000269	0.0100269	2000	-5.38	1618.937057	-4.354940684
9	0.0106	0.000315	0.010285	2120	63	1720.31517	51.12257344
10	0.011	0.000767	0.010233	2200	153.4	1789.990546	124.811159
11	0.0117	0.0012	0.0105	2340	240	1908.91139	195.7857835
12	0.0121	0.00148	0.01062	2420	296	1979.783271	242.1553091
13	0.0126	0.00187	0.01073	2520	374	2067.660595	306.8670884
14	0.013	0.00219	0.01081	2600	438	2139.785358	360.4715334
15	0.0134	0.00271	0.01069	2680	542	2212.492542	447.4518499
16	0.0137	0.00298	0.01072	2740	596	2268.865366	493.5196198
17	0.0143	0.00305	0.01125	2860	610	2375.469375	506.6560555
18	0.0146	0.0036	0.011	2920	720	2433.842532	600.1255558
19	0.015	0.00379	0.01121	3000	758	2508.800815	633.8903393
20	0.0153	0.00387	0.01143	3060	774	2567.947347	649.539623
21	0.0155	0.00424	0.01126	3100	848	2611.188653	714.2864444
22	0.0159	0.00471	0.01119	3180	942	2688.145276	796.2996382
23	0.0162	0.00497	0.01123	3240	994	2748.507813	843.2150513

Table C.12: Shows calculations of stress intensity factor using stress ranges (ε*E)

No. of cycles	Normal stress MPa (min)	Normal stress MPa (max)	Kmax=σmax √ π a	Kmin=σmin √ π a	ΔK=Kmax-Kmin
1	-269.98	359.03	284.35176	-213.82416	498.17592
2	-283.62	361.93	286.9140699	-224.8351021	511.749172
3	-371.64	429.84	340.7802502	-294.6388707	635.4191208
4	-377.9	429.84	340.8392611	-299.6537241	640.4929852
5	-416.34	473.38	375.4305469	-330.1929822	705.6235291
6	-421.33	470.17	372.9719997	-334.2286675	707.2006672
7	-453.21	507	402.282828	-359.6027623	761.8855902
8	-450.51	515	408.7496323	-357.564654	766.3142863
9	-478.04	530.6	421.2559595	-379.5273254	800.7832849
10	-478.04	521.88	414.4722147	-379.6548968	794.1271115
11	-487.53	540.65	429.5199791	-387.3187375	816.8387165
12	-489.93	538.86	428.2500721	-389.3637639	817.613836
13	-502.75	546.34	434.3493179	-399.6945484	834.0438663
14	-502.75	550.08	437.4874994	-399.8451868	837.3326862
15	-511.16	560.44	445.8967483	-406.6886408	852.5853891
16	-512.97	558.68	444.6746611	-408.2923336	852.9669947
17	-516.18	569.86	453.7551783	-411.0120871	864.7672653
18	-521.9	562.89	448.3921467	-415.7399516	864.1320984
19	-524.64	570.23	454.427952	-418.0963484	872.5243003
20	-530.18	570.23	454.6220402	-422.6917441	877.3137843
21	-534.4	574.1	457.9058647	-426.2408886	884.1467533
22	-532.67	574.1	458.1086845	-425.0492127	883.1578972
23	-538.32	585.2	467.1720226	-429.7471688	896.9191914

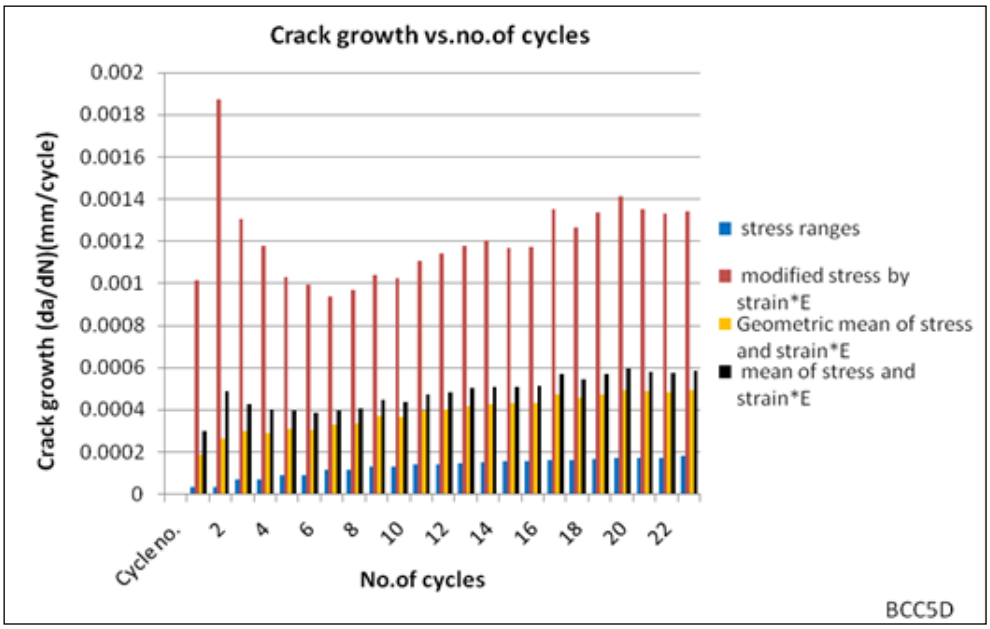

(a)

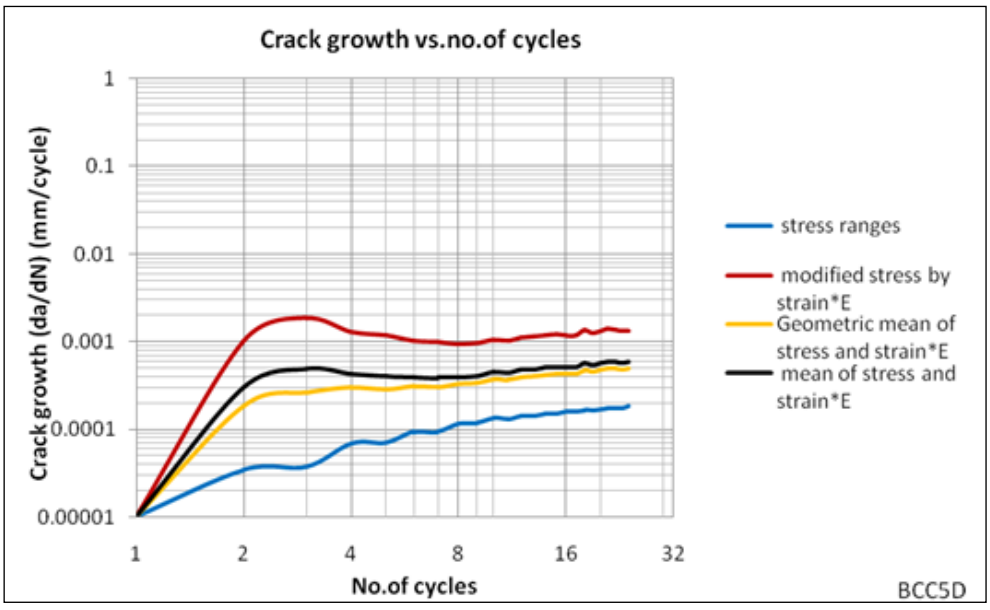

(b)

Figure C.4: Chart and (b) log- log crack growth vs. no. of cycles for BCC5D model represent crack growth represents stress ranges , modified stress by strain*E, Geometric mean of stress and strain*E and mean of stress and strain*E ranges, related to Table C.10 values

C.9 Summary

Appendix C was showing calculation of strain amplitude and fatigue damage index including: strain life formulas (strain amplitude calculation without using n`), relation among b, c and n` (strain amplitude calculation using n`), fatigue damage index, calculating fatigue damage index using MathCAD (including n'), calculating fatigue damage index using MathCAD (excluding n'), panel zone stiffness MathCAD calculations (stress-strain graph correction). And also calculate failure assessment diagram (FAD) calculation, fatigue damage index (FDI) and crack growth stress ranges, modified stress based on strain*E, Geometric mean of stress and strain*E and mean of stress and strain*E ranges.

Following Appendix D is showing failure location obtained from FE analysis compared with the failure location experimental tests by Calado [2010-2014, per. comm.], and it is showing contours for joints and sections of BCC5 FE models at critical point.

APPENDIX D
FAILURE LOCATION AND CONTOURS

This Appendix is showing failure location obtained from FE analysis compared with the failure location experimental tests by Calado [2010-2014, per. comm.], and it is showing contours for joints and sections of BCC5 FE models at critical point:

Section D.1 failure location
Section D.2 contours

D.1 Failure location

Failure location of experimental test for all BCC5 specimens is the same location where the FE analysis monitored the maximum normal stress and maximum total strain as explained in Sec.4.4.2.

Table 4.5 shows maximum total strain (maximum principle strain) and maximum normal stress (maximum principle stress) for BCC5 FE models at critical point where the failure occurred for BCC5 specimens in experimental tests.
Figure 4.21 shows that failure for FE base model (BCC5A) occurred at the same location point as experimental work.

Figures D.1-D.3 show failure location for the other BCC5 specimens of the experimental testes and FE analysis.

(a) [Calado, 2010-2014, per. comm.]

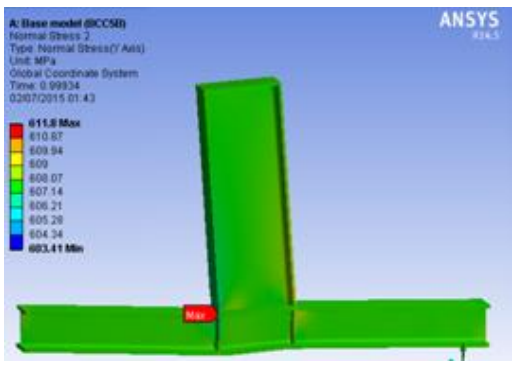

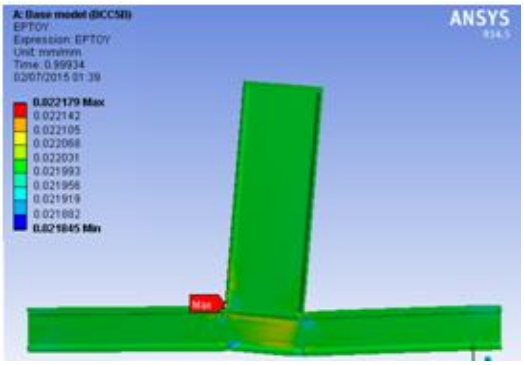

(b) (c)

Figure D.1: (a) Specimen location failure, (b) FE maximum normal stress location and (c) FE maximum total strain location for BCC5B base model

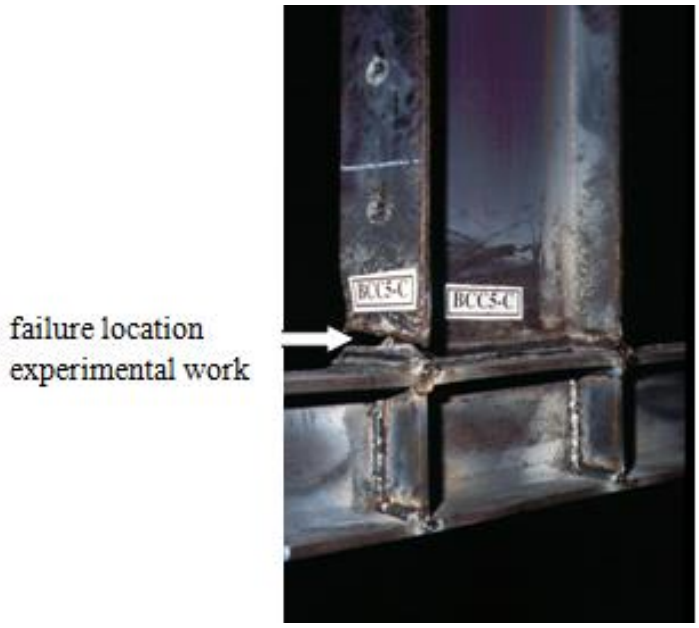

(a) [Calado, 2010-2014, per. comm.]

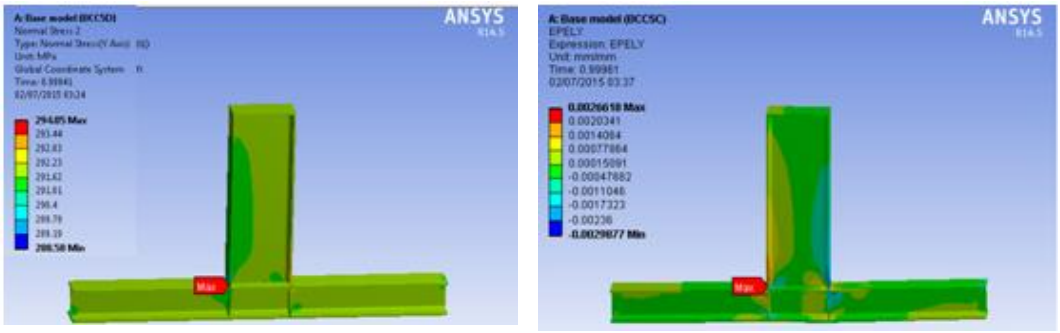

(b) (c)

Figure D.2: (a) Specimen location failure, (b) FE maximum normal stress location, and (c) FE maximum total strain location for BCC5C base model

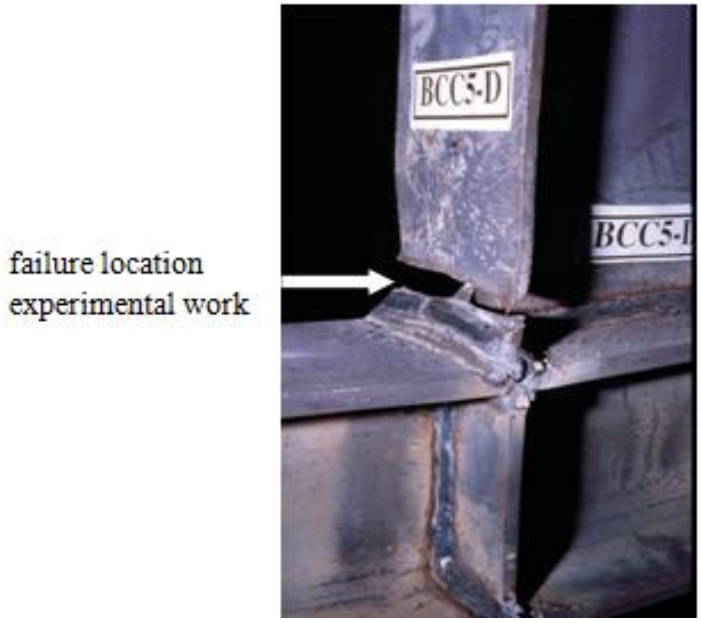

(a) [Calado, 2010-2014, per. comm.]

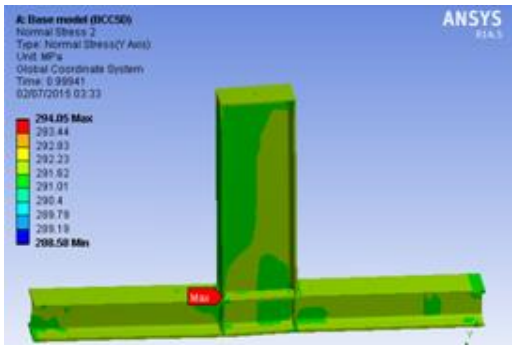

(b)

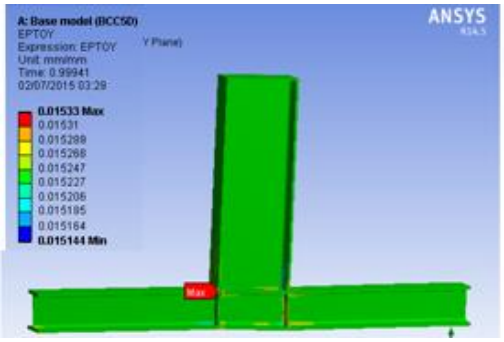

(c)

Figure D.3: (a) Specimen location failure, (b) FE maximum normal stress location and (c) FE maximum total strain location for BCC5D base model

D.2 Contours

Contours have been taken from FE ANSYS for all BCC5 models. Contours are taken in a different time (0.25,0.5,0.75) and last reading before the time ending, because at the end of time which is one second structure has failed and the reading is not going to be accurate. Time set the analysis is one second for each FE model, and it is different than the time for experimental test as explained in Sec. A.3.2.1.

BCC5 contours show red colour at the connection which is the failure location and it is clear at the contours section as well.
It is noticed that the high strain (red colour) position is been changed from left beam flange to right beam flange according to the time and cyclic loading.

In comparison, FE analysis with experimental work failure location. Specimens photos in Figure A.6 [Calado, 2010-2014, per. comm.] showed that failure occurred at the edge of left beam flange for all BCC5 specimen tests, but FE analysis monitored that the failure occurred at the middle of left beam flange for all BCC5 models as shown in Figure 4.23 and Figures D.4-D.6.

The reason of different failure location between experimental work specimens and FE ANSYS models, could be due to the shear yielding in the column panel zone is an efficient energy dissipation mechanism for MRFs, while also cautioning that excessive panel zone deformation can cause kinks in the column flanges, and consequently generate large strain demands in the region of the beam flange welds. The high strains imposed by these kinks can lead to premature fracture of the beam flange welds flange is affected by column web stress which is occurred in panel zone due to shear stresses, or could be due to lot of weld materials at the middle of left beam flange in specimen test, or might be due to the sensitivity of the left beam edge. Figures D.4-D.6 show joint and section contours for BCC5B, BCC5C and BCC5D FE models with different time respectively.

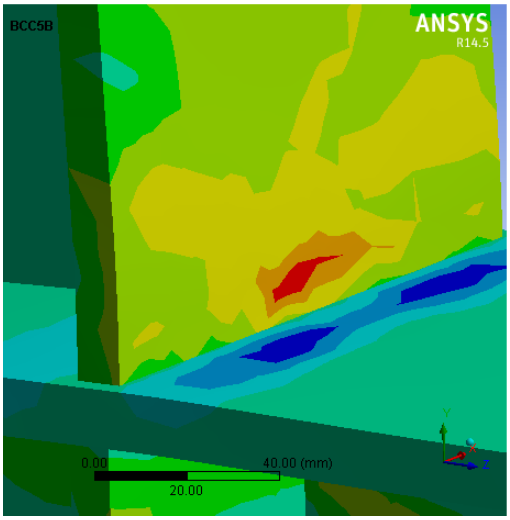

(a) right beam flange at 0.25s

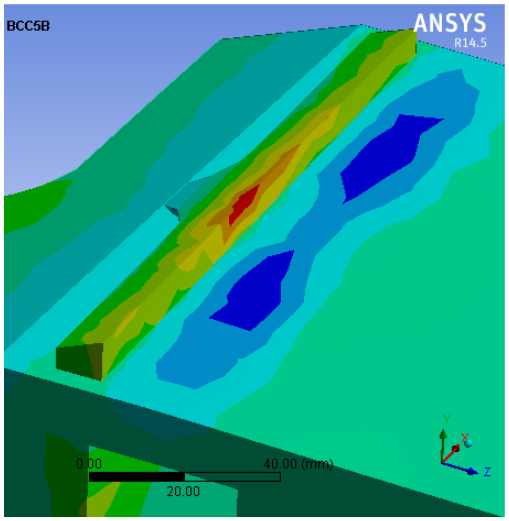

(b) section at right beam flange at 0.25s

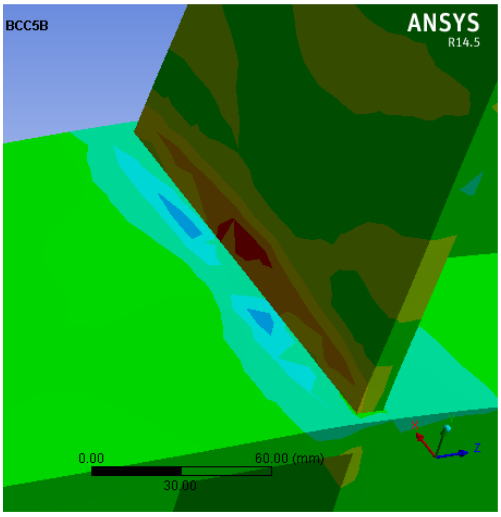

(c) left beam flange at 0.5s

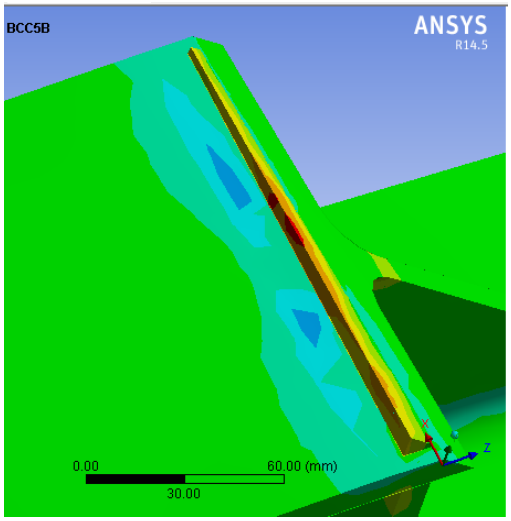

(d) section at left beam flange at 0.5s

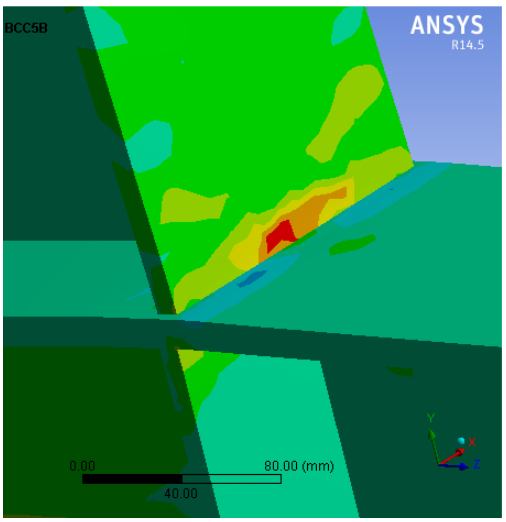

(e) right beam flange at 0.75s

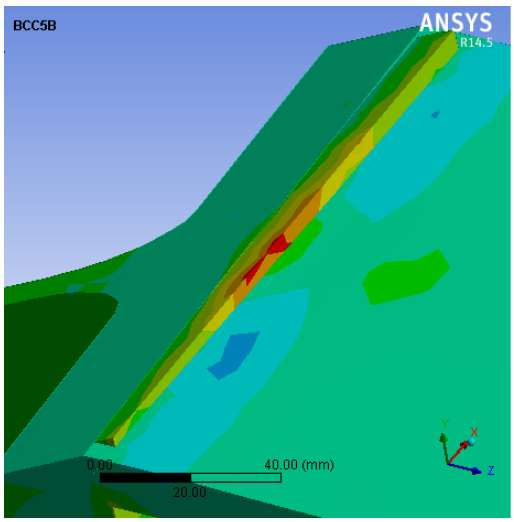

(f) section at right beam flange at 0.75s

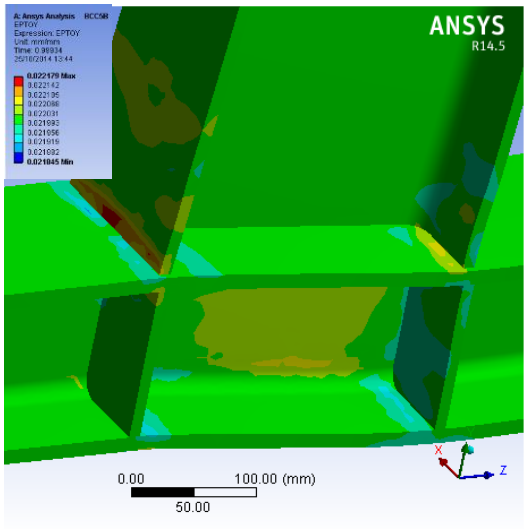

(g) right beam flange at 0.99934s

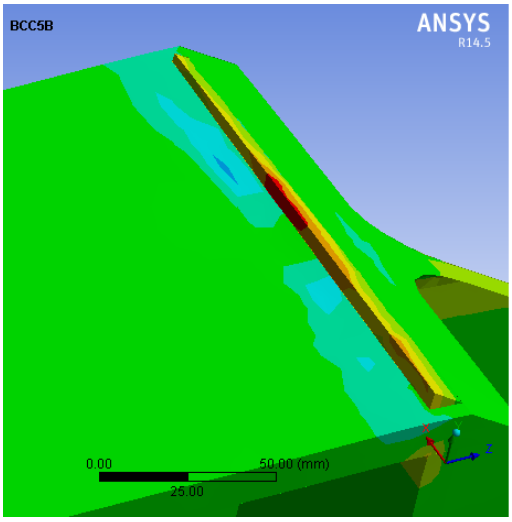

(h) section at right beam flange at 0.99934s

Figure D.4: (a) Right beam flange at 0.25s, (b) section at right beam flange at 0.25s, (c) left beam flange at 0.5s, (d) section at left beam flange at 0.5s, (e) right beam flange at 0.75s, (f) section at right beam flange at 0.75s, (g) left beam flange at 0.99934s and (h) section at left beam flange at 0.99934s for BCC5B

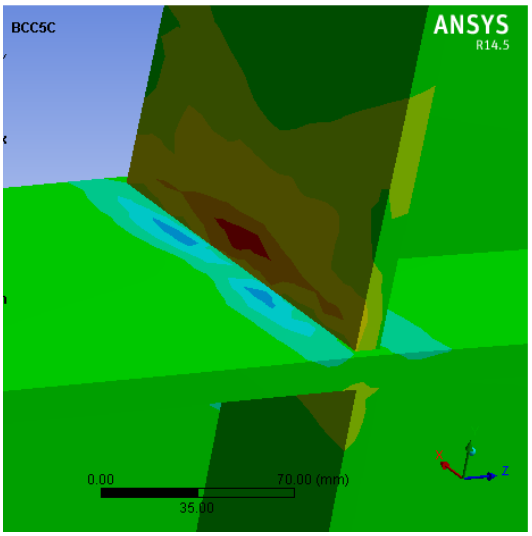

(a) left beam flange at 0.25s

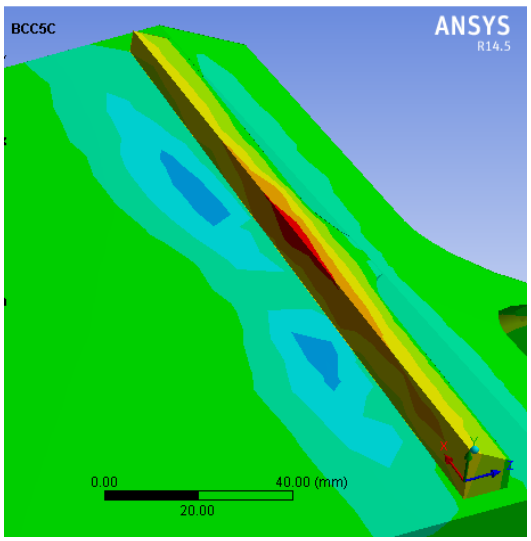

(b) section at left beam flange at 0.25s

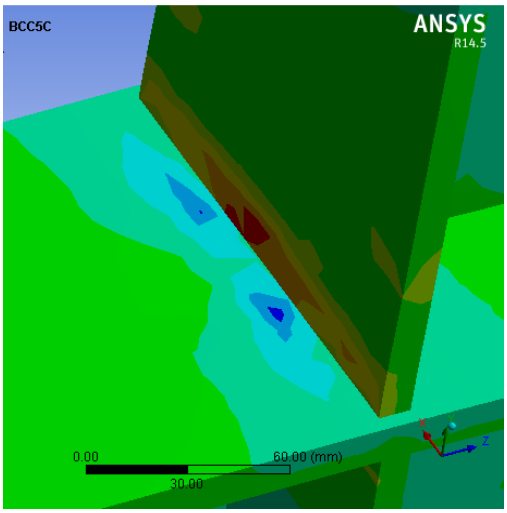

(c) left beam flange at 0.5s

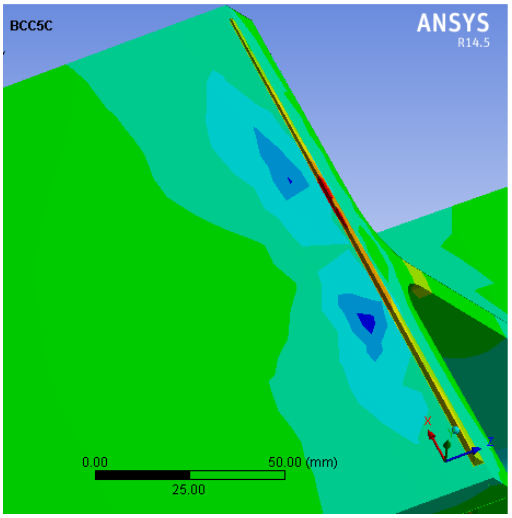

(d) section at left beam flange at 0.5s

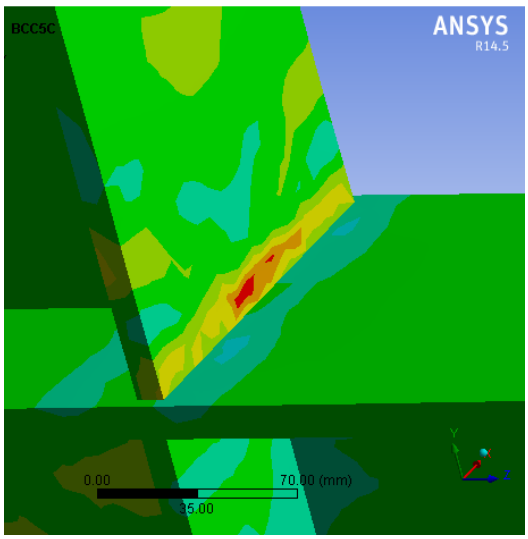

(e) right beam flange at 0.5s

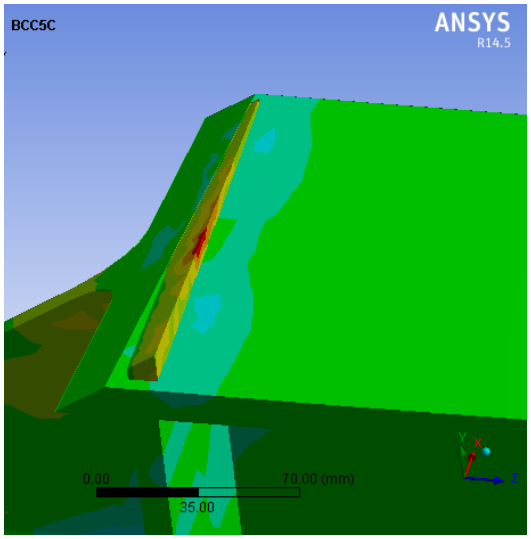

(f) section at right beam flange at 0.5s

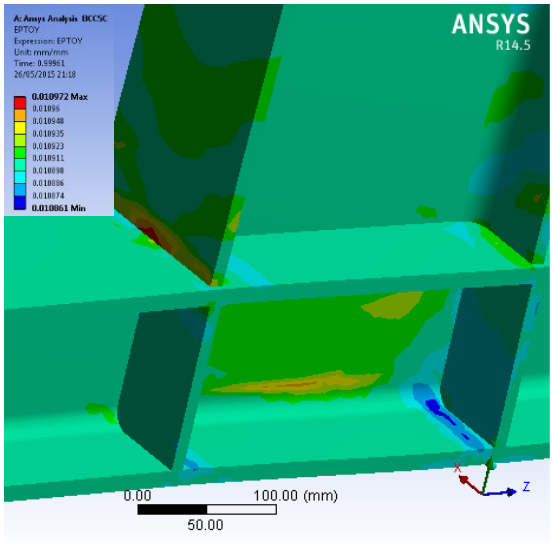

(g) left beam flange at 0.99961s

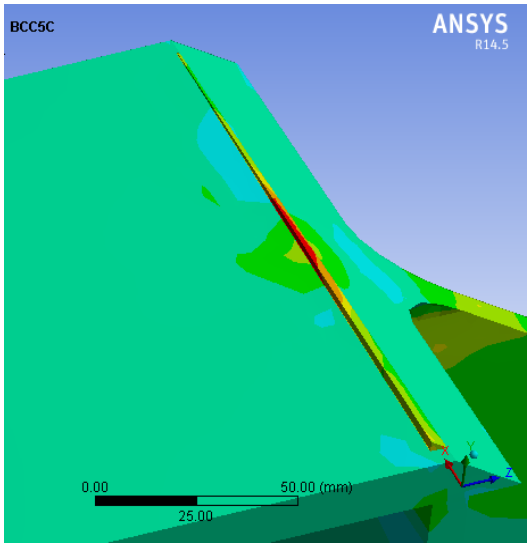

(h) section at left beam flange at0.99961s

Figure D.5:(a) Left beam flange at 0.25s, (b) section at left beam flange at 0.25s, (c) left beam flange at 0.5s, (d) section at left beam flange at 0.5s, (e) right beam flange at 0.75s, (f) section at right beam flange at 0.75s, (g) left beam flange at 0.99934s and (h) section at left beam flange at 0.99934s for BCC5C

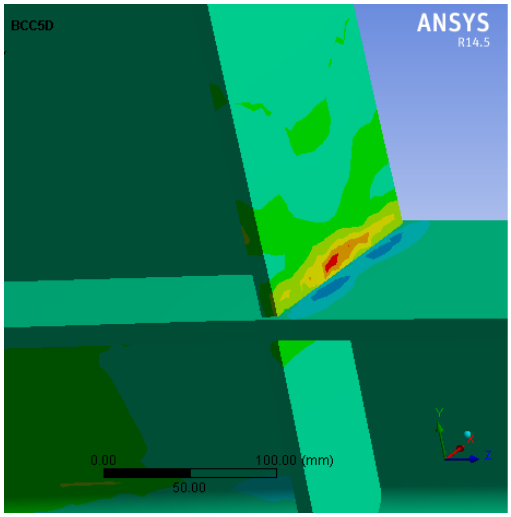

(a) right beam flange at 0.25s

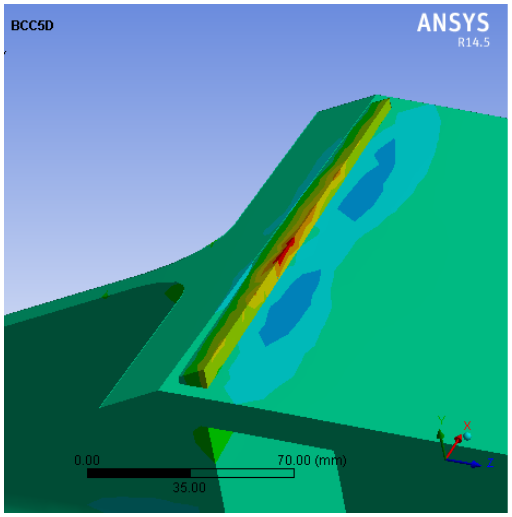

(b) section at right beam flange at 0.25s

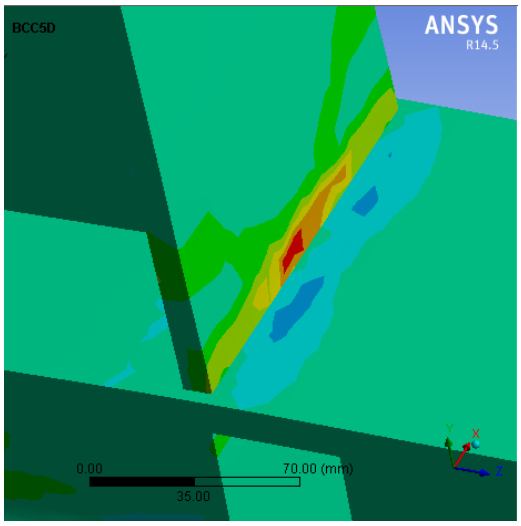

(c) right beam flange at 0.5s

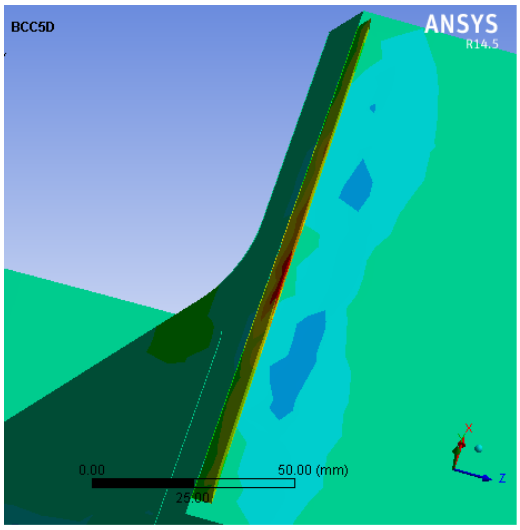

(d) section at right beam flange at 0.5s

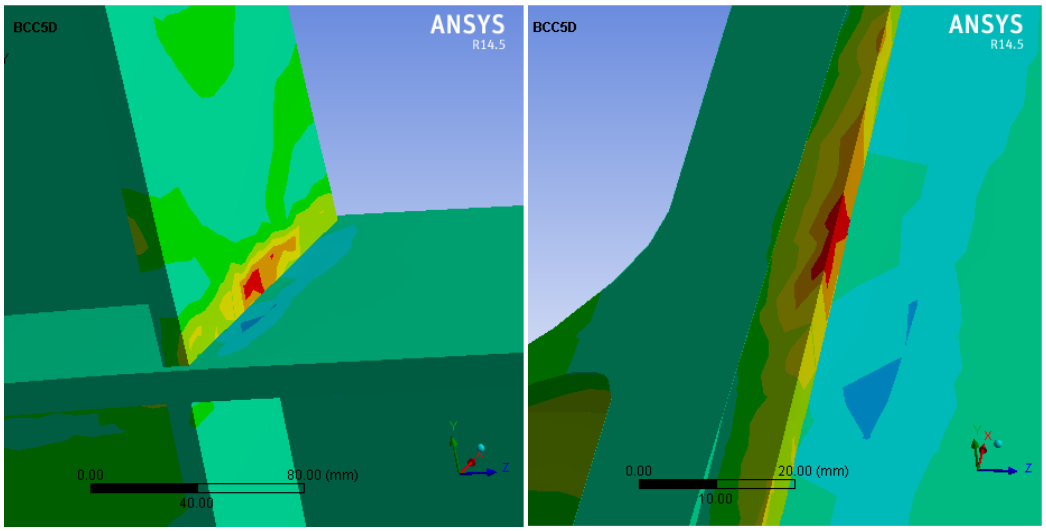

(e) right beam flange at 0.75s (f) section at right beam flange at 0.75s

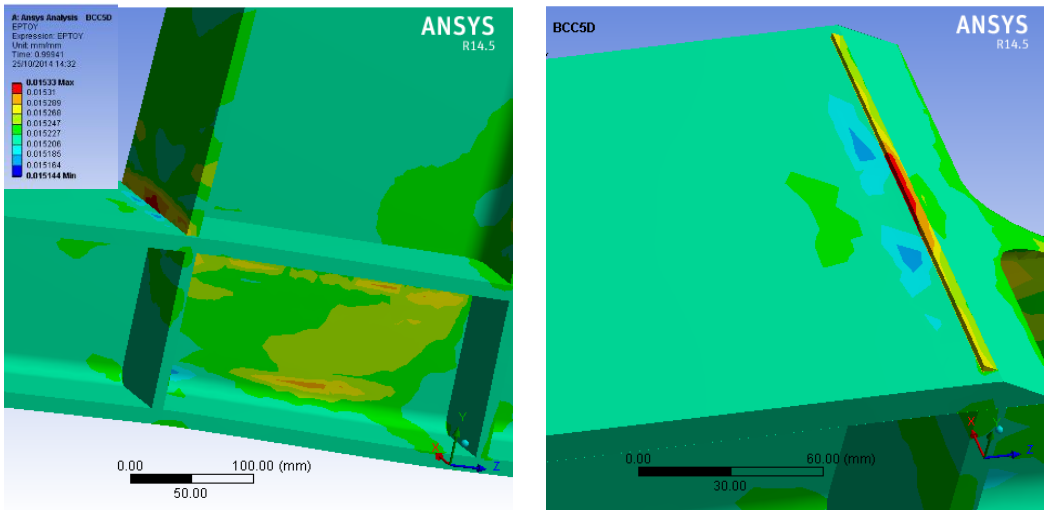

(g) left beam flange at 0.99941s (h) section at left beam flange at0.99941s

Figure D.6: (a) Right beam flange at 0.25s, (b) section at right beam flange at 0.25s,(c) right beam flange at 0.5s, (d) section at right beam flange at 0.5s, (e) right beam flange at 0.75s, (f) section at right beam flange at 0.75s, (g) left beam flange at 0.99941s and (h) section at left beam flange at 0.99941s for BCC5D

D.3 Summary

Appendix D was showing failure location obtained from FE analysis compared with the failure location experimental test by Calado [2010-2014, per. comm.], and it is showing contours for joints and sections of BCC5 FE models at critical point.

REFERENCES

Abdullah, S., Beden, S. M. and Ariffin A. K. (2011). *Fatigue Crack Growth Simulation of Aluminium Alloy under Cyclic Sequence Effects, Aluminium Alloys, Theory and Applications*, Prof. Tibor Kvackaj (Ed.), ISBN: 978-953- 307-244-9, InTech. [online]. Available from: http://www.intechopen.com/books/aluminium-alloys-theory-andapplications/fatigue-crack-growth-simulation-of-aluminium-alloy-under-cyclic-sequence-effects.

Adams R.D., J.A. Harris. (1984). *Strength prediction of bonded single lap joints by nonlinear finite element methods*. Int J Adhes 4, pp 65–78.

Adams R.D. and Harris J.A. (1987). *The Influence of local Geometry on the Strength of Adhesive Joints*. Int. J. Adhes, Adhes. 7,pp.69–80.

Adams R.D., Bell A.J., and Kinlock A.J. (1997). *The effect of the substrate material on the value of the adhesive fracture energy*. G(c). J. Mater. Sci. Lett. 16, pp150–1453.

Ahmed A.(2009). *eXtended finite element method (XFEM)Modeling arbitrary discontinuities and Failure analysis*. MSc thesis, Istituto Universitario di Studi Superiori di Pavia Universita degli Studi di Pavia. [Online]. Available from: www.roseschool.it/files/get/id/4486.

Alam M. (2005). *Structural integrity and fatigue crack propagation life assessment of welded and weld-repaired structures*. PhD thesis, Department of Mechanical Engineering , Louisiana State University and Agricultural and Mechanical College.

Alan, L.(2005). *Mechanics and Mechanisms of Fracture an Introduction*, ASM International.

Almar-Naess A. (1985). *Fatigue handbook Offshore Steel Structures*, pp 215, pp 245,Tapir.

Amandeep, W.,Singh, D. and Harvinder, S. (2008). *A text book for engineering material and metallurgy* , UEM-9212-275, 1st edition .University science press, New Dalhi.

American Society for Testing and Materials. (1969). *Manual on Low Cycle Fatigue Testing*, ASTM STP 465, ASTM (Philadelphia).

Anant P. A., and Srivastava. S. K. (2012). *Fatigue Life Prediction Of Crankshaft Based On Strain Life Theories*, Mechanical Engineering Department, M.M.M. Engineering College, Gorakhpur-273 010 (U.P.), International Journal of Engineering, Vol. 1 Issue 8, ISSN: 2278-0181, India.

Anderson T.L. (2005). *Fracture Mechanics Fundamentals and Applications*, 3rd Edition, pp. 453-455. Taylor& Francis group, Boca Raton. ISBN-10:0-8493-1656-1.

ANSYS release 14.5.(2012). *ANSYS Workbench help*. Southpointe, 275 Technology Drive 000410, Canonsburg, PA15317, USA. [online]. Available from: http://www.ansys.com

Arun, S.A.(2005). *Practical Fracture Mechanics in Design*. 2nd Ed, Marcel Dekker, New York.

ASCE/SEI Standard 41-06. (2006). *Seismic rehabilitation of existing buildings.* American Society of Civil Engineers, Reston, VA.

ASM Handbook.(1997). *ASM Fatigue and Fracture*.Vol.19,pp.56,146,274,591. ISBN:0-87170-385-8.USA.

Basquin, O.H. (1910). *The exponential law of endurance tests*, proceedings of ASTM,Vol. 10(II), pp. 625-630.

Bauschinger J.(1886). *On the change of the position of the elastic Limit of Iron and steel under cyclic variations of stress*, Mitt. Mech.-Tech. Lab., Munich, Vol. 13, No.1.

Becker A.A.(2004), *An introductory guide to finite element analysis*. Professional engineering publishing limited, ISBN: 1860584101, London and Bury St., Edmunds ,UK

Belytschko, T. and Black T. (1999). *Elastic crack growth in finite elements with minimal remeshing*. International journal for numerical methods in engineering 45, pp 601–620.

Bishop, N., and Sherratt, F. (2000). *Finite element based fatigue calculations*, The Int. Association for the Engg., NAFEMS Ltd., Analysis community Netherlands.

Björk, T., Marquis, G., Pellikka, V. and Ilvonen, R. (2006). *An experimental and numerical study of the fracture strength of welded structural hollow section X-joints*. Journal of ASTM International,Vol.3, No.6, paper ID JAI13183, West Conshohocken.

Bleck ,W.*et al*. (2009). *Numerical and experimental analyses of damage behaviour of steel moment connection*, Elsevier Ltd. Engineering fracture mechanics 76, pp. 1531–1547, Aachen, Germany.

British Standard, (2005). *BS7910:2005*: *Guide to methods for assessing the acceptability of flaws in metallic structures*.

British Standard, (2013). *BS7910:2013*: *Guide to methods for assessing the acceptability of flaws in metallic structures*.

British Standard, (2014). *BS7608*:*2014*: *Guide to fatigue design and assessment of steel structures*.

Buddena P.J., Sharplesb J.K. and Dowling A.R.(2000). *The R6 procedure: recent developments and comparison with alternative approaches*, International Journal of Pressure Vessels and Piping 77.pp 895-903. [online]. Available from: www.elsevier.com/locate/ijpvp

Byfield , M.P., Daviesb, J.M., and Dhanalakshmic, M. (2005). *Calculation of The Strain Hardening Behaviour of Steel Structures Based on Mill Tests*,. Elsevier Ltd, Journal of Constructional Steel Research 61 , pp 133–150, UK.

Byfield, M.P., and Nethercot, D.A.(1998). *An analysis of the true bending strength of steel beams*. Structures and buildings proceedings of the Institution of Civil Engineers 1998: 128:188–97.

Cafer H. (2009). *3-D Finite element analysis of semi-rigid steel connections*. [online]. Thesis (MSc). Civil engineering department, Middle East Technical University.

Calado, L., Castiglioni, C. A. and Bernuzzi, C. (2000). *Seismic behaviour of welded beam-to-column joints: Experimental and numerical analysis*. Dept. of Civil engineering and architecture, Instituto Superior Tecnico,Lisbon P.,and Dept. of structural engineering, Politecnico di Milano, Milan.

Campbell S.D., Richard R.M., and Partridge J.E. (2008). *Steel moment frame damage predictions using low-cycle fatigue*. The 14th World Conference on Earthquake Engineering, Beijing, China.

Campbell J.(2003). *Castings*, 2nd Edition, Elsevier Butterwirth - Heinemann, Oxford ,UK

Carlo, A. and Castiglioni (2005). *Effects of the loading history on the local buckling behaviour and failure mode of welded beam-to-column joints in moment-resisting steel frames*. Journal of engineering mechanics, ASCE.

Coffin, L. F. (1954). *A Study of the effects of cyclic thermal stresses on a ductile metal*. Trans. ASME**,** vol. 76, no. 6, August, pp. 931-949, discussion, pp. 949-950.

Chemin, L. (2009). *Low cycle fatigue life prediction of four bolt extended unstiffened end plate moment connections*. [online]. Thesis (PhD). North Carolina State University, Raleigh, North Carolina.

Chen, C.C., Lin, C.C. and Lin, C.H. (2006). *Ductile moment connections used in steel column-tree moment-resisting frames*. Elsevier Ltd, Journal of constructional steel research 62 , pp 793–801 , Taiwan.

Chen, W., ASCE, and Kishi, N.(1989). *Semi rigid steel beam-to-column connections: Data base and modeling*. Journal of structural engineering, Vol.115, ASCE No.1, paper No. 23104.

Chen, Y., Liu, Y. and Bian, R. (2006). *Numerical model for partial fracture failure of steel beam-to-column joints*. Tongji University, Shanghai, China, and Vanderbilt University, TN, USA.

Chen, Y., Bian, R., and Liao, F. (2008). *Tests on impact effect of partial fracture at steel frame connections*. Higher Education Press and Springer, Front.Archit.Civ.Eng.2 (4), pp.295-301, China.

Chi, W.M. *et al*.(2000). *Fracture toughness demands in welded beam-column moment connections*. Journal of structural engineering, January, Vol. 126, No. 1, ASCE, Paper No. 20622, pp. 88-97.

Clough R.W.(1960). *Second ASCE conference on electronic computation*, Pittsburgh.

Danielb. (1997).*Tool and manufacturing engineering handbook*, pp.20-1, 21-6, 20-9, 20-20, Dallas, USA.

Darrell, F .(2008,2013). *A trusted source for fatigue analysis* .[online]. Available from: https://www.efatigue.com/welds/background/strainlifewelds.html.

Da Silva ,L. F. M. and Campilho R. D. S. G.(2012). *Advances in numerical modelling of adhesive joints*, Springer Briefs in Computational Mechanics, DOI: 10.1007/978-3-642-23608-2-1, - Lucas F. M. da Silva .

David, R. (2001). *Department of materials science and engineering*, Massachusetts Institute of Technology, Cambridge.

Davies C. M., O'Dowd N. P., Dean D. W., Nikbin K. M., and Ainsworth R. A.(2003). *Failure assessment diagram analysis of creep crack initiation in 316H*

stainless steel , Department of mechanical engineering, Imperial College London, South Kensington campus, London , UK.

DET NORSKE VERITAS (DNV).(2012). DNV-OS-F101. *Offshore standard, submarine pipeline system.*[online] . Available from : http://www.dnv.com.

DET NORSKE VERITAS (DNV). (2006). DNV-RP-F108. *Fracture control for pipeline installation methods introducing cyclic plastic strain.* [online] Available from: http://www.dnv.com

Dubina , D. and Stratan , A. (2002). *Behaviour of welded connections of moment resisting frames beam-to-column joints*. Elsevier Science Ltd , Engineering structures 24 , pp. 1431–1440, Romania.

eFunda, Inc. (2014). *Definition of crack tip opening displacement* .[online]. Available from: https://www.efunda.com/formulae/solid_mechanics/fracture_mechanics/fm_epfm_CTOD.cfm.

eFunda, Inc. (2014). *Low-cycle fatigue*.[online] Available from: http://www.efunda.com/formulae/solid_mechanics/fatigue/fatigue_lowcycle.cfm.

eFunda, Inc. (2014). *High-cycle fatigue*.[online] Available from: http://www.efunda.com/formulae/solid_mechanics/fatigue/fatigue_highcycle.cfm.

Elber W. (1970). *Fatigue Crack Closure under Cyclic Tension*. Engineering Fracture Mechanics, Vol. 2, pp. 37–45.

Engineering Archives. (2008 – 2012). *Cyclic loading*.[online] Available from: http://www.engineeringarchives.com/les_machdes_cyclicloading.html

Erke W. (2006). ANSYS, Inc. *Thin wall structure simulation*. International ANSYS conference, Cadfem Gmbh ,Germany.

Eurocode 3 (2005). BS EN 1993-1-8:2005: *Design of Steel Structures – Part 1-8: Design of Joints*. European Committee for Standardization.

Eurocode 3 (2005). BS EN 1993-1-9:2005: *Design of Steel Structures – Part 1-9: Fatigue*. European Committee for Standardization.

European Convention for Constructional Steelwork (ECCS).(1986). *Seismic design. recommended testing procedure for assessing the behaviour of structural steel elements under cyclic loads*. Technical Communication 1-structural safety and loadings, TWG1.3-Rep, No. 45.

Fardis M. *et.al.* (2005). Eurocode 8 EN 1998-1 and 1998-5:2005: *Design of Steel Structures for earthquake resistance.* Thomas Telford ltd. ISBN:0 727733486.

Hart-Smith L.J.(1973). *Adhesive-bonded single-lap joints*. NASA Contract Report, NASA CR-112236.

Hedayat, A. A. and Celikag, M.(2009). *Fracture moment and ductility of welded connections*. The Institution of Civil Engineers, Issue SB6, pp. 405–418, London, UK.

Higashida Y.,Burk D.,and Lawrence F.V.(1978). *ASTM A36 and A514 grade F steels and 5083-0 Aluminium weld materials strain-controlled fatigue behaviour*. American society for testing and materials.

Hoeppner , D.W. (1981). *Estimation of component life by application of fatigue crack growth threshold knowledge, fatigue, creep, and pressure vessels for elevated temperature service*, MPC-17, ASME, pp. 1-84.

Höhler, S. and Sedlacek, G. (2005). *Selection of material for welded steel structures based on fracture mechanics*. Journal of ASTM International, Vol. 2, No.6, June,UK.

Jiaru, Q. *et al*.(2005). *Experimental study on full-scale steel beam-to-column moment connections*. Earthquake Engineering and Engineering Vibration, Vol.4, No.2, China.

Jones S.L., Fry G.T., and Engelhardt M.D. (2002). *Experimental evaluation of cyclically loaded reduced beam section moment connections*. Journal of Structural Engineering,128(4): pp.51- 441.

Kang G.Z., Li Y.G., Zhang J., Sun Y.F., and Gao Q.(2005). *Uniaxial ratcheting and failure behaviours of two steel*, Theoretical and Applied Fracture Mechanics, 43 ,pp. 199-209.

Khandelwal, K. and El-Tawil, S.(2007). *Collapse behaviour of steel special moment resisting frame connections*. Journal of Structural Engineering , ASCE

Kim T. and Kim J.(2009). *Collapse analysis of steel moment frames with various seismic connections*. Elsevier Ltd, Journal of Constructional Steel Research 65, pp. 1316-1322, Republic of Korea.

Kiral , B.G. and Erim , S. (2005). *Prediction of fracture behaviour of steel beam-to-column connections with weld defect using the SINTAP*, Elsevier Ltd, Engineering Structures 27,pp. 760–768, Izmir, Turkey.

Kiral, B. G. (2004). *Effects of the weld electrode on the fracture behaviour of welded steel beam-to-column joints*. Association for scientific research, Mathematical and Computational Applications, Vol. 9, No. 3, pp. 449-456,Izmir, Turkey.

Kuntiyawichai, K. and Burdekin, F.M.(2002). *Engineering assessment of cracked structures subjected to dynamic loads using fracture mechanics assessment*. Elsevier Ltd Engineering Fracture Mechanics 70, pp. 1991–2014, Thailand.

Kyungkoo L. & Bozidar S.(2004). *Low-cycle fatigue limit on seismic rotation capacity for us steel moment connections*,13th World Conference on Earthquake Engineering Vancouver, B.C., Paper No. 90, August 1-6, Canada.

Lawrence F.(1973). *Estimation of fatigue-crack propagation life in butt welds analytical model assesses the influence of joint geometry, weld reinforcement and other factors relative to the propagation of fatigue cracks*.Welding research supplement

Leo D. Bores, MD.(2002).[online] Available from: http://www.e-sunbear.com/biomech_05.html.

Lopez Z. and Fatemi A. (2012). *A method of predicting cyclic stress- strain curve from tensile properties for steels*, Materials Science and Engineering: A, Vol. 556, pp. 540-550.

Madi, Y., Recho, N. and Matheron, P.(2004). *Low-cycle fatigue of welded joints: coupled initiation propagation model*. Elsevier B.V, Nuclear Engineering and Design 228, pp. 179–194, Paris, France.

Manson, S.S. (1953). *Behaviour of materials under conditions of thermal stress*, Heat Transfer Symposium, pp. 9-75.

Manson, S. S.(1954). *Behaviour of materials under conditions of thermal stress*. NACA Rep. 1170, Supersedes NACA TN 2933**.**

Matsuishi, M. & Endo, T. (1968). *Wikipedia*. *Fatigue of metals subjected to varying stress*, Japan Soc. Mech. Engineering.

Mele, E., Calado, L., and De Luca. (2003). *An Experimental investigation on European welded connections*. ASCE 129, Journal of Structural Engineering, 0733-9445, pp. 1301-1311.

Melenk, J., and I. Babuska. (1996). *The partition of unity finite element method: Basic theory and application*. Computer Methods Appl. Mech. engrg 139, pp.289–314.

Miner, M. A. (1945).*Cumulative damage in fatigue*. Journal of Applied Mechanics, 67, A159-A164.

Morrow, J. (1968). *Fatigue design handbook- Advances in Engineering*, Warendale, PA, SAE, pp. 21- 29.

Morrow J. (1965). Cyclic plastic strain energy and fatigue of metals, *internal friction, damping, and cyclic plasticity,* ASTM STP 378, ASTM, West Conshohocken, pp.45.

MSC/NASTRAN, (2000). *Reference Manual*. MacNeal-Schwendler Corporation, Volumes 1, 2 and 3, Los Angeles ,California.

Nakano T., Masuda H., and Tanaka, A.(2003). *Experimental study on effect of reinforcements at web connected parts of WF Beam-to-SHS column connection*. Journal of Structural and Construction ,Transactions of AIJ, Vol 566, pp. 145-152, Japan.

Nastar, N., James C., Anderson, Gregg, E., Brandow, and Nigbor, R. L.(2010). *Effects of low-cycle fatigue on a ten-story steel building*. Wiley Interscisnce Struct , Design Tall Spec.Build.19, pp. 95-113, January, USA.

Nestor, P. (2004). *Fracture Mechanics*, Klumer Academic Publishers, Dordrecht.

Neuber H. (1961). *Theory of stress concentration for shear-strained prismatic bodies with arbitrary nonlinear stress-strain law*, Journal of Applied Mechanics Transactions of ASSM, Section Q, Vol. 28, pp. 544-550.

Nip, K., Gardner L., Davies C. and Elghazouli A.(2010). *Extremely low cycle fatigue tests on structural carbon steel and stainless steel*. Journal of Constructional Steel Research66,pp 96-110.[online]. Available from: http://www.elsevier.com/locate/jcsr.

Omer W., Blodgett P.E., Scott Funderburk R., Duane K., Miller P.E. and Marie Quintana, P.E.(1999). *Fabricators and erectors guide to welded steel construction*, Edition of the D1.1, The American Welding Society, Florida 33126, (800) ,pp.443-9353.

Özkumur (2004). *Ductile connection designs for welded steel column-beam subjected seismic loads*, Izmir.

Ronald, O., Hamburger, S.G., Heger and AISC. (2009). *Earthquakes and seismic design,* No.3. American Institute of Steel Construction (AISC).

Pook L. (2007). *Metal fatigue*, Spinger,ISBN 978-1-4020-5596-6, The Netherlands.

Rahman M. M., Kadirgama K., Noor M.M., Rejab M.R.M., Kesulai, S.A.(2009). *Fatigue life prediction of lower suspension arm using strain-life*, European J. of Scientific Research, 30(3), pp. 437-450.

Ralph,S. *et al.*(2001). *Metal fatigue in engineering* , 2nd edition, John Wiley & Sons.

Raman S. and Radhakrishnan V.M. (2002). *On cyclic stress-strain behaviour and low cycle fatigue life,* Department of Metallurgical Engineering, Indian Institute of Technology, Madras, Chennai-600 036, Materials and Design 23 Ž. 249_254,India

Ramberg, W., and Osgood, W. R. (1943). *Description of stress-strain curves by three parameters*, Technical Note No. 902, National Advisory Committee For Aeronautics, Washington.

Ramberg, W., and Osgood, W. R. (1943). *Description of stress-strain curves by three parameters*, Technical Note No. 902, National Advisory Committee For Aeronautics, Washington.

Ricles J.M., Mao C., Lu L., and Fisher J.W. (2002). *Inelastic cyclic testing of welded unreinforced moment connections*. Journal of Structural Engineering, American Society of Civil Engineers, 128(4), pp.429-440.

Ricles, J.M. *et al.(*2004). *Seismic performance of deep column-to-beam welded reduced beam section moment connections*. Connections in Steel Structures, Vol. 3-4, June , Amsterdam.

Righiniotis, T.D., Omer, E., and Elghazouli A.Y. (2002). *A simplified crack model for weld fracture in steel moment connections*, Elsevier Science Ltd, Engineering Structures 24, pp. 1133–1140, March, London, UK.

Righiniotis, T.D., and Imam, B.(2004). *Fracture reliability of a typical Northridge steel moment resisting connection*. Elsevier Ltd, Engineering Structures 26, pp. 381-390, UK.

Rosien, F.J.and Ostertag, C.P.(2009). *Low cycle fatigue behaviour of constraint connections part II: Influence of material parameters.* Materials and Structures 42, pp. 171-182, University of California, USA.

SAC (1997). *Protocol for fabrication, inspection, testing and documentation of beam-column connection tests and other experimental specimens*. Report no. SAC/BD-97/02, SAC Joint Venture.

Satish Kumar, S.R. and Prasada Rao, D.V. (2006). *RHS beam-to-column connection with web opening experimental study and finite element modeling*. Elsevier ltd, Journal of Constructional Steel Research 62, pp739–746, India.

Satyadevi A., Sivakumar S.M. and Bhattacharya S.S.(2007). *A new failure criterion for materials exhibiting ratcheting during very low cycle fatigue*, Materials Science and Engineering A, 452 ,pp. 380-385.

Schijve, J.(2003). *Fatigue of structures and materials in 20th Century and the State of the Art*. International Journal of Fatigue 25,Volume 25, Issue 8,pp. 679-702, Netherlands.

Shih, C.F., and German, M.D.(1981). *International journal of fracture*, Vol.17, No.1.

Smith, K.N., Watson, P. and Topper, T.H. (1970). *A stress-strain functions for the fatigue on materials*, Journal of Materials. 5(4), pp. 767-78.

Steven, R.L. (1997). *Fatigue and Fracture*. The Materials Information Society (ASM International),Vol.19.

Stojadinovic, B. (2003). *Stability and low-cycle fatigue limits of moment connection rotation capacity*. Elsevier Science Ltd, Engineering Structures 25, pp. 691–700, USA.

Surajit, K.P. (2010). *Ratcheting and low cycle fatigue behaviour of SA333 steel and their life prediction*, Journal of Nuclear Materials 40,1 17–24.

Swenson D., and Ingraffea A. (1988]). *Modelling mixed mode dynamic crack propagation using finite elements: Theory and application*. Computational mechanics 3, pp.381–397.

Tamin M.N., CSMLab, U. (2012). *Fatigue stress approach, fatigue and fracture understanding the basics*, ASM International, , ISBN-13:978-1-61503-976-0, USA.

Tevatia, A., and Srivastava, S.K. (2011). *Fatigue life prediction of connecting rod using strain-life theories* , Int. J. of Theoretical and App. Mechanics.

The British Standards Institution, (2013). *BS7910:2013 Guide to methods for assessing the acceptability of flaws in metallic structures*, ISBN 978 0 580 74334 4.

Tipple C. and Thorwald G. (2012). *Using the failure assessment diagram method with fatigue crack growth to determine leak before rupture*. SIMULIA customer conference**.**

Trajanoska B., Arsova-Miloshevska G. & Prof. Bogatinoski Z.(2000). *Numerical modeling of welded rigid beam-column connections at multi -story structures,* Faculty of Mechanical Engineering , Methodius" University Skopje, Republic of Macedonia, Balkanski, Sofia, Bulgaria.

Tucker L.E. (1972). *A procedure for designing against fatigue failure of notched parts of Automotive Engineers*. Inc., SAE paper ,720265, New York.

T73S04 (R5V2/3). (2013). *Session 38A: Ratcheting relates to knowledge & skills items1.47,1.48*.[online]. Available from: http://rickbradford.co.uk/T73S04TutorialNotes38A.pdf

Verma, P. (2011). *Ratcheting fatigue behaviour and post-fatigue tensile properties of commercial Aluminum*. [online].Thesis (MSc). Department of Metallurgical and Materials Engineering National Institute of Technology, Rourkela-769008.

Wells, A A. (1961). *Unstable crack propagation in metals: cleavage and fast fracture, Proceedings of the crack propagation symposium*, Cranfield, UK, Vol. 2, 210.

Wiesner C S, and MacGillivray H.(1999). Loading Rate Effects on Tensile Properties and Fracture Toughness of Steel. Presented at 1999 TAGSI Seminar, Held at TWI, Cambridge, UK.

Wikipedia.(2014). *The rain flow-counting algorithm*. [online]. Available from: http://en.wikipedia.org/wiki/Rainflow-counting_algorithm.

Wilkinson, S., Hurdman, G., and Crowther, A. (2006). *A Moment resisting connection for earthquake resistant structures*, Journal of Constructional Steel, Research 62 , pp. 295–302, UK.

Xue L. (2008). *A unified expression for low cycle fatigue and extremely low cycle fatigue and its implication for monotonic loading*. International Journal of Fatigue 30, pp1691–1698. [online]. Available from: http://www.elsevier.com/locate/ijfatigue

Yang X. (2005). *Low cycle fatigue and cyclic stress ratcheting failure behaviour of carbon steel 45 under uniaxial cyclic loading*. International Journal of Fatigue 27, pp1124–1132. [online]. Available from: http://www.elsevier.com/locate/ijfatigue

Yann Q., Chien-Hua H.,and Chi-Fang L. (2013), *Facture resistance of ship longitudinal members including fatigue crack*, ASME International Offshore and Arctic Engineering, OMAE, 32nd, June 9-14, Nantes, France.